DISS. ETH NO. 27748

A GEOMETRIC APPROACH TO NONLINEAR MECHANICAL VIBRATIONS: FROM ANALYTIC TO DATA-DRIVEN METHODS

a thesis submitted to attain the degree of
DOCTOR OF SCIENCES of ETH ZURICH
(Dr. sc. ETH Zurich)

presented by
MATTIA CENEDESE
M.Sc. in Mechanical Engineering, Politecnico di Milano
M.Sc. in Mechanical Engineering, Politecnico di Torino
born on 15.03.1992
citizen of Italy

accepted on the recommendation of
Prof. Dr. George Haller
Prof. Dr. Melih Eriten

2021

To my ladies,
Roberta, Sophie & Zoe

ABSTRACT

This doctoral thesis devises analytical and data-driven methods for the analysis of nonlinear vibrations in mechanical systems, potentially with a large number of degrees of freedom. Modern challenges in engineering require deeper understanding of nonlinear oscillations in mechanical systems, as well as extracting data-driven models for their predictions.

In the first part of this thesis, the focus is set on analytical models, with forced-damped nonlinear mechanical systems viewed as small perturbations from their energy-preserving counterpart. Indeed, weakly damped mechanical systems under small periodic forcing tend to showcase periodic response in a close vicinity of some periodic orbits of their conservative limit. Specifically, amplitude frequency plots for the conservative limit have frequently been observed, both numerically and experimentally, to serve as backbone curves for the near-resonance peaks of the forced response. A systematic mathematical analysis is then derived, allowing to predict which members of conservative periodic orbit families will survive in the forced-damped response. Moreover, the method is not limited to predicting existence, but can also forecast stability type of vibrations in the forced response. Not only does this method provide a rigorous analytical tool, but it also finds precise mathematical conditions under which approximate numerical and experimental approaches, such as energy balance and force appropriation, are justified.

The second part of this thesis looks at oscillatory dynamics from a data-driven perspective. The objective is to determine reduced-order models from trajectory data of dynamical systems. Based on the theory of spectral submanifolds, a method is developed for simultaneous dimensionality reduction and identification of the dynamics in normal form. In contrast with other data-driven modeling techniques, the normal form of the dynamics offers valuable insights and is capable of predictions when small perturbations, such as external forcing, are added to systems. Moreover, there are, in principle, no restrictions of dimensionality or constraints on the states observed in the trajectory data. The algorithm based on this approach automatically detects the appropriate normal form for a given set of trajectories, thereby providing an intelligent, unsupervised learning strategy for dynamical systems. The accuracy and the validity of the method is demonstrated on different examples, featuring data from numerical simulations and physical experiments.

SOMMARIO

Lo scopo della presente tesi di dottorato è quello di sviluppare metodi sia analitici che basati su dati per lo studio di vibrazioni non lineari in sistemi meccanici, potenzialmente caratterizzati da un elevato numero di gradi di libertà. In tale ambito, le sfide ingegneristiche dell'epoca contemporanea necessitano, come fondamento, sia di una profonda comprensione fenomenologica, sia della possibilità di estrarre, da misure di oscillazioni, modelli predittivi in modo diretto.

La prima parte di questo lavoro è focalizzata sui modelli analitici. Specificatamente, si esaminano sistemi meccanici, aventi smorzamento e forzanti esterne, i quali vengono considerati come perturbazioni della loro controparte ideale, ove l'energia si conserva. Infatti, suddetti sistemi hanno la tendenza a mostrare risposte periodiche nel tempo, molto vicine a quelle del limite conservativo, almeno per smorzamenti deboli e forzanti piccole. In particolare, da osservazioni sia numeriche che sperimentali, si riscontra come i diagrammi ampiezza-frequenza caratteristici del sistema conservativo, tendano a strutturare le risposte in frequenza per i sistemi perturbati nelle regioni di risonanza. La giustificazione di queste considerazioni è presentata dallo sviluppo di uno studio matematico rigoroso, il quale mira a predire quali delle traiettorie del sistema conservativo sopravvivano all'avvento di forzanti esterne e di dissipazioni dovute allo smorzamento. Il metodo implementato inoltre, riesce anche a stimare la stabilità delle vibrazioni presenti nella risposta forzata. Le implicazioni di tale teoria stabiliscono quindi, le condizioni matematiche precise per cui metodi approssimati, sia numerici che sperimentali, si possano rivelare esatti.

La seconda parte di questa tesi esamina la dinamica delle oscillazioni da una prospettiva basata interamente sui dati. L'obiettivo dello studio consiste nel determinare modelli ridotti, a partire dalle misure sperimentali di un sistema meccanico. Viene perciò sviluppato un metodo, basato sulla teoria delle varietà differenziabili spettrali (*spectral submanifolds*), il quale, simultaneamente, riduce le dimensioni e identifica la forma normale della dinamica. In confronto con altre tecniche di modellazione fondate sui dati, la forma normale non solo permette una profonda comprensione della dinamica, ma risulta anche molto proficua per l'indagine del sistema considerato qualora fossero presenti perturbazioni, *exempli gratia* dovute a forzanti esterne. Inoltre, in principio, il numero di gradi di libertà e la tipologia di misure eseguite non sono in alcun modo vincolati o limitati. Per tali motivazioni, l'algoritmo risultante da tale teoria stima automaticamente la forma normale, la cui dinamica descrive i dati. Conseguentemente, il codice delinea una strategia adattiva per l'apprendimento intelligente dei sistemi dinamici. In ultima istanza, l'accuratezza e la validità del metodo descritto vengono dimostrate con l'ausilio di molto esempi, i cui dati derivano da simulazioni numeriche o da esperimenti di laboratorio.

Considerate la vostra semenza:
fatti non foste a viver come bruti,
ma per seguir virtute e canoscenza.
Dante Alighieri, Divina Commedia,
Inferno XXVI, 118-120 (1321).

ACKNOWLEDGMENTS

The mechanics of several spectacular phenomena happening in nonlinear dynamics often depend on a multitude of different elements, each of which, either more or less, is unavoidably necessary for achieving the result. The developments described in this doctoral thesis, in a similar way, are the outcome of an intense work that could not have been accomplished without the contributions, either direct or not, of several people.

I wish to express my deepest gratitude to my supervisor, George Haller. From the very first day, working with him has been a pleasure, and I am thankful for all technical discussions, professional advice, personal conversations, incredible opportunities and unconditional support I have received from him during my years of doctoral studies. I truly admire George's never-ending curiosity, deep passion, analytical mindset with which he inspires people around him, bringing the best out of them. I am honored to have worked with him.

I would like to thank my co-examiner, Melih Eriten, not only for taking the time to go through my work, but also, most importantly, for actively collaborating in some of my projects. I thank Melih for being a part of my examination committee and Dennis Kochmann for chairing it. I also need to say a big thank you to my M.Sc. thesis supervisor Francesco Braghin, for his dedication and support on helping me in reaching my goals, both academically and professionally.

My life during the doctorate as well as the evolution of this work would not have been the same without all the distinguished members of George's group. Besides sharing daily routines and valuable intellectual exchanges with talented colleagues, I found some true friends for life. I would address special thanks to Shobhit, Sten, Thomas, Stergios, Jacopo, Andrea and Joar for their important contributions in directing my journey on the right tracks. I am also thankful to Beate for her attentive support.

I thank Harry Dankowicz and Jan Sieber for organizing the Advanced Summer School on Continuation Methods for Nonlinear Problems 2018. Moreover, I wish to thank Matthew Brake for having me at Tribomechadynamics Research Camp 2019 and for his guidance during all this project. These two experiences contributed considerably to giving me tools and knowledge for advancing in my doctoral work.

There are no words to stress enough the importance of the unconditional support of my family and friends, all of them. I was really lucky to grow up with the passion of understanding how things work and with the perseverance to commit. I wish to express my deepest gratitude to my parents Antonella and Fabio for being my genuine and perpetual foundations, to my grandparents for inspiring me with their example, to my siblings Maddalena and Alberto for their contagious proactivity, to my eternal friend Riccardo for his enthusiasm and to Giusy and Gian Piero for their trust. I also need to thank Zoe, for giving me mindfulness in viewing life from an always-in-motion, four-legged perspective. Finally, thank to my fiancée Roberta, for giving me never-ending strength, steel-plated motivation, sharp resolution, and, simply, her true love.

CONTENTS

1

PREFACE

Oscillations are ubiquitous. From the essence of subatomic particles to gravitational waves in the universe, from the terrific sound of an engine to the precise beating of a clock, from the dramatic motions during an earthquake to the gentle swinging of a cradle. Human life is strongly connected to oscillations, being these either beneficial or detrimental. Oscillations can appear in time as steady states, such as periodic, quasi-periodic and chaotic signals, and as decaying or growing vibrations, cf. Fig. 1.1. Scientists and engineers historically seek to understand oscillations for making predictions, to take advantage of them in applications, or to control them to avoid potentially critical consequences.

Engineering systems keep pushing the limit to reach new frontiers in the technological development. Unavoidably, this innovation requires more accurate models, faster computations and deeper understanding of data. For example, sustainability constraints in airplane fuel consumption or economical ones in reusable launch systems can be satisfied by removing weight, hereby making the structure more prone to large-amplitude oscillations. Here, linear-only models would fail in their predictions. In general, performance improvements in mechanical systems, either on the structural side or on the control one, can be achieved via accurate identification of their nonlinear characteristics. Nowadays, the abundance of data is changing world's perspective, and extracting nonlinear equations of motion directly from data is becoming more and more important, especially in areas where analytical models struggle in giving satisfactory results (e.g., assembled structures, fluid dynamics, epidemiology). However, due to their complexity, nonlinear models entail a consistent change in the mindset with respect to that adopted for their linear counterpart, both in numerical simulations and in analyses of data.

From pioneering studies in nonlinear oscillations by Poincaré [1], Van der Pol [2] and Duffing [3] through the milestone contributions of Guckenheimer and Holmes [4] and of Nayfeh and

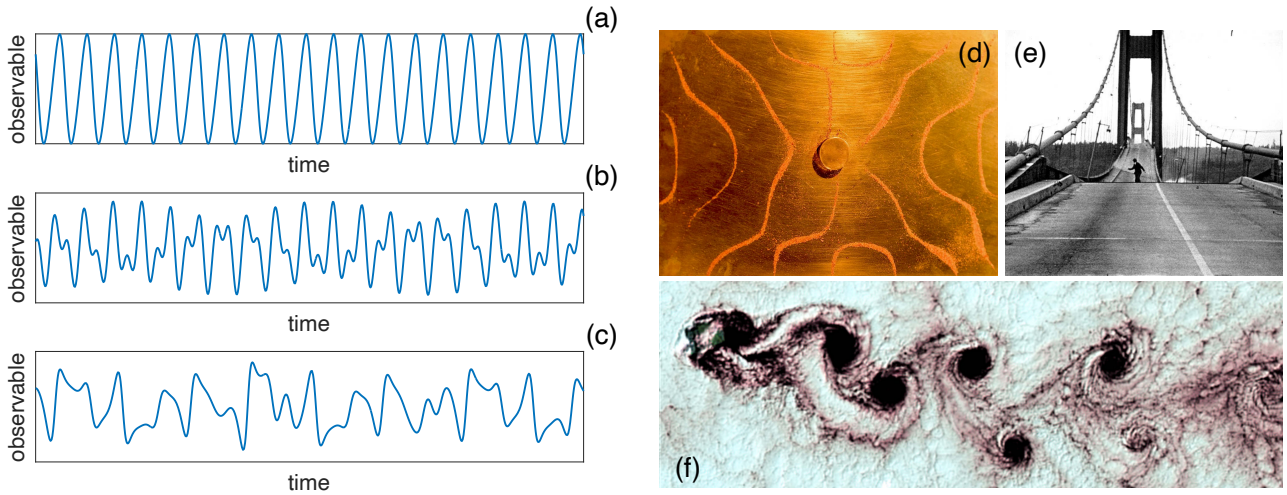

Figure 1.1: Vibrations in pictures. Plots (a,b,c) show the time evolution of periodic (a), quasi-periodic (b) and chaotic (c) signals. Picture (d) visualizes the oscillation patterns of a plate using sand (Matemateca IME-USP / Rodrigo Tetsuo Argenton). Picture (e) catches the writer and photographer Howard Clifford running off the Tacoma Narrows Bridge during collapse in 1941 due to massive oscillations (Wikimedia Commons / UW Digital Collections). Picture (f) shows swirling clouds arranging in a vortex street over Alexander Selkirk island in the southern Pacific ocean (USGS National Center for EROS / NASA Landsat Project Science Office).

Mook [5], current challenges in this field typically deal with high-dimensional systems and, more frequently, call for a data-driven attitude. For mechanical systems in this context, there is demand for understanding their dynamics, building reduced-order models for computational speed ups and identifying nonlinear features from data. Implications for advances in these fields range from design to testing or operational phases of mechanical devices. For example, deeper understanding unlocks innovation for designs and controls, allows for diminutions of computational time and targets experiments for testing. Another example is the quantitative determination of dissipative effects that, due their complexity, can only be addressed through the investigation of system measurements [6].

1.1 BACKGROUND

1.1.1 *Analytical models*

Modeling in the context of mechanical engineering relies on three principal ingredients, namely kinematics, constitutive relations and first principles [7, 8]. Blending these together generates the equations of motion, which typically appears in the form of differential equations that can be integrated in time from a prescribed initial state, after having applied eventual boundary conditions. These models can be either made up by lumped elements or by continuous media. In the latter case, the modeling phase is followed by a discretization in finite elements [8, 9], which allows numerical simulations.

Hence, analytical models for mechanical systems generally take the form of nonlinear ordinary differential equations [10, 11], potentially featuring a very high number of degrees of freedom. Closed-form solutions are seldom available and computer simulations, despite the constant rise in computational capabilities, remain still unfeasible for some applications (e.g., design, control) and for several classes of systems. An example is the case of system characterized by weak damping, strong nonlinearity and high dimensionality [12].

To cope with the curse of dimensionality, researchers tackle the development of reduced-order models. The key idea is to manipulate the equations of motion to compress the dynamics into a low number of meaningful directions, so that the resulting surrogate model preserves the accuracy of the full-order one, while being evaluated at insignificant computational cost. Available approaches range from techniques based on linear projections [8, 9, 13, 14], to rigorous exact model reduction supported by invariant manifolds (e.g., Lyapunov subcenter manifolds [15, 16], nonlinear normal modes [17], spectral submanifolds [18–20]). Nevertheless, the validity of the reduced-order models in replacing full-order ones ultimately depends on the motion amplitudes and on the characteristics of external forcing [21, 22].

A primary objective in the study of oscillations in mechanical systems is the computation of the forced-frequency response curve [5, 23], examples of which are shown in Fig. 1.2(a). This curve represents the system response at different frequencies under periodic forcing, which is among the most common types of excitations in engineering applications. In particular, the near resonance zones, where forcing frequency is almost aligned with one of the system natural frequencies, are of critical interest because of possible dynamic amplification effects. Indeed, the system response in these zones can be dramatically large even with tiny external forcing. Hence, the forced-frequency response curve is of paramount importance, both for the design and the operational phase of a mechanical apparatus. Having said that, the forced-frequency response curve for nonlinear systems only shows periodic trajectories of the system, whereas for linear system, due to the superposition principle [8], depicts all information about system motions. Indeed, trajectories in the presence of nonlinearities can converge to other attractors (either quasi-periodic or chaotic), which are not reported in the forced-frequency response curve. Therefore, these diagrams require attentive interpretation for nonlinear dynamical systems.

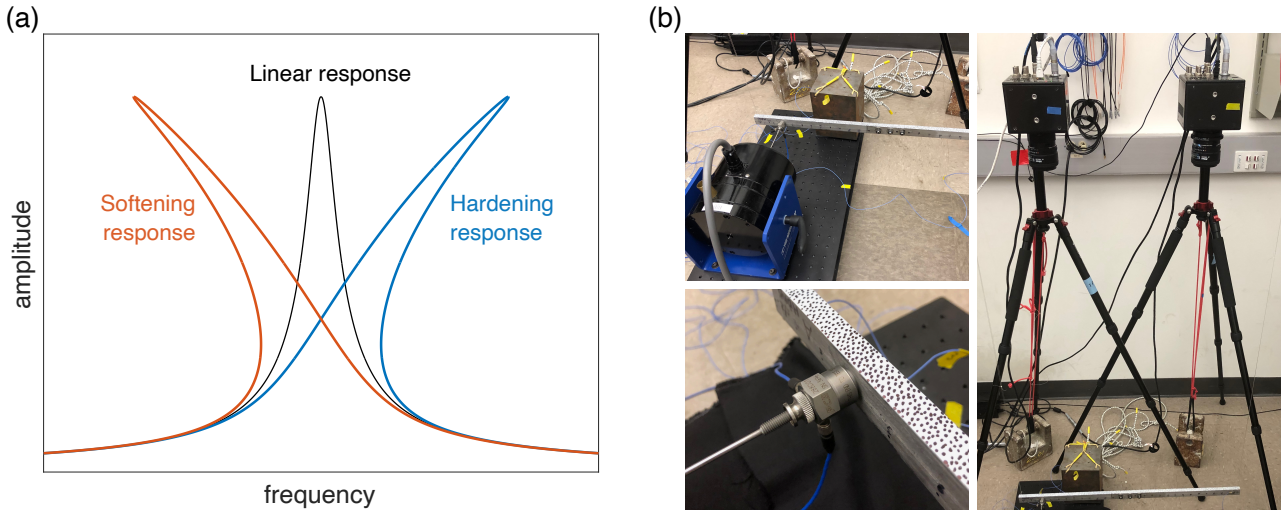

Figure 1.2: Plot (a) illustrates forced-frequency response curves for classic model of Duffing oscillator, in the linear case and in presence of softening and hardening nonlinearity. The collection of pictures in (b) shows the experimental setup for a test structure, later discussed in chapter 10.3 of this thesis. Measurements are taken using accelerometers and high-speed cameras for digital image correlation.

The derivation of the forced response curve from numerical models can be performed using direct time integration or numerical continuation techniques, either via shooting methods [24], harmonic balance [25] or collocation [26]. Approximate solutions, whose validity may be limited in time or in motion amplitude, can be extrapolated from these models, although this is often attainable only for low-degree-of-freedom systems (e.g., multiple scales [5], averaging [27], the first-order normal form technique [28] or the second-order normal form technique [29]). Both numerical integration and continuation methods scale dramatically with dimensionality, and the performances of the former are also extremely affected by the amount of damping.

1.1.2 *Experimental techniques*

Over the last two decades, there have been significant investments in developing nonlinear system identification methods in experimental modal analysis [30, 31]. This identification problem is currently tackled using a toolbox approach, where different techniques are employed depending on the structural system under investigation, the identification goals and the type of excitation used.

Typical excitations trigger either decaying oscillations (also called ringdown signals or responses) or forced steady-states. While a shaker is typically used to achieve the latter, decaying oscillations are initiated via imposed initial conditions, through hammer impacts or with the aid of a shaker, which is then turned off or relased from the structure [32,33]. As a consequence of technological developments, the possible measurements of the system is constantly growing. From the classic point measurements of accelerometers and strain gauges, nowadays non-contact 2D or 3D field measurements are becoming increasingly popular, either performed using laser scanner vibrometer (displacement, velocity) [34] or digital cameras in the context of digital image correlation (displacement, strain) [35–37], cf. Fig. 1.2(b).

Experimental techniques that are well-consolidated in the field of nonlinear mechanical vibrations typically deal with single-mode oscillations. Indeed, when additional modes are present, it is common practice to filter the signal or to look at it as a linear combination of multiple modes [38]. While insightful, these practices may miss potential coupling among modes. When applied to decaying

single-mode oscillations, these techniques seek to reconstruct the curves representing amplitude-dependent properties of frequency and damping [31]. The zero crossing method, the Hilbert method, the short-time Fourier transform, and the wavelet-based identification methods [30,39–41] are popular non-parametric identification methods. As shown by recent advances, these amplitude-dependent properties play a key role in shaping the forced-damped frequency response in near-resonance zones, at least for small forcing [23,42,43]. Alternatively, forced-frequency response curves can be directly extracted using a shaker with force appropriation [44] and experimental continuation [45]. Each method may be suitable depending on the specific system to analyze, the available measurements, the possible excitations and the scope of the identification.

1.1.3 *Data-driven models*

Advances in machine learning and in data science are stimulating a consistent growth in this field, justified by the shortfall of empirical models or of those based on first principles, at least in some classes of problems [46,47]. From the parameter identification in classic models in nonlinear vibrations [48] (e.g., the Duffing oscillator and its coupled versions) or finite element updating techniques [49], new advances push towards models that accurately reconstruct the data exploiting machine learning techniques. Regression estimates in different forms (ridge [50], LASSO [51], SINDy [52]), neural networks [53] (fully connected, convolutional, recurrent) are increasingly used by practitioners for devising either equations of motion [54] or constitutive relations [55].

Dimensionality reduction is frequently unavoidable in the data-driven context too. From the canonical principal component analysis [56] to modern manifold learning methods [57], dimensionality reduction is often the first step for identifying data-driven models in high-dimensional datasets. Dynamic mode decomposition [58], which became popular in the last decade within the fluid dynamics community [59], manages to recognize a low-number of patterns in the dynamics that are used for building a reduced-order data-driven model.

Not being based on first principles, these models may generate unphysical results [60,61]. Therefore, research is also focusing on hybrid models [62,63], for which a high-confidence first-principles-based term is augmented with an additional black-box component that, capitalizing on data, models effects that are difficult to grasp by analytical inference [64]. Alternatively, research advances towards physics-informed machine learning methods, fitting their algorithms with first principles [60,61].

Despite their success in some areas, data-driven models are currently suffering from three drawbacks. First, the results are very sensitive to the model hyperparameters (e.g., the architecture for neural networks), so that, fine tuning of this models is a challenge and typically requires extensive periods of time [46]. Second, the majority of these models is difficult to interpret. Third, extrapolations to datapoints outside the training range are notoriously unreliable.

1.2 SUMMARY OF THE RESULTS AND THESIS ORGANIZATION

This thesis consists of two main parts, with Part I dealing with analytical models, and with Part II discussing data-driven models. Despite an intrinsic difference, the overall aim remains capturing the complexity of oscillations occurring in nonlinear dynamical systems, providing both predictive and quantitative tools for engineers and scientists. The methods developed for pursuing this goal are built on exact mathematical results, which guarantee universal applicability and reliability, without compromising the performances. Indeed, we undertake a geometric approach [4] to dive into nonlinear oscillations, so that, by understanding the phase-space geometry of nonlinear oscillations, we construct a framework that is, at the same time, capable of gaining insights beyond providing quantitative tools.

Part I regards the analysis of forced-damped mechanical systems as perturbations from their conservative limit, motivated by the fact that mechanical systems are often characterized by weak damping and small forcing. Here, we develop an exact mathematical theory that establishes an important connection between ideal energy-preserving dynamics and that of real-life systems that are unavoidably affected by non-conservative forces. For the case of periodic orbits, similar results were available in literature, but only restricted to weakly nonlinear and/or low-degrees-of-freedom systems. With our approach, we generalize these results to potentially high-dimensional models, without any limitation on the amplitudes or on the type of nonlinearities affecting the system. This analytical connection can be exploited to predict existence and stability of forced-damped frequency responses in near-resonance regions, which is of fundamental importance in engineering applications. This prediction is only based on the knowledge of the conservative limit and on the type of non-conservative forces acting on the system. Hence, we do not require any direct simulation of the forced-damped system. Our approach expedites the study of parameter variations in non-conservative forces. This finding is particularly valuable for damping, which is often affected by consistent uncertainty. Moreover, our method is also useful to predict potentially critical isolated responses, whose existence is challenging to assess via direct numerical simulations. Another important implication of our analytical method is the justification of experimental methods that track backbone curves of forced frequency responses. The outcomes of this research were published in the peer-reviewed journal articles:

1. M. Cenedese and G. Haller. How do conservative backbone curves perturb into forced responses? A Melnikov function analysis. *Proceedings of the Royal Society of London A: Mathematical, Physical and Engineering Sciences*, 476:20190494, 2020. DOI: 10.1098/rspa.2019.0494.

2. M. Cenedese and G. Haller. Stability of forced–damped response in mechanical systems from a Melnikov analysis. *Chaos: An Interdisciplinary Journal of Nonlinear Science*, 30(8):083103, 2020. DOI: 10.1063/5.0012480.

Part I of this thesis is based on these two publications. Here, after a detailed introductory chapter, we discuss some relevant background on conservative families of periodic orbits in chapter 3, while chapters 4 and 5 present our method for predictions of existence and stability for perturbed periodic orbits, respectively. These chapters contain the mathematical proofs of our results and discuss several examples dealing with mechanical oscillators. In particular, we show how isolated responses can arise due to nonlinear damping, and we analyze the stability of periodic motions in a gyroscopic system.

Part II deals with a method developed for learning nonlinear dynamics from trajectory data, where this latter is either coming from numerical simulations or from physical experiments. The objective of this work is the discovery of explicit, nonlinear, reduced-order models for potentially high-dimensional dynamical systems. We focus on transient data in the neighborhood of an equilibrium point and, by capitalizing on spectral submanifold theory, we develop a methodology for data-driven model reduction and for the identification of the dynamics. Our models, based on the concept of normal forms, provide analytical insights and can make predictions outside the range of the training data. This is an advantage with respect to several machine learning techniques, which indeed perform poorly when extrapolating datapoints outside the training data. We illustrate the power of this method on examples from different areas of mechanics, from structural vibrations to fluid dynamics. The examples also feature different types of measurements, ranging from scalar quantities (e.g., the velocity of a material point) to partial-state or full-state measurements. In the context of mechanical systems, we show how our model, built on transient data decaying towards the equilibrium, is able to predict the forced-frequency response in near-resonant zones with high accuracy. Developments of this work were presented at international conferences, and took advantage

of a research collaboration project focusing on nonlinear system identification, communicated in the papers:

3. W. Chen, D. Jana, A. Singh, M. Jin, M. Cenedese, G. Kosova, M. R. W. Brake, C. W. Schwingshackl, S. Nagarajaiah, K. J. Moore & J. Noël. Measurement and identification of the nonlinear dynamics of a jointed structure using full-field data; Part I – Measurement of nonlinear dynamics, *Mechanical Systems and Signal Processing* 166:108401, 2022. DOI: 10.1016/j.ymssp.2021.108401.

4. M. Jin, G. Kosova, M. Cenedese, W. Chen, A. Singh, D. Jana, M. R. W. Brake, C. W. Schwingshackl, S. Nagarajaiah, K. J. Moore & J. Noël. Measurement and identification of the nonlinear dynamics of a jointed structure using full-field data; Part II - Nonlinear system identification, *Mechanical Systems and Signal Processing* 166:108402, 2022. DOI: 10.1016/j.ymssp.2021.108402.

The data-driven reduced-order modeling technique described in the second part of this thesis has been implemented in the MATLAB®-based computational package `SSMLearn` (available at github.com/mattiacenedese/SSMLearn), and this research has been reported in the articles:

5. M. Cenedese, J. Axås, B. Bäuerlein, K. Avila and G. Haller, Data-driven modeling and prediction of non-linearizable dynamics via spectral submanifolds. *Nature Communications*, accepted for publication, 2022. Preprint available on *arXiv*:2201.04976.

6. M. Cenedese, J. Axås, H. Yang, M. Eriten and G. Haller. Data-driven nonlinear model reduction to spectral submanifolds in mechanical systems. Under revision at *Philosophical Transactions of the Royal Society A: Mathematical, Physical and Engineering Sciences*, 2022. Preprint available on *arXiv*:2110.01929.

After the introduction of Part II, in chapter 8 we present some background on spectral submanifolds and their embeddings in observable spaces. Our data-driven method is discussed in detail in chapter 9, while the case studies of application are discussed in chapter 10. Concluding remarks for the two parts are given in sections 6, 11, while chapter 12 concludes this thesis and discusses future outlooks.

Part I

FORCED-DAMPED MECHANICAL SYSTEMS AS PERTURBATIONS FROM THEIR CONSERVATIVE LIMIT

2

INTRODUCTION

Conservative families of periodic orbits, broadly known as nonlinear normal modes (NNMs) in the field of structural engineering, often appear to shape the behavior of mechanical systems even in the presence of additional damping and time-periodic forcing. Not only has this influence been noted for low-amplitude vibrations of a small number of coupled oscillators, but it also appears to hold for large amplitude motion in arbitrary degrees of freedom. Various descriptions of this phenomenon are available in the literature, ranging from the original introduction of NNMs by Rosenberg [65] to the more recent reviews lead by Vakakis [66–68], Avramov and Mikhlin [69,70] and Kerschen [17]. These studies suggest that forced-damped frequency responses might bifurcate from conservative NNMs. To summarize features of such bifurcations, Fig. 2.1 qualitatively represents possible nonlinear phenomena in the frequency response. Dark and light red curves show steady-state solutions for a periodically forced-damped mechanical system for low and high forcing amplitudes, respectively. Blue curves correspond to amplitude-frequency relations of periodic orbit families of the underlying conservative system, which we refer to as conservative backbone curves. Grey curves depict backbone curves of the forced-damped response, defined as the frequency locations of amplitude maxima under variation of the forcing amplitude [5]. Solid and dashed lines distinguish stable and unstable responses respectively. The first and fifth resonances in Fig. 2.1 show the classic hardening and softening resonance trends respectively, characterized with their hysteretic behavior in the stability. As most frequently observed behaviors, these two phenomena have been broadly studied: see, e.g. [5,17,71,72] for analytical and numerical treatments and [73,74] for experimental results. In these settings, as the response amplitude increases, the backbone curves of the conservative limit and those of the forced-damped system have been noted to pull apart [75]. Th

The backbone curves of the second peak from the left in Fig. 2.1 feature a non-monotonic trend in frequency, i.e., softening for lower amplitudes and hardening for higher ones. This type of behavior is relevant for shallow-arch systems [76], MEMS devices [77] and structural elements [78], while a simple mechanical example is available at [79,80]. The third peak of Fig. 2.1 shows an isolated response curve (isola) that may occur due to the influence of nonlinear damping [81] or symmetry breaking mechanisms [82]. In the former case, the isola can join with the main branch when the forcing amplitude exceeds a certain threshold [83], as indicated by the light-red curve, and can have multiple types of stability. Subharmonic responses, displayed along the second blue line from the right, also show up as isolated branches, as they cannot originate from the linear limit [5]. Finally, as highlighted in [84] with the analysis of a simple model of nonlinear beam, not all NNMs contribute to shaping the forced-response, as illustrated by the second-last backbone curve in Fig. 2.1. Instead, the rightmost backbone curve shows split in multiple branches, and this could trigger also change in stability for periodic solutions [85,86]. Branching could potentially trigger isolated responses of the frequency response, as well as complex dynamical behavior near the bifurcation point [82,87].

Analytic relations between conservative families of periodic orbits and frequency responses are only available for specific, low-dimensional oscillators from perturbation expansions that assume the conservative periodic limit to have small amplitudes. These expansions may arise from the method of multiple scales [5], averaging [27], the first-order normal form technique [28] or the second-order normal form technique [29]. Based on this latter method, Hill *et al.* [88] developed an energy-transfer formulation for locating maxima of the frequency response along conservative backbone curves. However, the authors a priori postulate a relation between conservative oscillations and frequency responses, and also discuss potential limitations arising from this assumption in [88]. Vakakis and Blanchard in [89] show the exact steady states of a strongly nonlinear periodically forced and damped Duffing oscillator. They also clarify how these forced-damped periodic motions are

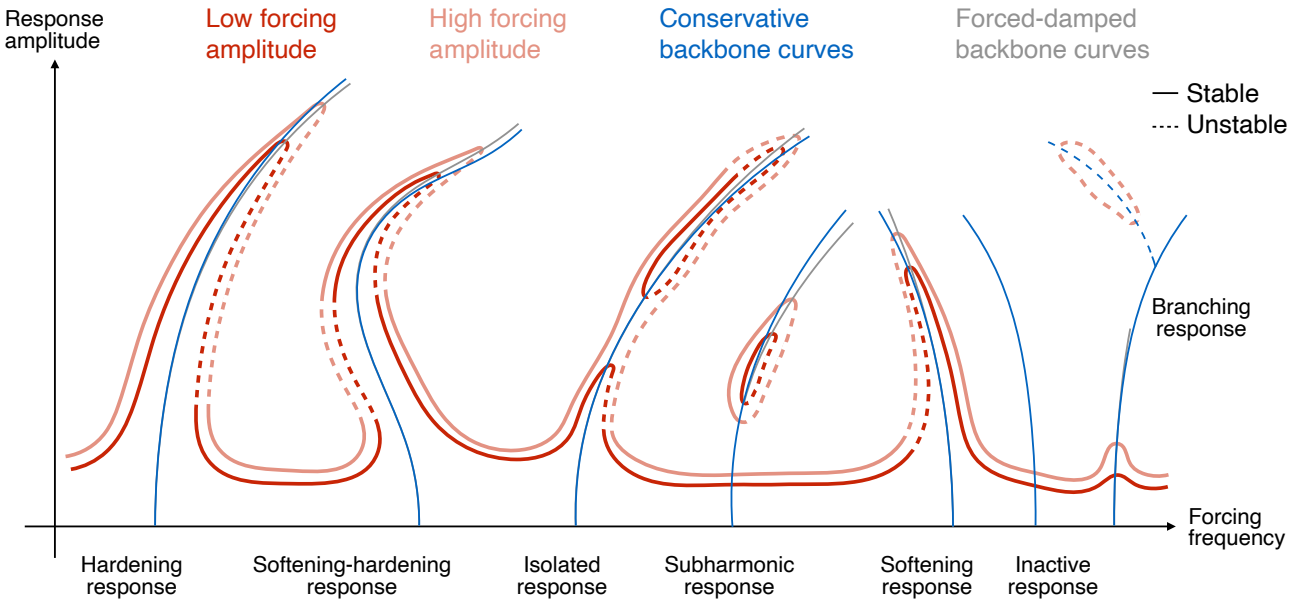

Figure 2.1: Illustration of frequency response phenomena in mechanical systems. The dark and light red curves identify the frequency response for low and high forcing amplitudes, respectively, while blues curves depict conservative backbone curves and grey curves represent forced-damped backbone curves. Solid and dashed lines distinguish stable and unstable responses respectively.

related the conservative backbone curve, but they restrict the discussion to specific types of periodic forcing.

Relying on exact mathematical results, spectral submanifold (SSM) theory [18, 23] has been developed for the local analysis of damped, nonlinear oscillators. This approach is insensitive to the number of degrees of freedom thanks to the automated procedure developed in [90] and can be hence used for exact nonlinear model reduction. SSMs, however, do not exist in the limit of zero forcing and damping, in which case they are replaced by Lyapunov subcenter manifolds (LSMs) [91]. The relationship between the dynamics on damped, unforced SSMs and LSMs is now established in a small enough neighborhood of the unforced equilibrium point [23, 83].

Even though diverse numerical options are available to explore forced responses, analytical tools applicable to arbitrary degrees of freedom and motion amplitudes are still particularly valuable. Not only can such tools help with the analysis of several perturbation types by relying only on the knowledge of conservative orbits, but they can also overcome limitations of numerical routines. For a thorough review of these limitations, we refer the reader to [21]. For example, direct numerical integration needs long computational time for high degrees of freedom systems with small damping and it is limited to stable periodic orbits. Despite being very accurate, numerical continuation (shooting methods [24], harmonic balance [25] or collocation [26]) suffers from the curse of dimensionality. Furthermore, it can efficiently compute the main branch of the forced response for frequencies away from resonance, but fails to find isolated branches when their existence and location is not a priori known. For the assessment of stability, common approaches rely either on Floquet's theory [4, 92] in the time domain, or on Hill's method in the framework of harmonic balance [93, 94], which may suffer of issues due to computational complexity and convergence problems.

In a parallel development, SSMs, backbone curves, main and isolated branches can now be computed efficiently for general, forced-damped, multi-degree-of-freedom mechanical systems up to any required order of accuracy [83]. This approach also yields analytic approximations for backbone curves and isolas, as long as these stay within the domain of convergence of Taylor expansions constructed for the forced-damped SSMs [83]. Based on the relationship of SSMs with

their conservative limit [16, 23, 95], known as Lyapunov subcenter manifold [15, 91], the stability of forced-damped response can be analytically and numerically determined for small amplitudes [23, 83].

Beyond these numerical approaches, experimental methods would also be aided by a rigorous mathematical relation between conservative backbone curves and forced-damped responses. One of such methods has been developed by Peeters *et al.* [44, 73], who propose an extension of the phase-lag quadrature criterion, well-known for linear systems, to nonlinear systems in order to isolate conservative NNMs experimentally. Their method assumes that the nonlinear periodic motion is synchronous [65], the damping is linear (or at least odd in the velocity) and the excitation is multi-harmonic and distributed. The idea is to subject the system to forcing that exactly balances damping along a periodic orbit of the conservative limit. Peeters *et al.* find that such a balance holds approximately when each harmonic of the conservative periodic orbit has a phase lag of 90° relative to the corresponding forcing one. Force appropriation [32, 96] and control-based continuation [45] exploit the phase-lag quadrature criterion for systematic tracking of backbone curve.

Another related experimental method in need of a mathematical justification is resonance decay [44], which uses a force appropriation routine to isolate a periodic orbit, then turns off the forcing and assumes the response to converge to the equilibrium position along a two-dimensional SSM, sometimes called a damped-NNM [97]. This technique is expected to provide an approximation of conservative backbone curves, but it remains partially unjustified for two reasons. On the analytical side, it assumes a yet unproven purely, parasitic effect of damping on the response. On the experimental side, decoupling the shaker from the system remains a challenge that affects the accuracy of the results.

Despite available experimental and numerical observations, it is unclear if and when conservative NNMs perturb into forced-damped periodic responses. This is because periodic orbits in conservative systems are never structurally stable under generic perturbations, which tend to destroy them [4]. Indeed, any conservative periodic orbit has at least two Floquet multipliers equal to $+1$ due to the conservation of energy [85], rendering the orbit structurally unstable. Classic analytic approaches [98–100] to generic, non-autonomous perturbations of normally hyperbolic periodic orbits are therefore inapplicable in this setting. Conservative NNMs exist in families that are only guaranteed to persist under small, smooth conservative perturbations [85, 101].

In its simplest form, the study of dissipative perturbations on a conservative family of periodic orbits dates back to Poincaré [1], developed further by Arnold [102]. An important contribution was made by Melnikov [103], who focused on dissipative perturbations of planar Hamiltonian systems. His approach reduces the persistence problem of periodic orbits to the analysis of the zeros of the *subharmonic Melnikov function* [4, 104, 105]. As extensions of Melnikov's approach, studies on two-degree-of-freedom Hamiltonian systems are available: [106, 107] consider the fate of periodic orbit families in an integrable system subject to Hamiltonian perturbations, while [108] analyzes two fully decoupled oscillators under generic dissipative perturbations. Subharmonic Melnikov-type analysis for non-smooth systems is also available; see [109] for examples of planar oscillators and [110, 111] for a system with two degrees of freedom. All these results, therefore, require low-dimensionality and integrability before perturbation, neither of which is the case for the conservative limits of nonlinear structural vibrations problems arising in practice.

As an alternative to these analytic methods, Chicone [112–114] established a perturbation method for manifolds of isochronous periodic orbits without any restriction on their Floquet multipliers or assumptions on integrability/coupling before perturbation. This elegant approach exploits the Lyapunov-Schmidt reduction to obtain a generic multi-dimensional bifurcation function for the persistence of single orbits. Furthermore, this method has also been extended for non-smooth (but Lipschitz) dynamical systems [115]. However, these results are not directly applicable to the typical setting of nonlinear structural vibrations. Moreover, an exact resonance condition is required in

Chicone's method, even though perturbed periodic orbits are often observed when the forcing frequency clocks in near-resonance with the frequency of a periodic orbit of the conservative limit.

In this thesis, we develop an exact analytical criterion for the perturbation of conservative NNMs into forced-damped periodic responses, thereby predicting the variety of behaviors depicted in Fig. 2.1, including their stability type. We assume that the conservative limit of the system has a one-parameter family of periodic orbits, satisfying generic nondegeneracy conditions. We then study the persistence or bifurcation of these periodic orbits under small damping and time-periodic forcing. Utilizing ideas from Rhouma and Chicone [114], we reduce this perturbation problem to the study of the zeros of a Melnikov-type function, generalizing therefore the original Melnikov method to multi-degree-of-freedom systems. Our approach relies on the smallness of dissipative and forcing terms which is generally satisfied in structural dynamics, but we will not assume that the unperturbed periodic orbit has small amplitude. This distinguishes our approach from various classic perturbation expansions that assume closeness from the unforced equilibrium. Our analysis also differs from classic Melnikov-type approaches in that it does not require the conservative limit of the system to be integrable. Indeed, for our unperturbed conservative limit, we only require the existence of a generic family of periodic orbits that may only be known from numerical continuation. For the analytical assessment of stability, we recover powerful formulas when the system is written in Hamiltonian form.

When our Melnikov-type method is applied to mechanical systems, it provides a rigorous justification for the classic energy principle, a broadly used but heuristic necessary condition for the existence of periodic response in forced-damped nonlinear oscillations [44, 82, 88]. Our analysis shows that under further conditions, the energy principle becomes a rigorous sufficient condition for nonlinear periodic response and extends to arbitrary number of degrees of freedom, multi-harmonic forcing, large-amplitude periodic orbits and higher-order external resonances.

In addition to giving a mathematical formulation for general dynamical systems, we also consider the classic setting of nonlinear structural vibrations. In that context, our results reveal how the near-resonance part of the main and isolated branches of the periodic response diagram are born out of the conservative backbone curve, including a general analytical condition for the hysteretic behavior. We also discuss how our results justify the phase-lag quadrature criterion under more general conditions than prior studies assumed. Finally, we illustrate the power of our analytic predictions on examples in a six-degree-of-freedom mechanical system, subharmonic resonances in a gyroscopic system and isolated responses generated by parametric forcing in a system of three coupled nonlinear oscillators.

3 MECHANICAL SYSTEMS AND PERIODIC SOLUTIONS

3.1 SETUP

We consider a mechanical system with n degrees of freedom and denote its generalized coordinates by $q \in \mathbb{R}^n$, $n \geq 1$. We assume that this system is a small perturbation of a conservative limit described by the Lagrangian

$$L(q,\dot{q}) = K(q,\dot{q}) - V(q), \quad K(q,\dot{q}) = \frac{1}{2}\langle\, \dot{q}\,,\, M(q)\dot{q}\rangle + \langle\, \dot{q}\,,\, G_1(q)\rangle + G_0(q), \tag{3.1}$$

where, $M(q)$ is the positive definite, symmetric mass matrix, $K(q,\dot{q})$ is the kinetic energy and $V(q)$ the potential. The kinetic terms $G_1(q)$ and $G_0(q)$ may appear in conservative rotating mechanical systems after one factors out the cyclic coordinates whose corresponding angular momenta are conserved. The total energy or first integral associated to the Lagrangian in (3.1) is defined as its Legendre transform [116, 117]

$$H(q,\dot{q}) = \langle\, \partial_{\dot{q}} L(q,\dot{q})\,,\, \dot{q}\rangle - L(q,\dot{q}) = \frac{1}{2}\langle\, \dot{q}\,,\, M(q)\dot{q}\rangle - G_0(q) + V(q), \tag{3.2}$$

while the equations of motion for system (3.1) take the form

$$M(q)\ddot{q} + G(q,\dot{q}) + DV(q) = \varepsilon Q(q,\dot{q},t;\delta,\varepsilon), \tag{3.3}$$

where $G(q,\dot{q}) = D_t(M(q))\dot{q} + DG_1(q)\dot{q} - \partial_q K(q,\dot{q})$, $\varepsilon \geq 0$ is the perturbation parameter and $\varepsilon Q(q,\dot{q},t;\delta,\varepsilon) = \varepsilon Q(q,\dot{q},t+\delta;\delta,\varepsilon)$ denotes a small, generic perturbation of time-period δ. We use the notation D and ∂ for total and partial differentiation with respect to the variable in subscript (for D, to all of them if the subscript is absent). System in Eq. (3.3) is then a weakly non-conservative mechanical system.

Introducing the notation $x = (q,\dot{q}) \in \mathbb{R}^{2n}$ the equivalent first-order form reads

$$\dot{x} = f(x) + \varepsilon g(x,t;\delta,\varepsilon), \tag{3.4}$$

where we assume that $f \in C^r$ with $r \geq 2$, while g is C^{r-1} in t and C^r with respect to the other arguments. These vector fields are defined as

$$f(x) = \begin{pmatrix} \dot{q} \\ -M^{-1}(q)(DV(q) + G(q,\dot{q})) \end{pmatrix}, \qquad g(x,t;\delta,\varepsilon) = \begin{pmatrix} 0 \\ M^{-1}(q)Q(q,\dot{q},t;\delta,\varepsilon) \end{pmatrix}. \tag{3.5}$$

We assume any further parameter dependence in our upcoming derivations to be of class C^r and that the model (3.4) is valid in a subset $\mathcal{U} \subseteq \mathbb{R}^{2n}$ of the phase space. Trajectories of (3.4) that start from $\xi \in \mathbb{R}^{2n}$ at $t = 0$ will be denoted with $x(t;\xi,\delta,\varepsilon) = (q(t;\xi,\delta,\varepsilon), \dot{q}(t;\xi,\delta,\varepsilon))$. We will also use the shorthand notation $x_0(t;\xi) = (q_0(t;\xi,), \dot{q}_0(t;\xi,)) = x(t;\xi,\delta,0)$ for trajectories of the unperturbed (conservative) limit of system (3.4). We recall that, for $\varepsilon = 0$, energy is conserved, i.e., $H(x_0(t;\xi)) = H(\xi)$ holds as long as $x_0(t;\xi) \in \mathcal{U}$. The equation of (first) variations for system (3.4) about the solution $x(t;\xi,\delta,\varepsilon)$ reads

$$\dot{X} = \big(Df(x(t;\xi,\delta,\varepsilon)) + \varepsilon \partial_x g(x(t;\xi,\delta,\varepsilon),t;\delta,\varepsilon)\big)X, \quad X(0) = I_{2n\times 2n}, \tag{3.6}$$

whose solutions for $\varepsilon = 0$ will be denoted as $X_0(t;\xi) = X(t;\xi,\delta,0)$. When related to a periodic orbit with initial condition z at $t = 0$ and period τ, i.e., $x(0;z,\delta,\varepsilon) = x(l\tau;z,\delta,\varepsilon)$ for any integer l, the

(a)

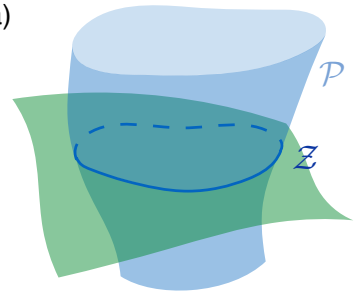

$\mathcal{H} := \{x \in \mathcal{U} \subseteq \mathbb{R}^{2n} \mid H(x) = H(p)\}$

(b)

m-normality	$\mu_{a,m}$	$\mu_{g,m}$
(i) $\tau' \neq 0 \quad h' \neq 0$	2	1
(ii) $\tau' = 0 \quad h' \neq 0$	2	2
(iii) $\tau' \neq 0 \quad h' = 0$	≥ 3	1
(iv) $\tau' = 0 \quad h' = 0$	≥ 3	2

(c)

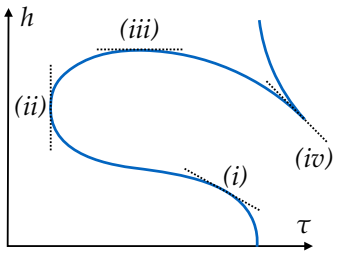

Figure 3.1: Plot (a) illustrates the periodic orbit $\mathcal{Z}$, its associate family $\mathcal{P}$ and its energy level $\mathcal{H}$ in the phase space. Table (b) and plot (c) show different types of m-normal periodic orbits and the associated geometry of the backbone curve, i.e., the relation between the energy h of the periodic response the period τ of the response. With respect to table (b), $\mathcal{Z}$ in plot (a) belongs to case *(i)* or *(ii)*, as $\mathcal{P}$ intersects transversally with $\mathcal{H}$.

matrix solution of (3.6) at $t = \tau$, i.e. $X(\tau; \xi, \delta, \varepsilon)$, is called the monodromy matrix or linearized time-τ map [11]. We recall that the eigenvalues of the monodromy matrix, or Floquet multipliers [4, 10, 11], determine the stability of a periodic orbit. In particular, the orbit is asymptotically stable if all of its Floquet multipliers lay inside the unit circle in the complex plane, while it is unstable if there exist a multiplier outside the unit circle.

3.2 CONSERVATIVE PERIODIC ORBITS

For the $\varepsilon = 0$ limit of system (3.4), we assume that there exists a periodic orbit $\mathcal{Z} \subset \mathcal{U}$ of minimal period $\tau > 0$ and we use the shorthand notation $\Pi(p)$ the monodromy matrix based at any point $p \in \mathcal{Z}$. For conservative systems $\Pi(p)$ is nonsingular and it has at least two eigenvalues equal to $+1$ [85, 118]. We consider $m \in \mathbb{N}^+$ multiples of the period, so that $\mathcal{Z}$ is regarded as a period-m motion, and let $\mu_{a,m}$ denote the algebraic multiplicity of the $+1$ eigenvalue of $\Pi^m(p)$ and $\mu_{g,m}$ denote its geometric multiplicity. Note that these two multiplicities are invariant under translations along the orbit, while they may change for different values of m.

We will need the following definition from [118].

Definition 3.1. *A conservative periodic orbit $\mathcal{Z}$ is m-normal if one of the following holds:*

(a) $\mu_{g,m} = 1$;

(b) $\mu_{g,m} = 2$ *and* $f(p) \notin range(\Pi^m(p) - I)$.

This normality is a nondegeneracy condition under which a one-parameter family, $\mathcal{P}$, of m-normal periodic solutions of the vector field f emanates from $\mathcal{Z}$ (see Theorem 4 of [118] or Theorem 7 of [119]), as shown in Figure 3.1(a). We denote with $\lambda \in \mathbb{R}$ the parameter identifying each individual orbit in the family $\mathcal{P}$. The orbits within the family can be either be unstable or neutrally stable.

Figure 3.1(b,c) describes the types of m-normal periodic orbits covered by Definition 3.1, with their associated backbone-curve geometry, as given in Theorem 5 of [118]. The backbone curve can be parametrized as $(\tau(\lambda), h(\lambda))$, with τ denoting the orbit period and h the value of the first integral. The value of the parameter λ is given by a scalar mapping $\lambda = L(\xi, \tau)$ depending on the initial condition $\xi \in \mathbb{R}^n$ and the period $\tau \in \mathbb{R}^+$. We also require L to be invariant under translations of ξ along the orbit. For an m-normal periodic orbit belonging to case *(a)* in Definition 3.1, one can simply choose $L(\xi, \tau) = \tau$. Instead, when $\mu_{a,m} = 2$ (see *(i)* and *(ii)* in Fig. 3.1), the orbit family can be locally parametrized with the value of the first integral h, i.e., $L(\xi, \tau) = H(\xi)$. Other possible

parametrizations include the value of a coordinate determined by a Poincaré section, the L^2 norm of the trajectory or the maximum value of a coordinate along the trajectory. For continuation through cusp points of backbone curves, i.e., *(iv)* in Fig. 3.1, L may be chosen to provide a pre-defined relation between energy and period (see [118]). Note that if a periodic orbit is not m-normal, then two or more families of periodic orbits may bifurcate from this periodic orbit. Moreover, a periodic orbit can be 1-normal and not m-normal for some $m > 1$, as in the case of subharmonic branching [85,86]. This type of phenomena can also induce changes in the stability of different branches.

4 THE MELNIKOV METHOD

4.1 FORMULATION

4.1.1 *Perturbation of a single orbit*

Our starting point in the analysis of the fate of perturbed periodic orbits is the displacement map

$$\Delta_l : \mathbb{R}^{n+2} \to \mathbb{R}^n, \qquad \Delta_l(\xi, \delta, \varepsilon) = x(l\delta; \xi, \delta, \varepsilon) - \xi, \qquad \Delta_l \in C^r, \tag{4.1}$$

whose zeros correspond to $l\delta$-periodic orbits for system (3.4) for $l \in \mathbb{N}^+$. We aim to smoothly continue normal periodic orbits in the family $\mathcal{P}$ that exists at $\varepsilon = 0$. We consider an m-normal periodic orbit $\mathcal{Z} \subset \mathcal{P}$ and assume that l and m are relatively prime integers, i.e., 1 is their only common divisor. We then look for zeros of (4.1) that can be expressed as

$$\xi = x_0(s; p) + O(\varepsilon), \qquad p \in \mathcal{Z}, \qquad \delta = \tau m/l + O(\varepsilon), \tag{4.2}$$

under the additional constraint

$$L(\xi, l\delta) = L(p, m\tau). \tag{4.3}$$

Equation (4.3) represents a resonance condition as it relates, either explicitly or implicitly, the periods of the perturbation with that of the periodic orbit $\mathcal{Z}$. With the notation $L(p, m\tau) = \lambda$, the zero problem to be solved reads

$$\Delta_{l,L} : \mathbb{R}^{n+2} \to \mathbb{R}^{n+1}, \qquad \Delta_{l,L}(\xi, \delta, \varepsilon) = \begin{cases} \Delta_l(\xi, \delta, \varepsilon) \\ L(\xi, l\delta) - \lambda \end{cases}, \qquad \Delta_{l,L}(\xi, \delta, \varepsilon) = 0. \tag{4.4}$$

Defining the smooth, L-independent, $m\tau$-periodic function $M_{m:l} : \mathbb{R} \to \mathbb{R}$ as

$$M_{m:l}(s) = \int_0^{m\tau} \left\langle DH(x_0(t+s; p)) \, , \, g(x_0(t+s; p), t; \tau m/l, 0) \right\rangle dt, \tag{4.5}$$

and using the notation $DM_{m:l}(s) = M'_{m:l}(s)$ we obtain the following main result.

Theorem 4.1. *If the Melnikov function $M_{m:l}(s)$ has a simple zero at $s_0 \in \mathbb{R}$, i.e.,*

$$M_{m:l}(s_0) = 0, \qquad M'_{m:l}(s_0) \neq 0, \tag{4.6}$$

then the m-normal periodic orbit $\mathcal{Z}$ of the $\varepsilon = 0$ limit smoothly persists in system (3.4) for small $\varepsilon > 0$. Moreover, in this case, there exists at least another topologically transverse zero in the interval $(s_0, s_0 + m\tau)$. If $M_{m:l}(s)$ remains bounded away from zero, then $\mathcal{Z}$ does not smoothly persists for small $\varepsilon > 0$.

We prove Theorem 4.1 in section 4.4. The proof reduces the $(2n+1)$-dimensional persistence problem to the analysis of the zeros of the scalar function (4.5). This function formally agrees with the one derived originally by Melnikov for a planar oscillator, but the proof for $n > 1$ is more involved compared to the simple geometric treatment in [4] for single-degree-of-freedom systems.

When the Melnikov function has a simple or transverse zero, the perturbed orbit emanating from the m-normal periodic orbit $\mathcal{Z}$ and its period are $O(\varepsilon)$-close to $\mathcal{Z}$ and to τm, respectively. Since topologically transverse zeros of functions are generically simple, we expect from Theorem 4.1 that an even number of perturbed periodic orbits bifurcates from the m-normal periodic orbit at the $\varepsilon = 0$

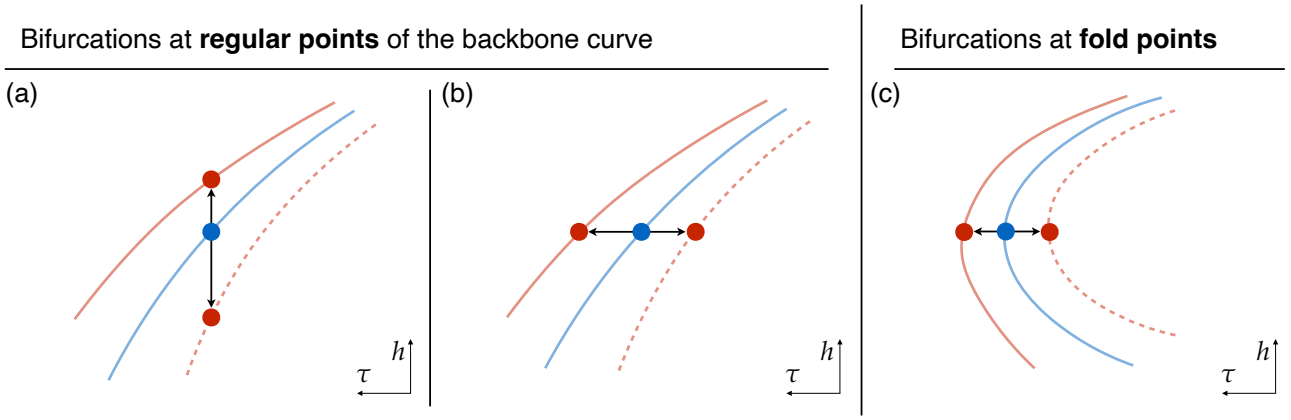

Figure 4.1: Bifurcations in case the Melnikov function (4.5) has two simple zeros. Regular points of the backbone curve generate perturbed solutions either in the isochronous (a) or isoenergetic (b) directions. In contrast, in case (c), perturbed solutions are guaranteed to exist in the isoenergetic direction for a fold point in τ. Blue lines identify conservative backbone curves while red lines mark perturbed periodic orbits. Solid and dashed lines identify different local branches of solutions.

limit, as indeed typically observed in literature. Moreover, since the Melnikov function (4.5) does not depend on the parametrization function L used in Eq. (4.3), Theorem 4.1 and its consequences hold for any possible parametrizing direction used for the unperturbed periodic orbit family.

Theorem 4.1 can be interpreted directly in terms of the backbone curve of $\mathcal{P}$ and the frequency response of system (3.4). Suppose that the backbone curve of $\mathcal{P}$ shows only regular points near the m-normal periodic orbit $\mathcal{Z}$ so that we can select $L(p, m\tau) = m\tau = \lambda$. In this case, Eq. (4.3) imposes the exact resonance condition $l\delta = m\tau$. For a pair of simple zeros of $M_{m:l}$, Theorem 4.1 guarantees that the point in the backbone curve corresponding to $\mathcal{Z}$ bifurcates in two frequency responses along the isochronous direction, as depicted in Fig. 4.1(a). If, instead, $\mathcal{Z}$ corresponds to a fold point in τ, then Theorem 4.1 does not hold for this choice of L, but we can still use the energy h as parametrization variable. In that case, our perturbation method constrains the perturbed initial condition ξ to lie in the same energy level as that of $\mathcal{Z}$. At the same time, the time period δ for the perturbed orbit is $O(\varepsilon)$-close to $\tau m/l$, i.e., a near-resonance condition is satisfied. For two simple zeros of $M_{m:l}$, $\mathcal{Z}$ can be smoothly continued in two frequency responses along the isoenergetic direction, as shown in Fig. 4.1(b) and 4.1(c).

4.1.2 *Perturbation of a family and parameter continuation*

Here we consider an additional parameter $\kappa \in \mathbb{R}$ in Eq. (4.4), where κ is either a feature of the vector fields in system (3.4) or the family parameter λ. The Melnikov function $M_{m:l}$ in (4.5) clearly inherits this smooth parameter dependence.

Next we investigate the fate of the m-normal periodic orbit $\mathcal{Z}$ in the family $\mathcal{P}$ for which the Melnikov function features a quadratic zero at (s_0, κ_0) defined as:

$$M_{m:l}(s_0, \kappa_0) = \partial_s M_{m:l}(s_0, \kappa_0) = 0, \qquad \partial^2_{ss} M_{m:l}(s_0, \kappa_0) \neq 0. \tag{4.7}$$

The following theorem describes what generic bifurcations may arise in this setting.

Theorem 4.2. *Assume that $M_{m:l}(s, \kappa)$ has a quadratic zero at (s_0, κ_0), as defined in Eq. (4.7). If $\partial_\kappa M_{m:l}(s_0, \kappa_0) \neq 0$, then $\kappa_{sn} = \kappa_0 + O(\varepsilon)$ is a bifurcation value at which a saddle-node bifurcation of periodic orbits occurs. If $\partial_\kappa M_{m:l}(s_0, \kappa_0) = 0$ and $\det(D^2 M_{m:l}(s_0, \kappa_0)) > 0$ (resp. < 0), then isola births (resp. simple bifurcations) arise for small $\varepsilon > 0$.*

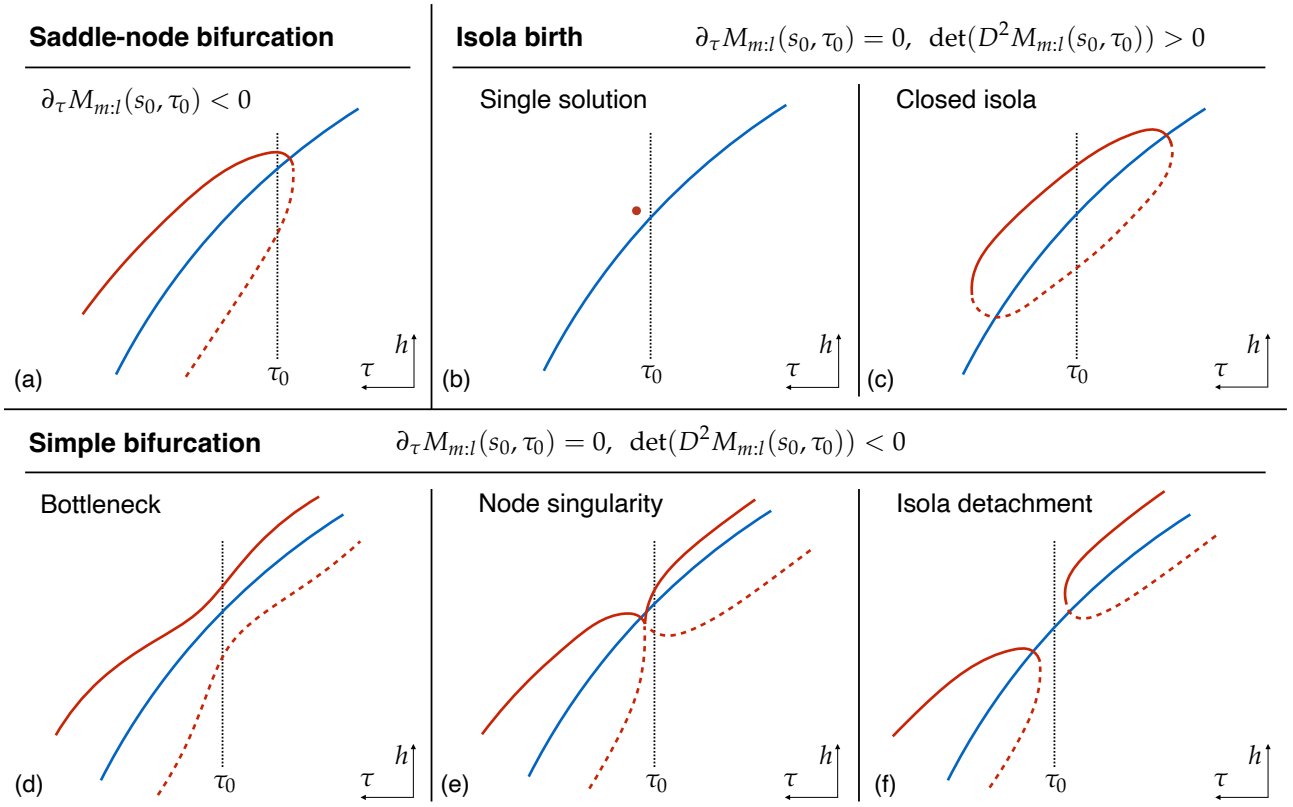

Figure 4.2: Illustration of the bifurcation phenomena described in Theorem 4.1 along a τ-parametrized conservative backbone curve close to a quadratic zero of the Melnikov function. Blue lines identify conservative backbone curves while red lines mark perturbed periodic orbits. Solid and dashed lines identify different local branches of solutions.

We prove Theorem 4.2 in section 4.4. Note that the bifurcations described in the last sentence of Theorem 4.2 are singular ones. Under these, the local, qualitative behavior of the solutions of Eq. (4.4) may change for different small $\varepsilon > 0$ as we describe below in an example. On the other hand, periodic orbits arising from either simple zeros or quadratic and κ-nondegenerate zeros persist for small $\varepsilon > 0$. We refer the reader to [120–122] for detailed analyzes of such singular bifurcations.

Figure 4.2 illustrates the bifurcations described in Theorem 4.2 when the family $\mathcal{P}$ can be locally parametrized with the period, which is also the selected continuation parameter, $\kappa = \tau$. This means sweeping along orbits of the family, indicated with a blue line, and analyzing when these orbits give rise to perturbed ones in the frequency response, denoted in red.

Plot (a) shows a saddle-node bifurcation in τ, also known as *limit* or *fold* bifurcation. For this type of quadratic zero, the conservative orbit at τ_0 and the period τ_0 itself are $O(\varepsilon)$-close to a locally unique saddle-node periodic orbit in τ of the frequency response. This unique orbit originates as two solutions branches of Eq. (4.4) join together. After this point, conservative orbits of $\mathcal{P}$ do not smoothly persist, at least locally.

The singular case of isola birth, illustrated in Fig. 4.2(b) and Fig. 4.2(c), has three possible bifurcation outcomes, depending on the value of the parameters. It is typically observed that either no solution persists from the ones in $\mathcal{P}$ (not show in Fig. 4.2) or a closed branch of solutions appears, i.e., an *isola* as shown in Fig. 4.2(c). Instead, the *single solution* case of Fig. 4.2(b) may occur, but it is non-generic.

Similarly, simple bifurcations may manifest themselves in three scenarios. The *bottleneck*, in Fig. 4.2(d), and the *isola detachment*, in (f), are generic, while the *node singularity* of Fig. 4.2(e) is an extreme case.

Remark 4.1. The results we have presented in Theorems 4.1-4.2 apply to general, non-autonomous perturbations of conservative systems with a normal family of periodic orbits, not just to mechanical systems. Moreover, the perturbation may be also of type $g(x, \dot{x}, t; \delta, \varepsilon)$.

4.1.3 *Significance of the Melnikov function*

The underlying physics of the full system in Eq. (3.3) implies that any periodic solution with minimal period $l\delta$ must necessarily experience zero energy balance in one oscillation cycle. Defining the energy function

$$E_b(\xi, \varepsilon)_{[0,l\delta]} = \varepsilon \int_0^{l\delta} \left\langle \dot{q}(t; \xi, \delta, \varepsilon)\,,\, Q(q(t; \xi, \delta, \varepsilon), \dot{q}(t; \xi, \delta, \varepsilon), t; \delta, \varepsilon) \right\rangle dt, \tag{4.8}$$

we deduce that, along such a periodic orbit, we must have

$$E_b(\xi, \varepsilon)_{[0,l\delta]} = 0, \tag{4.9}$$

given that the work done by the non-conservative forces must vanish over one cycle of that orbit. Equation (4.9) is commonly called the *energy principle* in literature [82, 88, 96].

By imposing $\xi = (q_0(s; p), \dot{q}_0(s; p)) + O(\varepsilon)$ and $l\delta = m\tau + O(\varepsilon)$ in the energy balance equation, one can easily verify that the Melnikov function of Eq. (4.5) is the leading-order term of the Taylor expansion of Eq. (4.9), i.e.,

$$E_b(\xi, \varepsilon)_{[0,l\delta]} = \varepsilon M_{m:l}(s) + O(\varepsilon^2), \tag{4.10}$$

where

$$M_{m:l}(s) = \int_0^{m\tau} \left\langle \dot{q}_0(t + s; p)\,,\, Q(q_0(t + s; p), \dot{q}_0(t + s; p), t; \tau m/l, 0) \right\rangle dt, \tag{4.11}$$

in which we have used Eq. (3.5) and the relation

$$DH(x) = DH(q, \dot{q}) = \left(DV(q) - DG_0(q) + \frac{1}{2}\partial_q\big(\langle \dot{q}\,,\, M(q)\dot{q}\rangle\big),\quad M(q)\dot{q} \right). \tag{4.12}$$

Therefore, the Melnikov function equals the work done by non-conservative forces along the periodic orbit $\mathcal{Z}$ of the conservative limit. Before exploring the implications of this peculiar form of the Melnikov function in specific cases, it is useful to recall the definitions of *subharmonic* and *superharmonic* resonances [5] in terms of l and m. These integers define the relation between the minimal period of the orbit and that of the perturbation. A subharmonic resonance occurs when the forcing frequency is a multiple of the orbit frequency, i.e., $l \neq 1$ and $m = 1$. The converse holds for a superharmonic resonance, for which we have $l = 1$ and $m \neq 1$. The attribute *ultrasubharmonic* [4] indicates higher-order resonances, when both m and l are different from 1.

4.2 MONOHARMONIC FORCING WITH ARBITRARY DISSIPATION

Due to their importance in the structural vibrations context, we now consider perturbations Q in Eq. (3.3) whose leading-order term in ε is of the form

$$Q(q, \dot{q}, t; \delta, e, 0) = e f_e \cos(\Omega t) - C(q, \dot{q}), \qquad \Omega = 2\pi/\delta, \tag{4.13}$$

where $e \in \mathbb{R}$ is a forcing amplitude parameter, $f_e \in \mathbb{R}^N$ is a constant vector of unit norm and $C(q, \dot{q})$ is a smooth, dissipative vector field. The actual forcing amplitude and the dissipative vector field are both rescaled by the value of the perturbation parameter ε.

First, we discuss the possible bifurcations that single orbits can experience in such systems when perturbed into forced-damped frequency responses, then we discuss the fate of periodic orbit families. Finally, we also illustrate the implications of the Melnikov method for the phase-lag quadrature criterion used in experimental vibration analysis.

4.2.1 *Bifurcations from single orbits*

We consider bifurcations from the conservative orbit $\mathcal{Z}$ with $p \in \mathcal{Z}$ and seek to perform continuation with the parameter e. In this case, the Melnikov function takes the form

$$\begin{aligned} M_{m:l}(s,e) = \; & e\int_0^{m\tau} \langle \dot{q}_0(t+s;p), f_e\rangle \cos\left(\frac{2l\pi}{m\tau}t\right) dt + \\ & - \int_0^{m\tau} \langle \dot{q}_0(t+s;p), C(q_0(t+s;p),\dot{q}_0(t+s;p))\rangle dt \\ = \; & w_{m:l}(s,e) - mR, \end{aligned} \tag{4.14}$$

where we have introduced the *resistance*

$$R = \int_0^{\tau} \langle \dot{q}_0(t;p), C(q_0(t;p),\dot{q}_0(t;p))\rangle dt, \tag{4.15}$$

measuring the dissipated energy along one period τ of $\mathcal{Z}$. This function is independent of s since C does not explicitly depend on time and the factor m arises in (4.14) because (4.15) is τ-periodic. In contrast,

$$w_{m:l}(s,e) = e\int_0^{m\tau} \langle \dot{q}_0(t+s;p), f_e\rangle \cos\left(\frac{2l\pi}{m\tau}t\right) dt \tag{4.16}$$

is the work done by the force along m periods of the conservative solution.

To simplify Eq. (4.14) further, we express the conservative periodic solution $\mathcal{Z}$ using the Fourier series

$$q_0(t;p) = \frac{a_0}{2} + \sum_{k=1}^{\infty} a_k \cos(k\omega t) + b_k \sin(k\omega t), \qquad \omega = \frac{2\pi}{\tau}, \tag{4.17}$$

where a_k, $b_k \in \mathbb{R}^N$ are the Fourier coefficients of the displacement coordinates. By inserting this expansion in Eq. (4.14), we obtain for $w_{m:l}(s,e)$ the expression

$$w_{m:l}(s,e) = \begin{cases} 0 & \text{if } m \neq 1 \\ W_{1:l}(e)\cos(l\omega s - \alpha_{l,e}) & \text{if } m = 1 \end{cases}, \tag{4.18}$$

where

$$W_{1:l}(e) = eA_{l,e}, \qquad A_{l,e} = l\pi\sqrt{\langle a_l, f_e\rangle^2 + \langle b_l, f_e\rangle^2}, \qquad \alpha_{l,e} = \arctan\left(\frac{\langle a_l, f_e\rangle}{\langle b_l, f_e\rangle}\right). \tag{4.19}$$

We provide the details of these derivations in section 4.4. The quantity $W_{1:l}(e)$ measures the maximum work done by the forcing along one cycle of the conservative periodic orbit. This work depends linearly on the forcing amplitude parameter e. Equation (4.18) implies that superharmonics or ultrasubharmonics cannot occur for the considered perturbation, which is consistent with literature observations. As a consequence, we have the following proposition characterizing primary and subharmonic resonances, where the relation between the forcing frequency Ω and the conservative orbit frequency ω reads $\Omega = l\omega + O(\varepsilon)$.

Proposition 4.3. *The Melnikov function for the perturbation in Eq. (4.13) takes the specific form*

$$M_{1:l}(s,e) = W_{1:l}(e)\cos(l\omega s - \alpha_{l,e}) - R. \tag{4.20}$$

Assuming $M_{1:l}(s,e_0) \not\equiv 0$ for some $e_0 \neq 0$, the following bifurcations of the conservative periodic orbit $\mathcal{Z}$ are possible for small $\varepsilon > 0$:

(i) *if* $|W_{1:l}(e_0)| < |R|$, *the conservative solution* $\mathcal{Z}$ *does not smoothly persist;*

(ii) *if* $|W_{1:l}(e_0)| > |R|$, *two periodic orbits bifurcate from* $\mathcal{Z}$*;*

(iii) *if* $|W_{1:l}(e_0)| = |R| > 0$, *there exist a forcing amplitude parameter* $e_{sn} = e_0 + O(\varepsilon)$ *for which a unique periodic orbit emanates from* $\mathcal{Z}$*.*

Proof. Since $M_{1:l}(s, e_0)$ remains bounded away from zero for $|W_{1:l}(e_0)| < |R|$, statement *(i)* follows from Theorem 4.1. When $|W_{1:l}(e_0)| > |R|$, $M_{1:l}(s, e_0)$ features $2l$ simple zeros for $s \in [0, \tau)$ for which Theorem 4.1 applies again. Considering that the forcing signal passes l times the zero phase in $[0, \tau)$, l of these zeros correspond to a single perturbed orbit so that two periodic solutions bifurcate from $\mathcal{Z}$, proving statement *(ii)*. Finally, we will argue that statement *(iii)* is a direct consequence of Theorem 4.2. First, note that the Melnikov function (4.20) features l quadratic zeros in s as defined in Eq. (4.7), corresponding to the l maxima or minima of $\cos(l\omega s - \alpha_{l,e})$ for $s \in [0, \tau)$, depending on the signs of $W_{1:l}(e)$ and R. Considering a location s_{qz} among these quadratic zeros, we obtain

$$|\partial_e M_{1:l}(s_{qz}, e_0)| = |DW_{1:l}(e_0)| = A_{l,e} > 0 \tag{4.21}$$

by the assumption $|W_{1:l}(e_0)| = |R| > 0$. Thus, these quadratic zeros are nondegenerate in κ and, since l of them correspond again to a single orbit, we conclude that a saddle-node bifurcation occurs from Theorem 4.2. More precisely, there exists a value $e_{sn} = e_0 + O(\varepsilon)$ for which a periodic orbit $O(\varepsilon)$-close to $\mathcal{Z}$ corresponds to a fold point for continuations in e.
Due to the specific form of the function in Eq. (4.20), no further degeneracies in s are possible (e.g. cubic zeros) for $M_{1:l}(s, e)$ so that the cases *(i-iii)* are the only possible bifurcations. □

From Proposition 4.3, we can derive necessary conditions for the persistence of a periodic orbit under forcing and damping. Either for case *(ii)* and *(iii)*, $W_{1:l}(e)$ must be nonzero, i.e., $e \neq 0$ and $A_{l,e} > 0$. The latter quantity is zero if the l-th harmonic is not present in Eq. (4.17) or if f_e is orthogonal to both its Fourier vectors. In the non-generic case of $M_{1:l}(s, e_0) \equiv 0$, the Melnikov function does not give any information on the persistence problem.

4.2.2 *Bifurcations from normal families*

We now investigate possible bifurcations that a conservative, 1-normal family $\mathcal{P}$ of periodic orbits may exhibit when perturbed with Eq. (4.13) into frequency responses at fixed e. Specifically, we study phenomena that occur with respect to the forcing frequency Ω and an amplitude measure a of interest.

We assume that either ω or a can be locally used as the family parameter λ for $\mathcal{P}$ and we denote $\mathcal{B}$ the conservative backbone curve in the plane $(l\omega, a)$. We then introduce the following definition.

Definition 4.1. *A ridge* $\mathcal{R}_l$ *is the curve in the plane* (e, λ) *identifying the forcing amplitudes and the orbits of* $\mathcal{P}$ *at which quadratic zeros of* $M_{1:l}$ *in* s *occur.*

The significance of ridges for frequency responses is clarified by the following proposition.

Proposition 4.4. *Assume that* $eR(\lambda_0) > 0$ *and* $A_{l,e}(\lambda_0) > 0$ *hold for the periodic orbit* $\mathcal{Z}$ *identified by* λ_0*. Then, the explicit local definition of* $\mathcal{R}_l$ *becomes* $e = \Gamma_l(\lambda)$*, where*

$$\Gamma_l(\lambda) = R(\lambda)/A_{l,e}(\lambda). \tag{4.22}$$

If $D\Gamma_l(\lambda_0) > 0$ *(resp.* < 0*), then the forced-damped response for* $e_0 = \Gamma_l(\lambda_0)$ *shows a maximal (resp. minimal) response with respect to* λ $O(\varepsilon)$*-close to* $\mathcal{B}$ *at* $\mathcal{Z}$*. If* $D\Gamma_l(\lambda_0) = 0$ *and* $D^2\Gamma_l(\lambda_0) > 0$ *(resp.* < 0*), then the forced-damped response for* $e_0 = \Gamma_l(\lambda_0)$ *includes an isola birth (resp. simple bifurcation) in* λ *which is* $O(\varepsilon)$*-close to* $\mathcal{B}$ *at* $\mathcal{Z}$*.*

Proof. We rewrite the Melnikov function as

$$M_{1:l}(s,e,\lambda) = A_{l,e}(\lambda)\Big(e\cos\big(l\omega(\lambda)s - \alpha_{l,e}(\lambda)\big) - \Gamma_l(\lambda)\Big), \tag{4.23}$$

which features l quadratic zeros in s for $e = \Gamma_l(\lambda)$. When $D\Gamma_l(\lambda_0) \neq 0$, Theorem 4.2 identifies a saddle-node bifurcation because

$$\partial_\lambda M_{1:l}\big(s_{qz}(\lambda_0), \Gamma_l(\lambda_0), \lambda_0\big) = -A_{l,e}(\lambda_0) D\Gamma_l(\lambda_0) \neq 0, \tag{4.24}$$

at any of the l locations $s_{qz}(\lambda_0)$ of quadratic zeros of $M_{1:l}$ in s. As already discussed in Proposition 4.3, there exists a unique periodic orbit $O(\varepsilon)$-close to $\mathcal{Z}$, corresponding to a fold for continuations in λ. If $D\Gamma_l(\lambda_0) > 0$, we can choose a small positive ϵ defining a $\lambda_1 = \lambda_0 - \epsilon$ for which

$$W_{1:l}(e_0, \lambda_1) = e_0 A_{l,e}(\lambda_1) = \Gamma_l(\lambda_0) A_{l,e}(\lambda_1) > \Gamma_l(\lambda_1) A_{l,e}(\lambda_1) = R(\lambda_1), \tag{4.25}$$

so that, according to Proposition 4.3, two periodic orbits bifurcate at $e_0 = \Gamma_l(\lambda_0)$ from the orbit of $\mathcal{P}$ described by λ_1. For $\lambda_2 = \lambda_0 + \epsilon$, we can similarly conclude that no orbit persists smoothly. Thus, the periodic orbit at the fold in λ represents a maximal response. An analogous reasoning holds for the minimal response case arising for $D\Gamma_l(\lambda_0) < 0$.

The last statement of Proposition 4.4 holds again, based on Theorem 4.2, since we have that $\partial_\lambda M_{1:l}\big(s_{qz}(\lambda_0), \Gamma_l(\lambda_0), \lambda_0\big) = 0$ from Eq. (4.24) and

$$\det\big(\partial^2_{s,\lambda} M_{1:l}\big(s_{qz}(\lambda_0), \Gamma_l(\lambda_0), \lambda_0\big)\big) = e\big(A_{l,e}(\lambda_0)\omega(\lambda_0)\big)^2 D^2\Gamma_l(\lambda_0) \neq 0. \tag{4.26}$$

□

Ridges, as introduced in Definition 4.1, are effective tools for the analysis of forced-damped responses in the vicinity of backbone curves as they can track fold bifurcations and generations of isolated responses. These phenomena are the most generic bifurcations for the perturbation type in Eq. (4.13). Ridge points may be used to detect further singular bifurcation behaviors under additional degeneracy conditions on λ [121].

4.2.3 *The phase-lag quadrature criterion*

We now discuss the relevance of the phase of the Melnikov function and the next proposition illustrates an important result in this regard.

Proposition 4.5. *Consider a perturbed periodic orbit $q_{qz}(t;\xi,\delta,\varepsilon)$ corresponding to a quadratic zero of the Melnikov function (4.20) related to the conservative limit $\mathcal{Z}$. Then, the l-th harmonic of the function $\langle q_{qz}(t;\xi,\delta,\varepsilon), f_e\rangle$ has a phase lag (resp. lead) of $90^\circ + O(\varepsilon)$ with respect to the forcing signal if $eR > 0$ (resp. $eR < 0$).*

Proof. To determine the phase lag, we consider, without loss of generality, the phase condition for $\mathcal{Z}$

$$\langle a_l, f_e\rangle > 0, \qquad \langle b_l, f_e\rangle = 0, \tag{4.27}$$

under which the l-th term in the Fourier series of the function $\langle q_0(t;p), f_e\rangle$ is equal to $\langle a_l, f_e\rangle \cos(l\omega t)$, having the same phase of the forcing. In that case, the Melnikov function becomes

$$M_{1:l}(s,e) = W_{1:l}(e)\cos(l\omega s + 3\pi/2) - R = -W_{1:l}(e)\sin(l\omega s) - R. \tag{4.28}$$

Eq. (4.28) shows that the l quadratic zeros of the Melnikov function occur for $|W_{1:l}(e)| = |R|$ and $l\omega s_{qz} = -\mathrm{sign}(eR)\pi/2 + 2k\pi$ with $k = 0, 1, \dots l-1$. Thus, we obtain

$$\langle q_{qz}(t;\xi,\delta,\varepsilon), f_e\rangle = \langle q_0(t + s_{qz}; p), f_e\rangle + O(\varepsilon), \tag{4.29}$$

whose l-th harmonic is equal to $\langle a_l, f_e\rangle \cos(l\omega t - \mathrm{sign}(eR)\pi/2) + O(\varepsilon)$, independent of k. □

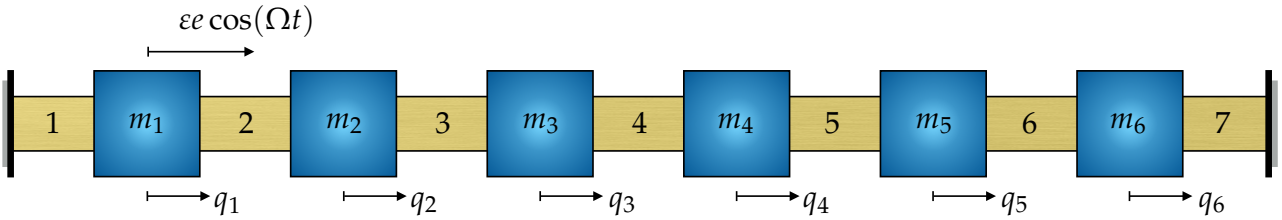

i		1	2	3	4	5	6	7
$k_{i,1}$	N/m	2.971	1.231	1.844	1.015	1.226	1.971	2.728
$k_{i,3}$	N/m^3	0.036	0.849	0.934	0.679	0.758	0.743	0.392
$k_{i,5}$	N/m^5	0.547	0.958	0.965	0.158	0.971	0.957	0.485
ω_i	rad/s	0.628	1.130	1.686	1.996	2.360	2.492	–

Figure 4.3: Illustration of the mechanical system in (4.31) and table containing elastic coefficients $k_{i,j}$ of the constitutive law in (4.30) for the nonlinear elements and natural frequencies ω_i of the system linearized at the origin.

In numerical or experimental continuation, one can track the relation between the forcing amplitude parameter e and either the amplitude a or the forcing frequency Ω under the phase criterion of Proposition 4.5. The resulting curve of points is an $O(\varepsilon)$-approximation of the ridge curve $\mathcal{R}_l$ whose interpretation is available in Proposition 4.4.

Proposition 4.5 relaxes some restrictions of the phase-lag quadrature criterion derived in [44]. Indeed, Eq. (4.17) allows for arbitrary periodic motion, not just synchronous ones along which all displacement coordinates reach their maxima at the same time. Moreover, our criterion is not limited to velocity-dependent, odd damping, but it admits arbitrary, smooth dissipations. For this general case, we proved that the phase-lag must be measured in *co-location*, i.e., when the output (displacement response) is observed at the same location where the input (force) excites the system.

4.3 EXAMPLES

In this section, we study a conservative multi-degree of freedom system subject to non-conservative perturbations in the form of Eq. (4.13). First, we consider frequency responses with monoharmonic forcing and linear damping. Then, we introduce nonlinear damping to investigate the presence of isolas. In both cases, we show how the Melnikov analysis can predict forced-damped response bifurcations under a $1:1$ resonance between the forcing and periodic orbits of the conservative limit.

We analyze a system composed of six masses m_i with $i = 1, 2, \dots 6$ that are connected by seven nonlinear massless elements, as shown in Fig. 4.3. All masses are assumed unitary and the external forcing acts on the first degree of freedom only. The seven nonlinear elements exert a force depending on the elongation Δl and its speed $\dot{\Delta l}$, modelled as

$$F_i(\Delta l, \dot{\Delta l}, \varepsilon) = F_{i,el}(\Delta l) + \varepsilon F_{i,nc}(\dot{\Delta l}) = \begin{array}{l} k_{i,1}\Delta l + k_{i,3}\Delta l^3 + k_{i,5}\Delta l^5 + \\ +\varepsilon(\alpha k_{i,1}\dot{\Delta l} + \beta k_{i,3}\dot{\Delta l}^3 + \gamma k_{i,5}\dot{\Delta l}^5) \end{array} \tag{4.30}$$

for $i = 1, 2, \dots 7$. The coefficients $k_{i,1}$, $k_{i,3}$ and $k_{i,5}$ are reported in the table in Fig. 4.3, while the

values of α, β, γ and ε will vary from case by case below. The equations of motion read

$$\begin{cases} \ddot{q}_1 + F_1(q_1, \dot{q}_1, \varepsilon) + F_2(q_1 - q_2, \dot{q}_1 - \dot{q}_2, \varepsilon) = \varepsilon e \cos(\Omega t), \\ \quad \vdots \\ \ddot{q}_i + F_i(q_i - q_{i-1}, \dot{q}_i - \dot{q}_{i-1}, \varepsilon) + F_{i+1}(q_i - q_{i+1}, \dot{q}_i - \dot{q}_{i+1}, \varepsilon) = 0, \quad \text{for } i = 2, 3, \dots 5, \\ \quad \vdots \\ \ddot{q}_6 + F_6(q_6 - q_5, \dot{q}_6 - \dot{q}_5, \varepsilon) + F_7(q_6, \dot{q}_6, \varepsilon) = 0. \end{cases} \tag{4.31}$$

To compute conservative periodic orbits and frequency responses for system (4.31), we use the MATLAB®-based numerical continuation package COCO [26]. We specifically exploit its periodic orbit toolbox that solves the continuation problem via collocation. In this method, solutions to the governing ordinary differential equations are approximated by piecewise polynomial functions and continuation is performed using a refined pseudo-arclength algorithm.

First, we focus on the study of the conservative limit ($\varepsilon = 0$), in which the nonlinear elements are springs with convex potentials and the origin is an equilibrium whose eigenfrequencies ω_i are reported in the table of Fig. 4.3. Since no resonance arises among these frequencies, the system features six families of periodic orbits emanating from the origin by the Lyapunov subcenter manifold theorem [91]. Using numerical continuation starting from small-amplitude linearized periodic motions, we compute the conservative backbone curve for each mode, shown in Figure 4.4(a). We plot these curves using the normalized frequency $\underline{\omega} = \omega/\omega_1$ and the L^2 norm $||x||_{L^2,[0,\tau]}$ of the conservative periodic orbits. We consider the latter norm as the amplitude measure A. With the exception of the first periodic orbit family, the monodromy matrix of the periodic orbits has two Floquet multipliers equal to $+1$, whose geometric multiplicity is 1 in the selected frequency-amplitude range. Therefore, these five orbit families are 1-normal, precisely belonging to case *(a)* of Definition 3.1, and showing a hardening trend (Da, $D\omega > 0$). The first family also shows normality with hardening behavior up to the magenta point, where branching phenomena takes place and a further family originates from the continuation of the first linearized mode. As 1-normality does not hold in the vicinity of the branch point, depicted in magenta in Fig. 4.4(a), we restrict our analysis of the first family to amplitudes below the branch point amplitude.

4.3.1 *Resonant external forcing with linear damping*

In this first example, we take the damping to be linear with $\alpha = 0.04$ and $\beta = \gamma = 0$ in Eq. (4.30). We focus on the orbits surviving from primary resonance conditions, where $m = l = 1$, and we perform the analysis of $M_{1:1}$ for each mode of the system as described in section 4.2.

Figure 4.4(b) shows the work done by non-conservative contributions along the first modal family of conservative orbits parametrized with the non dimensional frequency $\underline{\omega}$. The black solid line is the resistance $R(\underline{\omega})$, while colored lines represent $W_{1:1}(e, \underline{\omega})$ for three forcing amplitudes. According to Proposition 4.3, we find that two orbits bifurcate from the conservative one when the lines illustrating $W_{1:1}(e, \underline{\omega})$ lay in the grey zone of this plot, i.e., when $W_{1:1}(e, \underline{\omega}) > R(\underline{\omega})$. No orbit bifurcates in the white area and unique solutions appear at intersection points between colored lines and the black one. We also note that $A_{1,e}$ is never zero, except when $\underline{\omega} = 1$. Similar trends and considerations hold for the other modes, except for the last one. For that mode, the active work contribution of the forcing is very small compared to the dissipative terms: the forcing is nearly orthogonal to the mode shape. Thus, no orbits arise from the conservative limit for the forcing amplitude ranges under investigation.

Figure 4.5(d) shows the curves $\Gamma_1(\underline{\omega})$ for the first five modes of the system using different colors; all of them show a strictly increasing monotonic trend. Thus, according to Proposition 4.4, ridge

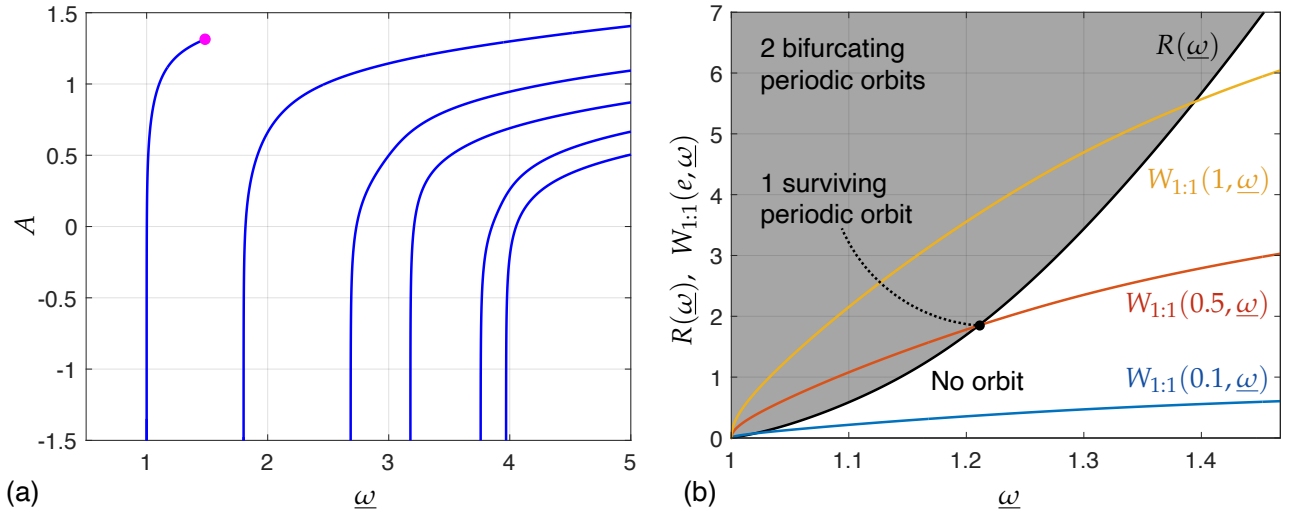

Figure 4.4: (a) Conservative backbone curves of the unperturbed system and (b) Melnikov analysis for the first mode of the system with linear damping $\alpha = 0.04$: the black solid line is the resistance $R(\underline{\omega})$; colored lines show the amplitude of the active work $W_{1:1}(e, \underline{\omega})$ for different forcing amplitude values. The amplitude A denotes the L^2 norm $||x||_{L^2,[0,\tau]}$ of periodic motions, while $\underline{\omega}$ is the frequency normalized by the first linearized frequency of system (4.31).

orbits are $O(\varepsilon)$ approximations for maximal responses in ω and a, since all the conservative backbone curves can be parametrized with both quantities. By selecting a forcing value in Fig. 4.5(d), we can predict the frequencies and the amplitudes of the maximal responses in the forced-damped setting. Moreover, since the damping is linear and proportional, ridges are defined as

$$e = \frac{R(\underline{\omega})}{A_{1,e}(\underline{\omega})} = \alpha \frac{1}{A_{1,e}(\underline{\omega})} \int_0^{\tau(\underline{\omega})} \langle \dot{q}_0(t; p(\underline{\omega})), DV(0)\dot{q}_0(t; p(\underline{\omega}))\rangle dt, \tag{4.32}$$

where $DV(0)$ is the stiffness matrix of system (4.31), and we expressed initial conditions p, periods τ and coefficients $A_{1,e}$ as functions of the non-dimensional frequency $\underline{\omega}$. From Eq. (4.32), we obtain that the location of maximal frequency responses close to backbone curves is determined by the ratio between the forcing amplitude parameter e and the damping term α, with $O(\varepsilon)$ accuracy.

These theoretical findings are confirmed by the direct numerical computation of frequency responses presented in Fig. 4.5. To obtain them, we continue in frequency an initial guess acquired through numerical integration for a forcing frequency away from resonance with any of the linearized natural frequencies. The existence of this orbit is guaranteed by the asymptotic stability of the origin when $\varepsilon > 0$ and $e = 0$. Plot (a) in Fig. 4.5 shows two frequency sweeps for $e = 1$ and for $\varepsilon = 0.05$ (grey line), 0.1 (black line), while this plot is zoomed in (b) around the first and fifth peaks. The sixth mode shows some tiny responses with the rightmost peaks in these two frequency sweeps, more evident for the case $\varepsilon = 0.05$ where the physical damping is lower. Figures 4.5(a) and 4.5(b,c) are completed with our analytic predictions in green for the maxima, with a zoom around resonance peaks of the first and the fifth families. By imposing the forcing parameter in the ridges of Fig. 4.5(d), we obtain the frequencies of each mode around which maximal response occur that are validated when carried over with green dotted lines in Fig. 4.5(a). Moreover, Fig. 4.5(e) shows the frequency response surface keeping $e = 1$ and varying the damping value[1] for two orders of magnitude. Green curves show analytic predictions for the maxima that closely approximate the peaks of this surface.

1 For purposes of better illustration, we decided to sweep with the damping parameter α instead of the forcing amplitude one.

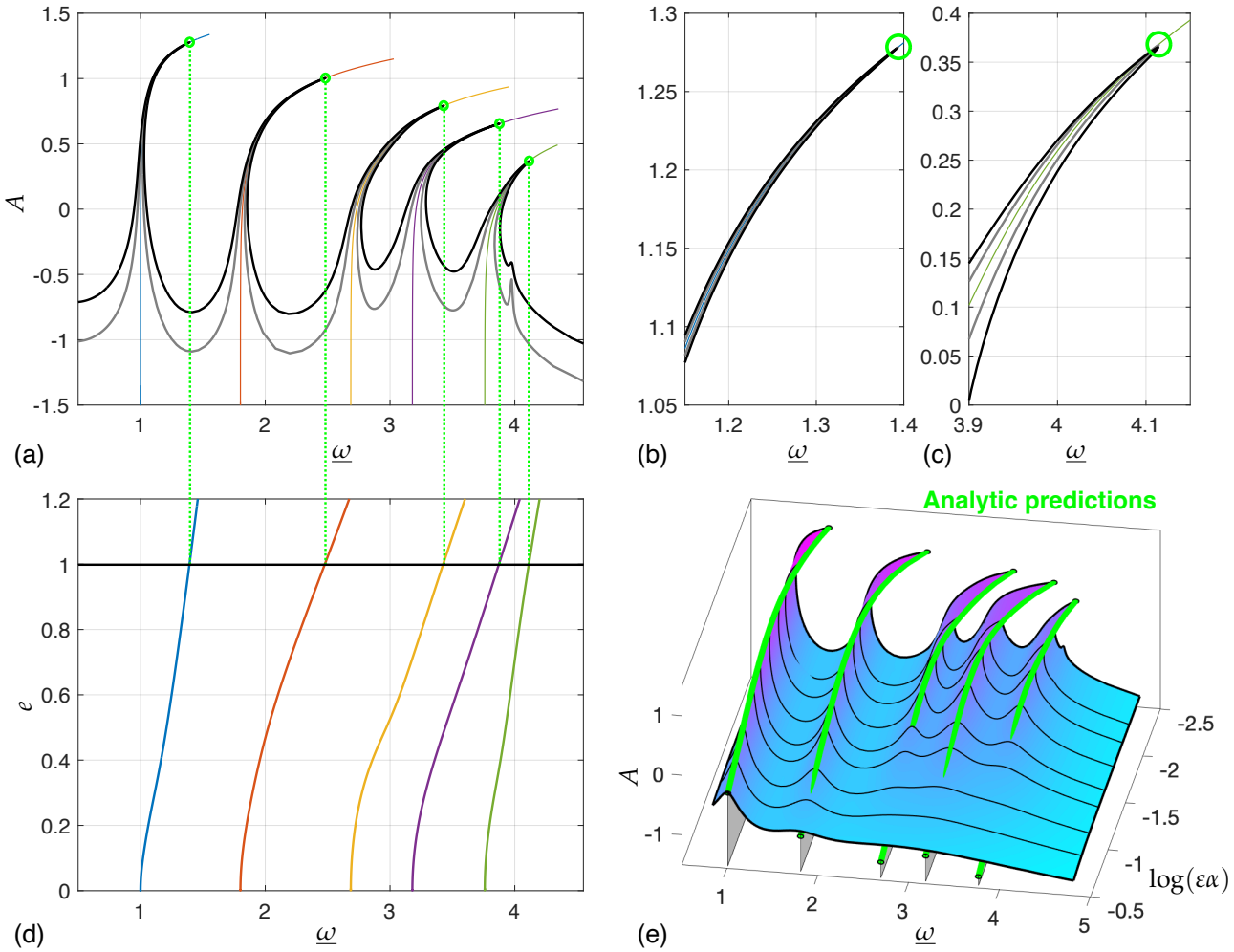

Figure 4.5: Plots (a,b,c) show frequency responses with $\alpha = 0.04$ and $e = 1$ for $\varepsilon = 0.05$, grey line, and $\varepsilon = 0.1$, black line. With respect to (a), plot (b) zooms near the first and plot (c) near the fifth one. The five relevant conservative periodic orbit families are highlighted with colored lines. Plot (d) shows the ridges $\mathcal{R}_1$ for each mode in different colors and the black line represents the forcing amplitude parameter of the frequency response in (a), so that, carrying over this intersection frequencies with green dotted lines, we obtain an analytic approximation for turning points. These approximations are described by green circles in (a,b,c). Plot (e) shows the frequency response surface with $e = 1$ and $\varepsilon = 0.1$, varying the proportional damping term α completed with conservative families in grey surfaces and analytic predictions for maxima in green.

4.3.2 *Resonant external forcing with nonlinear damping*

We now repeat the analysis of the previous section including also the nonlinear damping characteristic of the connecting elements. In order to break the monotonic trend of the resistance in the linear damping case, cf. Fig. 4.4(b), we select $\alpha = 0.2481$, $\beta = -1.085$ and $\gamma = 0.8314$. We also restrict our attention solely to the first mode of the system.

The Melnikov analysis is reported in Figure 4.6(a), which outlines a behavior change for increasing forcing amplitudes. Indeed, an isola birth occurs at $e \approx 0.4$ as was also displayed in Fig. 4.2. The branch persists up to connecting with the main branch for $e \approx 1$ through a simple bifurcation.

These predictions are confirmed by the numerical simulations shown in Figures 4.6(b) and 4.6(c). The former illustrates several frequency responses for different physical forcing amplitudes, with $\varepsilon = 0.1$. The green line is the ridge $\mathcal{R}_1$, also plotted in Fig. 4.6(c), and the two singular bifurcations show up at its folds, as explained in Proposition 4.4. From a computational perspective, main

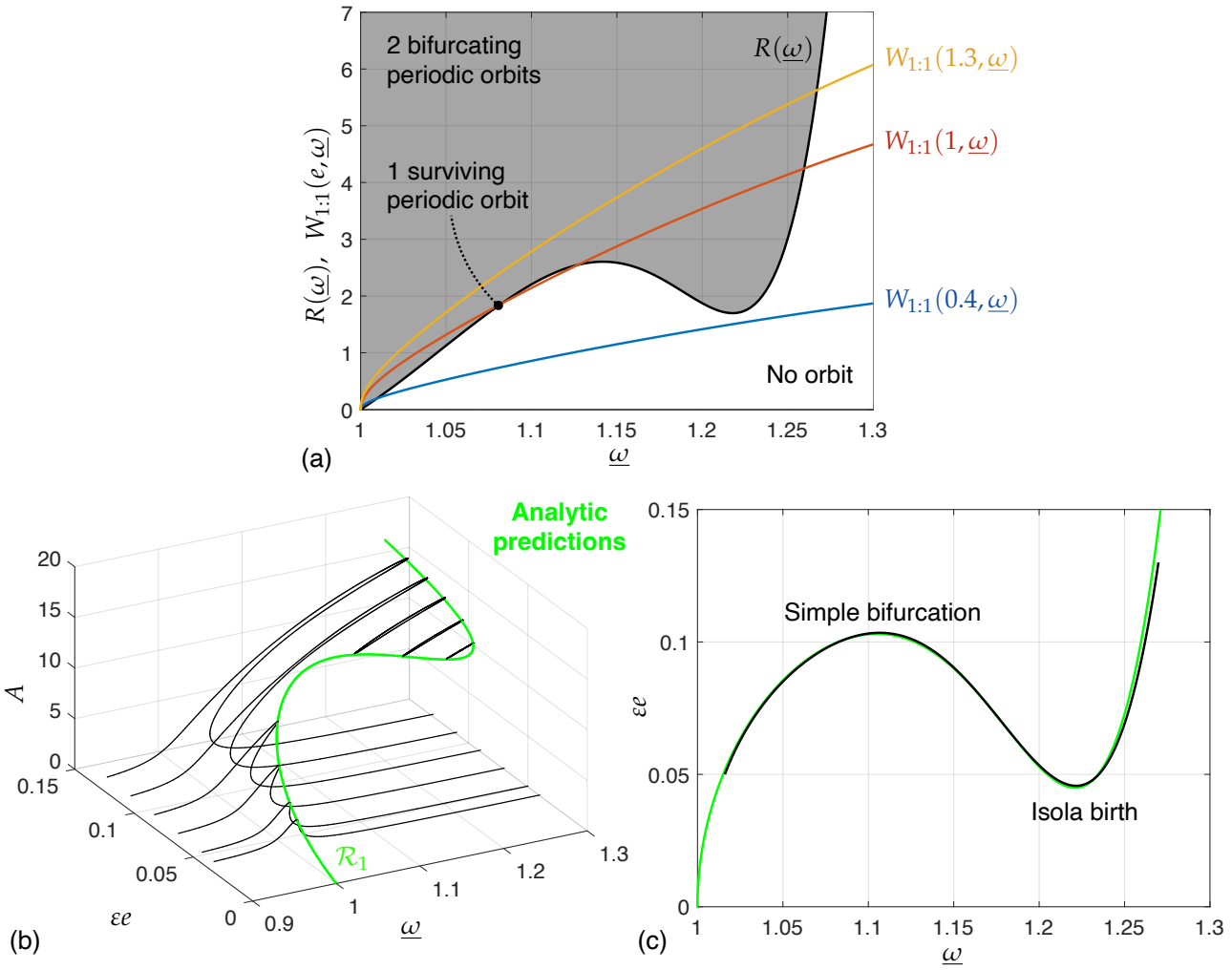

Figure 4.6: Plot (a) shows the Melnikov analysis for $\alpha = 0.2481$, $\beta = -1.085$ and $\gamma = 0.8314$ regarding the first mode. Plot (b) shows frequency responses varying the forcing amplitude parameter and fixing $\varepsilon = 0.1$ with the ridge curve $\mathcal{R}_1$. The latter is compared in plot (c) with the relation between the e and $\underline{\omega}$ obtained through the numerical continuation of saddle-nodes orbits occurring close to the maximal point of the frequency response.

branches of the frequency response are computed with the same strategy of the previous section. For isolated branches, we obtain initial guesses from a numerical continuation in e of saddle-node periodic orbits[2] that started near the maximal response of the frequency sweep at $e = 1.3$. We also plot the relation between frequency and forcing amplitude in this latter numerical continuation with the black line of Fig. 4.6(c). This curve is $O(\varepsilon)$-close to the ridge (in green), which was obtained solely from the knowledge of the conservative limit. We remark that a 18-core workstation with 2.3 GHz processors required 18 minutes and 15 seconds to compute the black curve, while the green curve took 1 minute and 45 seconds to compute.

2 This functionality is directly available in the periodic orbit toolbox of coco [26] through the constructor `ode_SN2SN`.

4.4.1 *A preparatory theorem*

We first need some technical results to set the stage for the proofs of the theorems stated in section 4.1. For a one-parameter family $\mathcal{P}$ of periodic orbits emanating from a m-normal periodic orbit $\mathcal{Z}$, the smooth map $T : \mathbb{R} \to \mathbb{R}_+$ describes the minimal period $T(\lambda)$ of each orbit. Introducing a Poincaré section $\mathcal{S}$ passing through the point of $z \in \mathcal{P}$, we can find a smooth curve $\vartheta_{\mathcal{S}} : \mathbb{R} \to V \cup \mathcal{P} \pitchfork \mathcal{S}$ parametrizing initial conditions under λ where $V \subset \mathbb{R}^n$ is a open neighborhood of z. For more detail on these mappings, we refer the reader to [10]. We denote the tangent space of the 2-dimensional manifold $\mathcal{P}$ at the point z by $\mathcal{T}_z\mathcal{P}$, to which $f(z)$ belongs due to invariance. We consider vectors as column ones and we use the superscript $^\top$ to denote transposition. We refer to the column and row spaces of a matrix A with the notations $\mathrm{col}(A)$ and $\mathrm{row}(A)$, respectively.

Next, we discuss a useful result on the properties of the monodromy matrices for normal periodic orbits. Specifically, we restate Proposition 2.1 of [114] for the setting of m-normal period orbits.

Proposition 4.6. *Consider an m-normal periodic orbit $\mathcal{Z}$ of period $m\tau$ in the periodic orbit family $\mathcal{P}$. The smooth invertible matrix families K, $R : \mathcal{Z} \to \mathbb{R}^{n\times n}$, defined as*

$$\begin{gathered} K(z) = [\,K_r(z) \;\; v(z) \;\; f(z)], \qquad v(z) \in \mathcal{T}_z\mathcal{P} : \langle v(z), f(z)\rangle = 0,\ \langle v(z), v(z)\rangle = 1, \\ \mathrm{col}(K_r(z)) = \mathcal{T}_z^{\perp}\mathcal{P}, \quad R(z) = \begin{bmatrix} R_r(z) \\ -f^\top(z) \\ DH(z) \end{bmatrix}, \quad \mathrm{row}(R_r(z)) = \mathrm{span}^{\perp}\{f(z)\,,\, DH(z)\}, \end{gathered} \tag{4.33}$$

satisfy the identity

$$R(z)(\Pi^m(z) - I)K(z) = \begin{bmatrix} A_r(z) & 0 & 0 \\ w^\top(z) & m\tau_v & 0 \\ 0 & 0 & 0 \end{bmatrix}, \quad w^\top(z) = -f^\top(z)(\Pi^m(z) - I)K_r(z), \tag{4.34}$$

where $A_r(z) \in \mathbb{R}^{(n-2)\times(n-2)}$ is always invertible and the value $\tau_v \in \mathbb{R}$ describes the shear effect within $\mathcal{P}$ being zero if $\mathcal{Z}$ is a normal periodic orbit of case (b) and nonzero for case (a) of Definition 3.1.

Proof. For proving this factorization result, we need to characterize kernel and range of the monodromy operator for $\mathcal{Z}$ based at z. First, by [119], we have that

$$f(z) \in \ker(\Pi^m(z) - I), \qquad DH(z) \in \mathrm{range}^{\perp}(\Pi^m(z) - I). \tag{4.35}$$

Without loss of generality, we introduce a Poincaré section $\mathcal{S}$ orthogonal to $f(z)$ and the value λ_z identifies $\mathcal{Z}$ leading to $z = \vartheta_{\mathcal{S}}(\lambda_z)$, $\tau = T(\lambda_z)$. Consider the identity

$$x_0(mT(\lambda); \vartheta_{\mathcal{S}}(\lambda)) = \vartheta_{\mathcal{S}}(\lambda), \tag{4.36}$$

whose differentiation in λ and evaluation at $\lambda = \lambda_z$ yields

$$(\Pi^m(z) - I)D\vartheta_{\mathcal{S}}(\lambda_z) = -mDT(\lambda_z)f(z). \tag{4.37}$$

We then have $v(z) = D\vartheta_{\mathcal{S}}(\lambda_z)/||D\vartheta_{\mathcal{S}}(\lambda_z)||$ leading to a parametrization-independent relation and to the definition of τ_v in the form

$$(\Pi^m(z) - I)v(z) = -m\tau_v f(z), \qquad \tau_v = \frac{DT(\lambda_z)}{||D\vartheta(\lambda_z)||}. \tag{4.38}$$

If the orbit $\mathcal{Z}$ belongs to the case *(a)* of Definition 3.1, τ_v cannot be zero, otherwise the kernel of $\Pi^m(z) - I$ is two dimensional. Instead, for case *(b)*, τ_v must be zero, otherwise there exists a nonzero vector $v(z)$ whose image is parallel to $f(z)$. In both cases, the column space of $K_r(z)$ always lays in the complement of the kernel of $\Pi^m(z) - I$ by construction, so it maps through $\Pi^m(z) - I$ a $n-2$ dimensional linear subspace V_z such that $f(z)$, $DH(z) \notin V_z$. Since the row space of the matrix $R_r(z)$ does not contain the latter vectors, the matrix $A_r(z) = R_r(z)(\Pi^m(z) - I)K_r(z)$ is invertible $\forall z \in \mathcal{Z}$. □

We can now state and prove the following reduction theorem.

Theorem 4.7. *Perturbed solutions of Eq. (4.4) in the form of Eq. (4.2) are (locally) in one-to-one correspondence with the zeros of the bifurcation function*

$$B_L^{m:l}(s,\varepsilon) = M_{m:l}(s) + O(\varepsilon), \tag{4.39}$$

where the leading-order term, defined in Eq. (4.5), is independent from the choice of the mapping L used in the last equation of system (4.4).

Proof. With the shorthand notation $z = x_0(s;p)$, we consider the following change of coordinates

$$\hat{\zeta} \in \mathbb{R}^{n-1}, \quad \hat{\sigma} \in \mathbb{R}, \quad \begin{pmatrix} \zeta \\ \delta \end{pmatrix} = \hat{\varphi}(\hat{\zeta}, \hat{\sigma}, s) = \begin{cases} z + K(z) \begin{pmatrix} \hat{\zeta} \\ 0 \end{pmatrix} = z + K_{\mathcal{TZ}}(z)\hat{\zeta} \\ (\tau m + \hat{\sigma})/l \end{cases}, \tag{4.40}$$

where $K(z)$ is the matrix defined in Proposition 4.6. By construction, $D\hat{\varphi}(0,\hat{\sigma},s)$ is invertible for any s, $\hat{\sigma} \in \mathbb{R}$. Then, we rescale $\hat{\zeta} = \varepsilon\zeta$, $\hat{\sigma} = \varepsilon\sigma$ and, by calling $\eta = (\zeta, \sigma, s)$, we denote $\varphi(\eta,\varepsilon) = \hat{\varphi}(\varepsilon\zeta, \varepsilon\sigma, s)$. Note that $\varphi(\cdot,\varepsilon)$ is a family of diffeomorphisms for ε nonzero small enough. Note also that $\mathrm{col}(K_{\mathcal{TZ}}(z)) = \mathcal{T}_z^{\perp}\mathcal{Z}$.

By imposing this coordinate change and Taylor expanding in ε Eq. (4.4), we obtain $\Delta_{l,L}(\varphi(\eta,\varepsilon),\varepsilon) = \varepsilon\Delta_1(\eta,\varepsilon)$. The latter mapping is of C^{r-1} class and reads

$$\Delta_1(\eta,\varepsilon) = \begin{cases} \partial_{\tilde{\zeta}}\Delta(z, m\tau/l, 0)K_{\mathcal{TZ}}(z)\zeta + \partial_\delta\Delta(z, m\tau/l, 0)\sigma + \partial_\varepsilon\Delta(z, m\tau/l, 0) \\ \partial_{\tilde{\zeta}}L(z, m\tau)K_{\mathcal{TZ}}(z)\zeta + \partial_\delta L(z, m\tau)\sigma \end{cases} + O(\varepsilon), \tag{4.41}$$

in which

$$\begin{array}{lcll} \partial_{\tilde{\zeta}}\Delta(z, m\tau/l, 0) & = & x_{\tilde{\zeta}}(m\tau; z, m\tau/l, 0) - I & = \Pi^m(z) - I \\ \partial_\delta\Delta(z, m\tau/l, 0) & = & f(z) + x_\delta(m\tau; z, m\tau/l, 0) & = f(z) \\ \partial_\varepsilon\Delta(z, m\tau/l, 0) & = & x_\varepsilon(m\tau; z, m\tau/l, 0) & = \chi(z) \end{array}, \tag{4.42}$$

where we have denoted by $x_\kappa(m\tau; z, m\tau l, 0)$ the solution of the first variational problem in the parameter κ at time $m\tau$. The solution of the first variation in the period is zero since the period dependence of the vector field only appears at $O(\varepsilon)$. Exploiting Proposition 4.6, we project Δ_1 using the invertible matrix $R^\star(z)$ defined as

$$R^\star(z) = \begin{bmatrix} R_r(z) & 0 \\ -f^\top(z) & 0 \\ 0 & 1 \\ DH(z) & 0 \end{bmatrix}, \tag{4.43}$$

in order to obtain

$$\Delta_1'(\eta,\varepsilon) = R^\star(z)\Delta_1(\eta,\varepsilon) = \begin{pmatrix}\Delta_r(\zeta,\sigma,s,\varepsilon)\\ \Delta_c(\zeta,\sigma,s,\varepsilon)\end{pmatrix} = \begin{cases} A(z)\begin{pmatrix}\zeta\\ \sigma\end{pmatrix} + b(z) \\ \langle DH(z), \chi(z)\rangle \end{cases} + O(\varepsilon),$$

$$A(z) = \begin{bmatrix} A_r(z) & 0 & 0 \\ w^\top(z) & m\tau_v & -1 \\ \partial_{\tilde\xi} L(z, m\tau) K_r(z) & \langle \partial_{\tilde\xi} L(z, m\tau), v(z)\rangle & l\partial_\delta L(z, m\tau)\end{bmatrix}, \tag{4.44}$$

$$b(z) = \begin{pmatrix} R_r(z)\chi(z) \\ -\langle f(z), \chi(z)\rangle \\ 0\end{pmatrix}.$$

We now aim to show that $A(z)$ is an invertible matrix for any s. Due to its block matrix structure, its determinant reads

$$\det\big(A(z)\big) = \det\big(A_r(z)\big)\big(\langle \partial_{\tilde\xi} L(z, m\tau), v(z)\rangle + ml\tau_v \partial_\tau L(z, m\tau)\big), \tag{4.45}$$

where the first factor is nonzero due to Proposition 4.6. For the second factor, we use the identity

$$L(x_0(t; \vartheta_{\mathcal{S}}(\lambda)), mT(\lambda)) = \lambda, \tag{4.46}$$

whose differentiation in λ, evaluation $\lambda = \lambda_z$ and division by $||D\vartheta_{\mathcal{S}}(\lambda_z)||$ yields

$$\langle \partial_{\tilde\xi} L(z, m\tau), v(z)\rangle + ml\tau_v \partial_T L(z, m\tau) = 1/||D\vartheta_{\mathcal{S}}(\lambda_z)||, \tag{4.47}$$

proving that $A(z)$ is then invertible. Hence, we can solve for ζ and σ in the leading order term of Δ_r for any s, so that the implicit function theorem ($\Delta_1' \in C^{r-1}$ with $r \geq 2$) guarantees that we can locally express $\zeta = \zeta_r(s,\varepsilon)$ and $\sigma = \sigma_r(s,\varepsilon)$ such that $\Delta_r(\zeta_r(s,\varepsilon), \sigma_r(s,\varepsilon), s, \varepsilon) = 0$. Thus, we have shown that the perturbed solutions of $\Delta_{l,L}(\xi,\delta,\varepsilon) = 0$ have a one-to-one correspondence with the zeros of the bifurcation function $B_L^{m:l}(s,\varepsilon)$ defined as

$$B_L^{m:l} : \mathbb{R}\times\mathbb{R}\to\mathbb{R}, \quad B_L^{m:l}(s,\varepsilon) = \Delta_c(\zeta_r(s,\varepsilon), \sigma_r(s,\varepsilon), s, \varepsilon) = M_{m:l}(s) + O(\varepsilon), \tag{4.48}$$

where $M_{m:l}(s) = \langle DH(z), \chi(z)\rangle$. Moreover, this function does not depend on the mapping L used as a constraint in Eq. (4.4).

We now aim to simplify the Melnikov-type function $M_{m:l}(s)$ to the form in Eq. (4.5). Denoting with $X_0(t; x_0(s;p))$ the solution of the first variational problem for the vector field $f(x)$, we write explicitly the solution of the first variational problem in ε (see [11]) leading to

$$\begin{aligned} M_{m:l}(s) = &\ \langle\, DH(x_0(s;p))\,,\, x_\varepsilon(m\tau; x_0(s;p), m\tau/l, 0)\rangle \\ = &\ \big\langle\, DH(x_0(s;p))\,,\, X_0(m\tau; x_0(s;p))\cdot \\ &\cdot \int_0^{m\tau} X_0^{-1}(t; x_0(s;p))\, g(x_0(t; x_0(s;p)), t; m\tau/l, 0)dt\,\big\rangle, \end{aligned} \tag{4.49}$$

and we recall that the dynamics on an energy surface $H(x) = H(p)$ (that acts as a codim. 1 invariant manifold), is characterized by (see Proposition 3.2 in [123] for a proof)

$$DH(x_0(t+s;p)) = DH(x_0(s;p))X_0^{-1}(t+s;p), \quad DH(p)X_0(m\tau;p) = DH(p). \tag{4.50}$$

Equation (4.50) leads to

$$\begin{aligned} M_{m:l}(s) &= \left\langle DH(x_0(s;p))\,,\, \int_0^{m\tau} X_0^{-1}(t+s;p)\, g(x_0(t+s;p),t;m\tau/l,0)dt \right\rangle \\ &= \int_0^{m\tau} \left\langle DH(x_0(s;p))\,,\, X_0^{-1}(t+s;p)\, g(x_0(t+s;p),t;m\tau/l,0) \right\rangle dt \\ &= \int_0^{m\tau} \left\langle DH(x_0(t+s;p))\,,\, g(x_0(t+s;p),t;m\tau/l,0) \right\rangle dt, \end{aligned} \tag{4.51}$$

and this function is clearly smooth and $m\tau$-periodic. □

4.4.2 *Proof of theorem 4.1*

Proof. Thanks to Theorem 4.7, we are able to reduce the persistence problem of Eq. (4.4) to the study of $B_L^{m:l}(s,\varepsilon)$. The zeros of this function mark the existence of periodic orbits for ε small enough which smoothly connect to $\mathcal{Z}$ at $\varepsilon = 0$. Note that, if the $M_{m:l}(s) \equiv 0$, then no conclusions for persistence can be drawn solely from $M_{m:l}(s)$. Indeed, we need to analyze the $O(\varepsilon)$ term in $B_L^{m:l}$.

If the Melnikov function remains bounded away from zero, then we conclude the last statement thanks to the fact that no zeros of the bifurcation function exists for ε small enough.

We now analyze the case of simple zeros. Assuming that the conditions in Eq. (4.6) hold for s_0, the implicit function theorem guarantees that we can express $s = s(\varepsilon)$ from the bifurcation function $B_L^{m:l}(s,\varepsilon)$. According to the proof of Theorem 4.7, we can define

$$\zeta(\varepsilon) = \zeta_r(s(\varepsilon),\varepsilon), \quad \sigma(\varepsilon) = \sigma_r(s(\varepsilon),\varepsilon), \quad \eta(\varepsilon) = (\zeta(\varepsilon),\sigma(\varepsilon),s(\varepsilon)), \tag{4.52}$$

such that $\Delta_{l,L}(\varphi(\eta(\varepsilon),\varepsilon),\varepsilon) = 0$ for a sufficiently small neighborhood $C_0 \subset \mathbb{R}$. Hence, we can express the initial conditions and the periods

$$\begin{cases} \xi(\varepsilon) = x_0(s(\varepsilon);p) + \varepsilon K_{\mathcal{TZ}}\big(x_0(s(\varepsilon);p)\big)\zeta(\varepsilon) = x_0(s_0;p) + O(\varepsilon) \\ l\delta(\varepsilon) = m\tau + \varepsilon\sigma(\varepsilon) = m\tau + O(\varepsilon) \end{cases} \tag{4.53}$$

of periodic orbits solving system (3.4) and satisfying $L(\xi(\varepsilon), l\delta(\varepsilon)) = \lambda$ for small enough $\varepsilon > 0$.

Finally, the second statement of Theorem 4.1 is a direct consequence of the intermediate value theorem. Namely, the existence of a simple zero for the Melnikov function implies that $M_{m:l}(s)$ is not constant and there exist points $s_1 = s_0 - \epsilon$ and $s_2 = s_0 + \epsilon$ such that $M_{m:l}(s_1)M_{m:l}(s_2) < 0$ for $\epsilon > 0$ small enough. Due to periodicity, we also have $M_{m:l}(s_2)M_{m:l}(s_1 + m\tau) < 0$. Thus, there exists at least another $\hat{s}_0 \in (s_2,\, s_1 + m\tau)$ such that $M_{m:l}(\hat{s}_0) = 0$ due to Bolzano's theorem and it must be a zero at which the function changes sign, i.e., a topologically transverse zero. □

Remark 4.2. Theorem 4.1 guarantees smooth persistence only. There may be degenerate cases where there exist periodic orbits of system (3.4) that are still $O(\varepsilon)$-close to $\mathcal{Z}$, but they can only be continuously connected to the latter or not connected at all. The Melnikov function in (4.5) cannot prove existence of such orbits.

Remark 4.3. To analyze the type of zeros of the Melnikov function, it is convenient to have closed formulae for its derivatives. The first derivative can be computed as

$$DM_{m:l}(s) = M'_{m:l}(s) = -\int_0^{m\tau} \left\langle DH(x_0(t+s;p))\,,\, \partial_t g(x_0(t+s;p),t;\tau m/l,0) \right\rangle dt, \tag{4.54}$$

given that

$$\begin{aligned} M'_{m:l}(s) &= \int_0^{m\tau} \partial_s \langle\, DH\,,\, g\,\rangle dt = \int_0^{m\tau} D_t \langle\, DH\,,\, g\,\rangle dt - \int_0^{m\tau} \langle\, DH\,,\, \partial_t g\,\rangle dt \\ &= -\int_0^{m\tau} \langle\, DH\,,\, \partial_t g\,\rangle dt, \end{aligned} \tag{4.55}$$

which is again a smooth periodic function. Thus, a transverse zero s_0 of $M_{m:l}(s)$ must satisfy:

$$\begin{aligned} &\int_0^{m\tau} \langle\, DH(x_0(t+s_0;p))\,,\, g(x_0(t+s_0;p),t;\tau m/l,0)\,\rangle dt = 0, \\ &\int_0^{m\tau} \langle\, DH(x_0(t+s_0;p))\,,\, \partial_t g(x_0(t+s_0;p),t;\tau m/l,0)\,\rangle dt \neq 0. \end{aligned} \tag{4.56}$$

Assuming enough smoothness, the second derivative of $M_{m:l}(s)$ is likewise

$$D^2_{ss} M_{m:l}(s) = \int_0^{m\tau} \langle\, DH(x_0(t+s;p))\,,\, \partial^2_{tt} g(x_0(t+s;p),t;\tau m/l,0)\,\rangle dt \tag{4.57}$$

A similar formula follows for high-order derivatives.

Remark 4.4. Note that if the orbit family can be parametrized with the period, one can directly insert the exact resonance condition into the displacement map. In this case, the method developed in [114] applies in a straightforward way in what the authors call a non-degenerate case. Compared with the discussion in that reference, we simplified the final Melnikov function.

4.4.3 *Proof of theorem 4.2*

Once the reduction to a scalar bifurcation function has been performed as in Theorem 4.7, the statements in Theorem 4.2 follow from results of the bifurcation analysis outlined in [121]. Specifically, one can look at Theorem 2.1 and Table 2.3 in Chapter IV to recognize the bifurcation problem. In that reference, the singular bifurcation isola birth is called *isola centre*.

We further remark that a saddle-node bifurcation persists in the perturbed setting. Indeed, defining

$$B_{sn}(s,\kappa,\varepsilon) = \begin{cases} B_L^{m:l}(s,\kappa,\varepsilon) \\ \partial_s B_L^{m:l}(s,\kappa,\varepsilon) \end{cases}, \tag{4.58}$$

we find that

$$B_{sn}(s_0,\kappa_0,0) = 0, \quad \det\big(\partial_{s,\kappa} B_{sn}(s_0,\kappa_0,0)\big) = -\partial^2_{ss} M_{m:l}(s_0,\kappa_0)\partial_\kappa M_{m:l}(s_0,\kappa_0) \neq 0. \tag{4.59}$$

Therefore, the implicit function theorem applies, guaranteeing that a locally unique orbit persists at $s_{sn} = s_0 + O(\varepsilon)$, $\kappa_{sn} = \kappa_0 + O(\varepsilon)$.

4.4.4 *Melnikov function with monoharmonic, space-independent forcing*

We show the derivations that lead to Eq. (4.18). By substituting the Fourier series of Eq. (4.17) into (4.18), we find that

$$\begin{aligned} w_{m:l}(s,e) = \; & -e \sum_{k=1}^{\infty} \int_0^{m\tau} k\omega \langle a_k, f_e\rangle \sin\left(k\omega(t+s)\right) \cos\left(\frac{l}{m}\omega t\right) dt + \\ & +e \sum_{k=1}^{\infty} \int_0^{m\tau} k\omega \langle b_k, f_e\rangle \cos\left(k\omega(t+s)\right) \cos\left(\frac{l}{m}\omega t\right) dt. \end{aligned} \tag{4.60}$$

Expanding using trigonometric addition formulae, we obtain

$$\begin{aligned} w_{m:l}(s,e) = \quad & -e\sum_{k=1}^{\infty} k\omega\langle a_k, f_e\rangle \cos(k\omega s)\int_0^{m\tau}\sin(k\omega t)\cos\left(\frac{l}{m}\omega t\right)dt+ \\ & -e\sum_{k=1}^{\infty} k\omega\langle a_k, f_e\rangle \sin(k\omega s)\int_0^{m\tau}\cos(k\omega t)\cos\left(\frac{l}{m}\omega t\right)dt+ \\ & +e\sum_{k=1}^{\infty} k\omega\langle b_k, f_e\rangle \cos(k\omega s)\int_0^{m\tau}\cos(k\omega t)\cos\left(\frac{l}{m}\omega t\right)dt+ \\ & -e\sum_{k=1}^{\infty} k\omega\langle b_k, f_e\rangle \sin(k\omega s)\int_0^{m\tau}\sin(k\omega t)\cos\left(\frac{l}{m}\omega t\right)dt \end{aligned} . \tag{4.61}$$

We recall the following trigonometric integral identities with $k \neq j$:

$$\begin{aligned} &\int_0^{\tau}\sin(k\omega t)\cos(j\omega t) = \int_0^{\tau}\sin(k\omega t)\sin(j\omega t) = \int_0^{\tau}\cos(k\omega t)\cos(j\omega t) = 0, \\ &\int_0^{\tau}\sin(k\omega t)\cos(k\omega t) = 0, \quad \int_0^{\tau}\sin^2(k\omega t) = \int_0^{\tau}\cos^2(k\omega t) = \frac{\tau}{2}. \end{aligned} \tag{4.62}$$

Thus, the integrals in the first and last summations in Eq. (4.61) are always zero. We first discuss the case $m \neq 1$. We call $m\tau = \tau_o$ so that Eq. (4.61) becomes

$$\begin{aligned} w_{m:l}(s,e) = \quad & -e\sum_{k=1}^{\infty} k\omega\langle a_k, f_e\rangle \sin(k\omega s)\int_0^{\tau_o}\cos\left(\frac{2km\pi}{\tau_o}t\right)\cos\left(\frac{2l\pi}{\tau_o}t\right)dt+ \\ & +e\sum_{k=1}^{\infty} k\omega\langle b_k, f_e\rangle \cos(k\omega s)\int_0^{\tau_o}\cos\left(\frac{2km\pi}{\tau_o}t\right)\cos\left(\frac{2l\pi}{\tau_o}t\right)dt. \end{aligned} \tag{4.63}$$

Therefore, to obtain nonzero integrals in Eq. (4.63), we need that $km = l$ according to Eq. (4.62). However, since we choose l and m to be positive integers and relatively prime, that condition will never hold. We then conclude that $w_{m:l}(s,e) \equiv 0$ for $m \neq 1$.

For $m = 1$, only the terms for $k = l$ can be nonzero in Eq. (4.63), resulting in

$$w_{m:l}(s) = -l\pi\langle a_l, f_e\rangle \sin(l\omega s) + l\pi\langle b_l, f_e\rangle \cos(l\omega s). \tag{4.64}$$

Thus, we recover Eq. (4.18) with the proper definitions of $A_{l,e}$ and $\alpha_{l,e}$.

5

STABILITY OF FORCED-DAMPED MOTIONS

With respect to the previous chapter, here we adopt the Hamiltonian formalism, which allows us to derive closed-form expressions for the assessment of stability, without compromising the generality of our results.

Since the Lagrangian L of Eq. (3.1) is a convex function of $\dot{q}$, the conservative system can be written in Hamiltonian form [116, 117]. Introducing the generalized momenta

$$p = \partial_{\dot{q}} L = M(q)\dot{q} + G_1(q), \tag{5.1}$$

we can express the velocities as $\dot{q} = F(q,p) = M^{-1}(q)(p - G_1(q))$ and the total energy as

$$H(q,p) = \langle\, p\,,\, F(q,p)\rangle - L(q,F(q,p)) = \frac{1}{2}\langle\, p - G_1(q)\,,\, M^{-1}(q)(p - G_1(q))\rangle - G_0(q) + V(q), \tag{5.2}$$

which agrees with (3.2). Introducing the notation $x = (q,p) \in \mathbb{R}^{2n}$, we obtain the equations of motion in the form

$$\dot{x} = JDH(x) + \varepsilon g(x,t;\delta,\varepsilon), \quad J = \begin{bmatrix} 0_{n\times n} & I_{n\times n} \\ -I_{n\times n} & 0_{n\times n} \end{bmatrix}, \tag{5.3}$$

where we assume that $H \in C^{r+1}$ with $r \geq 3$, while g is C^{r-1} in t and C^r in the other arguments. The vector fields in (5.3) are defined as

$$DH(x) = \begin{pmatrix} \partial_q H \\ \partial_p H \end{pmatrix} = \begin{pmatrix} -\partial_q L(q,F(q,p)) \\ F(q,p) \end{pmatrix}, \quad g(x,t;\delta,\varepsilon) = \begin{pmatrix} 0 \\ Q(q,F(q,p),t;\delta,\varepsilon) \end{pmatrix}. \tag{5.4}$$

We assume that any further parameter dependence in our upcoming derivations is of class C^r and that the model (5.3) is again valid in a subset $\mathcal{U} \subseteq \mathbb{R}^{2n}$ of the phase space. With respect to chapter 4, we need to assume an additional degree of smoothness for the vector field because we have to compute higher order expansions for the stability assessment. Trajectories of (5.3) that start from $\xi \in \mathbb{R}^{2n}$ at $t = 0$ will be denoted with $x(t;\xi,\delta,\varepsilon) = (q(t;\xi,\delta,\varepsilon),\, p(t;\xi,\delta,\varepsilon))$. We will also use the shorthand notation $x_0(t;\xi) = (q_0(t;\xi), p_0(t;\xi)) = x(t;\xi,\delta,0)$ for trajectories of the unperturbed (conservative) limit of system (5.3). The equation of (first) variations for system (5.3) about the solution $x(t;\xi,\delta,\varepsilon)$ reads

$$\dot{X} = \big(JD^2H(x(t;\xi,\delta,\varepsilon)) + \varepsilon\partial_x g(x(t;\xi,\delta,\varepsilon),t;\delta,\varepsilon)\big)X, \quad X(0) = I_{2n\times 2n}, \tag{5.5}$$

whose solutions for $\varepsilon = 0$ will be denoted as $X_0(t;\xi) = X(t;\xi,\delta,0)$. As long as $x_0(t;\xi) \in \mathcal{U}$, we recall that $H(x_0(t;\xi)) = H(\xi)$ and that $X_0(t;\xi)$ is a symplectic matrix [124]. We also note that the Melnikov function (4.5,4.11) is not affected by the change of coordinates with respect to those of chapter 4.

5.1 STABILITY FROM THE MELNIKOV METHOD

In this section, we state our main mathematical results on the stability of solutions arising as perturbations from the conservative limit. We now make the following assumption:

(A.1) The periodic orbit $\mathcal{Z} \subset \mathcal{U}$ of system (5.3) for $\varepsilon = 0$ is m-normal and, after a possible phase shift, its Melnikov function $M_{m:l}(s)$ defined in Eq. (4.5) has a simple zero at 0.

By chapter 4, assumption (A.1) implies the existence of an $l\delta$-periodic orbit, denoted $\mathcal{Z}_\varepsilon$, satisfying system (5.3) for small $\varepsilon > 0$, with $l\delta = m\tau + O(\varepsilon)$ and with initial condition $O(\varepsilon)$-close to z. We denote by $\Pi = X_0(m\tau; z) = X_0^m(\tau; z)$ the monodromy matrix of $\mathcal{Z}$ based at the point $z \in \mathcal{Z}$ evaluated along m cycles of the periodic orbit $\mathcal{Z}$. Our first results is the following simple consequence of our assumptions.

Proposition 5.1. *If there exists an eigenvalue μ of Π such that $|\mu| > 1$, then $\mathcal{Z}_\varepsilon$ is unstable for ε small enough.*

Proof. The maximum distance between the Floquet multipliers of the orbit $\mathcal{Z}_\varepsilon$ and those of its conservative limit $\mathcal{Z}$ can be bounded with a suitable power of the parameter ε (see, for example, Theorem 1.3 in Chapter IV of [125]). Hence, if there exists a multiplier μ of the conservative limit such that $|\mu| > 1$, then, for ε sufficiently small, $\mathcal{Z}_\varepsilon$ has a multiplier with the same property by the smooth dependence of the flow map on the parameter ε. □

If the assumption of Proposition 5.1 is not satisfied, then perturbations of $\mathcal{Z}$ may result in orbits with different stability types. Henceforth we assume the following condition to be satisfied:

(A.2) The eigenvalues of the monodromy matrix Π lie on the unit circle in the complex plane.

In the literature on Hamiltonian systems, an orbit satisfying (A.2) is called spectrally stable [126]. From a practical viewpoint, such orbits are of great interest as small perturbations of them may create asymptotically stable (and hence observable) periodic responses. We also need the next nondegeneracy assumption:

(A.3) The algebraic and geometric multiplicities of the eigenvalue $+1$ of Π are 2 and 1, respectively.

This guarantees that the family $\mathcal{P}$ of chapter 3 can be locally parametrized either with the values of the first integral H or with the period of the orbits [119]. In the former case, there exists a scalar mapping $T : \mathbb{R} \to \mathbb{R}_+$ that locally describes the minimal period of the orbits in $\mathcal{P}$ near $\mathcal{Z}$ as function of H. Moreover, $\tau = T(h)$ and $DT(h) = T'(h) \neq 0$ hold, where $h = H(z)$ is the energy level of $\mathcal{Z}$.

To state further stability results, we need some definitions. Let $\mathcal{V}$ be a $2v$-dimensional invariant subspace for Π and let $R_\mathcal{V} \in \mathbb{R}^{2n\times 2v}$ be a matrix whose columns form a basis of $\mathcal{V}$. We then have the following identity

$$\Pi R_\mathcal{V} = R_\mathcal{V} B_\mathcal{V} \tag{5.6}$$

for a unique $B_\mathcal{V} \in \mathbb{R}^{2v\times 2v}$.

Definition 5.1. *We call $\mathcal{V}$ a strongly invariant subspace for Π if $\det(B_\mathcal{V}) = 1$ and all the eigenvalues of $B_\mathcal{V}$ are not repeated in the spectrum of Π.*

Strongly invariant subspaces persist under small perturbations of Π, as shown in [125, 127], and we exploit this property in our technical proofs. The even dimensionality of any $\mathcal{V}$ in real form is a consequence of the fact that the eigenvalues of any symplectic matrix either appear in pairs $(\mu, 1/\mu)$ or in quartets $(\mu, 1/\mu, \bar{\mu}, 1/\bar{\mu})$ [128]. For the matrix $R_\mathcal{V}$, we call the left inverse

$$S_\mathcal{V} = \left(R_\mathcal{V}^\top J R_\mathcal{V}\right)^{-1} R_\mathcal{V}^\top J \tag{5.7}$$

the symplectic left inverse of $R_\mathcal{V}$. As we later prove in the section 5.3, $S_\mathcal{V}$ is well-defined.

Finally, we will use the notation

$$C_\mathcal{V} = -\frac{1}{m\tau v}\int_0^{m\tau} \operatorname{trace}\left(S_\mathcal{V} X_0^{-1}(t;z)\partial_x g(x_0(t;z), t; m\tau/l, 0) X_0(t;z) R_\mathcal{V}\right) dt \tag{5.8}$$

for the (local) volume contraction of the vector field g along the orbit $\mathcal{Z}$ related to the strongly invariant subspace $\mathcal{V}$.

The quantity $C_{\mathcal{V}}$, that serves as a nonlinear damping rate for the orbit $\mathcal{Z}_\varepsilon$, will turn out to have a key role in some of our upcoming conditions for the stability of $\mathcal{Z}_\varepsilon$. We also remark that $C_{\mathcal{V}}$ is invariant under changes of basis for $\mathcal{V}$. Indeed, we can define $\tilde{R}_{\mathcal{V}} = R_{\mathcal{V}} R_c$ for some invertible $R_c \in \mathbb{R}^{2v \times 2v}$ and obtain $\tilde{S}_{\mathcal{V}} = R_c^{-1} S_{\mathcal{V}}$, so that the invariance of the trace guarantees the one of $C_{\mathcal{V}}$. In particular, if $\mathcal{V} = \mathbb{R}^{2n}$, we have

$$C_{\mathbb{R}^{2n}} = -\frac{1}{m\tau n} \int_0^{m\tau} \text{trace}\left(\partial_x g(x_0(t;z), t; m\tau/l, 0)\right) dt. \tag{5.9}$$

5.1.1 *Conditions for instability*

Due to assumption (A.3), the tangent space $\mathcal{T}_z\mathcal{P}$, abbreviated as $\mathcal{T}$ from here onwards, is the two-dimensional strongly invariant subspace for Π related to its eigenvalues equal to $+1$. Due to the non-trivial Jordan block corresponding to these eigenvalues, the assessment of stability requires careful consideration. For a single-degree-of-freedom system ($n = 1$), the tangent space is the only strongly invariant subspace for Π. For higher-dimensional systems ($n > 1$), instabilities may develop also in the normal space $\mathcal{N}_z\mathcal{P}$ of the family $\mathcal{P}$ at the point z, indicated with the shorthand notation $\mathcal{N}$. The normal space is the $2(n-1)$-dimensional strongly invariant subspace for Π related to its eigenvalues different from $+1$. The following theorem covers some generic cases of instability.

Theorem 5.2. *[**Sufficient conditions for instability**]. $\mathcal{Z}_\varepsilon$ is unstable for $\varepsilon > 0$ small enough, if one of the following conditions is satisfied.*

(i) Instabilities in $\mathcal{T}$: when $T'(h)M'_{m:l}(0) < 0$ or when both $T'(h)M'_{m:l}(0) > 0$ and $C_{\mathcal{T}} < 0$.

(ii) Further instabilities ($n > 1$): when $C_{\mathcal{V}} < 0$ in a strongly invariant subspace $\mathcal{V}$ for Π.

We prove this theorem in the section 5.3. In statement *(ii)*, $\mathcal{V}$ can be simply chosen as $\mathbb{R}^{2n}$ so its volume contraction can be directly computed with Eq. (5.9). To identify instability in the normal space, one can then analyze any $\mathcal{V} \subseteq \mathcal{N}$.

Remark 5.1. Theorem 5.2 provides analytic expressions that allow to assess instability of the perturbed orbit, at least for generic cases, solely depending on the conservative limit, its first variation and the perturbative vector field. From a geometric viewpoint, we can thus detect instabilities whenever the volume of a strongly invariant subspaces shows expansion under action of the perturbed flow.

Remark 5.2. If the existence of a perturbed periodic orbit arising from $\mathcal{Z}$ is unknown, one may still use Proposition 5.1 or statement *(ii)* of Theorem 5.2 to conclude the instability of any perturbed orbit originating from $\mathcal{Z}$.

5.1.2 *Conditions for asymptotic stability*

While instability can be detected from a single condition, asymptotic stability from the linearization requires, by definition, more conditions. The next theorem provides such a set of conditions.

Theorem 5.3. *[**Sufficient conditions for stability**]. Assume that, other than two eigenvalues equal to $+1$, the remaining eigenvalues of Π are $n-1$ distinct complex conjugated pairs. For $k = 1, ..., n-1$, denote by $\mathcal{N}_k \subset \mathcal{N}$ the strongly invariant subspace for Π related to the kth pair of eigenvalues. Then, $\mathcal{Z}_\varepsilon$ is asymptotically stable for $\varepsilon > 0$ small enough if each of the following conditions holds*

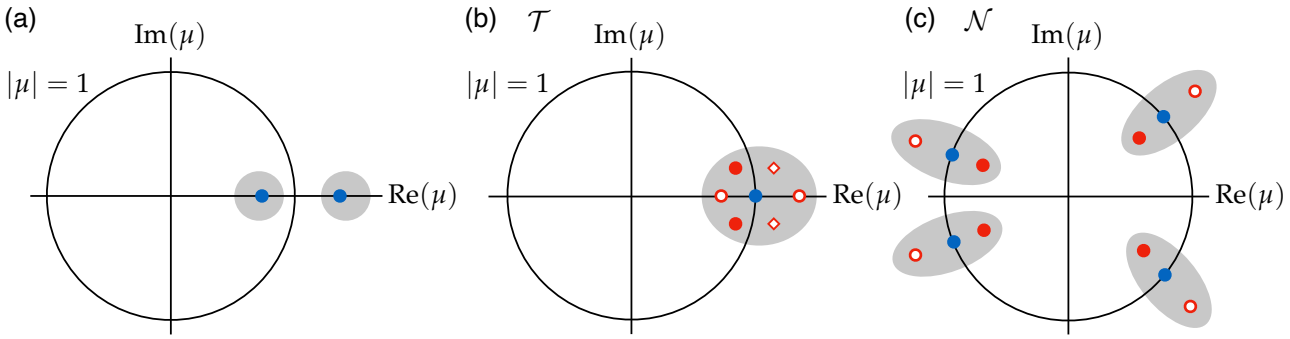

Figure 5.1: Summary of our stability results in terms of the perturbation (in red) of the Floquet multipliers of the conservative limit (in blue). Grey shaded areas show possible perturbation zones. Plot (a) refers to Proposition 5.1 where the conservative limit has a real pair $(\mu, 1/\mu)$ of Floquet multipliers. In contrast, plot (b) refers to the tangent space and illustrates the conditions *(i)* of Theorems 5.2 and of 5.3 (here with red dots). In the former case, two different white-faced markers are used for the two possible instabilities. For the normal space, plot (c) shows the conditions *(ii)* of Theorems 5.2 (with red rings) and of 5.3 (with red dots).

(i) $T'(h)M'_{m:l}(0) > 0$ *and* $C_{\mathcal{T}} > 0$,

(ii) $C_{\mathcal{N}_k} > 0$ *for all* $k = 1, ..., n-1$.

We prove this theorem in the section 5.3. The conditions *(i)* in Theorems 5.2 and 5.3 apply for systems with one degree of freedom. These conditions are consistent with the ones derived in [4, 104], up to sign changes due to the shift s present in the Melnikov function. For $n = 1$, the divergence of the perturbation, cf. Eq. (5.9), is sufficient to determine the volume contraction since $C_{\mathbb{R}^2} \equiv C_{\mathcal{T}}$.

Simple zeros of the Melnikov function typically appear in pairs moving in opposite directions, cf. Fig. 6.1b. Thus, assuming a pair of simple zeros and positive volume contractions in Theorem 5.3, two periodic orbits bifurcate from $\mathcal{Z}$ for $\varepsilon > 0$ small enough. One of them is unstable and the other asymptotically stable. This analytical conclusion matches with the results of several experimental and numerical studies present in the literature. Figure 5.1 summarizes our results on stability showing the perturbation (in red) of the Floquet multipliers of the conservative limit (in light blue).

Remark 5.3. If $C_{\mathcal{N}_k} = 0$, then $\mathcal{Z}_\varepsilon$ generically undergoes a Neimark-Sacker or torus bifurcation [85, 129, 130]. High-order nondegeneracy conditions have to be satisfied, but this bifurcation implies that a resonant torus appears near $\mathcal{Z}_\varepsilon$. As they might be attractors for system (5.3), their identification is relevant for the frequency response, as discussed in [131–133].

Remark 5.4. Theorem 5.3 does not discuss in detail cases in which Π admits either -1 as an eigenvalue or a repeated complex conjugated pairs. These configurations indicate that $\mathcal{Z}$ may be an orbit at which a period doubling or a Krein bifurcation, respectively, occurs [85]. One may still provide analytic expressions to evaluate the stability of $\mathcal{Z}_\varepsilon$, but we leave the discussion of these non-generic cases to dedicated examples.

5.1.3 *Determining contraction measures*

Especially for system with a large number of degrees of freedom, the volume contraction (or nonlinear damping rate) formula for $C_{\mathcal{V}}$ when $\mathcal{V} \subset \mathbb{R}^{2n}$ may be difficult to evaluate due to the presence of X_0, its inverse and the required subspace identification. Regarding the perturbative vector field as defined in Eq. (5.5), the following proposition illustrates the simple case of uniform volume contraction.

Proposition 5.4. *Let $\mathcal{V}$ be a strongly invariant subspace for Π. If $\partial_q Q(q, F(q,p), t; m\tau/l, 0)$ is a symmetric matrix-valued function and $\partial_p Q(q, F(q,p), t; m\tau/l, 0) = -\alpha I$, then $C_{\mathcal{V}} = \alpha$.*

We prove this statement in the section 5.3. In the Hamiltonian literature, the assumptions of Proposition 5.4 hold for conformally symplectic flows [134, 135] under appropriate forcing.

For example, the condition of uniform contraction is satisfied in mechanical systems with $G_1 \equiv 0$ when the leading-order perturbation terms are pure forcing and Rayleigh-type dissipation proportional to the mass matrix, i.e. $Q(q, \dot{q}, t; \gamma, 0) = f^{ext}(t; \gamma) - \alpha M(q)\dot{q}$. However, such uniform volume contraction is an overly simplified damping model for practical applications and hence may only be relevant for numerical experiments.

5.2 EXAMPLES

5.2.1 *Subharmonic response in a gyroscopic system*

The equations of motion of the two-degree-of-freedom system in Fig. 5.2 read

$$\begin{aligned} m_b\ddot{q} + 2G\dot{q} - m_b\Omega^2 q + DV(q) &= \hat{Q}(q, \dot{q}, t), \\ G = m_b \begin{bmatrix} 0 & -\Omega \\ \Omega & 0 \end{bmatrix}, \quad V(q) &= \frac{1}{2}\sum_{j=1}^{4} k_j \left(l_j(x,y) - l_0\right)^2, \\ l_{1,3}(x,y) = \sqrt{(l_0 \pm x)^2 + y^2}, \quad l_{2,4}(x,y) &= \sqrt{x^2 + (l_0 \pm y)^2}, \end{aligned} \tag{5.10}$$

where $q = (x, y)^\top$ are the generalized coordinates with respect to a reference frame rotating with constant angular velocity Ω. We assume that the Lagrangian component $\hat{Q}$ contains all the small, non-conservative forces acting on the system as follows:

$$\hat{Q}(q, \dot{q}, t) = \varepsilon\big(Q_{d,\alpha}(q, \dot{q}) + Q_{d,\beta}(q, \dot{q}) + Q_f(t)\big), \tag{5.11}$$

- uniform dissipation linearly depending on the absolute velocities of the mass m_b

$$\varepsilon Q_{d,\alpha}(q, \dot{q}) = -\varepsilon\alpha m_b(\dot{q} + m_b^{-1} G q); \tag{5.12}$$

- stiffness-proportional dissipation for the spring-damper elements, i.e. $c_j = \varepsilon\beta k_j$ for $j = 1, \dots 4$ and

$$\begin{aligned} \varepsilon Q_{d,\beta}(q, \dot{q}) &= -\varepsilon\beta C(q)\dot{q}, \\ C(q) = \sum_{j=1}^{4} k_j \begin{bmatrix} \left(\partial_x l_j(x,y)\right)^2 & \partial_x l_j(x,y)\partial_y l_j(x,y) \\ \partial_x l_j(x,y)\partial_y l_j(x,y) & \left(\partial_y l_j(x,y)\right)^2 \end{bmatrix}; \end{aligned} \tag{5.13}$$

- mono-harmonic forcing of frequency $l\Omega$

$$\varepsilon Q_f(t) = \varepsilon e \begin{pmatrix} +\cos(l\Omega t) \\ -\sin(l\Omega t) \end{pmatrix}, \quad l \in \mathbb{N}. \tag{5.14}$$

This simple model with strong geometric nonlinearities finds application in the fields of rotordynamics [136] or gyroscopic MEMS [137]. Here, sinusoidal forces whose frequencies clock at multiple of the rotating angular frequencies either appear due to diverse effects [138, 139] (e.g. asymmetries, nonrotating loads or multi-physical couplings) or are purposefully inserted in the system. From a physical standpoint [6], the dissipation controlled by the coefficient α models, for example, radiation damping, while β governs material or structural damping.

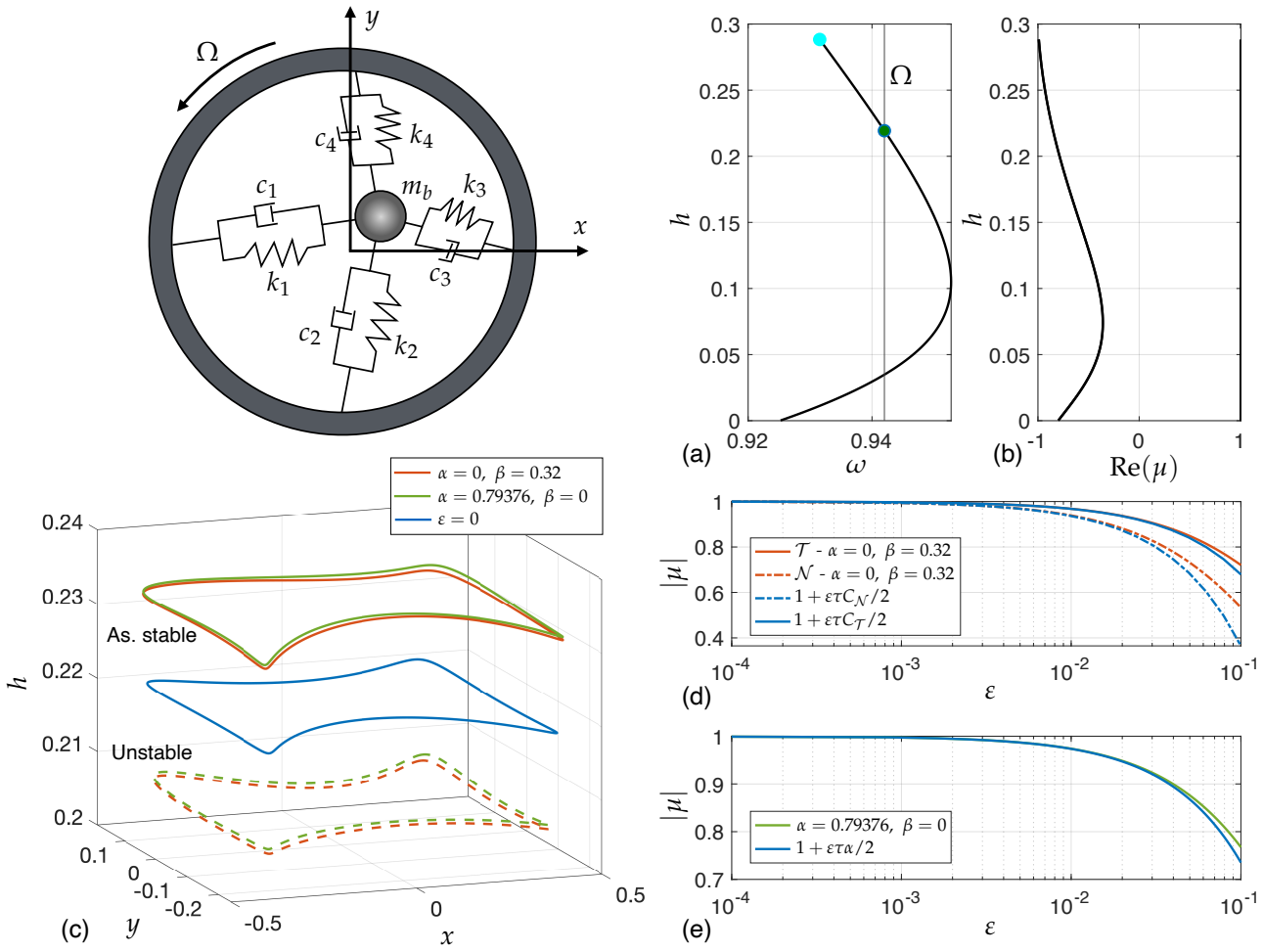

Figure 5.2: Plot (a) shows the conservative backbone curve in terms of frequency and value of the first integral for the family of periodic solutions for the dynamical system (5.16), while plot (b) the real part of the two couple of Floquet multiplier of the family. The blue dot in plot (a) corresponds to the periodic orbit illustrated in plot (c) in terms of the coordinates (x, y) and the value of the first integral. This plot also shows the stable (solid lines) and unstable (dashed lines) periodic orbits bifurcating from the conservative limit at $\varepsilon = 0.01$. The green lines indicate the orbit for $\alpha = 0.76376$ and $\beta = 0$, while orange ones for $\alpha = 0$ and $\beta = 0.32$. With consistent colors, plots (d) and (e) show the evaluation of the absolute value of the Floquet multipliers whose analytic predictions are depicted in blue. In plot (d), solid lines refers to the tangent space $\mathcal{T}$, while dashed-dotted ones to the normal space $\mathcal{N}$.

Introducing the transformation $p = m_b\dot{q} + Gq$, the Hamiltonian for the conservative limit takes the form

$$H(q,p) = \frac{1}{2m_b}\langle p, p\rangle - \frac{1}{m_b}\langle p, Gq\rangle + V(q). \tag{5.15}$$

Under the assumption $m_b = 1$, the equivalent, first-order equations for the two-degree-of-freedom system in Fig. 5.2 are

$$\begin{aligned} \dot{q} &= -Gq + p, \\ \dot{p} &= -DV(q) - Gp + \varepsilon\big(Q_f(t) - \alpha p - \beta C(q)(p - Gq)\big). \end{aligned} \tag{5.16}$$

For our analysis, we further assume that $\Omega = 0.942$, $l_0 = 1$, $k_1 = 1$, $k_2 = 4.08$, $k_3 = 1.37$, $k_4 = 2.51$ and $e = 1$. We begin with the study of the conservative limit ($\varepsilon = 0$), in which the origin is an equilibrium with the non-resonant linearized frequencies $(0.92513,\ 3.1431)$. Hence, according to the Lyapunov subcenter theorem [91], two families of periodic orbits (nonlinear normal modes) emanate

from the origin; we focus our attention on the one related to the slowest linearized frequency. By performing numerical continuation, we obtain the periodic orbit family of Fig. 5.2a (backbone curve) described in terms of the oscillation frequency $\omega = 2\pi/\tau$ and the value of the first integral h. We also plot the real part of the Floquet multipliers along the family in Fig. 5.2b. We stop continuation at the cyan point in Fig. 5.2a where a period doubling bifurcation occurs.

The backbone curve in Fig. 5.2a crosses two times the vertical line marking the rotating angular velocity Ω. We concentrate on the high-energy crossing point (depicted with a blue dot), where the family shows a softening trend, i.e., $T' > 0$ holds at this location. The corresponding periodic orbit is 1-normal and satisfies assumptions (A.2) and (A.3) of section 5.1.Moreover, this trajectory features a non-negligible third harmonic so that $1:3$ resonances with external forcing may occur, depending on the damping strength. Therefore, we fix $l = 3$ and we study forced-damped periodic orbits that may survive from this high-energy crossing point for the two damping mechanisms we have in our model.

For $\alpha = 0.76376$ and $\beta = 0$, the Melnikov function (4.5) evaluated for this periodic orbit reads

$$M_{1:3}(s) = 1.4402\cos(3\Omega s) - 1.1553. \tag{5.17}$$

This function has six simple zeros, but, as shown in section 4.2, they correspond to two perturbed orbits that occur as the amplitude of the work done by the forcing is greater than the dissipated energy, when evaluated at the conservative limit. Specifically, the zeros featuring a negative $M'_{1:3}(s)$ are related to an unstable orbit according to Theorem 5.2, while the others have a positive Melnikov-function derivative so that, due to Proposition 5.4 and to Theorem 5.3, they signal an asymptotically stable periodic orbit. Along with the conservative limit in blue, we plot these perturbed orbits using greens lines in Fig. 5.2c (solid for the asymptotically stable and dashed for the unstable) that have been obtained by setting $\varepsilon = 0.01$ in a direct numerical simulation with the periodic orbit toolbox of coco [26]. Qualitatively speaking, these periodic orbits are very similar to that of the conservative limit, but the average value of the first integral along them is higher (asymptotically stable orbit) or lower (unstable one).

By setting the damping values $\alpha = 0$ and $\beta = 0.32$, one retrieves the same Melnikov function as in Eq. (5.17). In particular, the dissipated energy is equal to the case $\alpha = 0.76376$ and $\beta = 0$. Thus, again, a stable and an unstable periodic orbit bifurcates from the conservative limit since the volume contractions are both positive. Again, direct numerical simulations with $\varepsilon = 0.01$ verify our predictions: we plot the asymptotically stable and unstable periodic orbits in Fig. 5.2c with orange solid and orange dashed lines, respectively.

The nonlinear damping rates (or volume contractions) $C_{\mathcal{V}}$ can be used to estimate the Floquet multipliers of perturbed solutions. As shown in the proofs reported in the section 5.3, the absolute value of a complex conjugated pair of eigenvalues arising from the perturbation of a strongly invariant subspace $\mathcal{V}$ reads

$$|\mu| = \sqrt{1 - \varepsilon\tau C_{\mathcal{V}} + o(\varepsilon)} = 1 - \varepsilon\frac{\tau}{2}C_{\mathcal{V}} + o(\varepsilon). \tag{5.18}$$

We illustrate these predictions for the asymptotically stable orbits of Fig. 5.2c. The blue lines in Fig. 5.2d show these estimates for $\mathcal{T}$ (solid line) and $\mathcal{N}$ (dashed-dotted line) that are in good agreement with the multipliers computed within the perturbed system for the case $\alpha = 0$ and $\beta = 0.32$, plotted in orange. Figure 5.2e represents the analogous curves for the case $\alpha = 0.76376$ and $\beta = 0$. Here, $C_{\mathcal{T}} = C_{\mathcal{N}} = \alpha$ and the blue line depicts predictions from the conservative limit, while the green one shows results from simulations in the forced-damped setting. We remark that, even though the dissipated energy is the same, stiffness-related damping provides higher volume contraction values with respect to the case of uniform damping. As expected, for high values of ε, our first-order computations may not be sufficient to adequately estimate the modulus of the perturbed multipliers.

For the low-energy crossing point between the backbone curve and the Ω vertical line, the Melnikov function is always negative. Therefore, no perturbed solution arises from this conservative limit for sufficiently small ε.

5.2.2 *Isolated response due to parametric forcing*

In this section, we study the parametrically-forced, three-degree-of-freedom system of nonlinear oscillators shown in Fig. 5.3. Parametric forcing [5] finds notable applications in the field of MEMS [137, 140]. By assuming a linear damping proportional to the mass matrix and unit masses, the equations of motion in Hamiltonian form read

$$\begin{aligned}
\dot{q} &= p, \\
\dot{p}_1 &= -k(q_1 - q_2) - k/3 q_1 - a q_1^2 - b q_1^3 - \varepsilon\alpha p_1, \\
\dot{p}_2 &= -k(q_2 - q_1) - k(q_2 - q_3) - \varepsilon\alpha p_2, \\
\dot{p}_3 &= -k(q_3 - q_2) + \varepsilon(q_3 f^{ext}(t);\Omega) - \alpha p_3),
\end{aligned} \qquad f^{ext}(t);\Omega) = \frac{4}{\pi}\sum_{j=1}^{3}\frac{1}{2j-1}\sin\big((2j-1)\Omega t\big), \tag{5.19}$$

where $q, p \in \mathbb{R}^3$, $k = 1$, $a = -1/2$, $b = 1$ and $\alpha, \varepsilon > 0$. The nonlinear behavior in this example arises from the material nonlinearity of the left-most spring in Fig. 5.3. We expect the appearance of isolas in the frequency response, at least for small ε. Indeed, as the forcing amplitude is controlled by q_3, it is necessary to exceed a threshold on the motion amplitude for the work done by the forcing to overcome energy dissipation by the damping.

For the conservative limit of the system, the origin is the unique fixed point[1] and no resonances occur among its linearized frequencies $(0.30394, 1.0854, 1.7501)$. Thus, three families of periodic orbits emanate from the origin [91], and they can be parametrized with the value of the first integral h. We focus on detecting perturbed solutions arising from the lowest-frequency family. We denote by $\underline{\omega}(h)$ the frequency of the periodic orbits in this family normalized by the linear limit at $h = 0$, i.e. $\underline{\omega}(h) = T(0)/T(h)$. When performing numerical continuation, the first family is 1-normal and satisfies assumptions (A.2) and (A.3) of section 5.1 for $1 < \underline{\omega}(h) < 1.165$, which is our frequency range of interest. The backbone curve for this family is illustrated in Fig. 5.3a in terms of the normalized frequency and the maximum amplitude of the coordinate q_3 along periodic orbits, denoted by $\max|q_3|$. This backbone curve displays a hardening trend, i.e., $\underline{\omega}'(h) > 0$, $T'(h) < 0$. Figures 5.3b and 5.3c respectively show the trend of real and imaginary parts of the Floquet multipliers of the family.

We select a perturbation in Eq. (5.19) to satisfy the assumptions of Proposition 5.4, so that the volume contractions $C_{\mathcal{V}}$ are always positive. Moreover, the forcing corresponds to the sixth harmonic approximation of a square wave with unit amplitude and period $2\pi/\Omega$. We now examine via our Melnikov approach perturbed periodic orbits when the forcing period is in $1:1$ resonance with the period of the orbits of the first family, thus we set $\Omega = 2\pi/T(h)$. Sweeping through the family, we evaluate the Melnikov function on every orbit and hence construct a scalar function $M_{1:1}(\theta, h, \alpha)$, using the phase $\theta = 2\pi s/T(h)$ instead of the shift s.

Figure 5.3d shows the zero level set of $M_{1:1}(\theta, h, 0.121)$, in green, and of $M_{1:1}(\theta, h, 0.141)$, in orange, plotted in the plane $(\theta, \underline{\omega})$. Solid lines indicate zeros in θ with $\partial_\theta M_{1:1} < 0$, while dashed ones indicate zeros with $\partial_\theta M_{1:1} > 0$. According to Theorem 5.2, the latter zeros predict unstable perturbed periodic orbits, while the former predict asymptotically stable ones Theorem 5.3. However, there are conservative orbits of the family that either feature a pair of Floquet multipliers related to the

1 The origin is the only point at which the potential is stationary. This condition is expressed by the following equations:

$$q_3 = q_2, \quad q_2 = q_1, \quad q_1(q_1^2 - q_1/2 + 1/3) = 0.$$

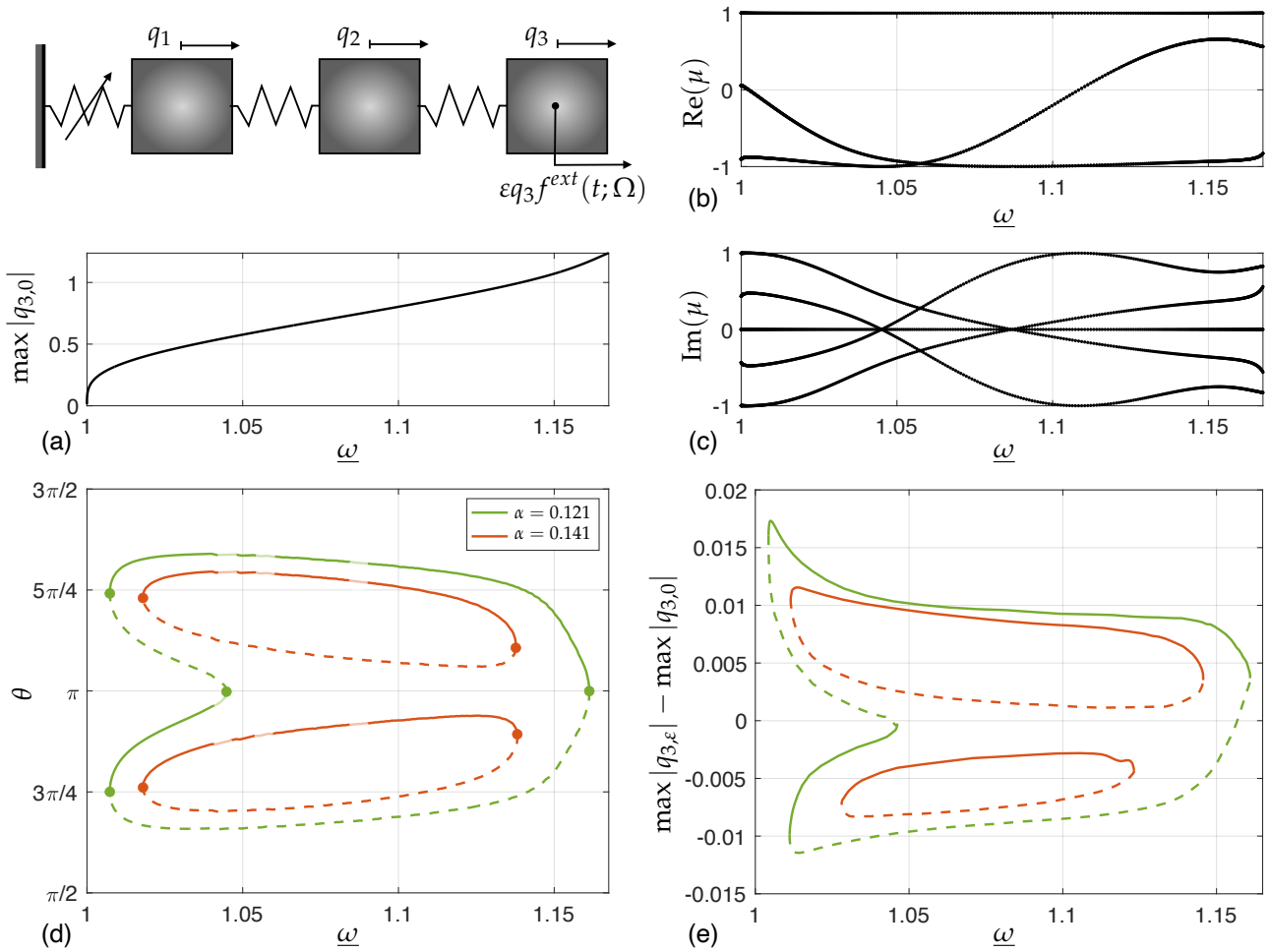

Figure 5.3: Plot (a) shows the backbone curve in terms of the normalized frequency $\underline{\omega}$ and the amplitude of the first family of periodic solutions for the conservative limit of system (5.19). The trend of Floquet multipliers of the family is shown in plot (b) in terms of their real part, while plot (c) regards the imaginary one. Plot (d) illustrates the level set of the Melnikov function for two values of the damping in the plane $(\underline{\omega}, , \theta)$, where the latter is the orbit phase. Here, dashed lines predict unstable perturbed orbits, while solid ones indicate asymptotically stable ones. The latter feature faded regions at which the predictions of Theorem 5.3 could turn out to be weak. The dots instead denote saddle-node bifurcations. Plot (e) shows the numerical simulations of the frequency response for the perturbed system at $\varepsilon = 0.0025$. The horizontal axis displays the normalized frequency and the vertical one the distance from the conservative backbone curve.

normal space equal to -1, or have two coincident complex conjugated pairs of Floquet multipliers (cf. Figs. 5.3b,c). At these resonances, Theorem 5.3 is not applicable and hence the prediction of asymptotic stability could fail in the vicinity of these orbits, shown with faded solid lines in Fig. 5.3d. Moreover, the dots in Fig. 5.3d depict quadratic zeros with respect to θ of $M_{1:1}$ at which saddle-node bifurcations occur.

From lower to higher frequencies for $\alpha = 0.121$, the Melnikov has two quadratic zeros when $\Omega \approx 1.01$. Afterwards, they evolve as four simple zeros, then the internal pair collapses in a quadratic zero and the remaining zeros persist until $\Omega(h) \approx 1.158$. For this value of α, the multi-harmonic, parametric forcing of Eq. (5.19) generates an inverse cup-shaped isolated response curve. In contrast, two disjoint isolas exist when damping is increased at $\alpha = 0.141$. These predictions are confirmed via direct numerical simulations of the perturbed system in Fig. 5.3e for $\varepsilon = 0.0025$, plotted with corresponding colors. Here we depict the frequency response by showing the distance, in terms of the amplitude $\max|q_3|$, to the conservative (isochronous) limit. When interpreting these results,

one has to recall from section 4, that the Melnikov function is the leading-order approximation of the bifurcation function governing the persistence problem. Hence, the level sets in Fig. 5.3b are approximate ones and, in particular, the symmetric appearance of zeros will be, generically, destroyed in the full bifurcation function.

5.3 PROOFS OF MATHEMATICAL RESULTS

In this section, we adopt the assumptions of section 5.1 and derive an approximation for the Floquet multipliers of the non-autonomous periodic orbit $\mathcal{Z}_\varepsilon$, to be used for the stability assessment [4, 10, 11]. This orbit solves system (5.3) with $\delta(\varepsilon) = m\tau/l + \varepsilon\tilde{\tau} + o(\varepsilon)$ and has initial condition $\xi(\varepsilon) = z + \varepsilon\tilde{z} + o(\varepsilon)$.

We aim at analyzing the evolution of the Floquet multipliers of $\mathcal{Z}_\varepsilon$ from those of its conservative limit $\mathcal{Z}$. Since we rely on the linearized flow and look at the $O(\varepsilon)$-perturbation as in the next lemma, our stability assessment is valid in a small neighborhood of z and for ε small enough.

Lemma 5.5. *The monodromy matrix $P(\varepsilon) = X(l\delta(\varepsilon); \xi(\varepsilon), T(\varepsilon), \varepsilon)$ of $\mathcal{Z}_\varepsilon$ is approximated at order $O(\varepsilon^2)$ by the following expansion*

$$P(\varepsilon) = \Pi + \varepsilon\Pi\left(\Psi_H^{m:l} + \Psi_g^{m:l}\right) + O(\varepsilon^2), \tag{5.20}$$

where

$$\Psi_H^{m:l} = \int_0^{m\tau} X_0^{-1}(t;z) J D^3 H(x_0(t;z), x_1(t;z,\tilde{z})) X_0(t;z) dt,$$

$$x_1(t;z,\tilde{z}) = X_0(t;z)\tilde{z} + X_0(t;z)\int_0^t X_0^{-1}(s;z) g(x_0(s;z), s; m\tau/l, 0) ds, \tag{5.21}$$

$$\Psi_g^{m:l} = \int_0^{m\tau} X_0^{-1}(t;z)\partial_x g(x_0(t;z), t; m\tau/l, 0) X_0(t;z) dt.$$

Proof. The smoothness assumption for the vector fields involved are sufficient to approximate the solutions of systems (5.3) and (5.5) at $O(\varepsilon^2)$. The periodic orbit $\mathcal{Z}_\varepsilon$ is approximated by $x_0(t,z) + \varepsilon x_1(t;z,\tilde{z})$, where $x_1(t;z,\tilde{z})$ solves the initial value problem

$$\dot{x}_1 = J D^2 H(x_0(t;z)) x_1 + g(x_0(t;z), t; m\tau/l, 0), \quad x_1(0) = x_1(m\tau) = \tilde{z}. \tag{5.22}$$

By substituting $x = x_0 + \varepsilon x_1$, $X = X_0 + \varepsilon X_1$ and $\delta = m\tau/l + O(\varepsilon)$ in system (5.5) and expanding the equation, one obtains at $O(\varepsilon)$ the following initial value problem

$$\begin{aligned} &\dot{X}_1 = J D^2 H(x_0(t;z)) X_1 + \left(J D^3 H(x_0(t;z), x_1(t;z,\tilde{z})) + \partial_x g(x_0(t;z), t; m\tau/l, 0)\right) X_0(t;z), \\ &X_1(0) = 0, \end{aligned} \tag{5.23}$$

whose analytical solution, expressed by Lagrange's formula [10], at time $m\tau$ is the $O(\varepsilon)$-term in Eq. (5.20). □

5.3.1 *Some results in linear algebra*

We now introduce some factorization results exploiting the properties of the symplectic group, denoted $\mathrm{Sp}(2n, \mathbb{R})$. The next lemma characterizes the relation between strongly invariant subspaces related to Π, as defined in section 5.1.

Lemma 5.6. *Let $\Pi \in \mathrm{Sp}(2n, \mathbb{R})$ and assume that Π has two distinct strongly invariant subspaces $\mathcal{V}$ and $\mathcal{W}$ of dimensions $2v$ and $2w$, respectively. Let these subspaces be represented by $R_{\mathcal{V}} \in \mathbb{R}^{2n\times 2v}$ and $R_{\mathcal{W}} \in \mathbb{R}^{2n\times 2w}$, respectively, so that, for a unique $B_{\mathcal{V}} \in \mathbb{R}^{2v\times 2v}$ and $B_{\mathcal{W}} \in \mathbb{R}^{2w\times 2w}$, the following identities hold:*

$$\Pi R_{\mathcal{V}} = R_{\mathcal{V}} B_{\mathcal{V}}, \quad \Pi R_{\mathcal{W}} = R_{\mathcal{W}} B_{\mathcal{W}}. \tag{5.24}$$

Then:

(i) $R_{\mathcal{V}}^\top J R_{\mathcal{W}} = 0$ *and* $R_{\mathcal{W}}^\top J R_{\mathcal{V}} = 0$,

(ii) $R_{\mathcal{V}}^\top J R_{\mathcal{V}}$ *and* $R_{\mathcal{W}}^\top J R_{\mathcal{W}}$ *are invertible.*

Proof. We first prove statement *(i)*. Recalling the standard symplectic identity $\Pi^\top J \Pi = J$, we find

$$R_{\mathcal{V}}^\top J R_{\mathcal{W}} = (\Pi R_{\mathcal{V}} B_{\mathcal{V}}^{-1})^\top \Pi R_{\mathcal{W}} B_{\mathcal{W}}^{-1} = B_{\mathcal{V}}^{-\top} R v^\top \Pi^\top J \Pi R_{\mathcal{W}} B_{\mathcal{W}}^{-1} = B_{\mathcal{V}}^{-\top} R v^\top J R_{\mathcal{W}} B_{\mathcal{W}}^{-1}. \tag{5.25}$$

By denoting $A = R_{\mathcal{V}}^\top J R_{\mathcal{W}}$ and considering the leftmost and the rightmost sides of Eq. (5.25), we obtain a homogeneous Sylvester equation

$$B_{\mathcal{V}}^\top A = A B_{\mathcal{W}}^{-1}. \tag{5.26}$$

The eigenvalues of $B_{\mathcal{V}}^\top$ are equal to those of $B_{\mathcal{V}}$. Since Π is symplectic and by Definition 5.1, $B_{\mathcal{W}}^{-1}$ and $B_{\mathcal{W}}$ have identical eigenvalues as well. By assumption, the eigenvalues of $B_{\mathcal{V}}$ and $B_{\mathcal{W}}$ are distinct. Hence, $B_{\mathcal{V}}^\top$ and $B_{\mathcal{W}}^{-1}$ have no common eigenvalue, which implies that Eq. (5.26) has the unique solution $A = R_{\mathcal{V}}^\top J R_{\mathcal{W}} = 0$ (see Chapter VIII in [141]). Transposing A and using the identity $J^\top = -J$, one also gets that $R_{\mathcal{W}}^\top J R_{\mathcal{V}} = 0$.

We now prove statement *(ii)*. Since $\mathcal{V}$ and $\mathcal{W}$ correspond to the direct sums of spectral subspaces (sometimes called root spaces) of distinct eigenvalues of Π, we have that, by construction, $\mathcal{V} \cap \mathcal{W} = \emptyset$ (see Theorem 2.1.2 in [142] for a proof). By letting $\mathcal{Y} = \mathcal{V} \oplus \mathcal{W}$, we then define the linear map $A_{\mathcal{V}} := R_{\mathcal{V}}^\top J$ and we analyze its restriction to $\mathcal{Y}$, i.e. $A_{\mathcal{V}}|_{\mathcal{Y}} : \mathcal{Y} \to \mathbb{R}^{2v}$. Since the kernel of this map is $\mathcal{W}$, then its image must have dimension $\dim(\mathcal{Y}) - \dim(\mathcal{W}) = 2v$ by the rank-nullity theorem. Hence, $A_{\mathcal{V}} R_{\mathcal{V}} = R_{\mathcal{V}}^\top J R_{\mathcal{V}}$ is invertible. An analogous reasoning holds for the linear map $A_{\mathcal{W}} := R_{\mathcal{W}}^\top J$. □

The next result follows as a consequence of Lemma 5.6.

Lemma 5.7. *Let $\Pi \in \mathrm{Sp}(2n, \mathbb{R})$ and assume Π has two distinct strongly invariant subspaces $\mathcal{V}$ and $\mathcal{W}$ be such that $\mathcal{V} \oplus \mathcal{W} = \mathbb{R}^{2n}$. Denote by $2v$ the dimension of $\mathcal{V}$ and let these subspaces be spanned by a linear combination of the columns in $R_{\mathcal{V}} \in \mathbb{R}^{2n\times 2v}$ and $R_{\mathcal{W}} \in \mathbb{R}^{2n\times 2(n-v)}$, respectively. Define the symplectic left inverse matrices for $R_{\mathcal{V}}$ and $R_{\mathcal{W}}$ respectively as*

$$S_{\mathcal{V}} = (R_{\mathcal{V}}^\top J R_{\mathcal{V}})^{-1} R_{\mathcal{V}}^\top J, \quad S_{\mathcal{W}} = (R_{\mathcal{W}}^\top J R_{\mathcal{W}})^{-1} R_{\mathcal{W}}^\top J. \tag{5.27}$$

Then, the following factorization holds

$$R^{-1} = \begin{bmatrix} S_{\mathcal{V}} \\ S_{\mathcal{W}} \end{bmatrix}, \quad R = \begin{bmatrix} R_{\mathcal{V}} & R_{\mathcal{W}} \end{bmatrix}, \quad R^{-1} \Pi R = \begin{bmatrix} B_{\mathcal{V}} & 0 \\ 0 & B_{\mathcal{W}} \end{bmatrix}, \tag{5.28}$$

where the eigenvalues of $B_{\mathcal{V}} \in \mathbb{R}^{2v\times 2v}$ are distinct from those of $B_{\mathcal{W}} \in \mathbb{R}^{2(n-v)\times 2(n-v)}$.

We also remark that one can obtain from Eq. (5.28) the further identities

$$S_{\mathcal{V}} \Pi = B_{\mathcal{V}} S_{\mathcal{V}}, \quad S_{\mathcal{W}} \Pi = B_{\mathcal{W}} S_{\mathcal{W}}. \tag{5.29}$$

We will also need the next result.

Lemma 5.8. *Let $A \in \mathbb{R}^{2n\times 2n}$ and let $\mathcal{V}$ be a strongly invariant subspace for Π. Let the columns of $R_{\mathcal{V}} \in \mathbb{R}^{2n\times 2v}$ be a basis for $\mathcal{V}$ and let $S_{\mathcal{V}}$ be the symplectic left inverse of $R_{\mathcal{V}}$. Then*

$$\text{trace}(S_{\mathcal{V}} A R_{\mathcal{V}}) = \frac{1}{2}\text{trace}\left(S_{\mathcal{V}}(A - JA^{\top}J)R_{\mathcal{V}}\right). \tag{5.30}$$

In particular, if $A = J\hat{A}$ where $\hat{A}$ is symmetric, then $\text{trace}(S_{\mathcal{V}} A R_{\mathcal{V}}) = 0$.

Proof. Recall that $J^{\top}J = I$ and that, for arbitrary matrices A_1 and A_2, $\text{trace}(A_1A_2) = \text{trace}(A_2A_1)$ as well as $\text{trace}(A_1) = \text{trace}(A_1^{\top})$. Equation (5.30) holds because

$$\begin{aligned}
\text{trace}(S_{\mathcal{V}} A R_{\mathcal{V}}) &= \text{trace}\left((R_{\mathcal{V}}^{\top}JR_{\mathcal{V}})^{-1}R_{\mathcal{V}}^{\top}JAR_{\mathcal{V}}\right) = \text{trace}\left(((R_{\mathcal{V}}^{\top}JR_{\mathcal{V}})^{-1}R_{\mathcal{V}}^{\top}JAR_{\mathcal{V}})^{\top}\right)\\
&= \text{trace}\left(R_{\mathcal{V}}^{\top}A^{\top}J^{\top}R_{\mathcal{V}}(R_{\mathcal{V}}^{\top}JR_{\mathcal{V}})^{-\top}\right) = \text{trace}\left(R_{\mathcal{V}}^{\top}A^{\top}J^{\top}R_{\mathcal{V}}((R_{\mathcal{V}}^{\top}JR_{\mathcal{V}})^{\top})^{-1}\right)\\
&= \text{trace}\left(R_{\mathcal{V}}^{\top}A^{\top}J^{\top}R_{\mathcal{V}}(R_{\mathcal{V}}^{\top}J^{\top}R_{\mathcal{V}})^{-1}\right) = \text{trace}\left((R_{\mathcal{V}}^{\top}J^{\top}R_{\mathcal{V}})^{-1}R_{\mathcal{V}}^{\top}A^{\top}J^{\top}R_{\mathcal{V}}\right)\\
&= \text{trace}\left((R_{\mathcal{V}}^{\top}JR_{\mathcal{V}})^{-1}R_{\mathcal{V}}^{\top}A^{\top}JR_{\mathcal{V}}\right) = \text{trace}\left((R_{\mathcal{V}}^{\top}JR_{\mathcal{V}})^{-1}R_{\mathcal{V}}^{\top}JJ^{\top}A^{\top}JR_{\mathcal{V}}\right)\\
&= \text{trace}(S_{\mathcal{V}}J^{\top}A^{\top}JR_{\mathcal{V}}) = -\text{trace}(S_{\mathcal{V}}JA^{\top}JR_{\mathcal{V}}).
\end{aligned} \tag{5.31}$$

The last statement can be found by direct substitution of $A = J\hat{A}$ in Eq. (5.30). □

5.3.2 *Perturbation of the Floquet multipliers*

We now apply the results in section 5.3.2 to the initial perturbation expansion and we use the following definition from [127].

Definition 5.2. *Let v, w be arbitrary integers, $B_v \in \mathbb{R}^{v\times v}$ and $B_w \in \mathbb{R}^{w\times w}$. The separation of B_v and B_w with respect to an arbitrary norm $||\cdot||$ is defined as*

$$\text{sep}(B_v, B_w) := \min_{Y\in\mathbb{R}^{w\times v}:||Y||=1} ||YB_v - B_wY||. \tag{5.32}$$

We remark that $\text{sep}(B_v, B_w) \neq 0$ if and only if the eigenvalues of B_v are different from those of B_w. We can then state the next fundamental result.

Theorem 5.9. *Consider the perturbation expansion of Lemma 5.5 and the setting of Lemma 5.7. If $\varepsilon << \text{sep}(B_{\mathcal{V}}, B_{\mathcal{W}})$, then the eigenvalues of $P(\varepsilon)$ coincide with the eigenvalues of the matrices*

$$B_{\mathcal{V}}\left(I + \varepsilon S_{\mathcal{V}}(\Psi_H^{m:l} + \Psi_g^{m:l})R_{\mathcal{V}}\right) + O(\varepsilon^2), \quad B_{\mathcal{W}}\left(I + \varepsilon S_{\mathcal{W}}(\Psi_H^{m:l} + \Psi_g^{m:l})R_{\mathcal{W}}\right) + O(\varepsilon^2). \tag{5.33}$$

Proof. We use the shorthand notation $\Psi = \Psi_H^{m:l} + \Psi_g^{m:l}$. We then define the matrix

$$A(\varepsilon) = R^{-1}P(\varepsilon)R = R^{-1}\Pi R + \varepsilon R^{-1}\Pi\Psi R + O(\varepsilon^2) = \begin{bmatrix} B_{\mathcal{V}}(I + \varepsilon\Psi_{\mathcal{V}}) & B_{\mathcal{V}}\varepsilon\Psi_{\mathcal{V}\mathcal{W}} \\ \varepsilon B_{\mathcal{W}}\Psi_{\mathcal{W}\mathcal{V}} & B_{\mathcal{W}}(I + \varepsilon\Psi_{\mathcal{W}}) \end{bmatrix} + O(\varepsilon^2), \tag{5.34}$$

where, exploiting the identities in Eq. (5.29), we used the notation

$$\Psi_{\mathcal{V}} = S_{\mathcal{V}}\Psi R_{\mathcal{V}}, \quad \Psi_{\mathcal{V}\mathcal{W}} = S_{\mathcal{V}}\Psi R_{\mathcal{W}}, \quad \Psi_{\mathcal{W}\mathcal{V}} = S_{\mathcal{W}}\Psi R_{\mathcal{V}}, \quad \Psi_{\mathcal{W}} = S_{\mathcal{W}}\Psi R_{\mathcal{W}}. \tag{5.35}$$

Note that, by similarity, $A(\varepsilon)$ has the same spectrum as $P(\varepsilon)$. Since the eigenvalues of $B_{\mathcal{V}}$ are different from those of $B_{\mathcal{W}}$, Corollary 2.4 in [127] guarantees, for ε small enough, the existence of a strongly invariant subspace for $A(\varepsilon)$ whose coordinates can be described by the asymptotic expansion

$$V(\varepsilon) = \begin{bmatrix} I \\ \varepsilon\left(\text{sep}(B_{\mathcal{V}}, B_{\mathcal{W}})\right)^{-1} W_V(\varepsilon) \end{bmatrix}, \tag{5.36}$$

which is justified if $\varepsilon << \text{sep}(B_{\mathcal{V}}, B_{\mathcal{W}})$ and for a unique $W_V : \mathbb{R} \to \mathbb{R}^{2(n-v)\times 2v}$. This result holds as a consequence of the implicit function theorem. By similarity, the strongly invariant subspace $\mathcal{V}$ for $P(0) = \Pi$ persist as $\mathcal{V}_\varepsilon$ for $P(\varepsilon)$ and $\mathcal{V}_\varepsilon$ is described by the columns of the product $RV(\varepsilon)$. Then, the invariance relation $A(\varepsilon)V(\varepsilon) = V(\varepsilon)B_V(\varepsilon)$ holds for a unique $B_V : \mathbb{R} \to \mathbb{R}^{2v\times 2v}$ whose eigenvalues are the ones related to $\mathcal{V}_\varepsilon$. By using this invariance relation, one obtains

$$\begin{bmatrix} B_{\mathcal{V}}(I + \varepsilon\Psi_{\mathcal{V}}) \\ \varepsilon B_{\mathcal{W}}\Psi_{\mathcal{W}\mathcal{V}} \end{bmatrix} + O(\varepsilon^2) = \begin{bmatrix} B_V(\varepsilon) \\ \varepsilon \left(\text{sep}(B_{\mathcal{V}}, B_{\mathcal{W}})\right)^{-1} W_V(\varepsilon)B_V(\varepsilon) \end{bmatrix}. \tag{5.37}$$

An analogous discussion also applies to $\mathcal{W}$, so the claim is proved. □

This result always holds asymptotically, but we have highlighted the fact that ε should stay below a critical threshold which guarantees that the eigenvalues related to $\mathcal{V}_\varepsilon$ and to $\mathcal{W}_\varepsilon$ remain separated. The references [125, 127] establish non-asymptotic bounds for this kind of perturbations.

Next, we show an important consequence of Lemma 5.8.

Lemma 5.10. *Let $\mathcal{V}$ be a strongly invariant subspace for Π, let the columns of $R_{\mathcal{V}} \in \mathbb{R}^{2n\times 2v}$ span $\mathcal{V}$ and let $S_{\mathcal{V}}$ be the symplectic left inverse of $R_{\mathcal{V}}$. Then, we have*

$$\det\left(B_{\mathcal{V}}\left(I + \varepsilon S_{\mathcal{V}}(\Psi_H^{m:l} + \Psi_g^{m:l})R_{\mathcal{V}}\right) + O(\varepsilon^2)\right) = 1 - \varepsilon m\tau v C_{\mathcal{V}} + O(\varepsilon^2) \tag{5.38}$$

where the value $C_{\mathcal{V}}$ is defined in Eq. (5.8).

Proof. We recall that $\det(B_{\mathcal{V}}) = 1$ by definition and the identity $D_\varepsilon \det(A(\varepsilon)) = \text{trace}\left(A^*(\varepsilon)D_\varepsilon A(\varepsilon)\right)$, also called Jacobi formula, which holds for some smooth matrix family $A(\varepsilon)$ with $A^*(\varepsilon)$ being the adjugated matrix of $A(\varepsilon)$. Since the determinant of a product of square matrices is equal to the product of their determinants, one obtains the Taylor expansion

$$\begin{aligned} \det\left(B_{\mathcal{V}}\left(I + \varepsilon S_{\mathcal{V}}(\Psi_H^{m:l} + \Psi_g^{m:l})R_{\mathcal{V}}\right) + O(\varepsilon^2)\right) &= \det\left(I + \varepsilon S_{\mathcal{V}}(\Psi_H^{m:l} + \Psi_g^{m:l})R_{\mathcal{V}} + O(\varepsilon^2)\right) \\ &= 1 + \varepsilon\text{trace}\left(S_{\mathcal{V}}(\Psi_H^{m:l} + \Psi_g^{m:l})R_{\mathcal{V}}\right) + O(\varepsilon^2). \end{aligned} \tag{5.39}$$

By linearity, the $O(\varepsilon)$-term above can be split in $\text{trace}\left(S_{\mathcal{V}}\Psi_H^{m:l}R_{\mathcal{V}}\right) + \text{trace}\left(S_{\mathcal{V}}\Psi_g^{m:l}R_{\mathcal{V}}\right)$ and we now prove that the first of these traces vanishes. Indeed, the third derivative in $\Psi_H^{m:l}$ can be expressed as

$$JD^3H(x_0(t;z), x_1(t;z,\tilde{z})) = \sum_{k=1}^{n} \frac{\partial}{\partial x_k}\left(JD^2H(x)\right)\Big|_{x=x_0(t;z)} x_{k,1}(t;z,\tilde{z}) = \sum_{k=1}^{n} JA_k(t)x_{k,1}(t;z,\tilde{z}), \tag{5.40}$$

where the scalars $x_{k,1}(t;z,\tilde{z})$ identify the components of the curve $x_1(t;z,\tilde{z})$ and the matrix families $A_k(t)$ are symmetric. Recalling the identity $X_0^{-1}(t;z) = JX_0^\top(t;z)J^\top$ [124], we can therefore write

$$\begin{aligned} \Psi_H^{m:l} &= \int_0^{m\tau} \sum_{k=1}^{n} X_0^{-1}(t;z)JA_k(t)X_0(t;z)x_{k,1}(t;z,\tilde{z})dt \\ &= J\int_0^{m\tau} \sum_{k=1}^{n} X_0^{\top}(t;z)A_k(t)X_0(t;z)x_{k,1}(t;z,\tilde{z})dt = J\hat{A}, \end{aligned} \tag{5.41}$$

where $\hat{A}$ is still symmetric. Thus, by Lemma 5.8, $\text{trace}\left(S_{\mathcal{V}}\Psi_H^{m:l}R_{\mathcal{V}}\right) = 0$ and, by linearity,

$$\begin{aligned} \text{trace}\left(S_{\mathcal{V}}\Psi_g^{m:l}R_{\mathcal{V}}\right) &= \text{trace}\left(S_{\mathcal{V}}\int_0^{m\tau} X_0^{-1}(t;z)\partial_x g(x_0(t;z), t; m\tau/l, 0)X_0(t;z)dt\, R_{\mathcal{V}}\right) \\ &= -m\tau v C_{\mathcal{V}}. \end{aligned} \tag{5.42}$$

□

5.3.3 *Proof of the main theorems*

Proof of Theorem 5.2. We will use the shorthand notation $\Psi = \Psi_H^{m:l} + \Psi_g^{m:l}$. Let us start with statement *(ii)*. For ε sufficiently small, Theorem 5.9 guarantees that, to unfold the evolution of some Floquet multipliers, it is sufficient to study the $2v$ eigenvalues $\mu_k(\varepsilon)$ of $B_{\mathcal{V}}\left(I + \varepsilon S_{\mathcal{V}} \Psi R_{\mathcal{V}}\right) + O(\varepsilon^2)$ related to some unperturbed, strongly invariant subspace $\mathcal{V}$. According to Lemma 5.10 and due to the fact that the determinant is equal to the product of the eigenvalues, we have

$$\prod_{k=1}^{2v} \mu_k(\varepsilon) = \det\left(B_{\mathcal{V}}\left(I + \varepsilon S_{\mathcal{V}} \Psi R_{\mathcal{V}}\right) + O(\varepsilon^2)\right) = 1 - \varepsilon m \tau v C_{\mathcal{V}} + O(\varepsilon^2). \tag{5.43}$$

Thus, for $\varepsilon > 0$ small enough and $C_{\mathcal{V}} < 0$, there exist at least one index $\tilde{k}$ for which $|\mu_{\tilde{k}}(\varepsilon)| > 1$, that implies instability.

We then prove statement *(i)*, for which the discussion is more involved. As a basis for the tangent space $\mathcal{T}$, we choose the vector field $JDH(z)$ and a vector $b(z) \in \mathcal{T}$ orthogonal to $JDH(z)$ and normalized such that $\langle b(z), DH(z)\rangle = 1$. From Proposition 4.6, the following identities hold

$$\Pi^m(z) JDH(z) = JDH(z), \quad \Pi^m(z) b(z) = b(z) - mT'(h) JDH(z), \tag{5.44}$$

where $h = H(z)$. Denoting $R_{\mathcal{T}} = [JDH(z) \;\; b(z)]$ and $a = mT'(h)$, from Eq. (5.44) the symplectic left inverse of $R_{\mathcal{T}}$ and their relative block $B_{\mathcal{T}}$ read

$$S_{\mathcal{T}} = \begin{bmatrix} Jb(z) & DH(z) \end{bmatrix}^\top, \quad B_{\mathcal{T}} = \begin{bmatrix} 1 & -a \\ 0 & 1 \end{bmatrix}. \tag{5.45}$$

According to Theorem 5.9, to evaluate the perturbation of these coincident Floquet multipliers of the conservative limit, we need to study the eigenvalues $(\mu_1(\varepsilon), \mu_2(\varepsilon))$ of the perturbed block

$$B_{\mathcal{T}}\left(I + \varepsilon S_{\mathcal{T}} \Psi R_{\mathcal{T}}\right) + O(\varepsilon^2) = \begin{bmatrix} 1 + \varepsilon(a_{11} - a a_{21}) & -a + \varepsilon(a_{12} - a a_{22}) \\ \varepsilon a_{21} & 1 + \varepsilon a_{22} \end{bmatrix} + O(\varepsilon^2), \tag{5.46}$$

where we denoted a_{jk} the components of the matrix $S_{\mathcal{V}} \Psi R_{\mathcal{V}}$. These eigenvalues are expressed as

$$\lambda_{1,2} = 1 + \varepsilon \frac{a_{11} + a_{22} - a a_{21}}{2} \pm \sqrt{\varepsilon}\sqrt{-a a_{21}} + o(\varepsilon). \tag{5.47}$$

The value $a a_{21} = mT'(h) a_{21}$ acts as discriminant and we later prove that $a_{21} = M'_{m:l}(0)$. Thus, if $T'(h) M'_{m:l}(0) < 0$ and $\varepsilon > 0$, then there exists a real eigenvalue greater than 1, which implies instability as in statement *(i)* of the Theorem for small $\varepsilon > 0$. Conversely, the two eigenvalues are complex conjugated for small $\varepsilon > 0$ whose squared modulus, using Lemma 5.10, reads

$$\mu_1(\varepsilon)\mu_2(\varepsilon) = |\mu_1(\varepsilon)|^2 = \det\left(B_{\mathcal{T}}\left(I + \varepsilon S_{\mathcal{T}} \Psi R_{\mathcal{T}}\right) + O(\varepsilon^2)\right) = 1 - \varepsilon m \tau C_{\mathcal{T}} + O(\varepsilon^2). \tag{5.48}$$

If $C_{\mathcal{T}} < 0$, the two eigenvalues evolve as a complex conjugated couple outside the unit circle in the complex plane for small $\varepsilon > 0$, proving then statement *(i)*.

We now show that $a_{21} = \langle DH(z), \Psi JDH(z)\rangle = DM_{m:l}(0) = M'_{m:l}(0)$. We first recall the following identities (see [11] or section 4.4.1 for a proof):

$$X_0(t;z) JDH(z) = JDH(x_0(t;z)), \quad DH(z) X_0^{-1}(t;z) = DH(x_0(t;z)). \tag{5.49}$$

We also recall the fact that the gradient of the first integral solves the adjoint variational equation of the conservative limit (see Proposition 3.2 in [123] for a proof), i.e.,

$$D_t\big(DH(x_0(t;z))\big) = -DH(x_0(t;z)) JD^2H(x_0(t;z)). \tag{5.50}$$

Exploiting Eq. (5.49), one obtains

$$\begin{aligned}\langle DH(z), \Psi JDH(z)\rangle = \int_0^{m\tau} \Big\langle DH(x_0(t;z)), \Big(JD^3H(x_0(t;z), x_1(t;z,\tilde{z}))+ \\ +\partial_x g(x_0(t;z), t; m\tau/l, 0)\Big) JDH(x_0(t;z))\Big\rangle dt\end{aligned} \tag{5.51}$$

and by taking the time derivative of the ODE in Eq. (5.22), one has the identity

$$\begin{aligned}\Big(JD^3H(x_0(t;z), x_1(t;z,\tilde{z})) + \partial_x g(x_0(t;z), t; m\tau/l, 0)\Big) JDH(x_0(t;z)) = \\ \ddot{x}_1(t;z,\tilde{z}) - JD^2H(x_0(t;z))\dot{x}_1(t;z,\tilde{z}) - \partial_t g(x_0(t;z), t; m\tau/l, 0).\end{aligned} \tag{5.52}$$

Substituting the latter result in Eq. (5.51), one can use integration by parts to obtain

$$\begin{aligned}\langle DH(z), \Psi JDH(z)\rangle = &- \int_0^{m\tau} \big\langle D_t\big(DH(x_0(t;z))\big), \dot{x}_1(t;z,\tilde{z})\big\rangle dt + \\ &- \int_0^{m\tau} \big\langle DH(x_0(t;z)), JD^2H(x_0(t;z_0))\dot{x}_1(t;z,\tilde{z})\big\rangle dt + \\ &- \int_0^{m\tau} \big\langle DH(x_0(t;z)), \partial_t g(x_0(t;z), t; m\tau/l, 0)\big\rangle dt,\end{aligned} \tag{5.53}$$

where we also used the fact that $\langle DH(x_0(t;z)), \dot{x}_1(t;z,\tilde{z})\rangle$ is $m\tau$-periodic. Moreover, the first two integrals cancel out due to Eq. (5.50) and one finds

$$a_{21} = \langle DH(z), \Psi JDH(z)\rangle = -\int_0^{m\tau} \big\langle DH(x_0(t;z)), \partial_t g(x_0(t;z), t; m\tau/l, 0)\big\rangle dt = M'_{m:l}(0), \tag{5.54}$$

according to the definition of remark 4.3. □

Proof of Theorem 5.3. We prove asymptotic stability by showing that under the conditions of the theorem all the Floquet multipliers lay within the unit circle in the complex plane for $\varepsilon > 0$ sufficiently small.

Condition *(i)* may be derived directly from the proof of Theorem 5.2. Indeed, in this case the two eigenvalues equal to $+1$ evolve as a complex pair with modulus less than 1, cf. Eq. (5.48).

By assumption, the complex conjugated complex pairs related to the normal space are distinct for $\varepsilon = 0$, so we can iteratively apply Theorem 5.9 considering $\mathcal{V}$ as each of the 2-dimensional strongly invariant subspaces $\mathcal{N}_k$ for $k = 1, ..., n-1$. Moreover, these eigenvalue pairs persist as complex ones since $P(\varepsilon)$ is real, so it is sufficient to evaluate their squared modulus to evaluate whether they move inside or outside the unit circle of the complex plane. As done in the proof of Theorem 5.2, this can be estimated as $1 - \varepsilon m\tau C_{\mathcal{N}_k}$ at first order. Hence, all the eigenvalues of the normal space have modulus lower than 1 if all the $n-1$ volume contractions related to the subspaces $\mathcal{N}_k$ are positive. □

We remark that, for the estimates of the last theorem to be valid, the value of ε must be much smaller than the minimal separation between the pairs of eigenvalues of Π. In particular, in the vicinity of bifurcation or crossing points, these approximations may turn out to be weak.

Remark 5.5. If the unperturbed system is not in Hamiltonian form, then one can still prove that the quantity $T'(h)M'_{m:l}(0)$ governs the stability in the tangential directions. However, the formulas for the volume contractions are more complicated in this case. The Hamiltonian form provides drastic simplifications so that these contractions only depend on the pullback of the linear vector field $\partial_x g$ under X_0. Moreover, all the results we have proved in these sections, also apply to more general perturbations of Hamiltonian systems rather than the specific form we assumed in chapter 2 2.

5.3.4 *Proof of Proposition 5.4*

Proof. With the shorthand notation

$$\begin{aligned}\partial_q Q &= \partial_q Q(q_0(t;z), F(q_0(t;z), p_0(t;z)), t; m\tau/l, 0),\\ \partial_p Q &= \partial_p Q(q_0(t;z), F(q_0(t;z), p_0(t;z)), t; m\tau/l, 0),\end{aligned} \tag{5.55}$$

we split

$$\begin{aligned}\partial_x g(x_0(t,z), t; m\tau/l, 0) &= \begin{bmatrix} 0 & 0 \\ \partial_q Q & \partial_p Q \end{bmatrix} = JA_q(t) + A_p(t),\\ A_q(t) &= \begin{bmatrix} -\partial_q Q & 0 \\ 0 & 0 \end{bmatrix}, \quad A_p(t) = \begin{bmatrix} 0 & 0 \\ 0 & \partial_p Q \end{bmatrix},\end{aligned} \tag{5.56}$$

so that, using Eq. (5.30), we have

$$\begin{aligned} C_{\mathcal{V}} = \; & -\frac{1}{2m\tau v}\int_0^{m\tau} \operatorname{trace}\left(S_{\mathcal{V}} X_0^{-1}(t;z)\left(JA_q(t) - JA_q^\top(t)\right) X_0(t;z) R_{\mathcal{V}}\right) dt \\ & -\frac{1}{2m\tau v}\int_0^{m\tau} \operatorname{trace}\left(S_{\mathcal{V}} X_0^{-1}(t;z)\left(A_p(t) - JA_p^\top(t)J\right) X_0(t;z) R_{\mathcal{V}}\right) dt. \end{aligned} \tag{5.57}$$

For $A_q(t) = A_q^\top(t)$, the first of the integrals above vanishes. By using the fact that

$$A_p(t) - JA_p^\top(t)J = \begin{bmatrix} \partial_p Q^\top & 0 \\ 0 & \partial_p Q \end{bmatrix}, \tag{5.58}$$

and by substituting $\partial_p Q = -\alpha I$, we obtain $C_{\mathcal{V}} = \alpha$ as claimed. This result agrees with the symmetry property of the Lyapunov spectra of conformal Hamiltonian systems [143]. □

6

CONCLUSION

In this first part of the thesis, we have discussed an analytic criterion that relates conservative backbone curves to forced-damped frequency responses in multi-degree-of-freedom mechanical system with small external forcing and damping. Our procedure uses a perturbation approach starting from the conservative limit to evaluate the persistence or bifurcation of periodic orbits in the forced-damped setting. We have shown that this problem can be reduced to the analysis of the zeros of a Melnikov-type function. In a general setting, we proved that, if a simple zero of the Melnikov function exists, generically two periodic orbits bifurcate the conservative limit. We also characterized quadratic zeros and eventual singular bifurcations that may arise. Our results assume the forcing to be periodic and small, but otherwise allow for arbitrary types of damping and forcing. In addition, our analysis yields analytic criteria for the creation of subharmonics, superharmonics and ultrasubharmonics arising from small forcing and damping.

The Melnikov function serves also to determine the stability of forced-damped oscillations of nonlinear, multi-degree-of-freedom mechanical systems. In addition to it, the frequency variation within the limiting conservative periodic orbits and the nonlinear damping rates (or volume contractions) play a role in the assessment of stability. These damping rates provide estimates for the Floquet multipliers of the forced-damped response, thereby predicting stability of perturbed trajectories from their conservative limit.

When applied specifically to mechanical systems, the Melnikov function turns out to be the leading-order term in the equation expressing energy balance over one oscillation period. In this context, we have worked out the Melnikov function in detail for the typical case of purely sinusoidal forcing combined with an arbitrary dissipation. Our method shows that either two, one or no orbits can arise from an orbit of the conservative limit. Typically, the two orbits have opposite stability type. Moreover, ridge curves allow to identify forcing amplitudes and orbits of conservative backbone curves that are close to bifurcations phenomena of the frequency response. Thus, saddle-node bifurcations of frequency continuations, maximal responses and isolas can be efficiently predicted directly from the analysis of the conservative limit of the system. Our analysis also justifies the phase-lag quadrature criterion of [44] in a general setting, without the assumptions of synchronous motion and linear damping.

We have confirmed these theoretical findings by numerical simulations. Specifically, we have considered a nonlinear mechanical system with six degrees of freedom, and implemented our Melnikov analysis on the six families of periodic orbits emanating from an equilibrium. We have verified our results both for linear and nonlinear damping. In the latter case, we successfully predicted the generation of isolated branches in the frequency response. Our six-degree-of-freedom example illustrates that the analytic tools developed here do not require the conservative limit of the mechanical system to be integrable. Indeed, one can apply the present Melnikov function approach directly to periodic orbit families obtained from numerical continuation in the conservative limit of the system. Two additional examples complete the validation for our analytical predictions on stability in the panorama of mechanical systems. In the first, we have studied subharmonic resonances with external forcing in a gyroscopic two-degree-of-freedom system considering two damping mechanisms. Even though these latter dissipate the same amount of energy along the conservative limit, their stability indicators (and potentially their basins of attraction) are different. In the second example, we have considered the case of parametric forcing on a three-degree-of-freedom oscillator with mass-proportional damping. By considering multi-harmonic excitation, we have

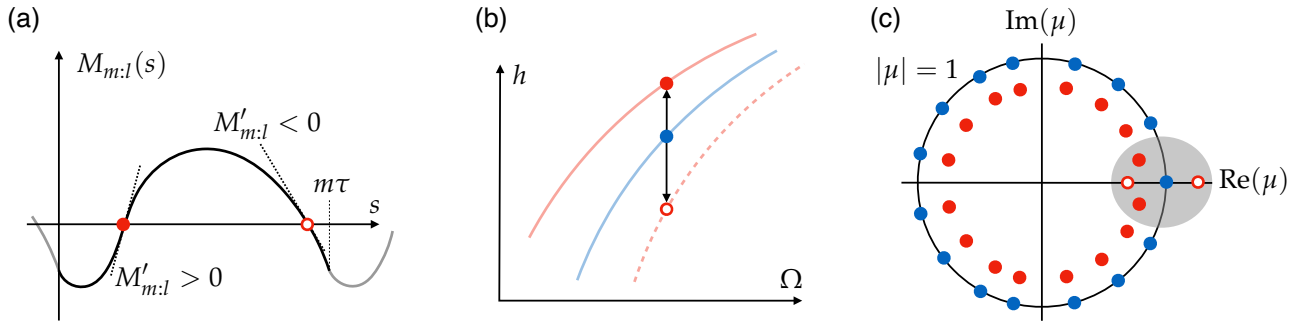

Figure 6.1: Review of the Melnikov method for generic bifurcation from the conservative limit. Plot (a) sketches one period of a Melnikov function (black line) with 2 simples zeros, corresponding to two perturbed orbits (red dots) from the conservative limit (blue dot) in plot (b), displayed in the (Ω, h) plane, where Ω is the forcing frequency and h is the energy of the initial condition of the periodic orbit. Plot (b) also illustrates the conservative backbone curve of $\mathcal{P}$ in blue and forced-frequency responses with red shaded lines. The stable branch is represented with a solid line, while the unstable one with a dashed line. Using corresponding colors, plot (c) shows the eigenvalues configurations for the conservative setting and the forced-damped cases. Assuming positive nonlinear damping, the Floquet multipliers different from $+1$ perturb inside the unit circle (for either bifurcating orbit). The difference in stability occurs only in the gray shaded area, which is related to the two multipliers equal to $+1$, whose motions are controlled by the Melnikov function as stated by our results.

successfully described the generation and the stability of periodic trajectories that lie on exotic isolas of the frequency response.

When the mechanical system has only one degree of freedom, the conditions we derived coincide with prior analyses of [4, 104]. The results we have presented, which closely follow our work in the original references [42, 43], are also consistent with numerical and experimental observations reported in available studies [5, 17, 27, 32, 44, 45, 66–75, 83, 84], in that they are able to explain hysteresis of frequency responses in mechanical systems as well as other stability or bifurcation phenomena. These predictions are synthetically illustrated in Fig. 6.1 for the typical bifurcation scenario that generates forced-damped periodic orbits from the conservative limit in near resonance regions.

Part II

DATA-DRIVEN EXPLICIT MODELS AND PREDICTIONS FOR NONLINEAR DYNAMICAL SYSTEMS

7 INTRODUCTION

In an increasingly data-based perspective, constructing dynamical models from data, either from numerical or physical experiments, is becoming of crucial importance to scientists and engineers. Often, these models are nonlinear and high-dimensional, so that data-driven models should also tackle a dimensionality reduction problem. Hence, the attention focuses on building data-driven reduced-order models, which can be evaluated at insignificant computational cost without compromising precision in the results. In the engineering context, these models are particularly appealing for design, testing or control purposes.

The most common approaches to data-driven reduced-order models are the Proper Orthogonal Decomposition (POD) coupled with Galerkin projections [8, 9, 13, 144] and the Dynamic Mode Decomposition (DMD) [58, 59]. The former approach requires the knowledge of the governing equations of motion and, once a relevant number of modes is identified from data, it projects these equations onto these modes to construct a reduced-order model. DMD and its improved versions [145–149], being connected with Koopman operator theory [150,151], assume linear dynamics for the observable data and find a low-rank approximation for its dynamics. DMD has the ability to find relevant modes and patterns in the dynamics, and, in contrast to Galerkin projections, is a purely data-driven approach that does not require the knowledge of the governing equations of motion. DMD has been used for control purposes as well [152]. However, the justification of DMD critically relies on theorems having very delicate assumptions [150, 151], making the method crucially dependent on the types of available observables [58, 153, 154]. Moreover, DMD is unable to approximate truly nonlinear dynamics that involve multiple disjoined steady states, such that fixed points and limit cycles [155]. The overall drawback of classic Galerkin-POD models and of standard DMD is that the only possible refinement of the model is to include additional dimensions. Hence, for complex dynamical systems, the number of dimensions tends to be large, nevertheless allowing for computational speed-ups in simulations, but making the reduced dynamics still complex.

Other methods treat the dimensionality reduction and the dynamical modeling as separated problems. Indeed, the data is first processed via dimensionality reduction algorithms, which range from POD or Principal Component Analysis (PCA) [56, 156], its kernelized version [157], manifold learning techniques [57, 158, 159] or autoencoders [53]. Afterwards, the dynamics is identified on the obtained reduced-coordinates using classic regression techniques (least-squares [50], LASSO [51], SINDy [52], sparse structural dynamics with hysteric/inelastic behavior [160]), Bayesian learning techniques [161] or neural networks in different architectures (fully connected, convolutional, recurrent) [53, 54, 162]. Some of these techniques return complex, black-box models (even non-physical sometimes), but some others offer sparse models (LASSO, SINDy, Bayesian learning), which allow easy interpretation or analysis of the dynamical behavior [52]. However, the resulting dynamics is intrinsically connected with the representation offered by the dimensionality reduction algorithms. Indeed, the advocated simplicity of sparse models is critically determined by the reduced representation. For example, even a simple linear coordinate change dramatically destroys the sparsity of a model. These methods feature a high number of hyperparameters, and hence good performances requires extensive tuning. Moreover, the eventual lack of predictive capabilities often makes these models unattractive for practical use. Indeed, the insertion of parameter variations, disturbances or external forcing into these models is heuristic at best and hence offers questionable conclusions. Also here, the dimension of the reduced model is either a user input or is treated as a hyperparameter, which is heuristically increased until the model shows reasonable performance.

The approach that we are going to undertake in constructing data-driven models aims to address most of the issues of available methods, by leveraging two main concepts of dynamical systems theory: invariant manifolds and normal forms. These two powerful theoretical notions are used together to unfold the complexity of the dynamics via the concept of spectral submanifolds.

Invariant manifolds are characterized by the property that trajectories starting on the manifold remain on the manifold throughout the course of their dynamical evolution. In some cases, their presence has dramatic consequences on the nearby dynamics, and they also provide an exact framework for model order reduction [19, 163]. The first invariant manifolds to be studied were the stable, unstable and center manifolds of fixed points or periodic orbits [4], typically used to shape the phase space and to study bifurcation phenomena [130]. In context of conservative or Hamiltonian dynamics, Lyapunov subcenter manifolds [15, 91] or KAM tori [116] are typically used to study these systems and can have a precious role when dissipative perturbations are added to the conservative dynamics. Normally hyperbolic invariant manifolds [164–166] help in identifying potential attractors of the phase space and to unfold the dynamics on them. Thanks to the developments of geometric singular perturbation theory [167], the concept of slow manifold became popular. A slow manifold governs the asymptotic behavior of the dynamics, which is often a primary objective in applications. Invariant manifolds justify the *manifold assumption* of machine learning dimensionality reduction [168] in the context of dynamics.

Recently, the concept of spectral submanifold (SSM) has been introduced [18], based on the theoretical developments in [169–172]. Originally conceived for forced-damped, nonlinear, multi-degree-of-freedom mechanical systems, spectral submanifolds theory provides a rigorous analytical framework for studying system motions around an attractor. When related to fixed points, SSMs are briefly the smoothest nonlinear continuations of eigenspaces of the linearized system. The local phase space is indeed organized in a hierarchy of invariant manifolds, which creates an opportunity for exact model reduction [19]. In particular, the SSM is a slow manifold that attracts nearby trajectories, and the SSM dimension depends on the spectral properties of the linearized system [18, 173]. Moreover, spectral submanifolds are robust features of the dynamics, surviving also in presence of non-autonomous perturbations of the system [18].

Not only does SSM theory offer a systematic basis for model reduction, but it also allows a simplification of the reduced dynamics via normal forms [4, 172, 174]. Normal forms bring dynamical systems to their simplest possible form, representing them with models featuring the lowest number of parameters. In other words, normal forms justify sparse, simple models describing dynamical phenomena. However, these models are only available in special coordinates, as highlighted by analytical computations dating back to Poincaré [1]. In the context of structural vibrations, spectral submanifolds and their normal forms are used for analytical, exact model reduction and computations of forced-responses [20, 22, 23, 83, 90, 173], while [74] offers an approach for the identification of reduced-order models for 2-dim. SSMs from trajectories of scalar observables. Another concept closely linked to SSMs is that of invariant foliations [175], which provides a rigorous nonlinear extension of classic linear modal analysis.

In this thesis, we develop a methodology for data-driven reduced-order modeling based on SSMs. Focusing on oscillatory dynamics near a fixed point, we discuss spectral submanifolds and their embedding in observable spaces. Our approach is valid for any (generic) observed state of the system, as we do not require either full or specific system measurements. We first construct a dimensionality-reduction approach for the embedded data, which is based on a nonlinear enhancement of PCA. Then, we seek the normal form dynamics from the resulting reduced-coordinates using the available data. Our approach automatically detects the appropriate normal form, making the algorithm an intelligent, unsupervised learning strategy for dynamical systems. In contrast to other sparse modeling techniques, we do not assume sparsity a priori in the coefficients describing the dynamics, but we create a setting in which sparsity is guaranteed. In this way, we are able to generate explicit,

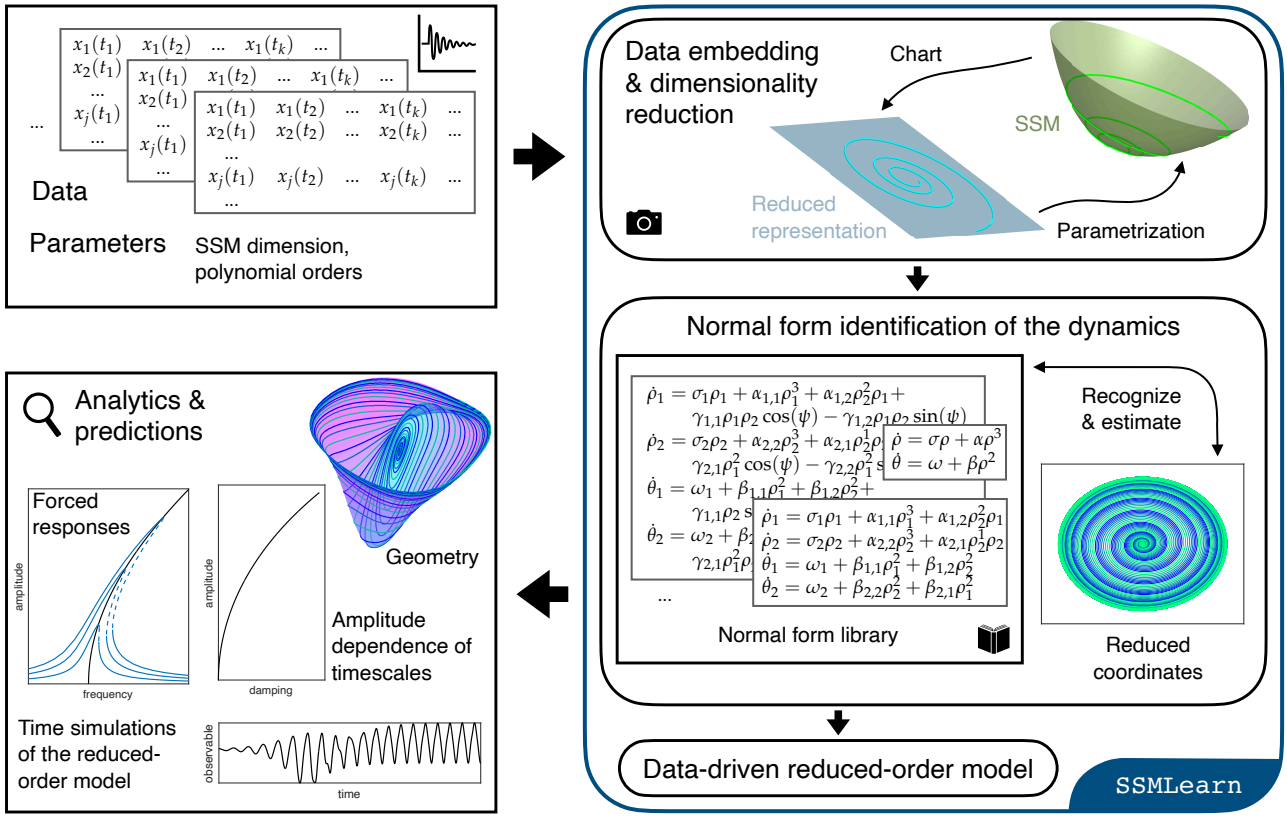

Figure 7.1: Data-driven reduced-order models via `SSMLearn`.

interpretable dynamical models that are independent of the reduced coordinates that represent the manifold. The normal form then allows an easy extraction of analytical insights from the dynamics and is also able to predict the impact of perturbations, including the addition of external time-dependent forces. Our approach can tackle either continuous-time dynamical systems or discrete-time evolution rules, making our model reduction strategy applicable to dynamics near stationary points and periodic orbits.

The normal forms that we employ can also help classic signal processing techniques in the framework of nonlinear system identification [31, 176]. In this context, several methods, e.g. Hilbert transform and its variants [39], are based on scalar, single-mode signals. When dealing with multi-modal oscillations, popular techniques either use filtering or exploit empirical mode decomposition [38], both of which ignore potential modal coupling. On the other hand, normal forms for oscillators can potentially detect modal interactions arising from resonances.

The theoretical and computational developments of this chapter have been implemented in the MATLAB® package `SSMLearn` (available at github.com/mattiacenedese/SSMLearn), synthetically illustrated in Fig. 7.1. Other than trajectory data, the only user inputs that we require are the maximal polynomial order for the approximation of nonlinearities and the dimension of the SSM. The algorithm then automatically embeds the data, performs dimensionality reduction and identifies the normal form that describes the dynamics on the SSM. For targeted experiments, the manifold dimension is known a priori. These experiments require some minimal prior knowledge on the system linearization at the equilibrium (e.g. eigenvalues, linear modes), that help in initializing properly the trajectories used for model identification. For estimating linear properties, well-consolidated tools are available in the literature [177, 178]. In case of general data, time-frequency signal processing techniques from nonlinear system identification (e.g. spectrograms, wavelet transforms [40]) help in estimating the dimension of the SSM that best approximates the data. Our method is complementary

to these signal processing techniques, allowing the construction of reduced-order models based on preliminary diagnostics obtained from such techniques.

We validate our approach on examples coming from different application domains, ranging from structural vibrations to fluid dynamics, using synthetic data or physical experiments. These examples also concern different dynamical behaviors (stable or unstable), different kinds of nonlinearities characterizing the system and different types of observables.

8

SPECTRAL SUBMANIFOLDS

8.1 CONTINUOUS-TIME DYNAMICAL SYSTEMS

We look at finite-dimensional dynamical systems

$$\dot{x} = f(x), \qquad x \in \mathbb{R}^n, \tag{8.1}$$

where the vector field f is of class C^r where r can be a positive integer for finite differentiability, $r = \infty$ for infinite differentiability and $r = a$ when f is an analytic function. We assume that the origin for system (8.1), after a possible translation, is a hyperbolic fixed point, i.e., $f(0) = 0$ and $\mathrm{Re}(\lambda_j) \neq 0$ for each $\lambda_j \in \mathcal{L} = \mathrm{spectrum}(Df(0))$ for $j = 1, 2, .., n$. We denote with $\mathcal{L}_s$ and $\mathcal{L}_u$ the stable and unstable splitting of the spectrum $\mathcal{L}$, while $\mathcal{E}_s$ and $\mathcal{E}_u$ are the related eigenspaces. We also use the notation $\Phi^t(x)$ for the time-t flow map of $f(x)$.

The local structure of the phase space near the fixed point is shaped by the stable and unstable manifolds [10, 11]. These are unique C^r invariant manifolds tangent to $\mathcal{E}_s$ and $\mathcal{E}_u$ at the origin, having the same dimensions of $\mathcal{E}_s$ and $\mathcal{E}_u$, respectively. Moreover, the stable and unstable manifolds possess a further internal hierarchy of submanifolds, as pointed out by the theoretical results in [169–171]. We define these submanifolds as follows.

Definition 8.1. ***(Spectral submanifold)***. *Let $\mathcal{E}_m$ be an m-dimensional spectral subspace either of the stable subspace $\mathcal{E}_s$ or of the unstable one $\mathcal{E}_u$. A spectral submanifold is the smoothest invariant manifold $\mathcal{W}_m$ of all invariant manifolds that are tangent to $\mathcal{E}_m$ at the origin and have the same dimension as $\mathcal{E}_m$.*

By denoting $\mathcal{L}_m$ the spectrum related to $\mathcal{E}_m$, we then define the spectral quotient as

$$\sigma(\mathcal{E}_m) = \begin{cases} \max\left(\mathrm{Int}\left[\dfrac{\min_{\lambda_j \in (\mathcal{L}_s - \mathcal{L}_m)} \mathrm{Re}(\lambda_j)}{\max_{\lambda_j \in \mathcal{L}_m} \mathrm{Re}(\lambda_j)}\right], 1\right) & \text{if } \mathcal{L}_m \subset \mathcal{L}_s, \\ \max\left(\mathrm{Int}\left[\dfrac{\max_{\lambda_j \in (\mathcal{L}_u - \mathcal{L}_m)} \mathrm{Re}(\lambda_j)}{\min_{\lambda_j \in \mathcal{L}_m} \mathrm{Re}(\lambda_j)}\right], 1\right) & \text{if } \mathcal{L}_m \subset \mathcal{L}_u, \end{cases} \tag{8.2}$$

which is the integer part of the ratio between the fastest decay/growth rate outside $\mathcal{L}_m$ and the slowest decay/growth rate inside $\mathcal{L}_m$. The next theorem characterizes spectral submanifolds.

Theorem 8.1. ***(Existence, uniqueness and robustness of SSMs for flows)***. *If*

(i) $\sigma(\mathcal{E}_m) < r$,

(ii) With the notation $\{\lambda_1, \lambda_2, ..., \lambda_m\} = \mathcal{L}_m$, *the outer non-resonance conditions*

$$\sum_{j=1}^{m} \sigma_j \lambda_j \neq \lambda, \qquad \forall\, \sigma_j \in \mathbb{N} : 2 \leq \sum_{j=1}^{m} \sigma_j \leq \sigma(\mathcal{E}_m),$$

hold for any $\lambda \notin \mathcal{L}_m$,

then there exists an m-dimensional, class C^r spectral submanifold $\mathcal{W}_m$ tangent to the spectral subspace $\mathcal{E}_m$ at the origin which is unique among all $C^{\sigma(\mathcal{E}_m)+1}$ invariant manifolds with the same property. The spectral submanifold $\mathcal{W}_m$ persists under small C^r perturbations of the vector field f.

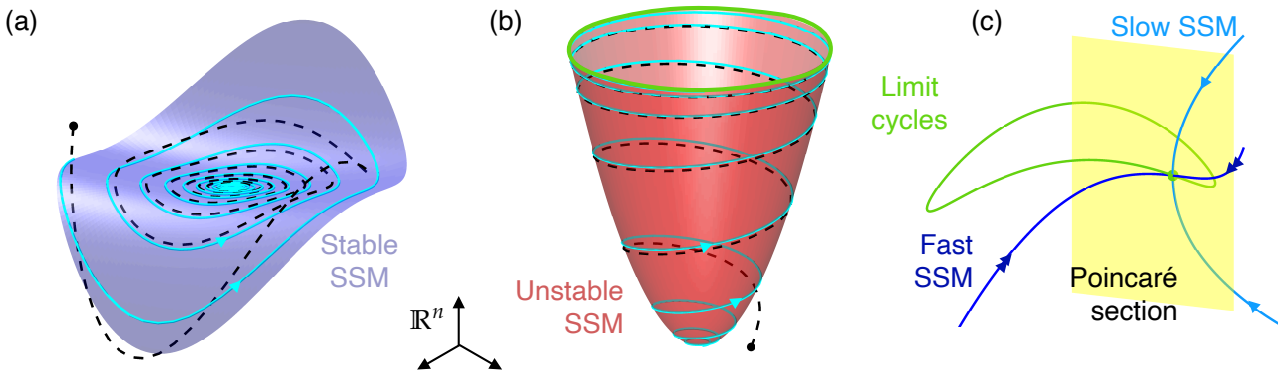

Figure 8.1: Examples of SSMs. Plot (a) shows a stable 2-dim. SSM in blue, while the red surface in (b) is the unstable manifold that connects the fixed point to a limit cycle. Plots (a,b) contains attracting SSM, as shown by the trajectories with dashed black lines that converges to the SSMs on the solid cyan lines. Plot (c) shows stable SSMs (fast and slow) for the Poincaré map of the limit cycle, depicted in green.

We sketch the proof of this theorem, adapted from Theorem 3 of [18], in section 8.3, where the case of SSMs for maps is discussed. Some examples of SSMs are shown in Fig. 8.1. The stable and unstable manifolds are special cases of Theorem 8.1, arising when $\mathcal{L}_m = \mathcal{L}_s$ or $\mathcal{L}_m = \mathcal{L}_u$, respectively, for which assumptions *(i-ii)* automatically hold. For all other SSMs, it is sufficient to check the linear combinations in *(ii)* for every $\lambda \in \mathcal{L}_s - \mathcal{L}_m$ if $\mathcal{L}_m \subset \mathcal{L}_s$ or for $\lambda \in \mathcal{L}_u - \mathcal{L}_m$ if $\mathcal{L}_m \subset \mathcal{L}_u$. We remark that assumptions *(i-ii)* are generically satisfied.

Among all types of SSMs, attracting SSMs (see plots (a,b) in Fig. 8.1) are of particular interest, that are characterized by the next definition.

Definition 8.2. ***(Attracting spectral submanifolds).*** *For an asymptotically stable equilibrium ($\mathcal{L}_u = \varnothing$), the unique m-dim. local attracting spectral submanifold for system (8.1) is the SSM tangent to the eigenspace $\mathcal{L}_m$ containing the eigenvalues with the m-largest real parts in the spectrum of $Df(0)$. If the equilibrium is unstable, then the local attracting spectral submanifold for system (8.1) is its unstable manifold.*

Attracting spectral submanifolds capture the leading, asymptotic dynamics of system (8.1), as stated in this result.

Proposition 8.2. *Let $\mathcal{W}_m$ be the m-dim. attracting spectral submanifold for system (8.1) and $\hat{x} \in \mathbb{R}^n$ be a point such that $\hat{x}$ is inside a sufficiently small neighborhood of the origin. Then $\mathcal{W}_m$ is an attracting, normally hyperbolic invariant manifold and $\hat{x}$ belongs to its stable fiber through the point $x \in \mathcal{W}_m$ for which there exists real positive constants C_s and λ_s such that*

$$\|\Phi^t(\hat{x}) - \Phi^t(x)\| < C_s e^{-\lambda_s t}. \tag{8.3}$$

Proof. For the proof that the unstable manifold is normally hyperbolic and attracting, see [179], while [18] shows this result for slow, stable SSMs. Regarding the attraction rate, $\hat{x}$ lies on the local, n-dim. stable manifold of $\mathcal{W}_m$, at least for sufficiently small neighborhood of the origin. This stable manifold is foliated by $(n-m)$-dim. submanifolds called stable fibers [165, 166, 179], for which the estimate of Eq. (8.3) holds. The existence of this foliation is also discussed in [175]. □

8.2 EMBEDOLOGY

We now consider to have a collection of observed trajectories of the dynamical system

$$x[k+1] = F(x[k]), \qquad x \in \mathbb{R}^n, \qquad k \in \mathbb{N}, \tag{8.4}$$

that lie on a certain m-dimensional SSM $\mathcal{W}_m$ attached to the origin and related to the spectrum $\mathcal{L}'_m$. The map F can be a discrete evolutionary rule or the flow map Φ^{t_s} of system (8.1), where $t_s > 0$ is the sampling time, i.e., the rate at which trajectory data is known. In this latter case, $x[k] = x(kt_s)$ and we have that $\mathcal{L}'_m = \exp(t_s \mathcal{L}_m)$.

The observable space, denoted $\mathbb{R}^p$, has a dimension $p \geq 1$ which is typically much lower than that of the full state space, i.e., $p \ll n$. These observables are connected to the system state via a measurement function $y = \Gamma(x)$. It is therefore necessary to ask whether $\mathcal{W}_m$ also shows up in the observable space. Whitney, with its celebrated result in [180], proved that, for $p > 2m$, the set of maps $\Gamma : \mathcal{W}_m \to \mathbb{R}^p$ forming an embedding for $\mathcal{W}_m$ is open and dense in the set of C^1 maps from $\mathcal{W}_m$ to $\mathbb{R}^p$.

Therefore, the invariant manifold $\mathcal{W}_m$ is guaranteed to survive in the observable space $\mathbb{R}^p$ without the loss of any differential information, when looking at p generic observables with $p \geq 2m + 1$. In other words, $\Gamma(\mathcal{W}_m)$ is a manifold in $\mathbb{R}^p$ constituting a diffeomorphic copy of $\mathcal{W}_m$. One may also try with a number of observables $p \leq 2m$ and be still able to obtain good results, but this cannot be guaranteed in general.

There are two typical cases for the measurement mapping Γ. The simplest one refers to an observable space $y \in \mathbb{R}^p$ made of independent and simultaneous measurements of the underlying dynamical system. Here, the map Γ has a clear physical meaning. However, a number of at least $2m + 1$ independent observables may not be available in some practical experiments. Therefore, we consider the case of a scalar measurement $s \in \mathbb{R}$ satisfying $s = g(x)$ for some generic smooth map $g : \mathbb{R}^n \to \mathbb{R}$ and the coordinates of observable space are those of the *delay coordinates vector* constructed as

$$y = \Gamma(x) = \Big(g(x),\ g\big(F(x)\big),\ g\big(F^2(x)\big),\ \dots,\ g\big(F^{p-1}(x)\big)\Big)^\top. \tag{8.5}$$

This type of embedding mixes dynamics and geometry so that Takens in [181] had to require some technical assumptions on periodic orbits contained in the manifold to conclude that a generic map Γ constructed as in Eq. (8.5) is actually an embedding [182]. Although methods are available for the optimal selection of p (and of t_s in case of a flow), standard cross-validation routines show good performances [176].

Remark 8.1. The statements of Whitney and Takens, however, do not say how likely a given map Γ constitutes an embedding [176]. Indeed, their statements guarantee that there exists an embedding in an arbitrary small neighborhood of this given map Φ in the space of C^1 maps. For practical uses, one would like to be sure that a given map is an embedding, i.e. with probability one. These results are available in [183] for the two particular cases discussed above, still with $p > 2m$. For the case of simultaneous independent measurements, the authors proved that almost all maps are indeed embeddings of $\mathcal{W}_m$ in $\mathbb{R}^p$. In the delay embedding case, the same result holds for almost all scalar mappings g and, in case of a flow, for almost all sampling times $t_s > 0$ if, for the system restricted to the manifold $\mathcal{W}_m$, there is a finite number of equilibria, there are no periodic orbits with period t_s or $2t_s$ and there are only a finite number of periodic orbits with period lt_s, $l > 2$.

8.2.1 *Preserving information between phase space and observable space*

The theoretical results on manifold embedding guarantee that there is no loss on differential information when passing from the full phase space to the observable space, for suitable number of observables $p \geq 2m + 1$. Figure 8.2 provides an illustration of this concept and we shall explore this connection further in the view of constructing reduced-order models from data.

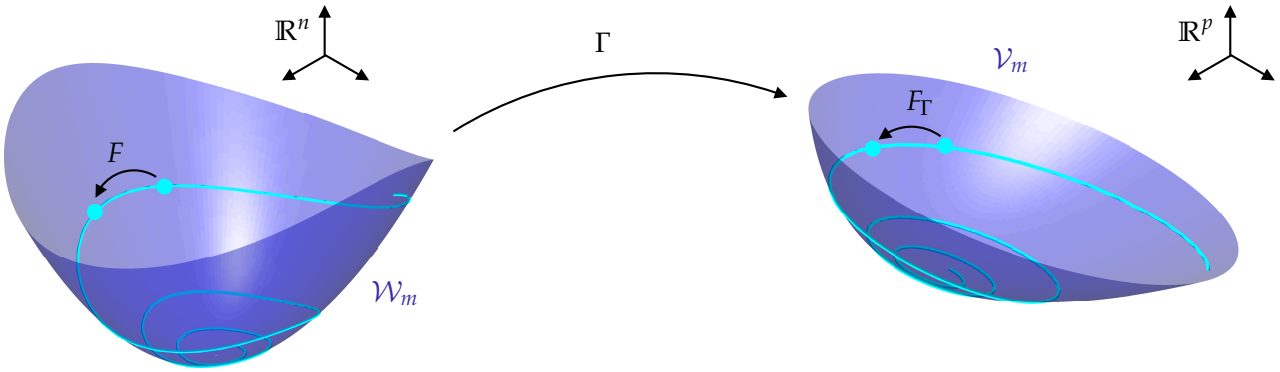

Figure 8.2: Illustration of an embedding Γ of an invariant manifold $\mathcal{W}_m$ from the phase space as an invariant manifold $\mathcal{V}_m$ in the observable space.

An embedding Γ of the manifold $\mathcal{W}_m$ is a diffeomorphism onto its image, denoted $\mathcal{V}_m = \Gamma(\mathcal{W}_m)$, hence invertible on $\mathcal{V}_m$. We then call $\Gamma^{-1}(\mathcal{V}_m)$ the preimage of Γ of the set $\mathcal{V}_m \subset \mathbb{R}^p$, defined as $\Gamma^{-1}(\mathcal{V}_m) = \{x \in \mathbb{R}^n : \Gamma(x) = \mathcal{V}_m\}$. The functional relationship

$$y[k+1] = F_\Gamma\left(y[k]\right), \qquad y = \Gamma(x) \in \mathbb{R}^p, \tag{8.6}$$

between successive observables is conjugated to the dynamical system (8.4) restricted to the manifold $\mathcal{W}_m$ via the formula

$$F_\Gamma = \Gamma \circ F \circ \Gamma^{-1} : \mathcal{V}_m \to \mathcal{V}_m. \tag{8.7}$$

Let us assume that, without loss of generality, $\Gamma(0) = 0$. Hence, we have that $F_\Gamma(0) = 0$ and the conjugacy (8.7) implies that $\mathcal{L}'_m \subset \text{spectrum}(DF_\Gamma(0))$ [74].

Remark 8.2. We briefly discuss the case of simultaneous, independent measurements where Γ is a linear map represented by a matrix $G \in \mathbb{R}^{p\times n}$. The observed coordinates $y = Gx$ are a good embedding for the m-dimensional manifold $\mathcal{W}_m$ with probability one if $p \geq 2m+1$ [183]. A final word of caution is worth adding for the case in which the rows of G are orthonormal vectors, as in the case of projections arising from proper orthogonal decompositions. One may be tempted to think that Γ^{-1} can be expressed as $G^\top$ and hence that the conjugacy relation in Eq. (8.7) is a Galerkin projection of the dynamical evolution law in Eq. (8.4). However, this is true only for special, non-generic cases, such as when $\mathcal{W}_m$ is linear or when curvilinear features of $\mathcal{W}_m$ appear only in directions spanned by the rows of G. Even if Γ is linear, the preimage $\Gamma^{-1}(\mathcal{V}_m)$ is generically a nonlinear map [19].

8.3 Discrete-time dynamical systems

We now consider the case of finite-dimensional discrete dynamical systems, i.e.,

$$x[k+1] = F(x[k]), \qquad x \in \mathbb{R}^n, \qquad F \in C^r, \tag{8.8}$$

where we assume that the origin for system (8.1), after an eventual translation, is a hyperbolic fixed point, i.e., $F(0) = 0$ and $|\mu_j| \neq 1$ for each $\mu_j \in \mathcal{L}' = \text{spectrum}(DF(0))$ for $j = 1, 2, .., n$. We also assume that $DF(0)$ is nonsingular. We denote with $\mathcal{L}'_s$ and $\mathcal{L}'_u$ the stable and unstable splitting of the spectrum $\mathcal{L}'$, while $\mathcal{E}'_s$ and $\mathcal{E}'_u$ are the related eigenspaces.

The local structure of the phase space near the fixed point is shaped by the stable and unstable manifolds that are characterized by properties similar to those of the flow case. Specifically, Definition 8.1 carries over to the present map setting. We then consider an m-dimensional subspace $\mathcal{E}'_m$ either of

the stable subspace $\mathcal{E}'_s$ or of the unstable one $\mathcal{E}'_u$ and we denote $\mathcal{L}'_m$ the spectrum related to $\mathcal{E}'_m$. We further define the spectral quotient for the map case as

$$\sigma(\mathcal{E}'_m) = \begin{cases} \max\left(\text{Int}\left[\dfrac{\min_{\mu_j \in (\mathcal{L}'_s - \mathcal{L}'_m)} \log|\mu_j|}{\max_{\mu_j \in \mathcal{L}'_m} \log|\mu_j|}\right], 1\right) & \text{if } \mathcal{L}'_m \subset \mathcal{L}'_s, \\ \max\left(\text{Int}\left[\dfrac{\max_{\mu_j \in (\mathcal{L}'_u - \mathcal{L}'_m)} \log|\mu_j|}{\min_{\mu_j \in \mathcal{L}'_m} \log|\mu_j|}\right], 1\right) & \text{if } \mathcal{L}'_m \subset \mathcal{L}'_u. \end{cases} \tag{8.9}$$

The next theorem describes spectral submanifolds for maps.

Theorem 8.3. ***(Existence, uniqueness and robustness of SSMs for maps)****. If*

(i) $\sigma(\mathcal{E}'_m) < r$,

(ii) With the notation $\{\mu_1, \mu_2, ..., \mu_m\} = \mathcal{L}'_m$*, the outer non-resonance conditions*

$$\prod_{j=1}^{m} \mu_j^{\sigma_j} \neq \mu, \qquad \forall\, \sigma_j \in \mathbb{N} : 2 \leq \sum_{j=0}^{m} \sigma_j \leq \sigma(\mathcal{E}'_m), \tag{8.10}$$

hold for any $\mu \notin \mathcal{L}'_m$*,*

then there exists a m-dimensional, class C^r*, spectral submanifold* $\mathcal{W}'_m$ *tangent to the spectral subspace* $\mathcal{E}'_m$ *at the origin which is unique among all* $C^{\sigma(\mathcal{E}'_m)+1}$ *invariant manifolds with the same property. The spectral submanifold* $\mathcal{W}'_m$ *persists under small* C^r *perturbations of the vector field* f*.*

Proof. This a restatement for our context of Theorem 3 of [18], which is Theorem 1.1 in [169] that deals with general mappings in Banach spaces. While we indicate the map F with the same notation, the authors of [169] adopts $X_1 = \mathcal{E}'_m$, $\mathcal{L}'_m = \text{spectrum}(A_1)$ and $\sigma(\mathcal{E}'_m) = L$. Assume that $\mathcal{L}'_m \subset \mathcal{L}'_s$. By construction, the map F, the space $\mathcal{E}'_m$ and the spectrum $\mathcal{L}'_m$ satisfy the assumptions *(o-3)* of Theorem 1.1 in [169], while the assumptions *(i,ii)* of this theorem are reformulations of assumptions *(5,4)* of the referenced theorem, respectively. If $\mathcal{L}'_m \subset \mathcal{L}'_s$, then Theorem 1.1 in [169] holds when considering the inverse map $F^{-1}(x)$. The statement on robustness follows from the results in [170]. □

The proof for Theorem 8.1 follows directly from Theorem 8.3 when considering the flow map of f, as also discussed in Remark 6 of [169]. Further theoretical results on SSMs and their analytical computations are available in literature [18, 90, 171].

Lastly, the discussion of section 8.1 after Theorem 8.1 regarding slow SSMs carries over for discrete-time dynamical systems, with the appropriate, minor modifications. Examples of SSMs for maps are shown in Fig. 8.1(c), where the underlying discrete-time dynamical system is the Poincaré map near a limit cycle.

9

DATA-DRIVEN REDUCED ORDER MODELS BASED ON SSMS

Model reduction to an invariant manifold requires the construction of three ingredients: a coordinate chart, the reduced dynamics and a parametrization. The coordinate chart transforms embedding coordinates into reduced coordinates, whose dynamics is governed by the reduced dynamics. The parametrization lifts the reduced coordinates to embedding ones.

We assume here that the m-dimensional SSM, $\mathcal{W}_m$, is embedded via a C^r measurement map Γ in the observable space $\mathbb{R}^p$ as $\mathcal{V}_m$ and that the origin in $\mathbb{R}^p$ is the equilibrium to which the SSM is attached. We aim to describe this manifold with its simplest representation, i.e., as a graph of a function. Therefore, we consider matrices $V_0 \in \mathbb{R}^{p\times m}$ and $U_0 \in \mathbb{R}^{p\times(p-m)}$, whose columns form an orthonormal basis for the tangent space $T_0\mathcal{V}_m$ of $\mathcal{V}_m$ at the origin and for the complement of $T_0\mathcal{V}_m$ in $\mathbb{R}^p$, respectively. Hence, the matrix $[V_0\ U_0] \in \mathbb{R}^{p\times p}$ is nonsingular and its inverse is

$$\begin{bmatrix} V_0^\top \\ U_0^\top \end{bmatrix} = \begin{bmatrix} V_0 & U_0 \end{bmatrix}^{-1}, \qquad V_0^\top \in \mathbb{R}^{m\times p}, \qquad U_0^\top \in \mathbb{R}^{(p-m)\times p}, \qquad \begin{matrix} V_0^\top V_0 = I, \qquad U_0^\top U_0 = I, \\ V_0^\top U_0 = 0. \end{matrix}$$

We select the coordinate chart for the manifold $\mathcal{V}_m$ as the linear projection $\eta = V_0^\top y$ onto the tangent space $T_0\mathcal{V}_m$ at the origin, with $\eta \in \mathbb{R}^m$ denoting the vector of reduced coordinates for $\mathcal{V}_m$. The next result characterizes the parametrization and the reduced dynamics for $\mathcal{V}_m$, which are also presented in Fig. 9.1.

Theorem 9.1. ***Parametrization and dynamics for embedded SSMs****. For a sufficiently small neighborhood $\mathcal{B} \subset \mathbb{R}^m$ of the origin, there exists a parametrization of the form*

$$y = V(\eta) = V_0\eta + U_0 h(\eta), \tag{9.1}$$

where $h : \mathcal{B} \to \mathbb{R}^{p-m}$ is a class C^r map such that $h(0) = 0$, $Dh(0) = 0$, which is unique up to the choice of the pair (V_0, U_0). Moreover, the dynamics on the manifold is described by the class C^r map $R : \mathcal{B} \to \mathcal{B}$

$$\eta[k+1] = R\left(\eta[k]\right), \qquad R(0) = 0, \qquad \text{spectrum}(DR(0)) = \mathcal{L}'_m. \tag{9.2}$$

Proof. The parametrization in Eq. (9.1) refers to the Monge coordinates [184, 185] or patches [186, 187], whose existence is shown in these references. The uniqueness holds due the fact that $\mathcal{V}_m$ is the C^r manifold defined as the embedding of the unique, class-C^r SSM $\mathcal{W}_m$. The reduced dynamics remains valid in the neighborhood $\mathcal{B} \subset \mathbb{R}^m$, and, with the definition $V^\star(y) = V_0^\top y$, the following semi-conjugacy holds

$$R = V^\star \circ \Gamma \circ F \circ \Gamma^{-1} \circ V : \mathcal{B} \to \mathcal{B}, \tag{9.3}$$

for which we have that the eigenvalues of R coincides with those of $DF(0)$ related to the SSM. □

The graph-style parametrization described in Theorem 9.1 may break down due to a fold in $\mathcal{V}_m$, but it is always guaranteed to exist in a sufficiently small neighborhood of the equilibrium. We shall discuss the case of a folding $\mathcal{V}_m$ later.

We now address the problem of identifying the reduced-order models from sampled trajectories in the observable space. Specifically, we assume to have a dataset of L trajectories, each consisting of L_j points for $j = 1, 2, \dots L$. We assume that all points $y^{(j)}[k]$, $k = 1, 2, \dots L_j$ lie on the embedded SSM $\mathcal{V}_m$ and the trajectories are uniformly sampled in time at $t_s > 0$ rate. We also assume that $\mathcal{V}_m$ does not present any fold in the neighborhood of the origin covered by this dataset. In section 9 we discuss how this procedure is also valid for trajectories that are not on the SSM.

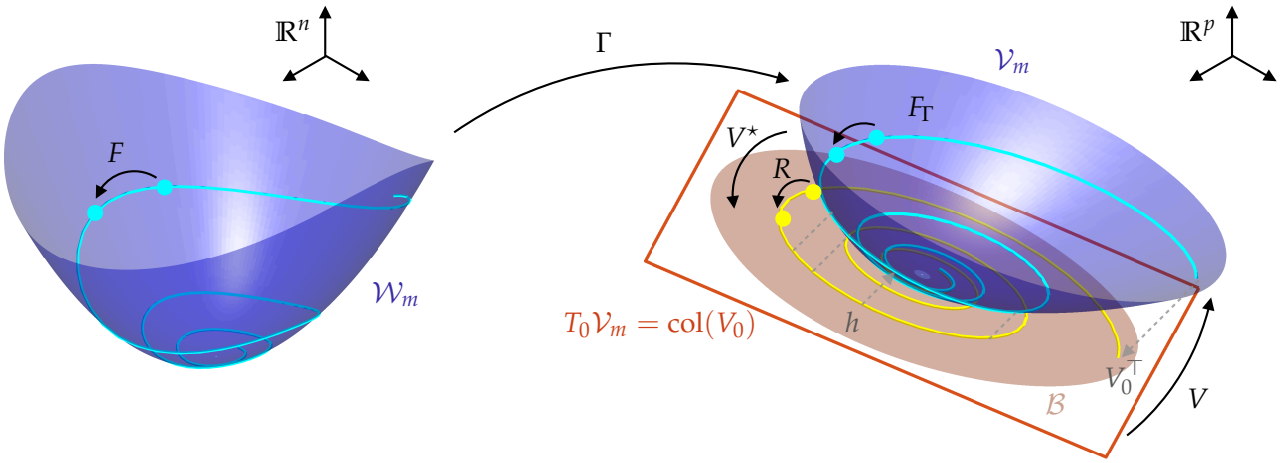

Figure 9.1: Illustration of an embedding Γ of an invariant manifold $\mathcal{W}_m$ from the phase space as an invariant manifold $\mathcal{V}_m$ in the observable space. Also sketched are the parametrization V and the reduced dynamics R presented in Theorem 9.1, including the tangent space $T_0\mathcal{V}_m$ at the origin, which is spanned by the column space of the matrix V_0.

9.1 PARAMETRIZATION AND REDUCED COORDINATES

The identification of the parametrization is performed by minimizing the static, squared reconstruction error of the map in Eq. (9.1), which reads

$$C_{para}(V) = \sum_{j=1}^{L}\sum_{k=1}^{L_j} \left\| y^{(j)}[k] - V\left(V^\star\left(y^{(j)}[k]\right)\right)\right\|^2. \tag{9.4}$$

We seek $h(\eta)$ as a multivariate polynomial of order M_V in η. Polynomials are justified by Taylor expansions in our local setting. More precisely, $h(\eta) = H\varphi(\eta;2{:}M_V)$ where the map $\varphi(\eta;2{:}M)$ is set of all the $m_{2:M}$ monomials in the coordinates of η from order 2 to order M, whose cardinality is

$$m_{2:M} = \sum_{l=2}^{M} m_l, \qquad m_l = \frac{(l+m-1)!}{l!(m-1)!}.$$

For example, for $m = 2$, $\eta = (\eta_1, \eta_2)$ and $M = 3$, we have

$$\varphi(\eta;2{:}3) = \left(\eta_1^2,\ \eta_1\eta_2,\ \eta_2^2,\ \eta_1^3,\ \eta_1^2\eta_2,\ \eta_1\eta_2^2,\ \eta_2^3\right)^\top, \qquad m_{2:M} = 7.$$

To comply with Theorem 9.1, the coefficient matrix $H \in \mathbb{R}^{p\times m_{2:M_V}}$ must be such that $V_0^\top H = 0$. Inserting the maps $V(\eta) = V_0\eta + H\varphi(\eta;2,M_V)$ and $V^\star(y) = V_0^\top y$ into the cost function (9.4), we formulate the minimization problem that identifies the optimal pair (V_0^*, H^*)

$$\begin{aligned}(V_0^*, H^*) = \ & \underset{V_0,H}{\operatorname{argmin}} \sum_{j=1}^{L}\sum_{k=1}^{L_j} \left\| y^{(j)}[k] - V_0V_0^\top y^{(j)}[k] - H\varphi\left(V_0^\top y^{(j)}[k];2{:}M_V\right)\right\|^2, \\ & \text{subject to } \ V_0^\top V_0 = I, \ \ V_0^\top H = 0.\end{aligned} \tag{9.5}$$

Regularizing terms, such as error weighting and a penalty function for the coefficients in H, may be also included in the cost function. The two constraints serve to fix the parametrization style for the manifold, i.e., to guarantee that it can be expressed as a graph of a function. Although there are infinite possible representations in this form, the minimization process extract the one that minimizes the reconstruction error for the assumed representation of h.

In general, problem (9.5) is a potentially non-convex optimization problem with nonlinear constraints that can be solved numerically with suitable optimization algorithms (see, for example, [188]). If the manifold $\mathcal{V}_m$ is assumed to be linear ($M = 1$ and $H = 0$), then problem (9.5) is the classic m-dim. PCA [56, 156], which can be solved in closed form via singular value decomposition of the data organized in matrix form. There can be cases in which a representation for tangent space at the origin is known a priori, so that minimization (9.5) can focus on the nonlinear coefficients in H. In that case, the problem becomes a least-squares regression with linear equality constraints (i.e., $V_0^\top H = 0$), for which exists a closed form solution [189]. The initial condition for the general optimization problem may be sought from these two analytically solvable sub-problems. Indeed, the initial guess for V_0 can be set as the PCA of the dataset, and, given this estimate, we can compute the initial condition for H in closed form, which typically ensures a fast convergence of the minimization process.

Remark 9.1. If the manifold $\mathcal{V}_m$ is very complex, one can leverage on manifold learning techniques coming from machine learning, such as locally linear embedding [158] or Hessian eigenmaps [159]. These algorithms can find usually good representation coordinates for the manifold, but obtaining the manifold parametrization is not trivial to achieve [57]. The manifold we are looking at are also not that complex in their geometry to require these approaches, at least with respect to the tangent space at the equilibrium. Indeed, canonical PCA augmented with some polynomial nonlinearities offers efficient and accurate performance for local trajectories near an equilibrium, and it simultaneously provides the coordinate chart and the parametrization for the manifold.

9.2 REDUCED DYNAMICS AND ITS NORMAL FORM

Once the parametrization is identified, the reduced coordinates $\eta = V_0^\top y$ can be used to identify the reduced dynamics. This problem may be formulated again as a minimization based on the 1-step prediction error

$$C_{map}(R) = \sum_{j=1}^{L} \sum_{k=1}^{L_j - 1} \left\| \eta^{(j)}[k+1] - R\left(\eta^{(j)}[k]\right) \right\|^2. \tag{9.6}$$

If the sampling time t_s is sufficiently small, one can numerically approximate the time derivative $\dot{\eta}$ via finite difference schemes. In that case, instead of 9.6, one can target the identification of the autonomous vector field $f_R(\eta)$ that induces the reduced flow map on the embedded SSM $\mathcal{V}_m$. Here, the cost function becomes

$$C_{flow}(f_R) = \sum_{j=1}^{L} \sum_{k=1}^{L_j - 1} \left\| \dot{\eta}^{(j)}[k] - f_R\left(\eta^{(j)}[k]\right) \right\|^2. \tag{9.7}$$

Although other representations may be selected, we focus on polynomial ones, in which either R or f_R can be represented by $\Theta\varphi(\eta; 1{:}M_R)$, where $\Theta \in \mathbb{R}^{m \times m_{1:M_R}}$. The resulting model is then linear in the parameters and classic regression techniques [50] (e.g., least-squares regression, ridge regression, LASSO) could be used to identify the dynamics from the cost functions (or their weighted/regularized versions) in Eqs. (9.6,9.7).

However, the resulting maps would be typically black-box models, being difficult to understand without additional manipulations. The assumption of sparsity for techniques like LASSO [51] or SINDy [52] is also heavily dependent on the reduced coordinates η. Indeed, model-based analytical SSM computations [18, 172] indicate that, for a graph-style parametrization, Θ is a fully populated matrix in general. For having an interpretable model with the minimal number of significant coefficients in its dynamics, we propose using normal forms for the reduced dynamics [4, 172, 174].

Normal forms permit to cluster dynamical systems into topologically similar families, i.e., exhibiting the same dynamical behavior, which can be described by the minimal number of coefficients.

The normal form for a vector field or a mapping is its simplest possible polynomial form near a fixed point. In the following, we describe the vector field case, while the map case is reported in section 9.5.2. Normal forms are achieved by a smooth coordinate change T that links the normalized and the non-normalized flow maps as

$$\Phi_N^t = T^{-1} \circ \Phi_R^t \circ T, \qquad N = T^{-1} \circ R \circ T. \tag{9.8}$$

Here we denoted Φ_R^t is the time-t flow map of f_R, while Φ_N^t is that of the normal form vector field f_N.

Using Eq. (9.8), we aim to find the simplest vector field f_N describing the dynamics. Near a hyperbolic fixed point, the Hartman-Grobman theorem [10] states that there exists a homeomorphism T that transforms the nonlinear system locally into its linearization. Siegel [190, 191] and Sternberg [192] strengthened this result showing that T is a diffeomorphism if the linearized eigenvalues at the origin satisfy certain non-resonance conditions. However, the domain of validity of the coordinate change for the system linearization is typically very small, as local nonlinear dynamical behavior (e.g. limit cycles, quasi-periodic motions, variations of time-scales) cannot be captured by a linear dynamical system.

The key idea of our normal form approach is to find a nonlinear, conjugated dynamical system of f_R that overcomes the limitations of the linearization approach. This method reveals to be particularly convenient for oscillatory dynamics in weakly dissipative systems, whose SSMs possess strongly meaningful normal forms [23, 90] as we shall now discuss.

We focus our attention on underdamped oscillatory normal forms, hence m must be even and the spectrum in $\mathcal{L}_m$ is made up by $m/2$ complex numbers and their conjugates. We further assume that $Df_R(0)$ is a diagonalizable matrix, i.e., we have that $Df_R(0)B = B\Lambda$, where Λ is a diagonal matrix whose entries are the elements of $\mathcal{L}_m$. Let us call the modal coordinates $\zeta = B^{-1}\eta$.

We seek to identify the triple (T^{-1}, f_N, T): the map $\zeta = T(z)$ is a nonlinear coordinate transformation mapping the normal form coordinates z to the modal coordinates with inverse $z = T^{-1}(\zeta)$, while the normal form dynamics is given by $\dot{z} = f_N(z)$. These maps can be expressed with a polynomial representation as

$$T^{-1}(\zeta) = \zeta + H_{T^{-1}}\varphi(\zeta; 2{:}M), \qquad f_N(z) = \Lambda z + H_N\varphi(z; 2{:}M), \qquad T(z) = z + H_T\varphi(z; 2{:}M), \tag{9.9}$$

where the matrices $H_{T^{-1}}, H_N, H_T \in \mathbb{C}^{m \times m_{2:M}}$. Note that the normal form order M may be different from that of the reduced coordinates dynamics M_R. We introduce the matrix of non-negative integers $S_{2:M}^{(m)} \in \mathbb{N}^{m \times m_{2:M}}$ corresponding to the exponents for the m-variate polynomial map $\varphi(\cdot\,; 2{:}M)$. In the case of Eq. (9.1), this matrix reads

$$S_{2:3}^{(2)} = \begin{bmatrix} 2 & 1 & 0 & 3 & 2 & 1 & 0 \\ 0 & 1 & 2 & 0 & 1 & 2 & 3 \end{bmatrix}. \tag{9.10}$$

Then, we construct the matrix $\Delta_{\Lambda,2:M} \in \mathbb{C}^{m \times m_{2:M}}$ of linear combinations of the eigenvalues in Λ as

$$(\Delta_{\Lambda,2:M})_{j,l} = (\Lambda)_{j,j} - \sum_{k=1}^{m} (\Lambda)_{k,k} \left(S_{2:M}^{(m)}\right)_{k,l}, \quad j = 1, 2, \dots m, \; l = 1, 2, \dots m_{2:M}, \tag{9.11}$$

which is needed for the next, fundamental result.

Theorem 9.2. *In the setting of Sternberg linearization theorem, i.e., for $H_N = 0$, the following estimates hold*

$$\left|(H_T)_{j,l}\right| \propto \frac{1}{\left|(\Delta_{\Lambda,2:M})_{j,l}\right|}, \qquad \left|(H_{T^{-1}})_{j,l}\right| \propto \frac{1}{\left|(\Delta_{\Lambda,2:M})_{j,l}\right|}, \qquad j = 1, 2, \dots m, \; l = 1, 2, \dots m_{2:M}. \tag{9.12}$$

This theorem, whose proof is reported in section 9.5.1, motivates the following definition.

Definition 9.1. *The normal form structure for the matrices $H_{T^{-1}}, H_N, H_T$ with tolerance δ is the set of row and column indexes defined as*

$$J_\delta := \left\{ (j,l) : \left| (\Delta_{\Lambda,2:M})_{j,l} \right| < \delta,\ j = 1,2,\dots m,\ l = 1,2,\dots m_{2:M} \right\}. \tag{9.13}$$

The terms within J_δ are called near-resonant, as they generate small denominators in the setting of Sternberg's linearization. Indeed, the change of coordinates here results to be ill-conditioned, hence limiting the validity of the conjugate system. To overcome this limitation, we set the coefficients of $H_{T^{-1}}, H_T$ to be zero at the locations J_δ, while the corresponding entry in H_N is nonzero and such that guarantees the solution of the conjugacy (9.8), as shown in section 9.5.1. The number of resonant terms is typically much smaller than the total number of terms, so that H_N is a sparse matrix and the dynamics is only described by a small yet meaningful number of coefficients. For instance, in a single-oscillator, cubic-order case ($m = 2$, $M_R = 3$) with eigenvalue $\lambda = \epsilon + i\omega$, we have

$$\Lambda = \begin{bmatrix} \lambda & 0 \\ 0 & \bar{\lambda} \end{bmatrix}, \quad \Delta_{\Lambda,2:3} = \begin{bmatrix} -\lambda & -\bar{\lambda} & \lambda - 2\bar{\lambda} & -2\lambda & -2\epsilon & -2\bar{\lambda} & \lambda - 3\bar{\lambda} \\ \bar{\lambda} - 2\lambda & -\lambda & -\bar{\lambda} & \bar{\lambda} - 3\lambda & -2\lambda & -2\epsilon & -2\bar{\lambda} \end{bmatrix} \tag{9.14}$$

so that, in case of small real part $|\epsilon|/|\omega| \ll 1$, resonant terms appear at the locations $J = \{(1,5),(2,6)\}$, and, with the notations $\zeta = (\zeta_1, \bar{\zeta}_1)^\top$ and $z = (z_1, \bar{z}_1)^\top$, the matrices $H_{T^{-1}}, H_N$ take the form

$$H_{T^{-1}} = \begin{bmatrix} h_{20} & h_{11} & h_{02} & h_{30} & 0 & h_{12} & h_{03} \\ \bar{h}_{02} & \bar{h}_{11} & \bar{h}_{20} & \bar{h}_{03} & \bar{h}_{12} & 0 & \bar{h}_{30} \end{bmatrix}, \quad H_N = \begin{bmatrix} 0 & 0 & 0 & 0 & \alpha & 0 & 0 \\ 0 & 0 & 0 & 0 & 0 & \bar{\alpha} & 0 \end{bmatrix}, \tag{9.15}$$

while the location of the nonzero entries for H_T is the same of that of $H_{T^{-1}}$. Other peculiar normal form for oscillators are synthetically collected in Table 9.1. Here, for the complex normal form, the dynamics of conjugated coordinates is omitted.

For the data-driven extraction of the normal form for f_R, we construct an initial estimate for $Df_R(0)$ from available data, as the Jacobian determines the structure of the normal form. An estimate for f_R can be obtained using classic, fast regression techniques from Eq. (9.6). The identification for the pair (T^{-1}, f_N) takes the form of a minimization over the squared conjugacy error

$$C\left(T^{-1}, f_N\right) = \sum_{k=1}^{L_j - 1} \left\| \frac{d}{dt}\left(T^{-1}\left(\zeta^{(j)}[k]\right)\right) - f_N\left(T^{-1}\left(\zeta^{(j)}[k]\right)\right) \right\|^2, \tag{9.16}$$

while the map T is determined via least-squares regression once normal form coordinates are known. By inserting the maps in Eq. (9.9) into the cost function (9.16), we formulate the minimization problem that identifies the optimal pair $(H^*_{T^{-1}}, H^*_N)$

$$\begin{aligned} c^{(j)}(k) = \ & \frac{d}{dt}\left(\zeta^{(j)}[k] + H_{T^{-1}}\varphi\left(\zeta^{(j)}[k]; 2{:}M\right)\right) - \Lambda\left(\zeta^{(j)}[k] + H_{T^{-1}}\varphi\left(\zeta^{(j)}[k]; 2{:}M\right)\right) + \\ & - H_N\varphi\left(\zeta^{(j)}[k] + H_{T^{-1}}\varphi\left(\zeta^{(j)}[k]; 2{:}M\right)\right) \\ (H^*_{T^{-1}}, H^*_N) = \ & \underset{H_{T^{-1}}, H_N}{\operatorname{argmin}} \sum_{j=1}^{L} \sum_{k=1}^{L_j - 1} \left(\bar{c}^{(j)}[k]\right)^\top c^{(j)}[k], \\ & \text{subject to } \ (H_N)_{(l,s)} = 0 \ \ \forall (l,s) \in J_\delta^c, \quad (H_{T^{-1}})_{(l,s)} = 0 \ \ \forall (l,s) \in J_\delta, \end{aligned} \tag{9.17}$$

where J_δ^c is complementary set of J_δ such that $J_\delta \cup J_\delta^c$ is set of the row and columns indexes for a matrix of dimension $m \times m_{2:M}$. From an implementation viewpoint, this problem can be recast as an

unconstrained minimization, which is nevertheless potentially non-convex. A good initial condition for iterative solvers is to set all the coefficients to 0. This initial guess supposes linear dynamics and the minimization should correct it with the best set of nonlinear coefficients in the normal form structure. The identification of normal form structure is clearly dependent on the tolerance δ of Definition 9.1. Although it may depend on the specific problem, a good candidate for weakly damped systems is $\delta = 10 \min_{\lambda \in \mathcal{L}_m} |\mathrm{Re}(\lambda)|$ [22] (see also the discussion in section 9.5.1.3).

Remark 9.2. An alternative method to extract the normal form relies on estimating either f_R or R and then uses this evolutionary rule in the analytic normal form computations reported in section 9.5 (see also [4, 174]). However, this strategy is not fully capitalizing on data. Analytic normal form computations have a certain domain of validity and it could be that this domain validity is smaller than the range of data. Moreover, this domain of validity may be influenced by the scaling used for the modal coordinates. Instead, by extracting the normal form directly from data, we are directly assuming that the range of data is within the domain of the normal form, for which the algorithm finds the best representation.

9.3 Analytics and predictions from normal forms

The normal form, by reducing the complexity of dynamics, offers unrivaled opportunities for learning the dynamical behavior and making predictions for small perturbations of the system.

From Table 9.1 below, one can note that the normal form for oscillators decouple the amplitude dynamics from the phase dynamics. This enables us to distinguish different modal contributions, and also allows a slow-fast decomposition and the analysis of the uncoupled oscillator limit. Moreover, the instantaneous dampings and frequencies for each mode j can be defined as

$$c_j = -\frac{\dot{\rho}_j}{\rho_j}, \quad \omega_j = \dot{\theta}_j, \tag{9.18}$$

from their normal form. The zero-amplitude limit for these quantities converges to the linearized damping and frequency of mode j. Indeed, c_j and ω_j are the nonlinear continuations of these linear quantities, and they characterize how dissipation (or activation for an unstable equilibrium) and frequency change with respect to the amplitudes (and phases for internally resonant systems). For a single oscillator, then $c(\rho)$ and $\omega(\rho)$ are the backbones of transient oscillations [23, 44, 74].

The normal form amplitude does not, however, have any direct physical meaning. A first option is to exhibit these curves with respect to time for a given trajectory. For further physical insights, we can express any amplitude of interest via the SSM parametrization V. For the single oscillator case, for the scalar quantity of interest $G : \mathbb{R}^p \to \mathbb{R}$ defined on the observable space $\mathbb{R}^p$, the amplitude of the oscillations can be defined as [90]

$$a(\rho) = \max_{\theta \in [0, 2\pi)} |G\left(V(T(\rho, \theta)\right)|\,. \tag{9.19}$$

Typically, $G(y)$ is simply a projection on an observable coordinate, but it can also be some other system property (e.g. kinetic energy, cf. section 10.3). Then, the damped backbone curves can be expressed as the parametric curves $\{c(\rho), a(\rho)\}$ and $\{\omega(\rho), a(\rho)\}$, as we will see in our example section 10. An analogous expression holds for any other quantity of physical interest in the observable space.

SSMs are robust features of the dynamics, hence they survive under small autonomous perturbations and even under some non-autonomous perturbations [18]. The latter include time-periodic perturbations, which will be our focus here. For mechanical systems, such perturbations represent small external periodic forcing. In that case, the autonomous SSM will serve as the leading

Table 9.1: Some oscillatory normal forms for weakly damped systems $\mathrm{Re}(\mathcal{L}_m) \ll 0$ with different dimensions m, orders M and resonances present in $\mathcal{L}_m$, which are indicated as $1:l$ for two coupled oscillators (while nonres. is the non-resonant case). We denote $z_j = \rho_j e^{i\theta_j}$ and $\bar{z}_j$ for the complex conjugated.

Case	Complex normal form	Polar normal form
$m=2$ $M=2S-1$ $S>1$	$\dot{z}_1 = \lambda z_1 + \sum_{l=1}^{S} \alpha_{2l} \lvert z \rvert_1^{2l} z_1$	$\dot{\rho}_1 = \left(\mathrm{Re}(\lambda) + \sum_{l=1}^{S} \mathrm{Re}\left(\alpha_{2l}\right) \rho_1^{2l}\right) \rho_1$ $\dot{\theta}_1 = \mathrm{Im}(\lambda) + \sum_{l=1}^{S} \mathrm{Im}\left(\alpha_{2l}\right) \rho_1^{2l}$
$m=4$ $M=3$ nonres.	$\dot{z}_1 = \lambda_1 z_1 + \alpha_{1,1} z_1^2 \bar{z}_1 + \alpha_{1,2} z_2 \bar{z}_2 z_1$ $\dot{z}_2 = \lambda_2 z_2 + \alpha_{2,2} z_2^2 \bar{z}_2 + \alpha_{2,1} z_1 \bar{z}_1 z_2$	$\dot{\rho}_1 = \mathrm{Re}(\lambda_1)\rho_1 + \mathrm{Re}(\alpha_{1,1})\rho_1^3 + \mathrm{Re}(\alpha_{1,2})\rho_2^2\rho_1$ $\dot{\rho}_2 = \mathrm{Re}(\lambda_2)\rho_2 + \mathrm{Re}(\alpha_{2,2})\rho_2^3 + \mathrm{Re}(\alpha_{2,1})\rho_2^1\rho_2$ $\dot{\theta}_1 = \mathrm{Im}(\lambda_1) + \mathrm{Im}(\alpha_{1,1})\rho_1^2 + \mathrm{Im}(\alpha_{1,2})\rho_2^2$ $\dot{\theta}_2 = \mathrm{Im}(\lambda_2) + \mathrm{Im}(\alpha_{2,2})\rho_2^2 + \mathrm{Im}(\alpha_{2,1})\rho_1^2$
$m=4$ $M=3$ $1:1$ res.	$\dot{z}_1 = \lambda_1 z_1 + \alpha_{1,1} z_1^2 \bar{z}_1 + \alpha_{1,2} z_2 \bar{z}_2 z_1 + \beta_{1,1} z_1^2 \bar{z}_2 + \beta_{1,2} z_1 \bar{z}_1 z_2 + \beta_{1,3} \bar{z}_1 z_2^2 + \beta_{1,4} z_2^2 \bar{z}_2$ $\dot{z}_2 = \lambda_2 z_2 + \alpha_{2,2} z_2^2 \bar{z}_2 + \alpha_{2,1} z_1 \bar{z}_1 z_2 + \beta_{2,1} z_1^2 \bar{z}_1 + \beta_{2,2} z_1^2 \bar{z}_2 + \beta_{2,3} \bar{z}_1 z_2^2 + \beta_{2,4} z_1 z_2 \bar{z}_2$ $\psi = \theta_2 - \theta_1$	See ‡ on the next page for the polar normal form
$m=4$ $M=3$ $1:2$ res.	$\dot{z}_1 = \lambda_1 z_1 + \alpha_{1,1} z_1^2 \bar{z}_1 + \alpha_{1,2} z_2 \bar{z}_2 z_1 + \beta_1 \bar{z}_1 z_2$ $\dot{z}_2 = \lambda_2 z_2 + \alpha_{2,2} z_2^2 \bar{z}_2 + \alpha_{2,1} z_1 \bar{z}_1 z_2 + \beta_2 z_1^2$ $\psi = \theta_2 - 2\theta_1$	$\dot{\rho}_1 = \mathrm{Re}(\lambda_1)\rho_1 + \mathrm{Re}(\alpha_{1,1})\rho_1^3 + \mathrm{Re}(\alpha_{1,2})\rho_2^2\rho_1 + \rho_1\rho_2 \mathrm{Re}\left(\beta_1 e^{i\psi}\right)$ $\dot{\rho}_2 = \mathrm{Re}(\lambda_2)\rho_2 + \mathrm{Re}(\alpha_{2,2})\rho_2^3 + \mathrm{Re}(\alpha_{2,1})\rho_2^1\rho_2 + \rho_1^2 \mathrm{Re}\left(\beta_2 e^{-i\psi}\right)$ $\rho_1\dot{\theta}_1 = \mathrm{Im}(\lambda_1)\rho_1 + \mathrm{Im}(\alpha_{1,1})\rho_1^3 + \mathrm{Im}(\alpha_{1,2})\rho_2^2\rho_1 + \rho_1\rho_2 \mathrm{Im}\left(\beta_1 e^{i\psi}\right)$ $\rho_2\dot{\theta}_2 = \mathrm{Im}(\lambda_2)\rho_2 + \mathrm{Im}(\alpha_{2,2})\rho_2^3 + \mathrm{Im}(\alpha_{2,1})\rho_1^2\rho_2 + \rho_1^2 \mathrm{Im}\left(\beta_2 e^{-i\psi}\right)$
$m=4$ $M=3$ $1:3$ res.	$\dot{z}_1 = \lambda_1 z_1 + \alpha_{1,1} z_1^2 \bar{z}_1 + \alpha_{1,2} z_2 \bar{z}_2 z_1 + \beta_1 \bar{z}_1^2 z_2$ $\dot{z}_2 = \lambda_2 z_2 + \alpha_{2,2} z_2^2 \bar{z}_2 + \alpha_{2,1} z_1 \bar{z}_1 z_2 + \beta_2 z_1^3$ $\psi = \theta_2 - 3\theta_1$	$\dot{\rho}_1 = \mathrm{Re}(\lambda_1)\rho_1 + \mathrm{Re}(\alpha_{1,1})\rho_1^3 + \mathrm{Re}(\alpha_{1,2})\rho_2^2\rho_1 + \rho_1^2\rho_2 \mathrm{Re}\left(\beta_1 e^{i\psi}\right)$ $\dot{\rho}_2 = \mathrm{Re}(\lambda_2)\rho_2 + \mathrm{Re}(\alpha_{2,2})\rho_2^3 + \mathrm{Re}(\alpha_{2,1})\rho_2^1\rho_2 + \rho_1^3 \mathrm{Re}\left(\beta_2 e^{-i\psi}\right)$ $\rho_1\dot{\theta}_1 = \mathrm{Im}(\lambda_1)\rho_1 + \mathrm{Im}(\alpha_{1,1})\rho_1^3 + \mathrm{Im}(\alpha_{1,2})\rho_2^2\rho_1 + \rho_1^2\rho_2 \mathrm{Im}\left(\beta_1 e^{i\psi}\right)$ $\rho_2\dot{\theta}_2 = \mathrm{Im}(\lambda_2)\rho_2 + \mathrm{Im}(\alpha_{2,2})\rho_2^3 + \mathrm{Im}(\alpha_{2,1})\rho_1^2\rho_2 + \rho_1^3 \mathrm{Im}\left(\beta_2 e^{-i\psi}\right)$
$m=2s$ $M=3$ nonres.	$\dot{z}_j = \lambda_j z_j + \sum_{l=1}^{s} \alpha_{j,l} \lvert z_l \rvert^2 z_j$ for $j = 1, 2, \ldots s$	$\dot{\rho}_j = \left(\mathrm{Re}(\lambda_j) + \sum_{l=1}^{s} \mathrm{Re}(\alpha_{j,l})\rho_l^2\right) \rho_j$ $\dot{\theta}_j = \mathrm{Im}(\lambda_j) + \sum_{l=1}^{s} \mathrm{Im}(\alpha_{j,l})\rho_l^2$

order approximation for the non-autonomous SSM that governs reduced, time-periodic dynamics [18, 22, 23, 83].

Let us focus on the single-oscillator case and consider

$$\dot{x} = f(x) + \varepsilon g(x, \Omega t), \quad f(0) = 0, \quad x \in \mathbb{R}^n, \quad \Omega \in \mathbb{R}_+, \quad 0 \leq \varepsilon \ll 1, \tag{9.20}$$

where we assume that, for $\varepsilon = 0$, the system has a 2-dim. SSM related to the eigenvalues $(\lambda, \bar{\lambda})$ with frequency ω_0, which resonates with the forcing frequency, i.e. $\Omega \approx \omega_0$ for primary resonances. An SSM also exists for the perturbed system. If $W_0(z)$ and $f_{R,0}(z)$ denote the parametrization and reduced dynamics for the autonomous SSM, then their non-autonomous counterparts read

$$W_\varepsilon(z) = W_0(z) + \varepsilon W_1(z) + O(\varepsilon^2), \quad f_{R,\varepsilon}(z) = f_{R,0}(z) + \varepsilon f_{R,1}(z) + O(\varepsilon^2). \tag{9.21}$$

For sinusoidal external forcing $g(x,t) = F^{ext}\cos(\Omega t)$, the reduced dynamics in complex coordinates $z = (z_1, \bar{z}_1)$ takes the form [193]

$$\dot{z}_1 = (-c(\rho) + i\omega(\rho))\, z_1 + F_R^{ext} e^{i\Omega t} + O(\varepsilon\rho), \tag{9.22}$$

where $|z_1| = \rho$ and $F_R^{ext} = v^\star F^{ext}/2$, in which $v^\star$ is the left eigenvector of $Df(0)$ related to the eigenvalue λ [23]. Note that the eigenvector v can be chosen such that F_r^{ext} is purely imaginary, as shown in Appendix A(c) of [23].

Among the $O(\varepsilon)$-corrections in (9.21), the one related to the reduced dynamics is clearly more important. Hence, by neglecting the parametrization correction but imposing external forcing as in (9.22), we can use the model trained on transient data to make predictions for the forced response. Namely, for a given value of forcing, we can study periodic orbits of the system and their stability type varying the forcing frequency. Note that this is valid regardless of the specific observable we use for model training. As expressed in (9.22), this approximation for the forced dynamics is valid for forcing and amplitude values that are not too large.

The forced responses described by Eq. (9.22) can be computed in closed form. By neglecting $O(\varepsilon\rho)$ terms and assuming the forcing parameter to be purely imaginary $F_R^{ext} = if_R^{ext}$, we rewrite Eq. (9.22) considering the phase shift $\psi = \theta - \Omega t$

$$\begin{aligned} \dot{\rho} &= -c(\rho)\rho + f_R^{ext}\sin(\psi), \\ \rho\dot{\psi} &= \rho\,(\omega(\rho) - \Omega) + f_R^{ext}\cos(\psi), \end{aligned} \tag{9.23}$$

whose fixed points correspond to periodic responses of Eq. (9.22), which must satisfy

$$\begin{aligned} c(\rho)\rho &= f_R^{ext}\sin(\psi), \\ \rho\,(\Omega - \omega(\rho)) &= f_R^{ext}\cos(\psi). \end{aligned} \tag{9.24}$$

Summing the squares of the two equations and solving for Ω lead to the analytic formula

$$\Omega = \omega(\rho) \pm \sqrt{\frac{\left(f_R^{ext}\right)^2}{\rho^2} - \left(c(\rho)\right)^2}, \tag{9.25}$$

which parametrizes forced responses with ρ for a certain value of external forcing f_R^{ext}. Physical amplitudes can be derived using Eq. (9.19). The stability of these solutions can be obtained from the eigenvalues of the jacobian of (9.23) [23].

‡:

$$\begin{aligned}
\dot{\rho}_1 &= \mathrm{Re}(\lambda_1)\rho_1 + \mathrm{Re}(\alpha_{1,1})\rho_1^3 + \mathrm{Re}(\alpha_{1,2})\rho_2^2\rho_1 + \rho_1^2\rho_2\mathrm{Re}\left(\beta_{1,1}e^{-i\psi} + \beta_{1,2}e^{i\psi}\right) + \rho_1\rho_2^2\mathrm{Re}\left(\beta_{1,3}e^{i2\psi}\right) + \rho_2^3\mathrm{Re}\left(\beta_{1,4}e^{i\psi}\right) \\
\dot{\rho}_2 &= \mathrm{Re}(\lambda_2)\rho_2 + \mathrm{Re}(\alpha_{2,2})\rho_2^3 + \mathrm{Re}(\alpha_{2,1})\rho_2^1\rho_2 + \rho_2^2\rho_1\mathrm{Re}\left(\beta_{2,3}e^{i\psi} + \beta_{2,4}e^{-i\psi}\right) + \rho_2\rho_1^2\mathrm{Re}\left(\beta_{2,2}e^{-i2\psi}\right) + \rho_1^3\mathrm{Re}\left(\beta_{2,1}e^{-i\psi}\right) \\
\rho_1\dot{\theta}_1 &= \mathrm{Im}(\lambda_1)\rho_1 + \mathrm{Im}(\alpha_{1,1})\rho_1^3 + \mathrm{Im}(\alpha_{1,2})\rho_2^2\rho_1 + \rho_1^2\rho_2\mathrm{Im}\left(\beta_{1,1}e^{-i\psi} + \beta_{1,2}e^{i\psi}\right) + \rho_1\rho_2^2\mathrm{Im}\left(\beta_{1,3}e^{i2\psi}\right) + \rho_2^3\mathrm{Im}\left(\beta_{1,4}e^{i\psi}\right) \\
\rho_2\dot{\theta}_2 &= \mathrm{Im}(\lambda_2)\rho_2 + \mathrm{Im}(\alpha_{2,2})\rho_2^3 + \mathrm{Im}(\alpha_{2,1})\rho_1^2\rho_2 + \rho_2^2\rho_1\mathrm{Im}\left(\beta_{2,3}e^{i\psi} + \beta_{2,4}e^{-i\psi}\right) + \rho_2\rho_1^2\mathrm{Im}\left(\beta_{2,2}e^{-i2\psi}\right) + \rho_1^3\mathrm{Im}\left(\beta_{2,1}e^{-i\psi}\right)
\end{aligned}$$

In practice, the collection of data belonging to a specific invariant manifold is hard to accomplish. For some dynamical systems, prior knowledge helps in finding good initial conditions for trajectories whose dynamics is at least close that of the SSM. If a reduced-order model is sought from numerical simulations data, then eigenvalues and eigenvectors of the linearized system at the equilibrium can be used to judiciously initialize trajectories, see sections 10.1, 10.2. For this purpose, we only require the knowledge of the spectrum related to the SSM of interest. For physical experiments, the data collection highly depends on the nature of the system under analysis. In the context of mechanical systems, the resonance decay method [32, 44, 73], by means of a shaker, is able to focus the energy on a specific 2-dim. SSM. More precisely, this method consists of isolating a resonant periodic motion of the SSM and, afterwards, releasing the shaker from the structure to activate transients towards the equilibrium, which lay very close to the SSM of interest. Alternatively, targeted initial conditions or hammer impacts may help in isolating specific systems motions. Regarding instabilities in fluid dynamics, data collection methods typical in modal analysis can be followed (see, for example, the recent review [178] and references therein).

If targeted experiments are not available, we can still tackle the identification of the leading attracting SSM of the system under analysis. Indeed, according to Proposition 8.2, a generic initial condition within the basin of attraction rapidly converges to this manifold. While the constant C_s mainly depends on the initial condition $\hat{x}$, the other constant λ_s is such that $-\lambda_s < \mathrm{Re}(\lambda)$ for all $\lambda \in \mathcal{L}_m$. So either one proceeds in cutting the acquired signal, or in weighting the losses in the cost functions Eqs. (9.4,9.6,9.7). By calling $c^{(j)}[k]$ the error for trajectory j at instant k and assuming a sampling time t_s, we can set

$$C = \sum_{j=1}^{L} \sum_{k=1}^{L_j - 1} \frac{\left\| c^{(j)}[k] \right\|^2}{(1 + C_s^{(j)} e^{\lambda_s k t_s})^2}. \tag{9.26}$$

The hyperparameters $C_s^{(j)}, \lambda_s$ can be established via cross validation. For the determination of the dimension, time-frequency analysis reveals to be a useful tool. For oscillatory SSMs, m can be set as twice the number of leading frequencies in each trajectories. Filtering, although it might be useful for signal cleaning, is not recommended for isolating the frequency components of interest, since it ignores potential modal coupling.

For an unbiased identification of parametrization and reduced dynamics, the dataset should properly span the manifold. Furthermore, good practice suggests to divide this dataset into training, testing and validation [50].

We have implemented the method described in this thesis in the MATLAB® package `SSMLearn`, as reported in Algorithm 1 and visualized in Fig. 7.1. If the number of observed states is not sufficient for manifold embedding, the data is automatically augmented with delays to reach the minimum embedding dimension $p : p > 2m$. Optionally, the embedding dimension can be further increased by the user, and this over-embedding helps in unfolding manifolds that present possible folds in the range of data. Moreover, the polynomial order can be increased to improve the accuracy, without compromising generalization. Since polynomials are used to represent nonlinearities, note also that data scaling may improve the performances. When dealing with noisy dataset, dimensionality reduction naturally de-noises data [50], provided that the polynomial order selected for the parametrization is not excessively large. Alternatively, filtering may be adopted.

We remark that 1 is a method for purely data-driven reduced-order modeling. Indeed, we do not require the knowledge of the generating vector field f, but only of some of its trajectories. As we discuss in chapter 10 prior knowledge of the model, which is particularly valuable for dataset from numerical simulations, can be optionally set as input in the algorithm, eventually improving its performance.

Algorithm 1: Data-driven reduced-order models via `SSMLearn`

Input parameters: SSM dimension m, polynomial orders M_V and M_R for the parametrization and the reduced dynamics, selection among discrete-time or continuous-time approximation for the dynamics

Output: Normal form reduced dynamics, manifold parametrization and coordinate chart

Input data: Observed training trajectories

1 Embed data in the prescribed observable space

2 Identify manifold graph-style parametrization and coordinate chart

3 Estimate the linearized eigenvalues for the selection of the appropriate normal form

4 Identify the normal form of the reduced dynamics

9.5 NORMAL FORMS AND THEIR COMPUTATIONS

In this section, we work out the normal forms in the notation of this chapter and we also discuss the data-driven identification of normal forms for maps.

9.5.1 *The case of flows*

In this section, we use the notation $\varphi(\eta; k)$ for to indicate the set of m-variate polynomial of order k. Therefore, the Taylor expansions for the coordinate change of section 9.2 and its inverse read

$$T(z) = z + \sum_{k=2}^{M} H^k_{T^{-1}} \varphi(z; k) + o(M), \quad T^{-1}(\zeta) = \zeta + \sum_{k=2}^{M} H^k_T \varphi(\zeta; k) + o(M). \tag{9.27}$$

We set the vector field in modal coordinates $\hat{f}_R(\zeta) = B^{-1} f_R(B\zeta)$ and we expand $\hat{f}_R$ and f_N with Taylor expansions, resulting in

$$\hat{f}_R(\zeta) = \Lambda\zeta + \sum_{k=2}^{M_R} H^k_R \varphi(\zeta; k) + o(M_R), \quad f_N(z) = \Lambda z + \sum_{k=2}^{M} H^k_N \varphi(z; k) + o(M). \tag{9.28}$$

9.5.1.1 *Proof of Theorem 9.2*

Proof. By substituting the coordinate change in the dynamics $\dot{\zeta} = \hat{f}_R(\zeta)$, one obtains

$$DT(z) f_N(z) = \hat{f}_R(T(z)), \tag{9.29}$$

and, by using the expansions of Eqs. (9.27,9.28), we have that

$$\begin{aligned} DT(z)f_N(z) = &\left(I + \sum_{k=2}^{M} H_T^k D\varphi(z;k)\right)\left(\Lambda z + \sum_{j=2}^{M} H_N^j \varphi(z;j)\right) \\ = &\ \Lambda z + \sum_{k=2}^{M}\left(H_N^k\varphi(z;k) + H_T^k D\varphi(z;k)\Lambda z + B_1^k\varphi(z;k)\right) + o(M) \\ \hat{f}_R(T(z)) = &\ \Lambda z + \sum_{k=2}^{M}\Lambda H_T^k\varphi(z;k) + \sum_{k=2}^{M_R} H_R^k\varphi\left(z + \sum_{j=2}^{M} H_T^j\varphi(z;j);k\right) \\ = &\ \Lambda z + \sum_{k=2}^{M}\left(\Lambda H_T^k\varphi(z;k) + B_2^k\varphi(z;k)\right) + \sum_{k=2}^{\min(M,M_R)} H_R^k\varphi(z;k) + o(M), \end{aligned} \tag{9.30}$$

where the matrices B_k^1, B_k^2 are obtained via algebraic manipulations from the definitions

$$\begin{aligned} \sum_{k=2}^{M} B_1^k\varphi(z;k) + o(M) = &\left(\sum_{l=2}^{M} H_T^l D\varphi(z;l)\right)\left(\sum_{j=2}^{M} H_N^j\varphi(z;j)\right), \\ \sum_{k=2}^{M} B_2^k\varphi(z;k) + o(M) = &\sum_{j=2}^{M_R} H_R^j\varphi\left(z + \sum_{l=2}^{M} H_T^l\varphi(z;l);j\right) - \sum_{k=2}^{\min(M,M_R)} H_R^k\varphi(z;k). \end{aligned} \tag{9.31}$$

It also holds that, given the matrix of non-negative integers $S_k^{(m)} \in \mathbb{N}^{m\times m_k}$ corresponding to the exponents for the m-variate polynomial map $\varphi(\cdot\,;k)$,

$$D\varphi(z;k)\Lambda z = \Lambda^k\varphi(z;k), \quad \left(\Lambda^k\right)_{j,s} = \begin{cases} \sum_{l=1}^{m}(\Lambda)_{l,l}\left(S_k^{(m)}\right)_{l,j} & \text{if } j = s, \\ 0 & \text{otherwise,} \end{cases} \tag{9.32}$$

for $j, s = 1, 2, \dots m_k$. By substituting Eqs. (9.30,9.32) in Eq. (9.29), one obtains a set of cohomological equations that is solved stepwise with increasing polynomial order. The linear terms cancel out, while, at order $1 < k \leq M$, we obtain the Sylvester matrix equation [141]

$$\Lambda H_T^k - H_T^k\Lambda^k = H_N^k - \mathbb{1}_{k\leq M_R}H_R^k + B_1^k - B_2^k, \tag{9.33}$$

where $\mathbb{1}_{k\leq M_R}$ is the indicator function returning 0 if $k > M_R$ or 1 otherwise. Note that the matrices B_1^k, B_2^k just depends from the coefficients of H_T^j, H_N^j, H_R^j with $1 < j < k$, as highlighted by Eq. (9.31). If the coefficients of $\hat{f}_R$ are known, then the unknowns in Eq. (9.33) are the $2mm_k$ coefficients of the matrices H_T^k, H_n^k, for the solutions of which we only have mm_k equations. We can solve this underdetermination by prescribing half of the unknowns and solve for the remaining ones. Stenberg linearization imposes that $H_N^k = 0$ so that, due to the diagonal form of Λ and Λ^k, we have

$$\left(H_T^k\right)_{j,l} = \frac{\left(B_1^k - B_2^k - \mathbb{1}_{k\leq M_R}H_R^k\right)_{j,l}}{(\Lambda)_{j,j} - \left(\Lambda^k\right)_{l,l}}, \tag{9.34}$$

which proves Theorem 9.2 for the coefficients H_T. For those of $H_{T^{-1}}$, an analogue reasoning holds. Indeed, one starts from the normal form dynamics $\dot{z} = f_N(z)$ and imposes the coordinate change

$z = T^{-1}(\zeta)$. Hence, with appropriate definitions for the terms $\hat{B}_1^k$, $\hat{B}_2^k$, the resulting cohomological equation at step k takes the form

$$\Lambda H_{T^{-1}}^k - H_{T^{-1}}^k \Lambda^k = \mathbb{1}_{k \leq M_R} H_R^k - H_N^k + \hat{B}_1^k - \hat{B}_2^k, \tag{9.35}$$

and the solution for Stenberg linearization is

$$\left(H_{T^{-1}}^k\right)_{j,l} = \frac{\left(\hat{B}_1^k - \hat{B}_2^k + \mathbb{1}_{k \leq M_R} H_R^k\right)_{j,l}}{(\Lambda)_{j,j} - \left(\Lambda^k\right)_{l,l}}. \tag{9.36}$$

□

9.5.1.2 *The regularizing normal form*

The normal form strategy presented in section 9.2 finds its justification in the derivations of section 9.5.1.1. Indeed, the model structure shaped in Definition 9.1 is based on a solution of the cohomological equations which is different from that of Stenberg linearization. In this normal form case, we do not impose that $H_N = 0$, but rather we check the denominators in Eqs. (9.34,9.36). If these denominators are smaller than a certain tolerance δ, we leverage on H_N to regularize the solution of these cohomological equations and to identify meaningful terms for the dynamics. Indeed, for the cohomological equations Eq. (9.33) we use the solution style

$$(\Delta_{\Lambda,k})_{j,l} = (\Lambda)_{j,j} - \left(\Lambda^k\right)_{l,l}, \qquad B^k = B_1^k - B_2^k - \mathbb{1}_{k \leq M_R} H_R^k,$$

$$\begin{cases} \left(H_T^k\right)_{j,l} = 0, \ \left(H_N^k\right)_{j,l} = -\left(B^k\right)_{j,l}, & \text{if } \left|(\Delta_{\Lambda,k})_{j,l}\right| < \delta, \\ \left(H_T^k\right)_{j,l} = \dfrac{\left(B^k\right)_{j,l}}{(\Delta_{\Lambda,k})_{j,l}}, \ \left(H_N^k\right)_{j,l} = 0, & \text{otherwise,} \end{cases} \tag{9.37}$$

and an analogous result follows from Eq. (9.35). Hence for our data-driven extraction of the normal form, we impose a model for the triple (T^{-1}, f_N, T) such that it satisfies

$$\begin{cases} \left(H_T^k\right)_{j,l} = 0, \ \left(H_{T^{-1}}^k\right)_{j,l} = 0, & \text{if } \left|(\Delta_{\Lambda,k})_{j,l}\right| < \delta, \\ \left(H_N^k\right)_{j,l} = 0, & \text{otherwise.} \end{cases} \tag{9.38}$$

9.5.1.3 *Troubleshooting the numerical normal form tolerance*

Analytical SSMs computations [20, 22, 74, 83, 90] sets the normal form tolerance based on the real part of the slowest eigenvalue appearing in the spectrum related to the SSM, as discussed in section 9.2. Selecting the best value for this tolerance depends on the polynomial order of the normal form and the specificity of the problem. A good choice is to set $\delta = 10 \min_{\lambda \in \mathcal{L}_m} |\mathrm{Re}(\lambda)|$.

In order to avoid issues related to tolerance selection, one can seek the normal form structure as the manifold of interest would be a center manifold, eventually with internal resonances. This is particularly relevant for very-weakly damped systems. Indeed, we can impose a normal form structure for a given $\hat{\Lambda}$ with $\delta = 0$. For non resonant eigenvalues, then we can set $\hat{\Lambda} = i\mathrm{Im}(\Lambda)$ and compute J_0 in Definition 9.1 using $\Delta_{\hat{\Lambda},k}$ instead of $\Delta_{\Lambda,k}$. For resonant cases, one can enforce resonances, e.g., for $1:l$ resonances in 2 coupled oscillators, we can set $\hat{\Lambda}$ to be the diagonal matrix with entries (i, li) and impose zero tolerance in the normal form structure identification.

We remark that, using the center-manifold-style approach of this section, we are only enforcing the matrices H_N, $H_{T^{-1}}$ and H_T to have zeros in prescribed locations, we do not affect the spectrum of $\mathcal{L}_m$ appearing in the reduced-order model.

9.5.2 *The case of maps*

The introduction on normal forms discussed in section 9.2 also applied to maps. In particular, the conjugacy (9.8) holds for the normal form map N and the reduced dynamics R, which replaces the flow maps in Eq. (9.8).

As in the flow case, we focus our attention on oscillatory normal forms, hence m must be even and the spectrum in $\mathcal{L}'_m$ is made up by $m/2$ complex numbers and their conjugate ones. We further assume that $DR(0)$ is a diagonalizable matrix, i.e., it holds that $DR(0)B = B\Lambda'$, where Λ' is a diagonal matrix whose entries are the elements of $\mathcal{L}'_m$. Let us call the modal coordinates $\zeta = B^{-1}\eta$. Then, we need to identify the triple (T^{-1}, f_N, T): the map $\zeta = T(z)$ is a nonlinear coordinate transformation mapping the normal form coordinates z to the modal coordinates with inverse $z = T^{-1}(\zeta)$, while the normal form dynamics is expressed by $z[j+1] = N(z[j])$.

9.5.2.1 *Computations*

In this section, we prove that an analogous version of Theorem 9.2 holds for the case of mappings. To do so, we adopt the notation in Eq. (9.27), while for the dynamics we set $\hat{R} = B^{-1}R(B\zeta)$ and expand as

$$\hat{R}(\zeta) = \Lambda'\zeta + \sum_{k=2}^{M_R} H_R^k \varphi(\zeta; k) + o(M_R), \quad N(z) = \Lambda' z + \sum_{k=2}^{M} H_N^k \varphi(z; k) + o(M). \tag{9.39}$$

Given the matrix of non-negative integers $S_k^{(m)} \in \mathbb{N}^{m \times m_k}$ corresponding to the exponents for the m-variate polynomial map $\varphi(\cdot\,; k)$, we define

$$\left(\Delta'_{\Lambda',k}\right)_{j,l} = (\Lambda')_{j,j} - \prod_{k=1}^{m} (\Lambda')_{k,k}^{\left(S_k^{(m)}\right)_{k,l}}, \quad j = 1, 2, \dots m, \ l = 1, 2, \dots m_k. \tag{9.40}$$

Theorem 9.3. *In the setting of Sternberg linearization theorem, i.e., for $H_N = 0$, the following estimates hold*

$$\left|(H_T)_{j,l}\right| \propto \frac{1}{\left|\left(\Delta'_{\Lambda',k}\right)_{j,l}\right|}, \quad \left|(H_{T^{-1}})_{j,l}\right| \propto \frac{1}{\left|\left(\Delta'_{\Lambda',k}\right)_{j,l}\right|}, \quad \begin{matrix} j = 1, 2, \dots m, \ l = 1, 2, \dots m_k, \\ k = 2, \dots M. \end{matrix} \tag{9.41}$$

Proof. By substituting the coordinate change in the dynamics $\zeta[l+1] = \hat{R}(\zeta[l])$, one obtains

$$T(N(z)) = \hat{R}(T(z)), \tag{9.42}$$

and, by using the expansions of Eqs. (9.27,9.39), we have that

$$\begin{aligned}
T(N(z)) = &\ \Lambda' z + \sum_{k=2}^{M} \left(H_N^k \varphi(z; k) + H_T^k \varphi\left(\Lambda' z + \sum_{j=2}^{M} H_N^j \varphi(z; j); k \right) \right) \\
= &\ \Lambda' z + \sum_{k=2}^{M} \left(H_N^k \varphi(z; k) + H_T^k \varphi(\Lambda' z; k) + B_1^k \varphi(z; k) \right) + o(M) \\
\hat{R}(T(z)) = &\ \Lambda' z + \sum_{k=2}^{M} \Lambda' H_T^k \varphi(z; k) + \sum_{k=2}^{M_R} H_R^k \varphi\left(z + \sum_{j=2}^{M} H_T^j \varphi(z; j); k \right) \\
= &\ \Lambda' z + \sum_{k=2}^{M} \left(\Lambda' H_T^k \varphi(z; k) + B_2^k \varphi(z; k) \right) + \sum_{k=2}^{\min(M, M_R)} H_R^k \varphi(z; k) + o(M),
\end{aligned} \tag{9.43}$$

where the matrices B_k^1, B_k^2 are obtained via algebraic manipulations from the definitions

$$\begin{aligned}\sum_{k=2}^{M} B_1^k \varphi(z;k) + o(M) = &\sum_{j=2}^{M} H_T^j \varphi\left(\Lambda' z + \sum_{l=2}^{M} H_N^l \varphi(z;l); j\right) - \sum_{k=2}^{M} H_T^k \varphi(\Lambda' z; k),\\ \sum_{k=2}^{M} B_2^k \varphi(z;k) + o(M) = &\sum_{j=2}^{M_R} H_R^j \varphi\left(z + \sum_{l=2}^{M} H_T^l \varphi(z;l); j\right) - \sum_{k=2}^{\min(M,M_R)} H_R^k \varphi(z;k).\end{aligned} \tag{9.44}$$

It also holds that

$$\varphi(\Lambda' z; k) = \Lambda'^k \varphi(z;k), \quad \left(\Lambda'^k\right)_{j,s} = \begin{cases} \sum_{l=1}^{m} (\Lambda')_{l,l}^{\left(S_k^{(m)}\right)_{l,j}} & \text{if } j = s,\\ 0 & \text{otherwise,}\end{cases} \tag{9.45}$$

for $j, s = 1, 2, \dots m_k$. By substituting Eqs. (9.43,9.45) in Eq. (9.42), one obtains a set of cohomological equations that is solved stepwise with increasing polynomial order. From here onwards, the discussion is the same of that of the proof of Theorem 9.2, where we only need to replace Λ and Λ^k with the equivalent matrix Λ' and Λ'^k of the current setting. □

9.5.2.2 *Data-driven identification*

The discussion following from Theorem 9.2 in section 9.2 applies *verbatim* also here. In particular, the regularizing normal form of Definition 9.1 and Eq. (9.38) carries over to the map setting by solely replacing the matrices $\Delta_{\Lambda,k}, \Delta_{\Lambda,2:M}$ with their finite time counterparts $\Delta'_{\Lambda',k}, \Delta'_{\Lambda',2:M}$, where the latter reads

$$\left(\Delta'_{\Lambda,2:M}\right)_{j,l} = (\Lambda')_{j,j} - \prod_{k=1}^{m} (\Lambda')_{k,k}^{\left(S_{2:M}^{(m)}\right)_{k,l}}, \quad j = 1, 2, \dots m, \ l = 1, 2, \dots m_{2:M}. \tag{9.46}$$

By setting T^{-1}, T as in Eq. (9.9) and $N(z) = \Lambda' z + H_N \varphi(z; 2{:}M)$, the only other modification is for the loss in the cost function of problem (9.17), which now takes the form

$$\begin{aligned}c^{(j)}[k] = \ &\zeta^{(j)}[k+1] + H_{T^{-1}} \varphi\left(\zeta^{(j)}[k+1]; 2{:}M\right) - \Lambda' \left(\zeta^{(j)}[k] + H_{T^{-1}} \varphi\left(\zeta^{(j)}[k]; 2{:}M\right)\right) +\\ &- H_N \varphi\left(\zeta^{(j)}[k] + H_{T^{-1}} \varphi\left(\zeta^{(j)}[k]; 2{:}M\right)\right).\end{aligned} \tag{9.47}$$

The tolerances for the normal form structure identification are set in an equivalent manner to the case of flows, just considering their finite time counterparts.

10 CASE STUDIES

We now discuss several examples that validate the SSM-based, data-driven model reduction method we propose. The first two examples deal with datasets obtained from numerical simulations, while rest from physical experiments. We remark that, especially for numerical examples, we do not use model knowledge to initialize the trajectories exactly onto the specific SSM, but we emulate realistic experimental procedures that yield trajectories rapidly converging to SSMs.

To express trajectory reconstruction errors, we use the relative root-mean-squared error $rRMSE$, which, for a dataset $\{x_j\}_{j=1}^M \in \mathbb{R}^n$ and its reconstruction $\{\hat{x}_j\}_{j=1}^M$, is defined as

$$rRMSE = \frac{1}{M\|\underline{x}\|} \sum_{j=1}^{M} \|x_j - \hat{x}_j\|. \tag{10.1}$$

Here $\underline{x}$ is a relevant normalization vector, which is usually considered as the datapoint x_j with the maximum norm in the dataset.

When validating the reduced dynamics for a given testing trajectory, we integrate or iterate the reduced-order model from the same initial condition and compare the results.

10.1 A CLAMPED-CLAMPED VON KARMAN BEAM

We consider a finite element discretization of a von Kármán beam with clamped-clamped boundary conditions [173], shown in Fig. 10.1(a). In contrast to the classic Euler-Bernoulli beam [194], the von Kármán model captures moderate deformations by including a nonlinear, quadratic term in the kinematics. No body forces are present in our case and the straight equilibrium configuration is asymptotically stable. We aim to learn from trajectory data the slowest 2-dim. SSM of the system. To do so, we initialize trajectories from beam deflections arising from static loading at the midpoint, cf. Fig. 10.1(a). Due to the high spectral gap among the first (lowest damped) mode and rest as well as to the prescribed initial conditions, the trajectories converge quickly to the slowest 2-dim. SSM of the beam.

The beam has length 1 [m], thickness 1 [mm], Young's modulus 70 [GPa], density 2700 [kg/m^3], Poisson's ratio 0.3 and material damping modulus equal to 20 [MPa·s]. The discretization is performed using elements with cubic shape functions for the transverse deflection and linear shape functions for the axial displacement. We use 16 elements, as in Fig. 10.1(a), which shows convergence in static and dynamic simulations in the range of interest over uniform grid refinements. The finite element model has 45 degrees of freedom in total, including transverse displacement, axial ones and rotations. The slowest eigenvalue is $-0.1545 + i32.885$, whose spectral gap (ratio between the real parts) with the second slowest one is 7.6. Hence, the decay along higher modes is more than seven times faster with respect to that of the slowest mode. The two trajectories in Fig. 10.1(b) are initialized on the static deflections arising from downwards loading at the midpoint of magnitude 2 (training set) and 1.75 (testing test) [N], and integrated for 30 [s]. From both trajectories, we excluded the first second, in which we note the convergence towards the SSM and we set the sampling time to be 2.5 [ms].

We identify reduced-order models considering two different observables. The first observable set is the full phase space of the beam ("PS case"), while the second is the delay-embedding space for the (scalar) displacement at the midpoint u ("DE case"). The embedding space has the minimum dimensions (4 delays) according to Takens theorem, so that the embedding coordinates are $y[k] = (u[k], u[k+1], u[k+2], u[k+3], u[k+4])$. The parametrization for the PS case is set to

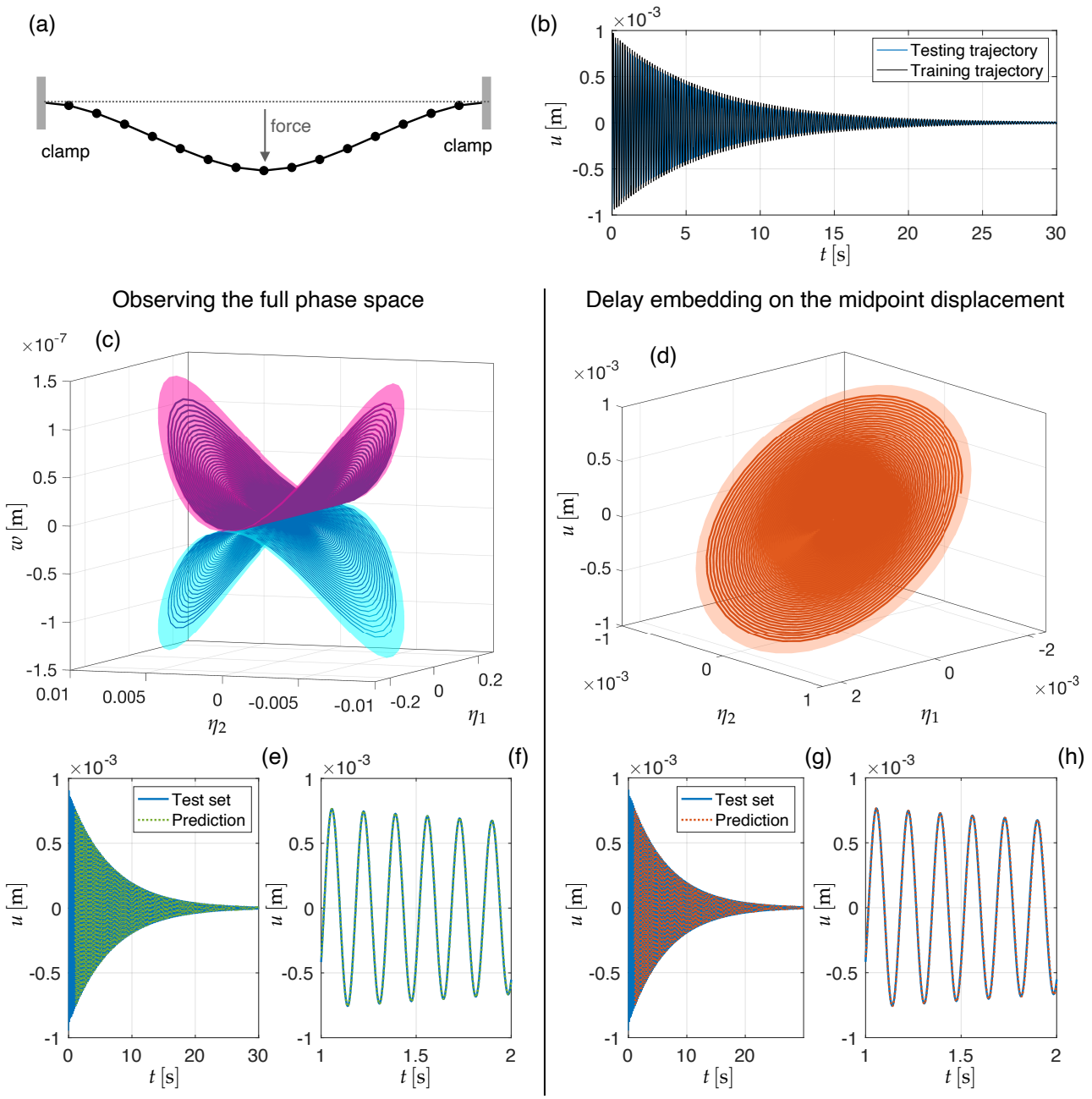

Figure 10.1: The picture in (a) illustrates the clamped-clamped von Kármán beam in its deformed configuration from point loading in the middle. This type of initial conditions are considered for the trajectories in plot (b), which are used for testing and training the reduced-order model. Plot (c) and (d) show the embedded SSMs in the phase space and in the delay-embedding space of the midpoint displacement, respectively. Plot (c) illustrates the SSM parametrizations for the axial displacements of the left (purple) and right (light blue) adjacent nodes to the middle one. Plots (e-h) show the models prediction on the testing dataset.

be $O(4)$ with V deduced from the model. Indeed, if v is the complex eigenvector of the slowest 2-dim. eigenspace, the orthonormal representation in V_0 can be deduced from the Gram-Schmidt orthogonalization process as

$$V_0 = [v_1\ v_2]\,, \quad v_1 = \frac{\mathrm{Re}(v)}{\|\mathrm{Re}(v)\|}, \quad v_2' = \left(I - v_1 v_1^\top\right)\mathrm{Im}(v), \quad v_2 = \frac{v_2'}{\|v_2'\|}. \tag{10.2}$$

For the DE case, the parametrization is assumed to be linear only, so that our parametrization and coordinate charts are given by the PCA of the embedded training trajectory. The SSM representations and the testing trajectory are shown in Fig. 10.1(c,d) with respect to the parametrizing coordinates (η_1, η_2). Fig. 10.1(c) shows the two SSM representations for the axial displacements w of the two nodes adjacent to the midpoint.

The reduced dynamics is set to be $O(7)$ for the PS and DE cases. For the PS case, the SSM-reduced normal form is

$$\begin{aligned} \dot{\rho} = &\quad -0.1545\rho + 0.075534\rho^3 - 1.6778\rho^5 + 5.1602\rho^7 = -c(\rho)\rho, \\ \dot{\theta} = &\quad +32.8854 + 30.7741\rho^2 - 32.6344\rho^4 + 29.2335\rho^6 = \omega(\rho), \end{aligned} \tag{10.3}$$

where the amplitude-dependent functions c and ω represent the instantaneous damping and frequency, respectively. For the observables made up by the full coordinates in the phase space, we can prescribe the linear part $Df_r(0)$ of the reduced dynamics in the coordinates $\eta = (\eta_1, \eta_2)$. By denoting λ the eigenvalue of the slowest 2-dim. eigenspace and its complex conjugated $\bar{\lambda}$, the eigenvectors of the linearization at the origin of the dynamics in our reduced coordinates are the columns of the matrix B (cf. section 9.2), which can be expressed as

$$B = V_0^\top \left[v \; \bar{v} \right], \quad Df_r(0) = B \begin{bmatrix} \lambda & 0 \\ 0 & \bar{\lambda} \end{bmatrix} B^{-1} \tag{10.4}$$

Both reduced order models capture well the dynamics of the testing trajectories, as seen in Fig. 10.1(e-h), with less than 2 % relative root-mean-squared error. The normalization considered here is the maximum norm datapoint of the signals. Furthermore, the reduced dynamics characteristics in the PS case show convergence as we increase the order of accuracy, see Fig. 10.2(a), and there is also very good agreement between the dynamics reconstructed from different observables. We choose $O(7)$ as this order features the lowest testing error.

Figure 10.2(c,d) shows the performances of DMD [58] in reconstructing the midpoint displacement signal for different hyperparameters [58]. The number of delays refers to dimension of the delay embedding space, while the rank is the number of DMD modes retained for the reduced-order model. We note that, in this case of nonlinear decaying vibrations, DMD fails in capturing phase and amplitude evolutions.

As discussed in section 9.3, our nonlinear data-driven reduced-order models can be used to predict periodic forced responses. For a given value of forcing in Eq. (9.22), we use the expression in (9.25) to compute forced responses. We validate our results with the analytical forced response [22] computed via `SSMTool` [193], which analytically computes the non-autonomous SSM for the beam model we used to generate the datasets. These analytical frequency sweeps are shown in Fig. 10.2(e,f) with blue lines for the forcing applied on the beam midpoint with 0.15, 0.35 and 0.6 [mN] and an $O(7)$ analytical model. To compare data-driven predictions with their analytical counterpart, we need to calibrate the forcing value feeding the data-driven normal form dynamics, which is a common fact in control and testing practices [177]. Here, we perform this calibration assuming to know that the maximal amplitude response for the full-order model forcing amplitude $\|\hat{F}^{ext}\|$ occurs at frequency $\hat{\Omega}$. Maximal amplitude responses occur when $\psi = \pi/2$ [23]. Hence if we know the frequency $\hat{\Omega}$ at which this response takes place, then we can get $\hat{\rho}$ solving $\omega(\rho) = \hat{\Omega}$, so that $f_R^{ext} = c(\hat{\rho})\hat{\rho}$. Since the normal form forcing is a pure projection in our approximation, then $\|F^{ext}\|$ and f_R^{ext} are proportional, and their ratio is obtained from this calibration process. The forced responses from the data-driven model shown in Fig. 10.2(e,f) have been calibrated on the sweep at 0.15 [mN] and they matches closely the analytical predictions of `SSMTool` and those obtained with numerical integration.

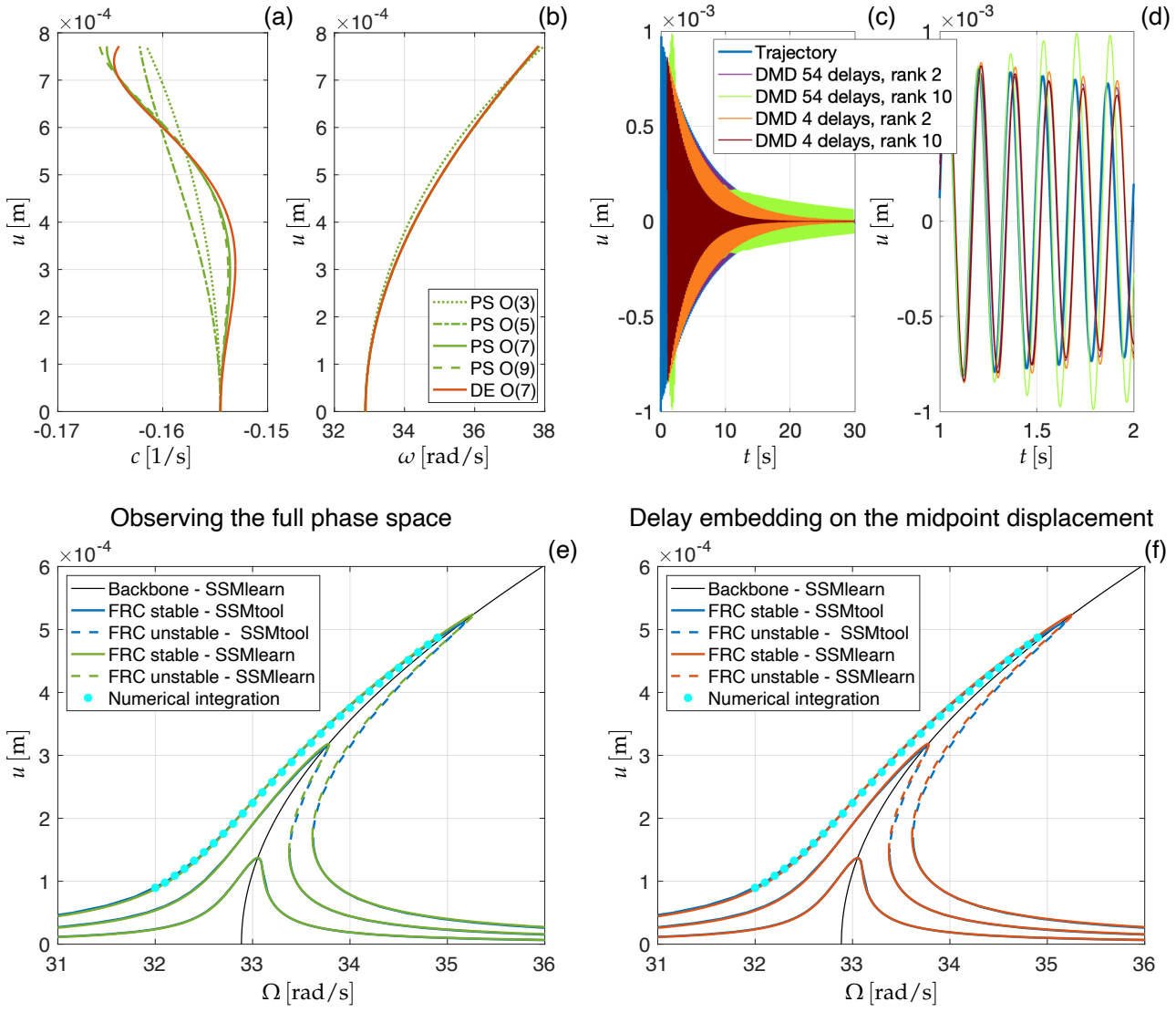

Figure 10.2: The backbone curves in plot (a,b) show minimal model sensitivity for the phase space (PS) reduced-order model. The backbones of the delay embedding reduced-order model (DE) are also in good accordance. Plots (c,d) show predictions using DMD for several ranks and delays. Plots (e,f) validate the reduced-order models using forced frequency responses that are compared with the analytical counterpart of `SSMLearn`, `SSMTool` [193], and with numerical integration.

10.2 VORTEX SHEDDING IN THE WAKE OF A CYLINDER

In this section, we investigate the classic, fluid dynamics problem of vortex shedding behind a cylinder [195, 196]. We look at the velocity and pressure fields over a planar, open fluid domain with a hole of diameter d, representing the cylinder section as shown in Fig. 10.3(a). The boundary conditions are no-slip on the circular inner boundary, standard outflow on the outer boundary at the right side and fixed horizontal velocity $(u_{in}, 0)$ on the three remaining sides [197]. The Reynolds number for this problem is defined as $Re = u_{in}d/\nu$, where ν is the kinematic viscosity of the fluid. The planar approximation for the flow is valid up to Reynolds number $Re < 188$, over which three-dimensional instabilities occur [197, 198].

For low Reynolds numbers, the flow features a stable steady solution, which loses stability at $Re \approx 48$ via Hopf bifurcation [4]. After this critical value, the steady solution is unstable and there exists a stable limit cycle, which corresponds to the observed regime of vortex shedding in

the wake [195]. Studies [196, 197, 199] report that a 2-dim. unstable manifold in the phase space of the Navier-Stokes equations connects the steady solution to the limit cycle for $48 < Re < 188$. Several approaches have been used to construct reduced-order models based on the unstable manifold reduction [147], the classic analytic center manifold reduction [200] or Principal Orthogonal Decomposition (POD) coupled with Galerkin projections [199], machine-learning based techniques exploiting sparse identification [196, 201] and neural networks [54, 202].

Here we look at the performances of `SSMLearn` in learning the unstable manifold and its dynamics from trajectory data. In contrast with available approaches that often restrict the observables to peculiar directions of flow only (e.g., POD modes) [54, 196, 199], our observables space coincides with the full phase space of the discretized Navier-Stokes equations used to numerically simulate the problem.

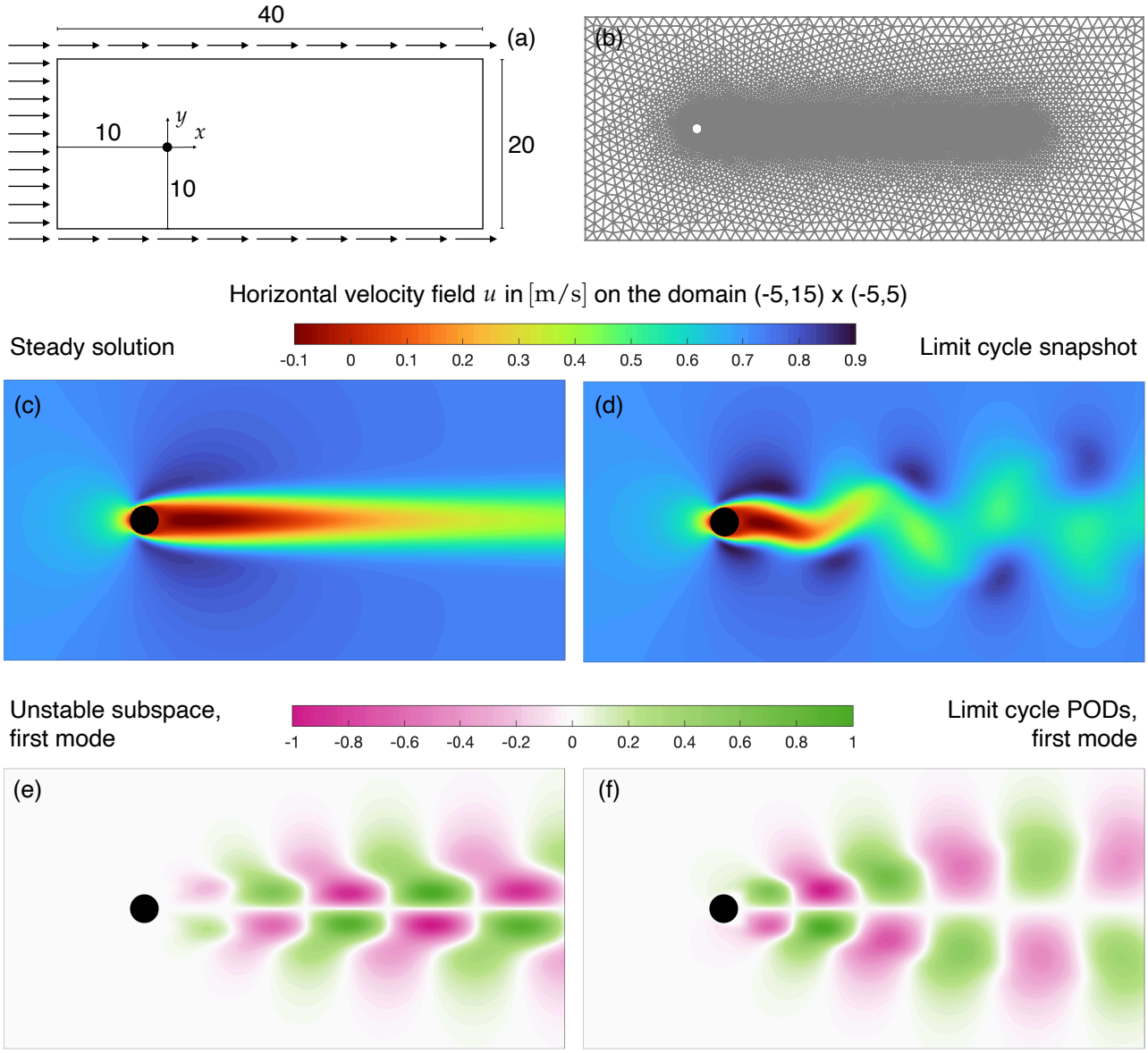

Figure 10.3: Plots (a,b) illustrate dimensions, mesh and boundary conditions for the CFD simulations. Plots (c,d) show snapshots of horizontal velocity fields of the unstable steady solution and of the stable limit cycle, respectively. Plots (e,f) illustrate the horizontal velocity fields for the first mode of the unstable subspace of the steady solution and for the first mode of the POD analysis of the limit cycle, respectively.

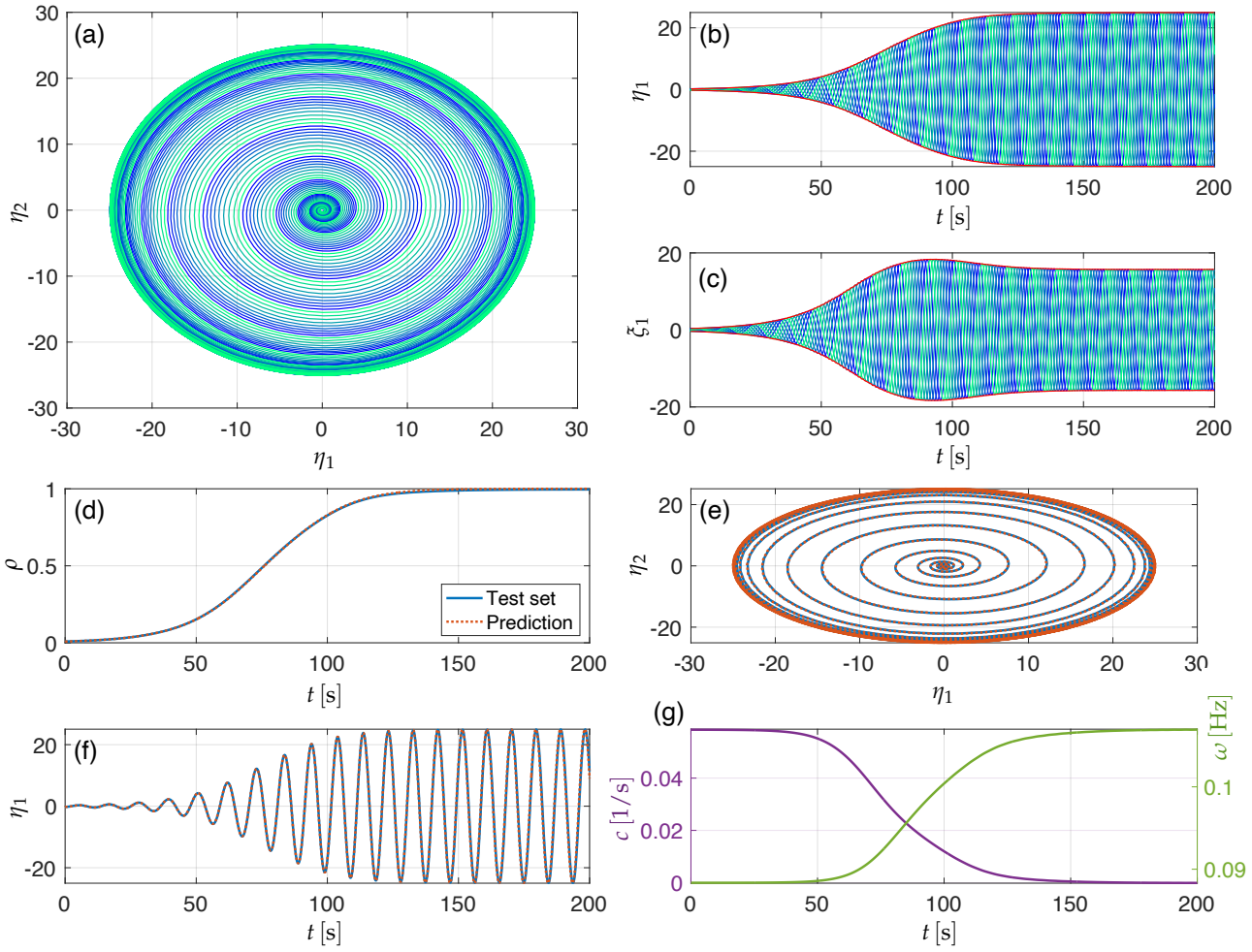

Figure 10.4: Plot (a) shows the projection of the 9 simulations on the first 2 POD modes of the limit cycle (η_1, η_2). Plot (b,c) illustrate the time evolution of the projection on the first POD mode of the limit cycle η_1 and of that on the first unstable mode of the steady solution ξ_1. The red lines depict the signals envelope evolution. Plot (d,e,f) compare the predictions of the data-driven model to the testing trajectory in terms of normal form amplitude (d) and projections on the first 2 POD modes of the limit cycle (e,f). Plot (g) shows the time evolutions of the normal form vector field.

The dimensions of the domain in [m] are shown in 10.3(a) and the other system parameters are $d = 1$ [m], $\nu = 0.01$ [m^2/s] and $u_{in} = 0.7$ [m/s], resulting in $Re = 70$. We simulate the flow using the Python-based computational platform FEniCS [203]. The mesh, made up by triangular elements of the Lagrange family, is visualized in 10.3(b) and the resulting discretized model with phase space $x = (u, v, p)$ has dimension $n = 76876$, where u is the horizontal velocity component, v is the vertical ones and p is the pressure. The governing ordinary differential equation $\dot{x} = f(x)$ is integrated using a modified version of Chorin's method [204] with a time stepping of 0.02 [s]. We compute the steady solution x_{steady}, cf. 10.3(c), and we perform a linear stability analysis [205] via Krylov-Arnoldi iterations [206], where the first mode of the 2-dim. unstable subspace is illustrated in 10.3(e). We also characterize the limit cycle, shown with a horizontal velocity snapshot in 10.3(d), and perform the POD [13] using the snapshot method [178]. We compute these POD modes from a dataset of points lying on the limit cycle, hence we do not require manipulation of the Navier-Stokes equations.

Organizing these l datapoints in a matrix $X = [x_1\ x_2,\ \ldots\ x_j,\ \ldots,\ x_l] \in \mathbb{R}^{n\times l}$, one first computes the time averaged flow x_{mean}, which can be estimated as

$$x_{mean} = \sum_{j=1}^{l} x_j, \tag{10.5}$$

then the POD modes are computed from the singular value decomposition [141] of the matrix $X - x_{mean}$, i.e., $X - x_{mean} = U_X S_X V_X^\top$. The POD modes are the orthonormal columns of the matrix U_X, which are ranked according to the singular values collected in the corresponding diagonal entries of S. The leading POD modes are those characterized by the largest singular values, the first of which is depicted in 10.3(f). For the vortex shedding, the two leading POD modes capture most the energy content of the flow on the limit cycle [199].

We then run 9 trajectories with time length 200 [s] whose initial conditions are small perturbations from the steady solution along its unstable directions, namely

$$x(0) = a w_1^{(u)} \cos(\psi) + a w_2^{(u)} \sin(\psi), \tag{10.6}$$

where $w_1^{(u)}$, $w_2^{(u)}$ is a real representation for the unstable subspace, $a = 0.2$ and ψ attains 9 uniformly spaced values in the interval $[0, 2\pi)$.

We now inspect these trajectories by projecting them onto principal directions. We call (ξ_1, ξ_2) the coordinates obtained as projections onto the unstable subspace of the steady solution (being the tangent space of the unstable manifold at the origin), while (η_1, η_2) are those obtained as as projections onto the 2 leading POD modes of the limit cycle. The simulated trajectories are shown in Fig 10.4(a-c) in terms of these coordinates and their time evolution. Note that this trajectories are centered around the unstable steady solution, here corresponding to the origin. In particular, plots (b,c) show the time evolution of η_1 and ξ_1, highlighting in red the envelope evolution. It can be noted that the envelope of the projection to the unstable subspace ξ_1 displays a fold in its time evolution, which implies trajectory crossing in the space (ξ_1, ξ_2). Hence, (ξ_1, ξ_2) cannot be used for the manifold parametrization, as seen in Fig. 10.5(b). On the other hand, the coordinates (η_1, η_2) obtained as projections onto the 2 leading POD modes of the limit cycle are good candidates for parametrizing the manifold, as their reduced phase space does not show trajectory crossing. Therefore, we consider the 2 leading PODs as columns for V_0 and the resulting projections (η_1, η_2) as reduced coordinates. We first proceed with the identification of the dynamics, considering 8 training trajectories and one for testing.

To capture the nonlinear dynamics with acceptable accuracy, we need to push the normal form dynamics up to polynomial order 9, resulting in

$$\begin{aligned} \dot{\rho} = &\ 0.05852\rho - 0.14984\rho^3 + 0.21878\rho^5 - 0.18226\rho^7 + 0.054358\rho^9 = c(\rho)\rho, \\ \dot{\theta} = &\ 0.55514 + 0.055636\rho^2 + 0.27973\rho^4 - 0.45144\rho^6 + 0.23452\rho^8 = \omega(\rho). \end{aligned} \tag{10.7}$$

Lower-order approximations are less accurate, including the classic cubic normal form [199]. Indeed, the latter results in a 9.57 % root-mean-squared error normalized with respect to the limit cycle amplitude, while (10.7) improves this error to 2.52 %. We clearly see the accuracy of (10.7) in Fig. 10.4(d-f), while plot (g) of this figure shows the time evolution of the vector field in (10.7). Both quantities $c(\rho)$ and $\omega(\rho)$ start from their linearized limit and settle to the limit cycle ones, being this latter zero for the amplitude dynamics.

Not only does this model show strong nonlinearities in the dynamics in (10.7), but also it does so for the phase space geometry of the unstable manifold. Indeed, to push the parametrization accuracy to less than 1 % in terms of root-mean-squared error, one needs polynomial order 18 for the parametrization model, see Fig. 10.5(a). The overall data-driven reduced-order model has an accuracy

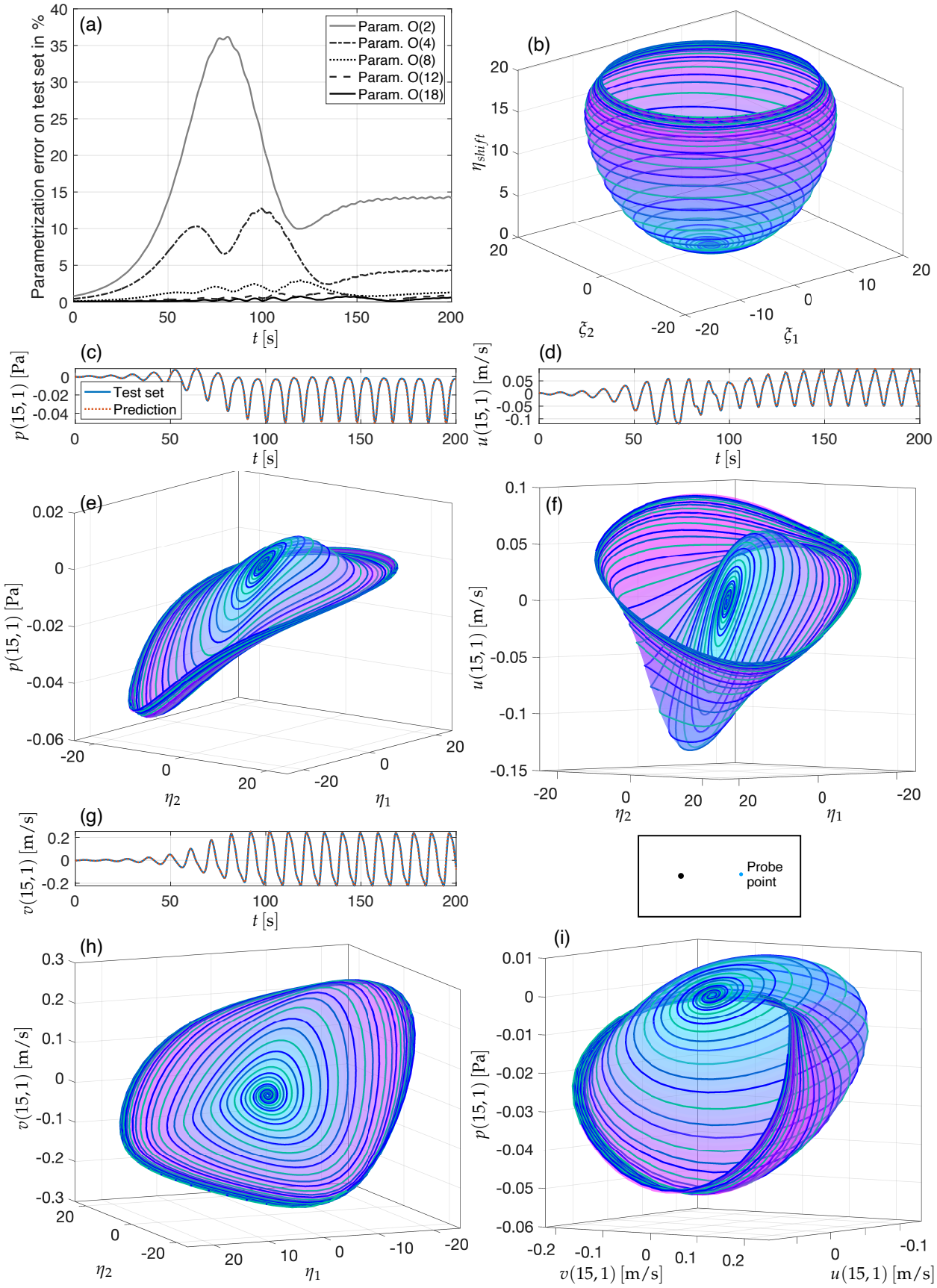

Figure 10.5: (Caption next page.)

Figure 10.5: Plot (a) shows the error on the testing set for parametrization models of different order. Plot (b) depicts the unstable manifold and some training trajectories in terms of the projections with respect to the unstable subspace of the steady solution and that with respect to the shift mode. Plots (c,e,g) illustrate the data-driven reduced order model performances in predicting the time evolutions of velocities and pressures at the probe point $(15, 1)$. The same quantities are shown in plots (d,f,h,i), where lines are different training trajectories, while surfaces represent the unstable manifold.

of 2.78 % on the testing trajectory. Figure 10.5(c-i) shows the model performances on reconstructing the evolution and the unstable manifold representation for the velocities and the pressure of the wake probe point at $(15, 1)$, where the aforementioned strong nonlinearity can be visually noted. In contrast, plot (b) in Fig. 10.5 shows the fold of the unstable manifold in the space of the projections onto the unstable subspace and the shift mode [199], which quantifies the change from the steady solution to the mean flow on the limit cycle and it is defined as

$$V'_{shift} = \left(I - V_0 V_0^\top\right)(x_{mean} - x_{steady}), \quad V_{shift} = V'_{shift}/\|V'_{shift}\|, \quad \eta_{shift} = V_{shift}^\top x. \tag{10.8}$$

Remark 10.1. It appears that `SSMLearn` is fitting the classic Stuart-Landau model for nonlinear oscillations near the onset of instability [199]. This model, originally proposed by Landau [207] to explain transition to turbulence, was linked to hydrodynamics [208–210] and to center-manifold reduction [211]. Far from bifurcations, this model can only be theoretically justified via SSM theory, and also it may be necessary to increase to order of approximation for an accurate model, as we show with our computations. Moreover, the Stuart-Landau model breaks up in case of resonances, while our approach can handle resonances by increasing the dimension of the SSM.

10.3 Resonance decay in the Brake-Reuss beam

The Brake-Reuß beam is a benchmark system in the study of the dynamics of jointed structures [36, 37, 212]. In this context, the construction of predictive reduced-order models is still a challenge, either from full-order finite element models or from data. The Brake-Reuß beam consists of two beams assembled with a lap joint, as shown in Fig. 10.6(a). The dataset for this example consists of measurements of a resonance decay test [44]. After a resonant periodic orbit is found in phase quadrature with the shaker forcing, see Fig. 10.6(c), the shaker is released from the structure, which settles down to its equilibrium. Therefore, provided that the forcing is not too large, the transient will follow closely the SSM that resonates with the forcing frequency.

The available data comprises a single resonance decay test on the slowest structural mode and the observables are the measurement from an accelerometer mounted in the correspondence of the shaker and the displacement field of the bottom side of the beam measured using digital image correlation. The latter dataset, consisting of 206 points over the 72 [cm] of beam length, has a limited time range due to limitations in camera memory. The first instances of the measured displacement field are depicted in Fig. 10.6(b).

Our goal in this example is to construct a nonlinear reduced-order model using displacement data and validate it using acceleration one. The time signals have been truncated after shaker release to eliminate the influence of disturbances from non-perfect detachment. Nevertheless, high frequency contributions decay rapidly and the transient settles along the slowest SSM. To diversify the data, we augment the displacement with 4 delayed measurements, so that the observable phase space has dimensionality 1030. The SSM is well-described by a plane in this space, but the reduced-dynamics

reveals itself to be highly nonlinear. For adequate accuracy, the normal form indeed needs terms up to $O(11)$ to unfold the dynamics, and it reads

$$\begin{aligned}\dot{\rho} = &\quad -0.82551\rho - 16.0435\rho^3 + 166.2684\rho^5 - 1421.2731\rho^7 + 5314.2153\rho^9 - 7138.3531\rho^{11},\\ \dot{\theta} = &\quad +504.3949 - 46.1553\rho^2 + 350.3187\rho^4 + 412.8726\rho^6 - 8468.2447\rho^8 + 16975.2863\rho^{10}.\end{aligned} \tag{10.9}$$

The model can be used to approximate the beam kinetic energy as

$$K = \frac{1}{2}\frac{M}{N}\sum_{j=1}^{N} \dot{u}_j^2(t), \tag{10.10}$$

where $N = 206$ is the number of DIC measurement locations and $M = 1.796$ [kg] is the total beam mass. As discussed in [37], the kinetic energy amplitude is a good proxy for the instantaneous decay properties, i.e., the instantaneous damping ratio and frequency, shown in Fig. 10.6(d,e), respectively. The instantaneous damping ratio is defined from the normal form dynamics as $\xi(\rho) = -c(\rho)/\omega(\rho)$, expressed in percentage. The damping is subject to consistent variation, while the frequency here shows an interesting softening-hardening trend. Figure 10.6(f) highlights changes in the mode shape for increasing kinetic energy, which, in contrast, does not show significant nonlinear behavior. Here

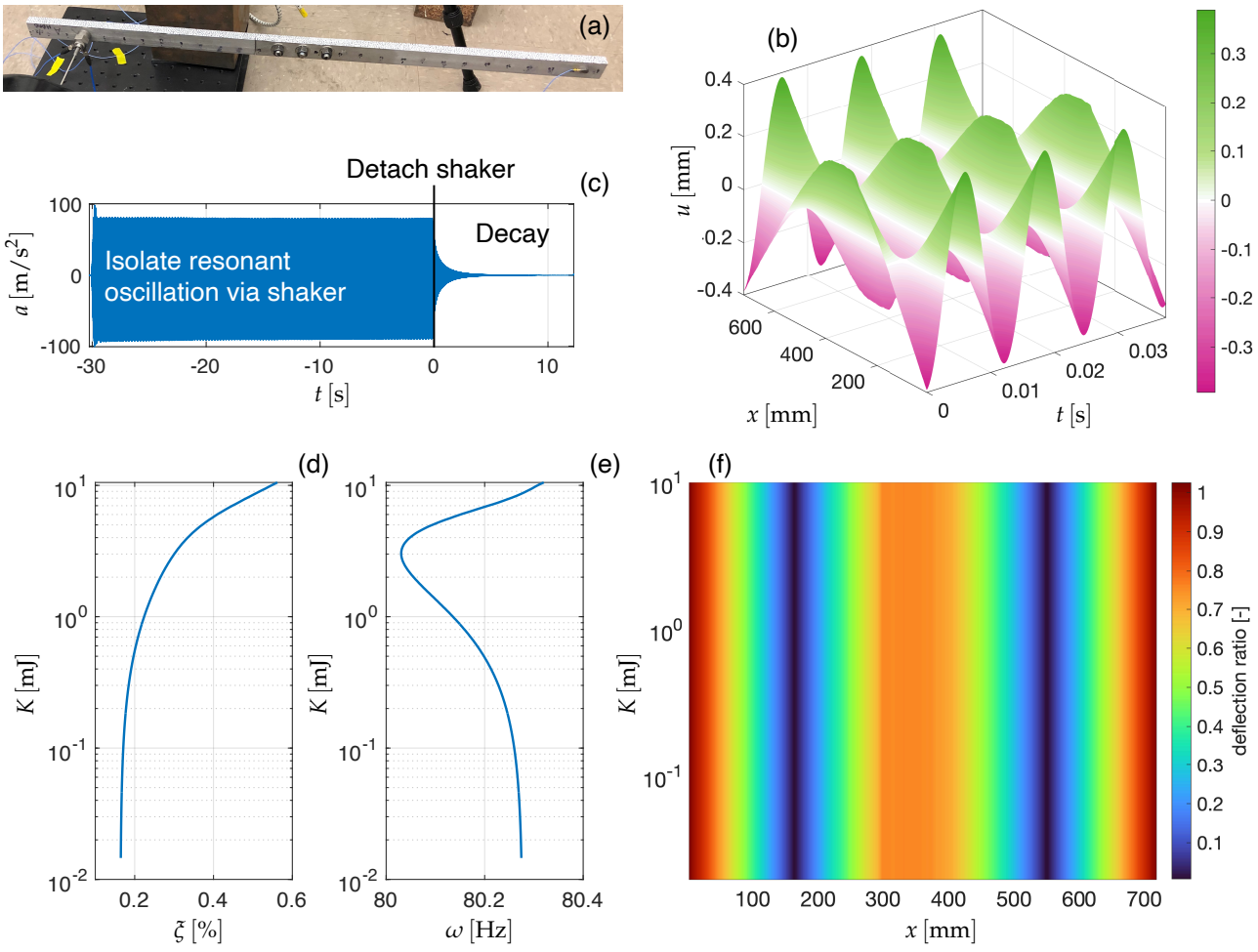

Figure 10.6: The picture in (a) illustrates the testing setup for the Brake-Reuß beam, while plots (b) and (c) show the measured displacement and accelerations data respectively. Plots (c-i) depict the results obtained by constructing a reduced-order model on displacements data. The backbone curves in (d,e) shows the instantaneous characteristics of the beam with respect to its kinetic energy, while (f) verifies changes in the modal shape.

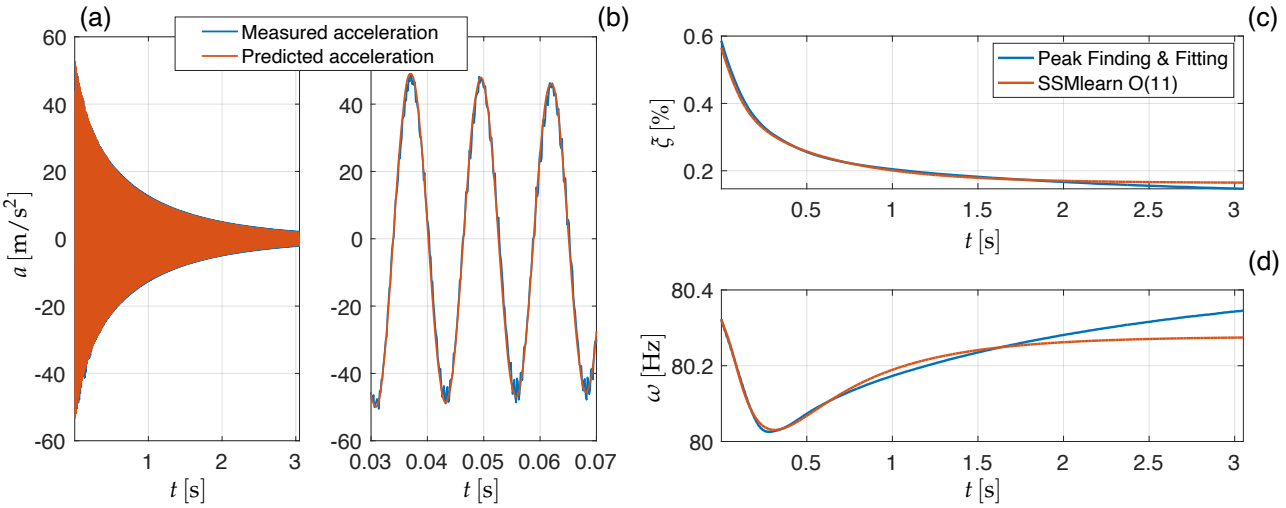

Figure 10.7: Plots (a,b) validate the predictions of accelerations from the model trained on displacement data. Plots (c,d) compares the instantaneous properties of the data-driven model with respect to those measured with the Peak Fitting and Finding method [41] on the acceleration signal.

the deflection ratio is defined as the amplitude of the displacement of every location divided by the amplitude displacement of the left beam tip. The areas close to nodal points, whose deflections approach zero, appear as vertical blue/black areas in Fig. 10.6(f).

Our displacement-based model is validated on the data measured by the accelerometer located at 77 [mm] from the left end of the beam, as shown in Fig. 10.6(a). Indeed, this signal is reconstructed from the model by interpolating in the grid to obtain the accelerometer location and differentiating in time. The relative root-mean-squared error amounts to 1.3% and the model also denoises the signal, cf. Fig. 10.7(a,b). A further validation in Fig. 10.7(c,d) compares the instantaneous decay characteristics obtained using the data-driven model with those extracted using the signal processing technique Peak Finding and Fitting [41]. There is close agreement among these curves, especially in the strongly nonlinear oscillation regime.

10.4 IMPACTS ON AN INTERNALLY RESONANT TESTER STRUCTURE

Our final example is the resonant tester shown in Fig. 10.8(a). It consists of two beam-like parts, where the external beam is C-shaped and clamped to the ground on one side, while the internal beam is jointed to the external one via bolts. These latter should be principal source of system nonlinearities. Additionally, there is a linear spring located on the external beam tip. The system possesses an internal $1:2$ resonance between its slowest modes, whose frequencies indeed estimated at 122.39 [Hz] and 243.44 [Hz]. We consider transverse vibrations occurring along the out of plane direction and the available observable is the velocity of the inner beam tip, measured via laser scanner vibrometry.

The dataset consists of 12 different trajectories generated by hammer impacts from 3 different locations (4 trajectories per location), cf. Fig. 10.8(d). We label these trajectories as (j, l) where j refers to the location and l to the test number. Time-frequency analyses of the velocity signals, some of which are reported in Fig. 10.8(b,c), show that only the two slowest frequencies are present in the signal, so that the time responses can be well-approximated by the slowest 4D SSM of the system. The impact locations, the hammer tip and the forcing amounts were selected to achieve a sufficient

The design and the experiments on this system were carried out by Haocheng Yang and Melih Eriten from Eriten Research Group of UW-Madison, USA.

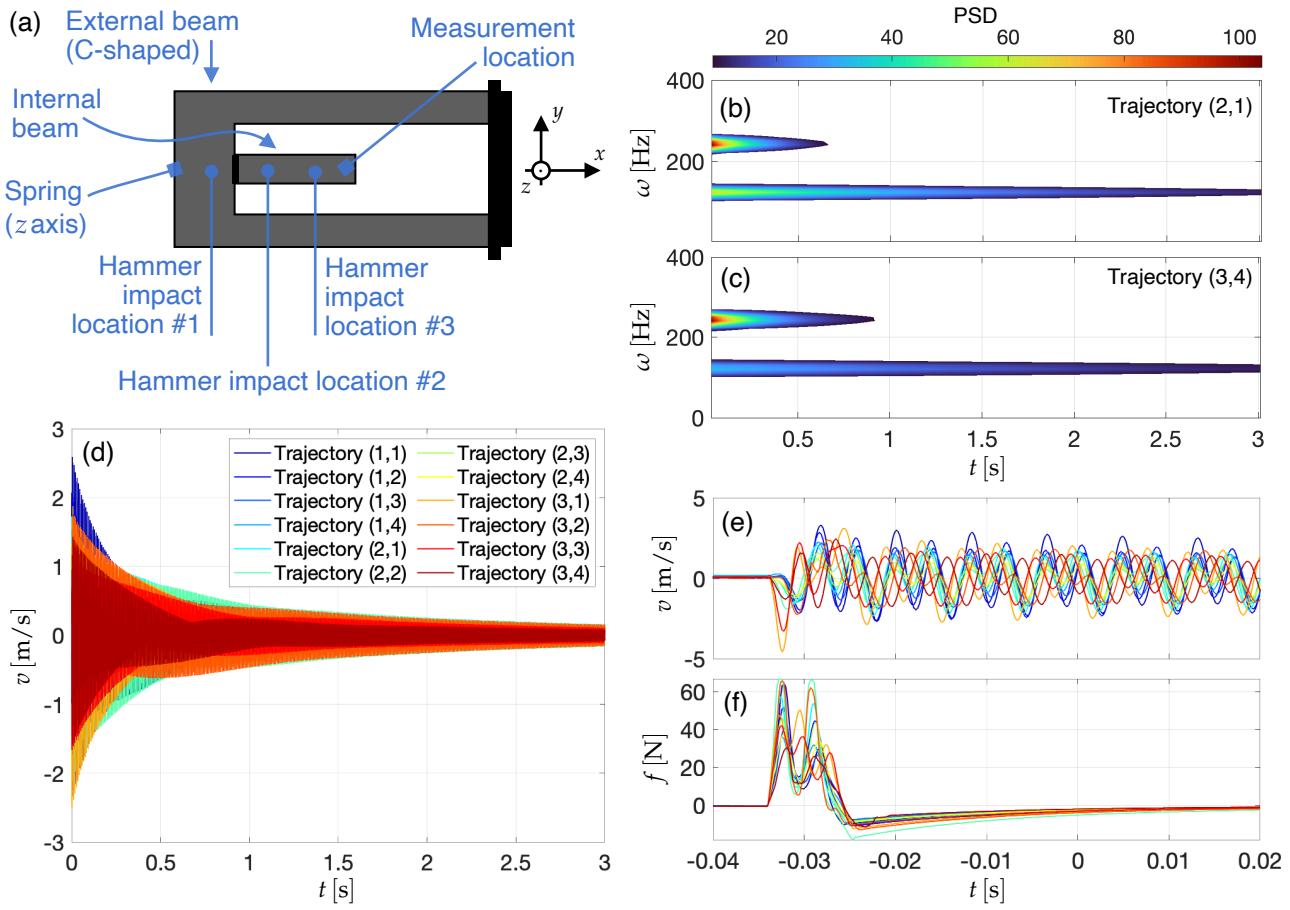

Figure 10.8: The picture in (a) sketches the system configuration. Plots (b,c) show the power spectral density computed via short-time Fourier transform (spectrogram) for two trajectories. These latter are also shown in plots (d,e), while (f) illustrates the time series of the hammer force.

trajectory diversity in the dataset without exciting further structural modes. The velocity time histories are shown in Fig. 10.8(d,e), whereas Fig. 10.8(f) the hammer force signals. For constructing a reduced order model, we truncate the velocity signals starting from some instances after the hammer impact, which is the 0 time reported in 10.8(c,d). We use 10 trajectories for training and leave 2 trajectories for testing.

The four-dimensional SSM is embedded in a 94 dimensional delay-embedding space. This amount of delays helps in unfolding dynamics complexity given this scalar measurement. Indeed, for the minimal embedding dimensions (being 9 for a four-dimensional manifold), even an arbitrary reduced dynamics in the style of Eq. (9.7) optimally identified via ridge regression fails in reconstructing trajectories. Hence, we augment the embedding space so that, for the sampling time 0.1953 [ms], each embedding vector captures approximately two cycles of the slowest oscillation. The result of our identification remains robust if one considers more embedding dimensions. A linear approximation to the embedded SSM has a good accuracy and generates the reduced-coordinates in Fig. 10.9(a).

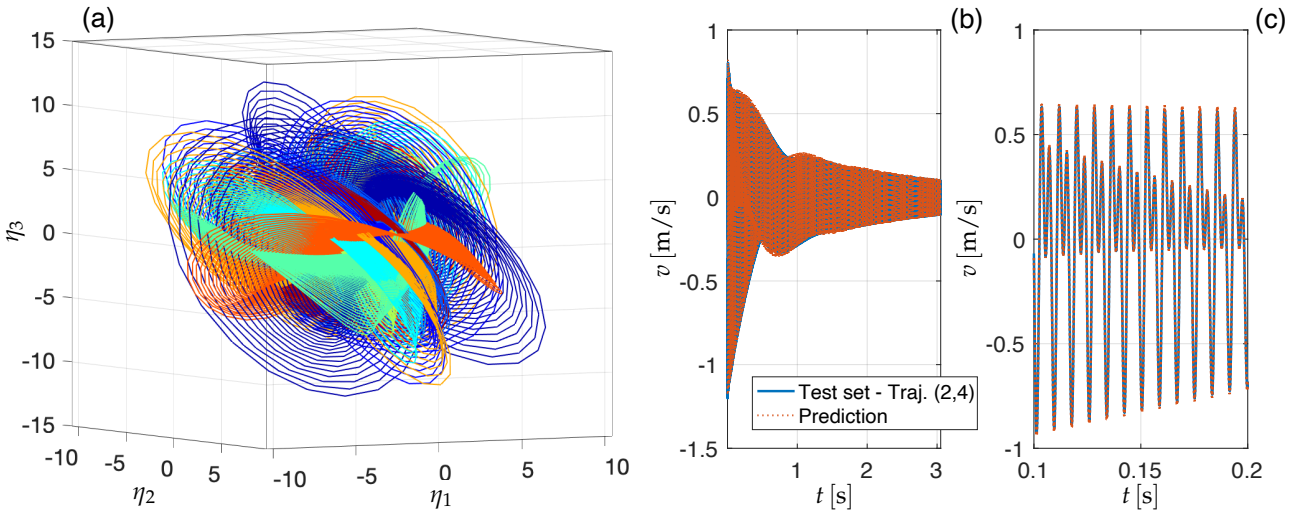

Figure 10.9: Plot (a) depicts 3 of the 4 reduced coordinates parametrizing the SSM, while plots (b,c) illustrate the data-driven reduced-order model performances in reconstructing a testing trajectory.

The automated normal form algorithm, after estimating linearized eigenvalues, identifies a resonance among them. Defining $\psi = \theta_2 - \theta_1$, we obtain the normal form dynamics at $O(4)$ as

$$\begin{aligned}
\dot{\rho}_1 = \; & -0.4129\rho_1 - 13.1749\rho_1^3 + 1.9348\rho_1\rho_2^2 + \mathrm{Re}((0.31585 - 0.20596i)\rho_2\rho_1 e^{i\psi}) + \\
& + \mathrm{Re}((31.2389 - 1.51249i)\rho_1^3\rho_2 e^{-i\psi}) + \mathrm{Re}((-28.0245 + 2.82748i)\rho_1^3\rho_2^2 e^{i\psi}) + \\
& + \mathrm{Re}((13.4184 - 0.718767i)\rho_2^3\rho_1 e^{i\psi}) = -c_1(\rho_1, \rho_2, \psi)\rho_1, \\
\dot{\rho}_2 = \; & -2.945\rho_2 - 21.2472\rho_1^2\rho_2 - 15.8484\rho_2^3 + \mathrm{Re}((0.47843 - 2.0623i)\rho_1^2 e^{-i\psi}) + \\
& + \mathrm{Re}((5.4655 + 3.9956i)\rho_1^4 e^{-i\psi}) + \mathrm{Re}((5.60777 + 13.9982i)\rho_1^2\rho_2^2 e^{-i\psi}) + \\
& + \mathrm{Re}((20.8319 - 29.8619i)\rho_1^2\rho_2^2 e^{i\psi}) = -c_2(\rho_1, \rho_2, \psi)\rho_2,
\end{aligned} \tag{10.11}$$

for the amplitudes, while for the phases

$$\begin{aligned}
\rho_1\dot{\theta}_1 = \; & +768.9692\rho_1 - 43.3409\rho_1^3 - 3.7108\rho_2^2\rho_1 + \mathrm{Im}((0.31585 - 0.20596i)\rho_2\rho_1 e^{i\psi}) + \\
& + \mathrm{Im}((31.2389 - 1.51249i)\rho_1^3\rho_2 e^{-i\psi}) + \mathrm{Im}((-28.0245 + 2.82748i)\rho_1^3\rho_2 e^{i\psi}) + \\
& + \mathrm{Im}((13.4184 - 0.718767i)\rho_1\rho_2^3 e^{i\psi}) = \omega_1(\rho_1, \rho_2, \psi)\rho_1, \\
\rho_2\dot{\theta}_2 = \; & +1529.5972\rho_2 - 25.3906\rho_1^2\rho_2 - 32.2919\rho_2^3 + \mathrm{Im}((0.47843 - 2.0623i)\rho_1^2\rho_2 e^{-i\psi}) + \\
& + \mathrm{Im}((5.4655 + 3.9956i)\rho_1^4\rho_2 e^{-i\psi})\mathrm{Im}((5.60777 + 13.9982i)\rho_1^2\rho_2^2 e^{-i\psi}) + \\
& + \mathrm{Im}((20.8319 - 29.8619i)\rho_1^2\rho_2^2 e^{i\psi}) = \omega_2(\rho_1, \rho_2, \psi)\rho_2.
\end{aligned} \tag{10.12}$$

In comparison with the $1:2$ internally resonant case reported in Table 9.1, Eqs. (10.11,10.12) feature additional resonant terms at quartic order, which improves model performance with respect to the cubic approximation. The data-driven model reconstructs both testing trajectories with less than 2 % relative root-mean-squared error, cf. Fig. 10.9(b,c). As anticipated in section 9.3, the normal form dynamics allows to perform slow-fast mode decomposition. The decay of the slow mode amplitude ρ_1 and that of the fast one ρ_2 are shown in Fig. 10.10(a). Due to modal interactions, these decays are not monotonically decreasing. From this plot, we notice a great diversity of decays depending on the impact location, and location 3 the one characterized by the highest amplitudes variability. Figure 10.10(b) shows the energy repartition among the modes for the third impact location. This repartition is defined as the instantaneous ratio between the amplitude of a mode and the amplitudes sum. Clearly, the slow mode tends to accumulate the energy over time, while the fast mode dissipates it quickly. However, the trends are not monotonic, showing simultaneous and opposite changes in growth/decay rates, which implies that the faster mode is absorbing energy from the slow one. This behavior can also be inferred by the instantaneous properties illustrated

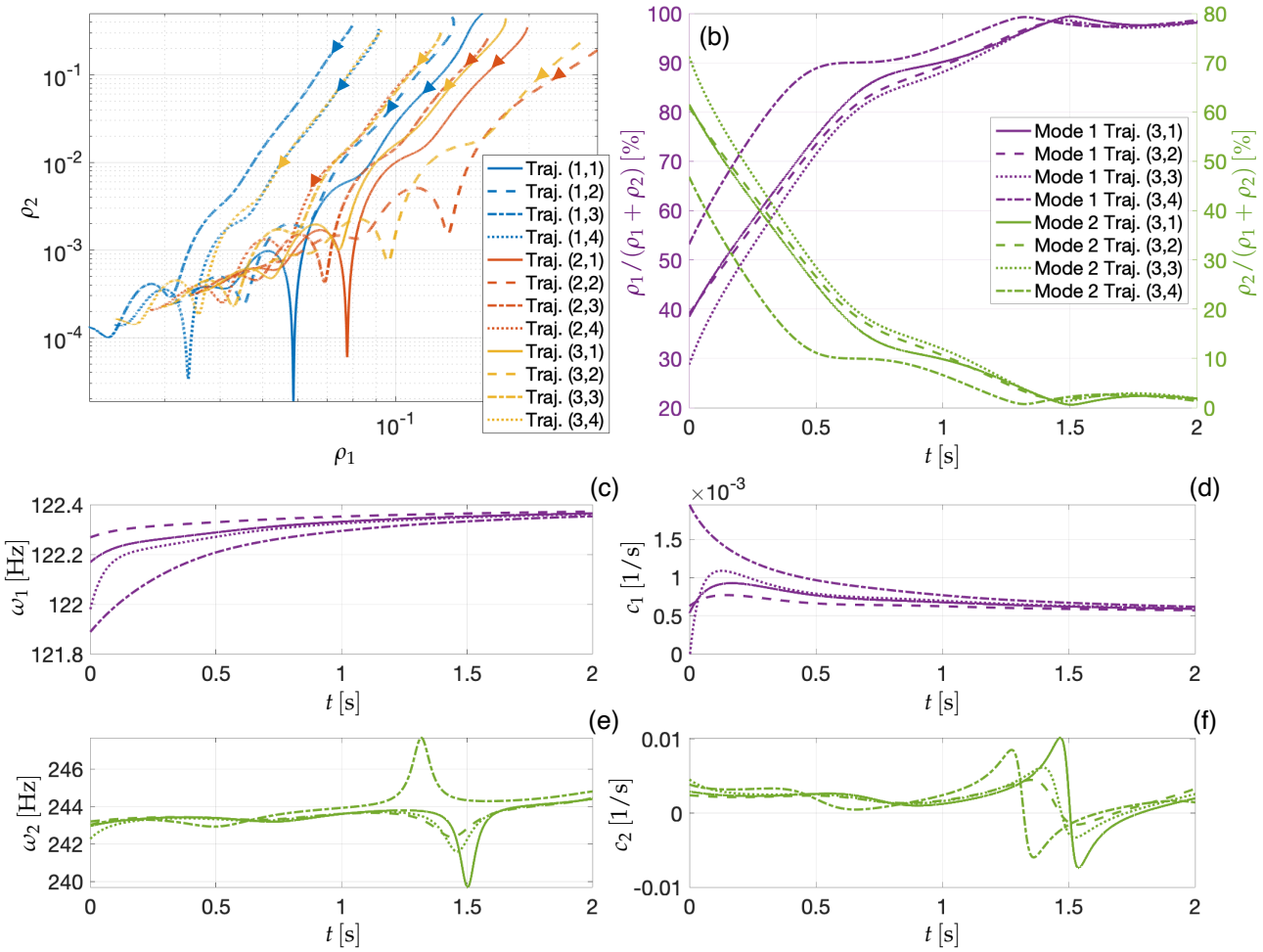

Figure 10.10: The picture in (a) shows the amplitudes decays for the slow ρ_1 and fast ρ_2 modes, for all available trajectories in the dataset. Plot (b) illustrates the energy repartitions along the decays arising from impact on the third impact location. Plots (c-f) show the trend of instantaneous characteristics of the normal form dynamics on the first two seconds of decays related to the third impact location.

in 10.10(c-f). The uncoupled limit of the oscillators suggests that the modes are characterized by frequency softening and by damping intensification when oscillation amplitudes increase. This is consistent with typical observations of jointed structures [212]. In particular, the fast mode is strongly coupled to the slow one and its damping shows consistent variations, becoming also negative for some times [213]. However, the damping terms of the dynamics that are not related to resonance, i.e., the first three terms of the last equation in (10.11), do not generate consistent energy transfer. Indeed, after 1 [s] in almost all trajectories, the second mode disappears from the signal, as seen in Fig. 10.8(b,c).

11

CONCLUSION

In this part of the thesis, we have derived a thorough framework for constructing explicit reduced-order model for high-dimensional dynamical systems from data. By merging exact theories from dynamical systems with simple yet effective machine learning principles, our method is able to build accurate, robust and predictive nonlinear models. The results and the applications discussed in this part of the thesis closely follow our work in the original references [33, 47].

Our approach tackles local dynamics near an equilibrium, which is a common working condition for several real-life systems, and digests any generic observed quantity. However, the domain of validity of our approach is larger with respect to that of Sternberg's classic linearization result [192], since our dynamical model is able to capture nonlinear phenomena. In this context, SSMs and their embedding guarantee dimensionality reduction. Most importantly, SSMs dictate the local geometry of the phase space and consequently allows for a deeper understanding of system motions, even in case of multi-frequency forcing applied to the system. While targeted experiments aspire to discover specific SSMs of a given system, an attracting SSM can be always devised and it allows to identify the leading order system dynamics. Additionally, SSMs appear around any dynamical equilibrium of hyperbolic type, and this fact guarantees a general applicability of our approach.

After embedding of data in a suitable observable space, a nonlinear model reduction based on PCA is performed, and the resulting reduced coordinates, which can be of arbitrary dimension in principle, are used to identify the normal form of the dynamics. In contrast with black-box or a priori sparse models, the normal form dynamics naturally clusters the trajectory data in the proper family, recognizing peculiar physical features of the dynamics and respecting topological conjugacy. The resulting simple and rigorous dynamical models are used to derive analytics, such as instantaneous damping and frequency, and to make predictions when perturbations are added to the system.

We have validated our method for different classes of systems, either dealing with numerical or physical experiments. In every case we have analyzed, we do not make the unrealistic assumption of having exact prior knowledge of system spectral submanifolds, but we rather deal with actual practical cases in which targeted experiments generate the necessary data to unfold the relevant dynamics via SSM theory. We have tested our method in examples coming from structural vibrations and fluid dynamics, concerning stable or unstable behaviors, with observables being scalar quantities or big data related to multiple system locations. In these examples, we have shown how our approach can give precious system insights, from the analysis of dynamical time-scales, to the assessment of modal interactions and predictions when periodic forcing acts on the dynamics. Specifically, we have dealt with a finite element model of a von Kármán beam where, after data-driven modeling based on transient data, we have used this model to accurately predict the frequency response. Then, the vortex shedding case study shows how our approach can deal with strongly nonlinear high-dimensional data coupled with some basic system knowledge. The experimental example on the Brake-Reuß beam illustrates that `SSMLearn` can attack diverse measurements, and that the model-derived amplitude properties are in good accordance with those obtained by signal processing algorithms. The last case study on an internally resonant tester has exemplified how complicated dynamics is unfolded by the normal form.

12

DISCUSSION AND OUTLOOK

This thesis began with looking at mechanical oscillations from a classic perspective, and it has ended with the discussion of a contemporary data-driven approach. The contrast between these two viewpoints is only superficial. Indeed, engineering problems in the current age require both approaches, which should therefore not be regarded as opposite and disconnected, but rather as complementary. Indeed, understanding data or identifying significant models is challenging without phenomenological knowledge, while analytical models should find correspondence in real-life measurements.

The first part of the thesis has focused on the prediction of forced-frequency responses from the conservative limit of mechanical systems. We developed an exact mathematical analysis whose findings agree with numerical and experimental observations. Our Melnikov method proves to be particularly beneficial for parametric studies and numerical simulations. Moreover, the implications of our results should motivate new experimental techniques for the extraction of forced-frequency responses and their backbone curves.

This Melnikov method is currently limited to well-defined conservative one-parameter families of periodic orbits subject to small damping and periodic external forcing. Although this setting is sufficiently generic, certain applications may further require the analysis of degenerate cases or resonance interactions (e.g. branching phenomena), examples of which could be encountered in mechanical systems with symmetries [116, 117, 119]. The persistence problem in these cases would require the analysis of a more general, multi-dimensional bifurcation function. Hence, we do not expect the energy principle alone to be completely predictive as it is in the setting discussed here. Relevant techniques for tackling these problems can be found in [114]. Other refinements of the Melnikov method discussed in this thesis could treat the case of superharmonic and ultrasubharmonic resonances for canonical monoharmonic, space-independent forcing. Indeed, the Melnikov function, from an engineering perspective, tells us that these motions require high forcing and low damping to be present, which is in accordance with asymptotic expansions from the linearized limit [5, 27]. However, more accurate predictive tools based on rigorous Melnikov analyses could be beneficial also for these nonlinear resonances. Further developments arising from the present discussion could address the investigation of perturbation approaches for mechanical systems in which the forcing can be large or non-smooth.

In the second part of this thesis, we discussed a method for the extraction of explicit data-driven models in high-dimensional dynamical systems. Based on spectral submanifold theory, this method delivers a systematic way of extracting dynamical models near fixed points. After data embedding, rigorous model-order reduction is applied to the data, squeezing its dimensionality to the bare minimum. Then, the reduced coordinates set the framework to identify a normal form, which provides an insightful dynamical model for oscillatory dynamics. Our method is publicly shared with the open-source computational package `SSMLearn` (available at github.com/mattiacenedese/SSMLearn). Despite the diversity in measurements, dynamical behaviors, and nonlinearities in our examples, this package produced accurate data-driven reduced-order models. This method constitutes a first step towards the unsupervised, intelligent learning of rigorous nonlinear dynamical models from data.

Additional progress in this line of research is expected to include further testing and predictions for experimental data from various applications. When predicting forced responses, challenges may arise due to calibration, since often the forcing amplitude in experimental setting is subject to variability. Moreover, further exploration is necessary for demanding applications in which the normal form still has moderate dimensionality.

The natural step forward for this research is to deal with more complex attractors and their dynamics in their vicinity. Indeed, beyond modeling the dynamics near fixed points, one should seek reduced-order models for the local dynamics near limit cycles, quasi-periodic motions or even chaotic attractors. Spectral submanifolds, also called whiskers in the case of quasi-periodic attracting invariant tori [214], guarantee the necessary theoretical framework for studying more complicated dynamical regimes. These data-driven models will be relevant both for structural vibrations in the presence of non-trivial time-dependent forcing and for turbulence in fluid dynamics [13]. In the latter case, the slow dynamics approaching a turbulent attractor could offer both a fundamental understanding of the dynamics and a new opportunity for flow control.

I would like to close my thesis with a well-known citation attributed to Einstein [215].

Everything should be made as simple as possible,
but no simpler.
Albert Einstein (1933).

I believe that, with this work, we have tried to approach Einstein's vision. The methods we have proposed are always backed by mathematical rigor, which unavoidably implies complications, but the aspiration is that of providing scientists and engineers with techniques that are *"as simple as possible"*. This simplicity helps to unfold the fascinating dynamics of nonlinear oscillations and explore new opportunities in technological development.

BIBLIOGRAPHY

[1] H. Poincaré. *Les Méthodes Nouvelles de la Mécanique Céleste*. Gauthier-Villars et Fils, Paris, 1892.

[2] I. Kovacic. Generalized van der Pol oscillators: overview of the properties of oscillatory responses. In A.K. Abramian, I.V. Andrianov, and V.A. Gaiko, editors, *Nonlinear Dynamics of Discrete and Continuous Systems*. Springer International Publishing, 2021.

[3] I. Kovacic and M.J. Brennan, editors. *The Duffing Equation: Nonlinear Oscillators and their Behaviour*. John Wiley & Sons, 2011.

[4] J. Guckenheimer and P.J. Holmes. *Nonlinear Oscillations, Dynamical Systems, and Bifurcations of Vector Fields*, volume 42 of *Applied Mathematical Sciences*. Springer-Verlag New York, 1983.

[5] A.H. Nayfeh and D.T. Mook. *Nonlinear Oscillations*. Wiley, 2007.

[6] S.H. Crandall. The role of damping in vibration theory. *Journal of Sound and Vibration*, 11(1):3–18, 1970.

[7] S. Salsa. *Partial Differential Equations in Action*, volume 99 of *La Matematica per il 3+2*. Springer International Publishing, 3rd edition, 2016.

[8] M. Geradin and D.J. Rixen. *Mechanical Vibrations: Theory and Application to Structural Dynamics*. John Wiley & Sons, 3rd edition, 2015.

[9] Z.-Q. Qu. *Model Order Reduction Techniques with Applications in Finite Element Analysis*. Springer-Verlag London, 2004.

[10] G. Teschl. *Ordinary Differential Equations and Dynamical Systems*, volume 140 of *Graduate Studies in Mathematics*. American Mathematical Society, 2012.

[11] C. Chicone. *Ordinary Differential Equations with Applications*, volume 34 of *Texts in Applied Mathematics*. Springer-Verlag New York, 1982.

[12] S. Jain, T. Breunung, and G. Haller. Fast computation of steady-state response for high-degree-of-freedom nonlinear systems. *Nonlinear Dynamics*, 97:313–341, 2019.

[13] P. Holmes, J.L. Lumley, G. Berkooz, and C.W. Rowley. *Turbulence, Coherent Structures, Dynamical Systems and Symmetry*. Cambridge Monographs on Mechanics. Cambridge University Press, 2nd edition, 2012.

[14] L. Wu and P. Tiso. Nonlinear model order reduction for flexible multibody dynamics: a modal derivatives approach. *Multibody System Dynamics*, 36:405–425, 2016.

[15] A. Kelley. On the Liapounov subcenter manifold. *Journal of Mathematical Analysis and Applications*, 18(3):472–478, 1967.

[16] Z. Veraszto, S. Ponsioen, and G. Haller. Explicit third-order model reduction formulas for general nonlinear mechanical systems. *Journal of Sound and Vibration*, 468:115039, 2020.

[17] G. Kerschen. *Modal Analysis of Nonlinear Mechanical Systems*, volume 555 of *CISM International Centre for Mechanical Sciences*. Springer-Verlag Wien, 2014.

[18] G. Haller and S. Ponsioen. Nonlinear normal modes and spectral submanifolds: existence, uniqueness and use in model reduction. *Nonlinear Dynamics*, 86(3):1493–1534, 2016.

[19] G. Haller and S. Ponsioen. Exact model reduction by a slow-fast decomposition of nonlinear mechanical systems. *Nonlinear Dynamics*, 90:617–647, 2017.

[20] S. Ponsioen, S. Jain, and G. Haller. Model reduction to spectral submanifolds and forced-response calculation in high-dimensional mechanical systems. *Journal of Sound and Vibration*, 488:115640, 2020.

[21] L. Renson, G. Kerschen, and B. Cochelin. Numerical computation of nonlinear normal modes in mechanical engineering. *Journal of Sound and Vibration*, 364:177–206, 2016.

[22] S. Jain and G. Haller. How to compute invariant manifolds and their reduced dynamics in high-dimensional finite-element models? *Nonlinear Dynamics*, 2021.

[23] T. Breunung and G. Haller. Explicit backbone curves from spectral submanifolds of forced-damped nonlinear mechanical systems. *Proceedings of the Royal Society of London A: Mathematical, Physical and Engineering Sciences*, 474:20180083, 2018.

[24] M. Peeters, R. Viguié, G. Sérandour, G. Kerschen, and J.-C. Golinval. Nonlinear normal modes, part II: toward a practical computation using numerical continuation techniques. *Mechanical Systems and Signal Processing*, 23(1):195–216, 2009. Special Issue: Non-linear Structural Dynamics.

[25] A. Grolet and F. Thouverez. On a new harmonic selection technique for harmonic balance method. *Mechanical Systems and Signal Processing*, 30:43–60, 2012.

[26] H. Dankowicz and F. Schilder. *Recipes for Continuation*. Society for Industrial and Applied Mathematics, 2013.

[27] J.A. Sanders, F. Verhulst, and J. Murdock. *Averaging Methods in Nonlinear Dynamical Systems*, volume 59 of *Applied Mathematical Sciences*. Springer-Verlag New York, 2nd edition, 2007.

[28] C. Touzé, O. Thomas, and A. Chaigne. Hardening/softening behaviour in non-linear oscillations of structural systems using non-linear normal modes. *Journal of Sound and Vibration*, 273(1):77–101, 2004.

[29] S.A. Neild and D.J. Wagg. Applying the method of normal forms to second-order nonlinear vibration problems. *Proceedings of the Royal Society of London A: Mathematical, Physical and Engineering Sciences*, 467(2128):1141–1163, 2011.

[30] G. Kerschen, K. Worden, A.F. Vakakis, and J.-C. Golinval. Past, present and future of nonlinear system identification in structural dynamics. *Mechanical Systems and Signal Processing*, 20(3):505–592, 2006.

[31] J.P. Noël and G. Kerschen. Nonlinear system identification in structural dynamics: 10 more years of progress. *Mechanical Systems and Signal Processing*, 83:2–35, 2017.

[32] D.A. Ehrhardt and M.S. Allen. Measurement of nonlinear normal modes using multi-harmonic stepped force appropriation and free decay. *Mechanical Systems and Signal Processing*, 76-77:612–633, 2016.

[33] M. Cenedese, J. Axås, H. Yang, M. Eriten, and G. Haller. Data-driven nonlinear model reduction to spectral submanifolds in mechanical systems. *arXiv:2110.01929*, under revision at *Philosophical Transactions of the Royal Society A: Mathematical, Physical and Engineering Sciences*, 2022.

[34] D. Di Maio, P. Castellini, M. Martarelli, S. Rothberg, M.S. Allen, W.D. Zhu, and D.J. Ewins. Continuous scanning laser vibrometry: A raison d'être and applications to vibration measurements. *Mechanical Systems and Signal Processing*, 156:107573, 2021.

[35] F. Hild, A. Bouterf, P. Forquin, and S. Roux. On the use of digital image correlation for the analysis of the dynamic behavior of materials. In K. Tsuji, editor, *The Micro-World Observed by Ultra High-Speed Cameras*. Springer International Publishing, 2018.

[36] W. Chen, D. Jana, A. Singh, M. Jin, M. Cenedese, G. Kosova, M.W.R. Brake, C.W. Schwingshackl, S. Nagarajaiah, K.J. Moore, and J.P. Noël. Measurement and identification of the nonlinear dynamics of a jointed structure using full-field data; Part I - Measurement of nonlinear dynamics. *Mechanical Systems and Signal Processing*, 166:108401, 2022.

[37] M. Jin, G. Kosova, M. Cenedese, W. Chen, A. Singh, D. Jana, M.W.R. Brake, C.W. Schwingshackl, S. Nagarajaiah, K.J. Moore, and J.P. Noël. Measurement and identification of the nonlinear dynamics of a jointed structure using full-field data; Part II - Nonlinear system identification. *Mechanical Systems and Signal Processing*, 166:108402, 2022.

[38] N.E. Huang, Z. Shen, S.R. Long, M.C. Wu, H.H. Shih, Q. Zheng, N.-C. Yen, C.C. Tung, and H.H. Liu. The empirical mode decomposition and the Hilbert spectrum for nonlinear and non-stationary time series analysis. *Proceedings of the Royal Society of London. Series A: Mathematical, Physical and Engineering Sciences*, 454(1971):903–995, 1998.

[39] M. Feldman. Hilbert transform in vibration analysis. *Mechanical Systems and Signal Processing*, 25(3):735–802, 2011.

[40] K.J. Moore, M. Kurt, M. Eriten, D.M. McFarland, L.A. Bergman, and A.F. Vakakis. Wavelet-bounded empirical mode decomposition for measured time series analysis. *Mechanical Systems and Signal Processing*, 99:14–29, 2018.

[41] M. Jin, W. Chen, M.R.W. Brake, and H. Song. Identification of instantaneous frequency and damping from transient decay data. *Journal of Vibration and Acoustics*, 142(5):051111, 2020.

[42] M. Cenedese and G. Haller. How do conservative backbone curves perturb into forced responses? A Melnikov function analysis. *Proceedings of the Royal Society of London A: Mathematical, Physical and Engineering Sciences*, 476:20190494, 2020.

[43] M. Cenedese and G. Haller. Stability of forced–damped response in mechanical systems from a Melnikov analysis. *Chaos: an Interdisciplinary Journal of Nonlinear Science*, 30(8):083103, 2020.

[44] M. Peeters, G. Kerschen, and J.C. Golinval. Dynamic testing of nonlinear vibrating structures using nonlinear normal modes. *Journal of Sound and Vibration*, 330(3):486–509, 2011.

[45] L. Renson, A. Gonzalez-Buelga, D.A.W. Barton, and S.A. Neild. Robust identification of backbone curves using control-based continuation. *Journal of Sound and Vibration*, 367:145–158, 2016.

[46] S.L. Brunton and J.N. Kutz. *Data-Driven Science and Engineering: Machine Learning, Dynamical Systems, and Control*. Cambridge University Press, 2019.

[47] M. Cenedese, J. Axås, B. Bäuerlein, K. Avila, and G. Haller. Data-driven modeling and prediction of non-linearizable dynamics via spectral submanifolds. *arXiv:2110.01929*, accepted for publication on *Nature Communications*, 2022.

[48] E. Collin, Yu. M. Bunkov, and H. Godfrin. Addressing geometric nonlinearities with cantilever microelectromechanical systems: beyond the Duffing model. *Physical Review B*, 82:235416, Dec 2010.

[49] T. Marwala. *Finite-element-model Updating Using Computional Intelligence Techniques: Applications to Structural Dynamics*. Springer London, London, 2010.

[50] C.M. Bishop. *Pattern Recognition and Machine Learning*. Information Science and Statistics. Springer-Verlag New York, 2006.

[51] R. Tibshirani. Regression shrinkage and selection via the lasso. *Journal of the Royal Statistical Society. Series B (Methodological)*, 58(1):267–288, 1996.

[52] S.L. Brunton, J.L. Proctor, and J.N. Kutz. Discovering governing equations from data by sparse identification of nonlinear dynamical systems. *Proceedings of the National Academy of Sciences*, 113(15):3932–3937, 2016.

[53] I. Goodfellow, Y. Bengio, and A. Courville. *Deep Learning*. MIT Press, 2016.

[54] H.F.S. Lui and W.R. Wolf. Construction of reduced-order models for fluid flows using deep feedforward neural networks. *Journal of Fluid Mechanics*, 872:963–994, 2019.

[55] T. Kirchdoerfer and M. Ortiz. Data-driven computational mechanics. *Computer Methods in Applied Mechanics and Engineering*, 304:81–101, 2016.

[56] K.F.R.S. Pearson. LIII. On lines and planes of closest fit to systems of points in space. *The London, Edinburgh, and Dublin Philosophical Magazine and Journal of Science*, 2(11):559–572, 1901.

[57] Y. Bengio, A. Courville, and P. Vincent. Representation learning: a review and new perspectives. *IEEE Transactions on Pattern Analysis and Machine Intelligence*, 35(8):1798–1828, 2013.

[58] J.N. Kutz, S.L. Brunton, B.W. Brunton, and J.L. Proctor. *Dynamic Mode Decomposition*. Society for Industrial and Applied Mathematics, Philadelphia, PA, 2016.

[59] P.J. Schmid. Dynamic mode decomposition of numerical and experimental data. *Journal of Fluid Mechanics*, 656:5–28, 2010.

[60] M. Raissi, P. Perdikaris, and G.E. Karniadakis. Physics-informed neural networks: a deep learning framework for solving forward and inverse problems involving nonlinear partial differential equations. *Journal of Computational Physics*, 378:686–707, 2019.

[61] M. Flaschel, S. Kumar, and L. De Lorenzis. Unsupervised discovery of interpretable hyperelastic constitutive laws. *Computer Methods in Applied Mechanics and Engineering*, 381:113852, 2021.

[62] Z.Y. Wan, P. Vlachas, P. Koumoutsakos, and T.P. Sapsis. Data-assisted reduced-order modeling of extreme events in complex dynamical systems. *PLoS ONE*, 13(5):e0197704, 2018.

[63] J.P. Noël and J. Schoukens. Grey-box state-space identification of nonlinear mechanical vibrations. *International Journal of Control*, 91(5):1118–1139, 2018.

[64] Z.Y. Wan and T.P. Sapsis. Machine learning the kinematics of spherical particles in fluid flows. *Journal of Fluid Mechanics*, 857:R2, 2018.

[65] R.M. Rosenberg. The normal modes of nonlinear n-degree-of-freedom systems. *Journal of Applied Mechanics*, 29:7–14, 1962.

[66] A.F. Vakakis. Non-linear normal modes, (NNMs) and their application in vibration theory: an overview. *Mechanical Systems and Signal Processing*, 11(1):3–22, 1997.

[67] A.F. Vakakis, editor. *Normal Modes and Localization in Nonlinear Systems*. Springer, Dordrecht, 2001.

[68] A.F. Vakakis, L.I. Manevitch, Y.V. Mikhlin, V.N. Pilipchuk, and A.A. Zevin. *Normal Modes and Localization in Nonlinear Systems*. Wiley Blackwell, 1 2008.

[69] K.V. Avramov and Y.V. Mikhlin. Nonlinear normal modes for vibrating mechanical systems. Review of theoretical developments. *ASME Applied Mechanics Reviews*, 63(6), 2011.

[70] K.V. Avramov and Y.V. Mikhlin. Review of applications of nonlinear normal modes for vibrating mechanical systems. *ASME Applied Mechanics Reviews*, 65(2), 2013.

[71] I. Kovacic, M.J. Brennan, and B. Lineton. On the resonance response of an asymmetric Duffing oscillator. *International Journal of Non-Linear Mechanics*, 43(9):858–867, 2008.

[72] K.V. Avramov. Analysis of forced vibrations by nonlinear modes. *Nonlinear Dynamics*, 53(1-2):117–127, 2008.

[73] M. Peeters, G. Kerschen, and J.C. Golinval. Modal testing of nonlinear vibrating structures based on nonlinear normal modes: experimental demonstration. *Mechanical Systems and Signal Processing*, 25(4):1227–1247, 2011.

[74] R. Szalai, D. Ehrhardt, and G. Haller. Nonlinear model identification and spectral submanifolds for multi-degree-of-freedom mechanical vibrations. *Proceedings of the Royal Society of London A: Mathematical, Physical and Engineering Sciences*, 473:20160759, 2017.

[75] C. Touzé and M. Amabili. Nonlinear normal modes for damped geometrically nonlinear systems: application to reduced-order modelling of harmonically forced structures. *Journal of Sound and Vibration*, 298(4):958–981, 2006.

[76] C.S.M. Sombroek, P. Tiso, L. Renson, and G. Kerschen. Numerical computation of nonlinear normal modes in a modal derivative subspace. *Computers & Structures*, 195:34–46, 2018.

[77] P.M. Polunin, Y. Yang, M.I. Dykman, T.W. Kenny, and S.W. Shaw. Characterization of MEMS resonator nonlinearities using the ringdown response. *Journal of Microelectromechanical Systems*, 25(2):297–303, April 2016.

[78] N. Carpineto, W. Lacarbonara, and F. Vestroni. Hysteretic tuned mass dampers for structural vibration mitigation. *Journal of Sound and Vibration*, 333(5):1302–1318, 2014.

[79] A. Mojahed, K.J. Moore, L.A. Bergman, and A.F. Vakakis. Strong geometric softening-hardening nonlinearities in an oscillator composed of linear stiffness and damping elements. *International Journal of Non-Linear Mechanics*, 107:94–111, 2018.

[80] Y. Liu, A. Mojahed, L.A. Bergman, and A.F. Vakakis. A new way to introduce geometrically nonlinear stiffness and damping with an application to vibration suppression. *Nonlinear Dynamics*, 96(3):1819–1845, May 2019.

[81] G. Habib, G.I. Cirillo, and G. Kerschen. Isolated resonances and nonlinear damping. *Nonlinear Dynamics*, 93(3):979–994, 2018.

[82] T.L. Hill, S.A. Neild, and A. Cammarano. An analytical approach for detecting isolated periodic solution branches in weakly nonlinear structures. *Journal of Sound and Vibration*, 379:150–165, 2016.

[83] S. Ponsioen, T. Pedergnana, and G. Haller. Analytic prediction of isolated forced response curves from spectral submanifolds. *Nonlinear Dynamics*, 98:2755–2773, 2019.

[84] T.L. Hill, A. Cammarano, S.A. Neild, and D.A.W. Barton. Identifying the significance of nonlinear normal modes. *Proceedings of the Royal Society of London A: Mathematical, Physical and Engineering Sciences*, 473:20160789, 2017.

[85] K.R. Meyer and D.C. Offin. *Introduction to Hamiltonian Dynamical Systems and the N-body Problem*, volume 90 of *Applied Mathematical Sciences*. Springer-Verlag New York, 3rd edition, 2017.

[86] A. Vanderbauwhede. Branching of periodic orbits in Hamiltonian and reversible systems. In R.P. Agarwal, F. Neuman, and J. Vosmanský, editors, *Proceedings of Equadiff 9, Conference on Differential Equations and Their Applications, Brno, August 25-29, 1997*, pages 169–181. Masaryk University Brno, 1998.

[87] O. Shoshani and S.W. Shaw. Resonant modal interactions in micro/nano-mechanical structure. *Nonlinear Dynamics*, 2021.

[88] T.L. Hill, A. Cammarano, S.A. Neild, and D.J. Wagg. Interpreting the forced responses of a two-degree-of-freedom nonlinear oscillator using backbone curves. *Journal of Sound and Vibration*, 349:276–288, 2015.

[89] A.F. Vakakis and A. Blanchard. Exact steady states of the periodically forced and damped Duffing oscillator. *Journal of Sound and Vibration*, 413:57–65, 1 2018.

[90] S. Ponsioen, T. Pedergnana, and G. Haller. Automated computation of autonomous spectral submanifolds for nonlinear modal analysis. *Journal of Sound and Vibration*, 420:269–295, 2018.

[91] A.M. Lyapunov. The general problem of the stability of motion. *International Journal of Control*, 55(3):531–534, 1992.

[92] G. Floquet. Sur les équations différentielles linéaires à coefficients périodiques. *Annales scientifiques de l'École Normale Supérieure*, 12:47–88, 1883.

[93] A. Lazarus and O. Thomas. A harmonic-based method for computing the stability of periodic solutions of dynamical systems. *Comptes Rendus Mécanique*, 338(9):510–517, 2010.

[94] L. Guillot, A. Lazarus, O. Thomas, C. Vergez, and B. Cochelin. A purely frequency based Floquet-Hill formulation for the efficient stability computation of periodic solutions of ordinary differential systems. *Journal of Computational Physics*, 416:109477, 2020.

[95] R. de la Llave and F. Kogelbauer. Global persistence of Lyapunov subcenter manifolds as spectral submanifolds under dissipative perturbations. *SIAM Journal on Applied Dynamical Systems*, 18(4):2099–2142, 2019.

[96] S. Peter, M. Scheel, M. Krack, and R.I. Leine. Synthesis of nonlinear frequency responses with experimentally extracted nonlinear modes. *Mechanical Systems and Signal Processing*, 101:498–515, 2018.

[97] G. Kerschen, M. Peeters, J.C. Golinval, and A.F. Vakakis. Nonlinear normal modes, part I: a useful framework for the structural dynamicist. *Mechanical Systems and Signal Processing*, 23(1):170–194, 2009.

[98] I.G. Malkin. On Poincaré's theory of periodic solutions. *Akad. Nauk SSSR. Prikl. Mat. Meh.*, 13:633–646, 1949.

[99] W.S. Loud. Periodic solutions of a perturbed autonomous system. *Annals of Mathematics*, 70(3):490–529, 1959.

[100] M. Farkas. *Periodic Motions*, volume 104 of *Applied Mathematical Sciences*. Springer-Verlag New York, 1994.

[101] J. Moser and E.J. Zehnder. *Notes on Dynamical Systems*, volume 12 of *Courant Lecture Notes*. American Mathematical Society, 2005.

[102] V.I. Arnol'd. Instability of dynamical systems with many degrees of freedom. *Dokl. Akad. Nauk SSSR*, 156(1):9–12, 1964.

[103] V.K. Melnikov. On the stability of a center for time-periodic perturbations. *Tr. Mosk. Mat. Obs.*, 12:3–52, 1963.

[104] K. Yagasaki. The Melnikov theory for subharmonics and their bifurcations in forced oscillations. *SIAM Journal on Applied Mathematics*, 56(6):1720–1765, 1996.

[105] M. Bonnin. Harmonic balance, Melnikov method and nonlinear oscillators under resonant perturbation. *International Journal of Circuit Theory and Applications*, 36(3):247–274, 2008.

[106] P. Veerman and P. Holmes. The existence of arbitrarily many distinct periodic orbits in a two degree of freedom Hamiltonian system. *Physica D: Nonlinear Phenomena*, 14(2):177–192, 1985.

[107] P. Veerman and P. Holmes. Resonance bands in a two degree of freedom Hamiltonian system. *Physica D: Nonlinear Phenomena*, 20(2):413–422, 1986.

[108] K. Yagasaki. Periodic and homoclinic motions in forced, coupled oscillators. *Nonlinear Dynamics*, 20(4):319–359, 1999.

[109] M. Kunze. *Non-Smooth Dynamical Systems*, volume 1744 of *Lecture Notes in Mathematics*. Springer-Verlag Berlin Heidelberg, 2000.

[110] S.W. Shaw and R.H. Rand. The transition to chaos in a simple mechanical system. *International Journal of Non-Linear Mechanics*, 24(1):41–56, 1989.

[111] J. Shaw and S.W. Shaw. The onset of chaos in a two-degree-of-freedom impacting system. *Journal of Applied Mechanics*, 56:168, 1989.

[112] C. Chicone. Lyapunov-Schmidt reduction and Melnikov integrals for bifurcation of periodic solutions in coupled oscillators. *Journal of Differential Equations*, 112(2):407–447, 1994.

[113] C. Chicone. A geometric approach to regular prturbation theory with an application to hydrodynamics. *Transactions of the American Mathematical Society*, 12(2):4559–4598, 1995.

[114] M.B.H. Rhouma and C. Chicone. On the continuation of periodic orbits. *Methods and Applications of Analysis*, 7(1):85–104, 2000.

[115] A. Buică, J. Llibre, and O. Makarenkov. Bifurcations from nondegenerate families of periodic solutions in Lipschitz systems. *Journal of Differential Equations*, 252(6):3899–3919, 2012.

[116] V.I. Arnol'd. *Mathematical Methods of Classical Mechanics*, volume 60 of *Graduate Texts in Mathematics*. Springer-Verlag New York, 1989.

[117] R. Abraham and J.E. Marsden. *Foundations of Mechanics*. AMS Chealsea Publishing, 2nd edition, 1989.

[118] J.A. Sepulchre and R.S. MacKay. Localized oscillations in conservative or dissipative networks of weakly coupled autonomous oscillators. *Nonlinearity*, 10(3):679, 1997.

[119] F.J. Muñoz-Almaraz, E. Freire, J. Galán, E. Doedel, and A. Vanderbauwhede. Continuation of periodic orbits in conservative and Hamiltonian systems. *Physica D: Nonlinear Phenomena*, 181(1):1–38, 2003.

[120] S.N. Chow and J.K. Hale. *Methods of Bifurcation Theory*, volume 251 of *Grundlehren der mathematischen Wissenschaften*. Springer-Verlag New York, 1982.

[121] M. Golubitsky and S. Schaeffer. *Singularities and Groups in Bifurcation Theory*, volume 51 of *Applied Mathematical Sciences*. Springer-Verlag New York, 1985.

[122] W.J.F. Govaerts. *Numerical Methods for Bifurcations of Dynamical Equilibria*. Society for Industrial and Applied Mathematics, 2000.

[123] M.Y. Li and J.S. Muldowney. Dynamics of differential equations on invariant manifolds. *Journal of Differential Equations*, 168(2):295–320, 2000.

[124] M. A. de Gosson. *Symplectic Methods in Harmonic Analysis and in Mathematical Physics*. Birkäuser, 2011.

[125] G. Stewart and J. Sun. *Matrix Perturbation Theory*. Computer Science and Scientific Computing. Academic Press, 1990.

[126] L. Sbano. Periodic orbits of Hamiltonian systems. In R.A. Meyers, editor, *Encyclopedia of Complexity and Systems Science*, pages 6587–6611. Springer New York, 2009.

[127] M. Karow and D. Kressner. On a perturbation bound for invariant subspaces of matrices. *SIAM Journal on Matrix Analysis and Applications*, 35(2):599–618, 2014.

[128] K. Meyer and G. Hall. *Introduction to Hamiltonian Dynamical Systems and the N-body Problem*, volume 90 of *Applied Mathematical Sciences*. Springer-Verlag New York, 1st edition, 1992.

[129] V.I. Arnol'd. *Geometrical Methods in the Theory of Ordinary Differential Equations*, volume 250 of *Grundlehren der mathematischen Wissenschaften*. Springer-Verlag New York, 1988.

[130] Y.A. Kuznetsov. *Elements of Applied Bifurcation Theory*, volume 112 of *Applied Mathematical Sciences*. Springer-Verlag New York, 1995.

[131] M. Amabili and C. Touzé. Reduced-order models for nonlinear vibrations of fluid-filled circular cylindrical shells: Comparison of POD and asymptotic nonlinear normal modes methods. *Journal of Fluids and Structures*, 23(6):885–903, 2007.

[132] L. Renson, J.P. Noël, and G. Kerschen. Complex dynamics of a nonlinear aerospace structure: numerical continuation and normal modes. *Nonlinear Dynamics*, 79:1293–1309, 2015.

[133] R.J. Kuether, L. Renson, T. Detroux, C. Grappasonni, G. Kerschen, and M.S. Allen. Nonlinear normal modes, modal interactions and isolated resonance curves. *Journal of Sound and Vibration*, 351:299–310, 2015.

[134] R. McLachlan and M. Perlmutter. Conformal Hamiltonian systems. *Journal of Geometry and Physics*, 39(4):276–300, 2001.

[135] R.C. Calleja, A. Celletti, and R. de la Llave. A KAM theory for conformally symplectic systems: efficient algorithms and their validation. *Journal of Differential Equations*, 255(5):978–1049, 2013.

[136] Y. Ishida and T. Yamamoto. *Nonlinear Vibrations*, chapter 6, pages 115–159. John Wiley & Sons, Ltd, 2012.

[137] M.I. Younis. *MEMS Linear and Nonlinear Statics and Dynamics*, volume 20 of *Microsystems*. Springer US, 2011.

[138] F. F. Ehrich. High order subharmonic response of high speed rotors in bearing clearance. *Journal of Vibration, Acoustics, Stress, and Reliability in Design*, 110(1):9–16, 1988.

[139] Y.S. Hamed, A.T. El-Sayed, and E.R. El-Zahar. On controlling the vibrations and energy transfer in MEMS gyroscope system with simultaneous resonance. *Nonlinear Dynamics*, 83(3):1687–1704, 2016.

[140] J.F. Rhoads, S.W. Shaw, K.L. Turner, and R. Baskaran. Tunable microelectromechanical filters that exploit parametric resonance. *Journal of Vibration and Acoustics*, 127(5):423–430, 01 2005.

[141] F.R. Gantmacher. *The Theory of Matrices*, volume 1. Chelsea Publishing Company New York, 1959.

[142] I. Gohberg, P. Lancaster, and L. Rodman. *Invariant Subspaces of Matrices with Applications*. Society for Industrial and Applied Mathematics, 2006.

[143] U. Dressler. Symmetry property of the Lyapunov spectra of a class of dissipative dynamical systems with viscous damping. *Physical Review A*, 38:2103–2109, 1988.

[144] S. Hijazi, G. Stabile, A. Mola, and G. Rozza. Data-driven POD-Galerkin reduced order model for turbulent flows. *Journal of Computational Physics*, 416:109513, 2020.

[145] K.K. Chen, J.H. Tu, and C.W. Rowley. Variants of dynamic mode decomposition: boundary condition, Koopman, and Fourier analyses. *Annual Review of Fluid Mechanics*, 22(6):887–915, 2012.

[146] M.O. Williams, C.W. Rowley, and I.G. Kevrekidis. A kernel-based method for data-driven Koopman spectral analysis. *Journal of Computational Dynamics*, 2(2):247–265, 2015.

[147] C.W. Rowley and S.T.M. Dawson. Model reduction for flow analysis and control. *Annual Review of Fluid Mechanics*, 49(1):387–417, 2017.

[148] A. Alla and J.N. Kutz. Nonlinear model order reduction via dynamic mode decomposition. *SIAM Journal on Scientific Computing*, 39(5):B778–B796, 2017.

[149] B. Lusch, J.N. Kutz, and S.L. Brunton. Deep learning for universal linear embeddings of nonlinear dynamics. *Nature Communications*, 9:4950, 2018.

[150] M. Budišić, R. Mohr, and I. Mezić. Applied koopmanism. *Chaos: An Interdisciplinary Journal of Nonlinear Science*, 22(4):047510, 2012.

[151] Igor Mezić. Analysis of fluid flows via spectral properties of the Koopman operator. *Annual Review of Fluid Mechanics*, 45(1):357–378, 2013.

[152] J.L. Proctor, S.L. Brunton, and J.N. Kutz. Dynamic mode decomposition with control. *SIAM Journal on Applied Dynamical Systems*, 15(1):142–161, 2016.

[153] J.H. Tu, C.W. Rowley, S.L. Luchtenburg, D.M. Brunton, and J.N. Kutz. On dynamic mode decomposition: theory and applications. *Journal of Computational Dynamics*, 1(2):391–421, 2014.

[154] J. Page and R.R. Kerswell. Koopman analysis of Burgers equation. *Physical Review Fluids*, 3:071901, Jul 2018.

[155] J. Page and R.R. Kerswell. Koopman mode expansions between simple invariant solutions. *Journal of Fluid Mechanics*, 879:1–27, 2019.

[156] M.P. Deisenroth, A.A. Faisal, and C. Soon Ong. *Mathematics for Machine Learning*. Cambridge University Press, 2020.

[157] B. Schölkopf, A. Smola, and K.-R. Müller. Nonlinear component analysis as a kernel eigenvalue problem. *Neural Computation*, 10(5):1299–1319, 07 1998.

[158] S.T. Roweis and L.K. Saul. Nonlinear dimensionality reduction by locally linear embedding. *Science*, 290(5500):2323–2326, 2000.

[159] D.L. Donoho and G. Carrie. Hessian eigenmaps: locally linear embedding techniques for high-dimensional data. 100(10):5591–5596, 2003.

[160] Z. Lai and S. Nagarajaiah. Sparse structural system identification method for nonlinear dynamic systems with hysteresis/inelastic behavior. *Mechanical Systems and Signal Processing*, 117:813–842, 2019.

[161] A. Ben Abdessalem, N. Dervilis, D.J. Wagg, and K. Worden. Model selection and parameter estimation of dynamical systems using a novel variant of approximate Bayesian computation. *Mechanical Systems and Signal Processing*, 122:364–386, 2019.

[162] S.A. Billings. *Nonlinear System Identification: NARMAX Methods in the Time, Frequency, and Spatio-Temporal Domains*. Springer, 2013.

[163] A.J. Roberts. The utility of an invariant manifold description of the evolution of a dynamical system. *SIAM Journal on Mathematical Analysis*, 20(6):1447–1458, 1989.

[164] N. Fenichel and J.K. Moser. Persistence and smoothness of invariant manifolds for flows. *Indiana University Mathematics Journal*, 21(3):193–226, 1971.

[165] N. Fenichel. Asymptotic stability with rate conditions. *Indiana University Mathematics Journal*, 23(12):1109–1137, 1974.

[166] N. Fenichel. Asymptotic stability with rate conditions, II. *Indiana University Mathematics Journal*, 26(1):81–93, 1977.

[167] N. Fenichel. Geometric singular perturbation theory for ordinary differential equations. *Journal of Differential Equations*, 31(1):53 – 98, 1979.

[168] J.E. van Engelen and H.H. Hoos. A survey on semi-supervised learning. *Machine Learning*, 109:373–440, 2020.

[169] X. Cabré, E. Fontich, and R. De la lLave. The parameterization method for invariant manifolds I: manifolds associated to non-resonant subspaces. *Indiana University Mathematics Journal*, 52(2):283–328, 2003.

[170] X. Cabré, E. Fontich, and R. De la lLave. The parameterization method for invariant manifolds II: regularity with respect to parameters. *Indiana University Mathematics Journal*, 52(2):329–360, 2003.

[171] X. Cabré, E. Fontich, and R. De la lLave. The parameterization method for invariant manifolds III: overview and applications. *Journal of Differential Equations*, 218(2):444–515, 2005.

[172] A. Haro, M. Canadell, J. Figueras, and J.M. Luque, A. Mondelo. *The Parameterization Method for Invariant Manifolds*, volume 195 of *Applied Mathematical Sciences*. Springer International Publishing, 1st edition, 2016.

[173] S. Jain, P. Tiso, and G. Haller. Exact nonlinear model reduction for a von Kármán beam: slow-fast decomposition and spectral submanifolds. *Journal of Sound and Vibration*, 423:195–211, 2018.

[174] J. Murdock. *Normal Forms and Unfoldings for Local Dynamical Systems*. Springer Monographs in Mathematics. Springer-Verlag New York, 2003.

[175] R. Szalai. Invariant spectral foliations with applications to model order reduction and synthesis. *Nonlinear Dynamics*, 101:2645–2669, 2020.

[176] H. Kantz and T. Schreiber. *Nonlinear Time Series Analysis*. Cambridge University Press, 2nd edition, 2003.

[177] P. Avitabile. *Modal Testing, A Practitioner's Guide*. Wiley, 2017.

[178] K. Taira, S.L. Brunton, S.T. M. Dawson, C.W. Rowley, T. Colonius, B.J. McKeon, O.T. Schmidt, S. Gordeyev, V. Theofilis, and L.S. Ukeiley. Modal analysis of fluid flows: an overview. *AIAA Journal*, 55(12):4013–4041, 2017.

[179] S. Wiggins. *Normally Hyperbolic Invariant Manifolds in Dynamical Systems*, volume 105 of *Applied Mathematical Sciences*. Springer-Verlag New York, 1994.

[180] H. Whitney. Differentiable manifolds. *Annals of Mathematics*, 37(3):645–680, 1936.

[181] F. Takens. Detecting strange attractors in turbulence. In D. Rand and L. Young, editors, *Dynamical Systems and Turbulence, Warwick 1980*, pages 366–381. Springer Berlin Heidelberg, Berlin, Heidelberg, 1981.

[182] J. Stark. Delay embeddings for forced systems. I. Deterministic forcing. *Journal of Nonlinear Science*, 9:255–332, 1999.

[183] T. Sauer, J.A. Yorke, and M. Casdagli. Embedology. *Journal of Statistical Physics*, 65:579–616, 1997.

[184] M. Monge. *Application de l'Analyse a la Géométrie*. Libraire de l'Eecole Impeériale Polytechnique, 1807.

[185] J.W. Robbin and D.A. Salamon. *Introduction to Differential Geometry*. Preprint, 2021.

[186] O. Barrett. *Elementary Differential Geometry, Revised 2nd Edition*. Academic Press, 2006.

[187] J.M. Lee. *Introduction to Smooth Manifolds*, volume 218 of *Graduate Texts in Mathematics*. Springer-Verlag New York, 2012.

[188] R.A. Waltz, J.L. Morales, J. Nocedal, and D. Orban. An interior algorithm for nonlinear optimization that combines line search and trust region steps. *Mathematical Programming*, 107(3):391–408, 2007.

[189] A.R. De Pierro and M. Wei. Some new properties of the equality constrained and weighted least squares problem. *Linear Algebra and its Applications*, 320(1):145–165, 2000.

[190] C.L. Siegel. Iteration of analytic functions. *Annals of Mathematics*, 43:607–612, 1942.

[191] C.L. Siegel. Über die normalform analytischer differentialgleichungen in der nähe einer gleichgewichtslösung. *Nachrichten der Akademie der Wissenschaften in Göttingen, Mathematisch-Physikalische Klasse*, pages 21–30, 1952.

[192] S. Sternberg. On the structure of local homeomorphisms of euclidean n-space, II. *American Journal of Mathematics*, 80(3):623–631, 1958.

[193] S. Jain, T. Thurnher, M. Li, and G. Haller. SSMTool-2.0: Computation of invariant manifolds & their reduced dynamics in high-dimensional mechanics problems, 2021.

[194] J.F. Doyle. *Wave Propagation in Structures*. Springer-Verlag, 1989.

[195] C.H.K. Williamson. Vortex dynamics in the wake of a cylinder. In S.I. Green, editor, *Fluid Vortices. Fluid Mechanics and Its Applications*, volume 30, pages 155–234. Springer, Dordrecht, 1995.

[196] J.-C. Loiseau, S.L. Brunton, and B.R. Noack. From the POD-Galerkin method to sparse manifold models. In P. Benner, editor, *Handbook of Model Order Reduction, Volume II: Applications*, pages 1–47. De Gruyter GmbH, 2019.

[197] D. Barkley and R.D. Henderson. Three-dimensional Floquet stability analysis of the wake of a circular cylinder. *Journal of Fluid Mechanics*, 322:215–241, 1996.

[198] G. Karniadakis and G.S. Triantafyllou. Three-dimensional dynamics and transition to turbulence in the wake of bluff objects. *Journal of Fluid Mechanics*, 238:1–30, 1992.

[199] B.R. Noack, K. Afanasiev, M. Morzyński, G. Tadmor, and F. Thiele. A hierarchy of low-dimensional models for the transient and post-transient cylinder wake. *Journal of Fluid Mechanics*, 497:335–363, 2003.

[200] M. Carini, F. Auteri, and F. Giannetti. Centre-manifold reduction of bifurcating flows. *Journal of Fluid Mechanics*, 767:109–145, 2015.

[201] J.-C. Loiseau and S.L. Brunton. Constrained sparse Galerkin regression. *Journal of Fluid Mechanics*, 838:42–67, 2018.

[202] S.L. Brunton, B.R. Noack, and P. Koumoutsakos. Machine learning for fluid mechanics. *Annual Review of Fluid Mechanics*, 52(1):477–508, 2020.

[203] A. Logg, K.-A. Mardal, G.N. Wells, et al. *Automated Solution of Differential Equations by the Finite Element Method*. Springer, 2012.

[204] H.P. Langtangen and A. Logg. *Solving PDEs in Python*, volume 3 of *Simula SpringerBriefs on Computing*. Springer, 2016.

[205] P.G. Drazin and W.H. Reid. *Hydrodynamic Stability*. Cambridge Mathematical Library. Cambridge University Press, 2nd edition, 2004.

[206] J.-C. Loiseau, M. A. Bucci, S. Cherubini, and J.-C. Robinet. Time-stepping and Krylov methods for large-scale instability problems. In A. Gelfgat, editor, *Computational Modelling of Bifurcations and Instabilities in Fluid Dynamics*, pages 33–73. Springer International Publishing, Cham, 2019.

[207] L.D. Landau. On the problem of turbulence. *Dokl. Akad. Nauk SSSR*, 44(8):339–349, 1944.

[208] E. Palm. On the tendency towards hexagonal cells in steady convection. *Journal of Fluid Mechanics*, 8(2):183–192, 1960.

[209] J.T. Stuart. On the non-linear mechanics of wave disturbances in stable and unstable parallel flows. Part 1. The basic behaviour in plane Poiseuille flow. *Journal of Fluid Mechanics*, 9(3):353–370, 1960.

[210] J. Watson. On the non-linear mechanics of wave disturbances in stable and unstable parallel flows. Part 2. The development of a solution for plane Poiseuille flow and for plane Couette flow. *Journal of Fluid Mechanics*, 9(3):371–389, 1960.

[211] K. Fujimura. Centre manifold reduction and the Stuart-Landau equation for fluid motions. *Proceedings: Mathematical, Physical and Engineering Sciences*, 453(1956):181–203, 1997.

[212] M.R.W. Brake. *The mechanics of jointed structures: recent research and open challenges for developing predictive models for structural dynamics*. Springer International Publishing, 2018.

[213] T.P. Sapsis, D.D. Quinn, A.F. Vakakis, and L.A. Bergman. Effective stiffening and damping enhancement of structures with strongly nonlinear local attachments. *Journal of Vibration and Acoustics*, 134(1):011016, 2012.

[214] A. Haro and R. de la Llave. A parameterization method for the computation of invariant tori and their whiskers in quasi-periodic maps: rigorous results. *Journal of Differential Equations*, 228(2):530–579, 2006.

[215] A. Robinson. Did Einstein really say that? *Nature*, 557(30), 2018.